UNIVERSITÀ DI GENOVA

FONDAZIONE ISTITUTO ITALIANO DI TECNOLOGIA (IIT)

Doctoral School on "Nanochemistry"

XXX Cycle

Production and processing of graphene and 2D crystal-based inks for energy conversion devices

Doctor of Philosophy (Ph.D.) Thesis

Ph.D. candidate:

Leyla Najafi

Supervisor:

Dr. Francesco Bonaccorso (Graphene Labs, Istituto Italiano di Tecnologia)

CO-Supervisors:

Dr. Vittorio Pellegrini (Graphene Labs, Istituto Italiano di Tecnologia)

Prof. Daniele Marrè (Department of Physics, University of Genova)

Tutor:

Dr. Sebastiano Bellani (Graphene Labs, Istituto Italiano di Tecnologia)

Reviewers:

Prof. Aldo Di Carlo (Dipartimento di Ingegneria Elettronica, Università di Roma)

Prof. Xinliang Feng (Technische Universitaet Dresden)

Thesis Submission: *February 2018*

Thesis Dissertation: *March 2018*

***Mom and Dad**, I have no words to acknowledge the sacrifices you made and the dreams you had to let go, just to give me a shot at achieving mine. Thanks.*

Acknowledgement

I am very happy and thankful to achieve at this stage in my life and career. Surely, I could not get where I am without the help and support of many people.

Firstly, I am grateful to my supervisor, Dr. Francesco Bonaccorso , His expertise, understanding, patience, generous guide and support, made it possible for me to work on a topic that was a great interest to me. It was pleasure working with him.

I am grateful to Dr. Vittorio Pellegrini for giving me full access to the research facilities at Graphene Labs “Istituto Italiano di Tecnologia” that allowed me for carrying out this research work.

I would like to express my gratitude to Prof. Daniele Marrè, my academic Co-supervisor at Department of Physics “ University of Genova”.

I would like to express my sincere gratitude to my mentor and friend Dr. Sebastiano Bellani for the continuous support of my Ph.D. thesis and related research, for his patience, motivation, and immense knowledge. His guidance helped me in all the time of research and writing of this thesis. I could not have imagined having a better advisor and mentor for my Ph.D. study.

I would like to acknowledge the valuable input of Dr. Antonio Esau Del Rio Castillo, who contributed to many stimulating discussions that helped to shape this projects.

My sincere thanks also go to Dr. Aldo Di Carlo and his group at Dept. Electronics Engineering, University of Rome, who provided me an opportunity to join their team, and who gave access to the laboratory and research facilities. Without their precious support it would not be possible to conduct this research.

My thanks also go out to the technicians of graphene lab, Elisa Mantero, Luca Gagliani, Manuel Crugliano. This work would be not materialized without their support. It was a great pleasure and honor working with them.

I would like to express my gratitude and many thanks to all my friends that made my time in IIT very pleasant. I feel the need to thank each of them personally at the end of this work.

My Special thanks go to my husband Dr. Reinier Oropesa-Nuñez, without his patience and support I couldn't make it. He made my road easier to walk on it and gave me the strength to continue over adversities.

Last but not the least, I would like to thank my family, specially my Mom and Dad for supporting me spiritually and unconditional throughout writing this thesis and my life in general.

Scientific Publications

1. Engineered MoSe2-based heterostructures for efficient electrochemical hydrogen evolution reaction

L. Najafi, S. Bellani, R. Oropesa-Nuñez, A. Ansaldo, A. E. Del Rio Castillo, M. Prato, and F. Bonaccorso. Adv. Energy Mater. 1703212, (2018).

2. Doped-$MoSe_2$ nanoflakes/3d metal oxide-hydr(oxy)oxides hybrid catalysts for pH-universal electrochemical hydrogen evolution reaction

L.Najafi, S. Bellani, R. Oropesa-Nuñez, A. Ansaldo, M. Prato, A. E. Del Rio Castillo and F. Bonaccorso. (submitted)(2018).

3. Conductive ITO nanoparticles break optical transparency/high-areal capacitance trade-off for advanced aqueous supercapacitors.

S. Bellani, ***L. Najafi***, G. Tullii, A. Ansaldo, R. Oropesa-Nuñez, M. Prato, M.Colombo, M. R. Antognazza, F. Bonaccorso. J. Mater. Chem. A. 5, 25177-25186 (2017).

4. Extending the continuous operating lifetime of perovskite solar cells with a molybdenum disulfide hole extraction interlayer

G. Kakavelakis, I. Paradisanos, B. Paci, A. Generosi, M. Papachatzakis, T. Maksudov, A. E. Del Rio Castillo, ***L. Najafi***, G. Kioseoglou, E. Stratakis, F. Bonaccorso, and E. Kymakis. Adv. Energy Mater., 1702287, (2018).

5. Thioethyl-porphyrazine/Nanocarbon Hybrids for Photoinduced Electron Transfer.

S. Belviso, A. Capasso, E. Santoro, ***L. Najafi***, F. Lelj, S. Superchi, D. Casarini, C. Villani, D. Spirito, S.Bellani, A. E. Del Rio Castillo, and F. Bonaccorso. (submitted)(2018).

6. Carbon coated MoS_2 flakes as anode for lithium-ion batteries.

D. A. Dinh, H. Sun, ***L. Najafi***, A. E. Del Rio Castillo, A. Ansaldo, Z. Dang, C. Di Giovanni, V. Pellegrini, and F. Bonaccorso. (submitted)(2018).

7. Graphene and 2D materials for high efficient and stable perovskite solar cells.

A. Agresti, S. Pescetelli, ***L. Najafi***, F. Bonaccorso, Y. Busby and A. Di Carlo, IEEE NANO 2017.

8. Solution-Processed Hybrid Graphene Flake/2H-MoS_2 Quantum Dot Heterostructures for Efficient Electrochemical Hydrogen Evolution.

L. Najafi, S. Bellani, B. Martin-Garcia, R. Oropesa-Nuñez, A. E. Del Rio Castillo, M. Prato, I. Moreels, and F. Bonaccorso, Chem. Mater. 29, 5782–5786 (2017).

9. Graphene-Based Hole-Selective Layers for High-Efficiency, Solution-Processed, Large-Area, Flexible, Hydrogen-Evolving Organic Photocathodes.

S. Bellani, ***L. Najafi***, B. Martin-Garcia, A. Ansaldo, A. E. Del Rio Castillo, M. Prato, I. Moreels and F. Bonaccorso, J. Phys. Chem. C. 121, 21887–21903 (2017).

10. Few-layer MoS2 flakes as a hole-selective layer for solution-processed hybrid organic hydrogen evolving Photocathodes.

S. Bellani, ***L. Najafi***, A. Capasso, A.E. Del Rio Castillo, M. Rosa Antognazza and F. Bonaccorso, J. Mater. Chem. A. 5, 4384-4396 (2017).

11. Ruthenium Tetrazole Based Electroluminescent Device: Key Role of Counter Ions for Light Emission Properties.

H. Shahroosvand, ***L. Najafi***, A. Sousaraei, E. Mohajerani, M. Janghouri, and F. Bonaccorso, J. Phys. Chem. C. 120, 24965–24972 (2016).

12. Few-Layer MoS_2 Flakes as Active Buffer Layer for Stable Perovskite Solar Cells.

A. Capasso, F. Matteocci, ***L. Najafi***, M. Prato, J. Buha, L. Cinà, V. Pellegrini, A.Di Carlo, F. Bonaccorso, Adv. Energy Mater. 6, 1600920 (2016).

13. Spray deposition of exfoliated MoS_2 flakes as hole transport layer in perovskite-based photovoltaics.

A. Capasso, A.E. Del Rio Castillo, ***L. Najafi*** , V. Pellegrini, F. Bonaccorso, F. Matteocci, L. Cinà, A. Di Carlo. IEEE NANO 2015.

Communications at Conferences

Orals

1. S. Bellani, F. Bonaccorso, ***L. Najafi***, M. Prato, A. Del Rio, A. Ansaldo, I. Moreels, B. Garcia, R. Oropesa-Nuñez "Graphene Related 2D Crystals and Hybrid Systems for High-Efficiency, Solution-Processed, Large-Area, Flexible, Stable Electrocatalysts and Photocathodes for Hydrogen Evolution Reaction" MRS 2017, 26-1 Dec. Boston.

2. D. A. Dinh, H. Sun, ***L. Najafi***, A. E. Del Rio Castillo, A. Ansaldo, C. Di Giovanni, V. Pellegrini and F. Bonaccorso *"Facile synthesis of MoS_2-flakes/amorphous-carbon composite as anode for lithium-ion Batteries"* Applied Nanotechnology and Nanoscience International Conference 2017, 18-20 Oct. 2017, Rome, Italy.

3. D. A. Dinh, H. Sun, ***L. Najafi***, C. Di Giovanni, A. E. Del Rio Castillo, A. Ansaldo, V. Pellegrini, and F. Bonaccorso, "*Carbon coated MoS_2 flakes as anode for lithium-ion batteries*" NanoMaterials for Energy and Environment, 28 - 30 June 2017, Paris, France.

4. S. Bellani, ***L. Najafi***, B. Martín-García, A. Ansaldo, A. E. Del Rio Castillo, M. Prato, I. Moreels and F. Bonaccorso "*Graphene-based Hole Selective Layers for High-efficiency, Solution-processed, Large-area, Flexible, Stable Hydrogen-Evolving Organic Photocathodes*" Graphene 2017, 28-31 March 2017, Barcelona, Spain.

5. ***L. Najafi***, S. Bellani, A. Capasso, A. E. Del Rio Castillo, M. R. Antognazza, and F. Bonaccorso, "*Few-layer MoS_2 Flakes as Hole-selective Layer for Solution-processed Hybrid Organic Hydrogen-evolving Photocathodes*" Graphene 2017, 28-31 March 2017, Barcelona, Spain.

6. A. Capasso, F. Matteocci, ***L. Najafi***, V. Pellegrini, A. Di Carlo, F. Bonaccorso, "*Stable perovskite solar cells with a MoS_2 active buffer layer"* RPGR 2016, 25-29 September 2016, Seoul, Korea.

7. A. Capasso, F. Matteocci, ***L. Najafi***, M. Prato, V. Pellegrini, A. Di Carlo, F. Bonaccorso, "*MoS_2 flakes as hole transport layer in perovskite-based photovoltaics"* Graphene Week 2016, June 13-17, 2016, Warsaw, Poland.

8. A. Capasso, F. Matteocci, L. Cinà, A.E. Del Rio Castillo, ***L. Najafi***, V. Pellegrini, A. Di Carlo, F. Bonaccorso "Spray deposition of exfoliated MoS_2 flakes as hole transport layer in perovskite-based photovoltaics" IEEE Nano 2015, 27-30 July, Rome (Italy).

Posters

1. ***L. Najafi***, A. Capasso, F. Matteocci, M. Prato, J. Buha, L. Cinà,V. Pellegrini, A. Di Carlo, F. Bonaccorso "Few-layer MoS_2 flakes as active buffer layer for stable perovskite solar cells." 2st International Conference on Perovskite Solar Cells and Optoelectronic. 26-28 September 2016, Genova, Italy.

2. ***L. Najafi*** , A. Capasso, A.E. Del Rio Castillo, V. Pellegrini, F. Bonaccorso, F. Matteocci, L. Cinà, A. Di Carlo. "Stable perovskite solar cells with spray deposition of exfoliated MoS_2 flakes as hole transport". XXth International Krutyn Summer School. 12-18 June 2016, Warsaw, Poland.

3. ***L. Najafi***, A. Capasso, F. Matteocci, M. Prato, J. Buha, L. Cinà,V. Pellegrini, A. Di Carlo, F. Bonaccorso." Exfoliated MoS_2 flakes as hole transport layer in perovskite-based photovoltaics." Graphene 2016. 19-22 April 2016, Genova, Italy. (Winner of student poster award)

4. S. Belviso, A. Capasso, E. Santoro, ***L. Najafi***, F. Lelj, S. Superchi, D. Casarini, C. Villani, D. Spirito, S.Bellani, A. E. Del Rio Castillo, and F. Bonaccorso. "Supramolecular hybrids of thio-ethylporphyrazine with graphene and carbon nanotubes for photo induced electron transfer." Graphene 2016 . 19-22 April 2016 , Genova, Italy.

5. ***L. Najafi***, A. Capasso, F. Matteocci, M. Prato, J. Buha, L. Cinà,V. Pellegrini, A. Di Carlo, F. Bonaccorso. "MoS_2 flakes as a hole transport material for stable perovskite solar cells. " 1st International Conference on Perovskite Solar Cells and Optoelectronic. 27-29 September 2015, Lausanne, Switzerland.

6. ***L. Najafi***, S. Belviso, A. Capasso, E. Santoro, F. Lelj, S. Superchi, D. Casarini, C. Villani, D. Spirito, S.Bellani, A. E. Del Rio Castillo, and F. Bonaccorso. "Hybrids of thio-ethylporphyrazine with nano carbons for photo induced electron transfer." International Conference on Hybrid and Organic Photovoltaics. 10-13 May 2015, Rome, Italy.

Table of Contents

List of Acronyms and Abbreviations

μ	Mobility
0D	Zero-dimensional
1D	One-dimensional
2D	Two-dimensional
3D	Three-dimensional
ABL	Active buffer layer
AFM	Atomic force microscopy
AgCl	Silver chloride
b	Tafel Slope
BHJ	Bulk heterojunction
BN	Boron nitride
CB	Conduction band
Cd^{2+}	Cadmium cations
CNTs	Carbon nanotubes
Co^{2+}	Cobalt cations
CSL	Charge-selective layer
Cu^{2+}	Copper cations
CVD	Chemical vapor deposition
DI	Deionized water
DMF	N,N-dimethylformamide
DMSO	Dimethyl sulfide
DSSC	Dye-sensitized solar cell
$E_{applied}$	Applied potentials
EC	Electrocatalyst
EDX	Energy-dispersive X-ray spectroscopy
EIS	Electrochemical impedance spectroscopy
EQE	External quantum efficiency
ESL	Electron-selective layer
ETL	Electron transporting layer
F4TCNQ	2,3,5,6-Tetrafluoro-7,7,8,8-tetracyanoquinodimethane
FE	Faradaic Efficiency
Fe^{2+}	Iron cations
FF	Fill factor
FGO	Functionalized graphite oxide
FLG	Few layers graphene
FoM	Figures of Merit
F-rGO	Functionalized reduced graphene oxide
FTO	Fluorine-doped tin oxide
FWHM	Full width half maximum
GC	Glassy carbon

GO	Graphene oxide
H_2O	Water
H_2SO_4	Sulfuric acid
H_3O^+	Hydronium ion
H_{ads}	Hydrogen adsorbed
$HAuCl_4$	Chloroauric acid
HER	Hydrogen evolution reaction
HOMO	Highest occupied molecular orbital
HOPG	Highly ordered pyrolytic graphite
HSL	Hole selective layers
HTL	Hole transporting layer
i0	Exchange current
IPA	2-Propanol
IPCE	Incident photonto current efficiency
IR	Infrared
ITO	Indium tin oxide
j_0	Exchange currenty density
$J_{0V\ vs\ RHE}$	Photocurrent at 0 V *vs.* RHE
J_{sc}	Short circuit current
J-V curve	Current-voltage measurements
K points	Dirac points
KCl	Potassium chloride
$KMnO_4$	Potassium permanganate
LED	Light-emitting diode
Li^+	Lithium cations
LIB	Lithium-ion battery
LiOH	Lithium hydroxide
Li-TFSI	Lithium bis(trifluoromethanesulfonyl)imide
LPE	Liquid phase exfoliation
LSV	Linear sweep voltammetry
LUMO	Lowest unoccupied molecular orbital
m*	Mass
MAI	Methylammonium iodide
MAPbBr3	Methyl-ammonium lead bromide
MAPbI3	Methyl-ammonium lead iodide
MC	Mechanical cleavage
MCl2	Transition metal chloride
MoO_3	Molybdenum trioxide
MoS2	Molybdenum diselenide
MoSe2	Molybdenum disulfide
MPTMS	3-mercaptopropyl)trimethoxysilane
MWCNT	Multi walled carbon nanotubes
η_{10}	Overpotential at 10 mA cm^{-2}-cathodic current density

$NaNO_3$	Sodium nitrate
n-BuLi	n-butyl lithium
Ni^{2+}	Nickel cations
NMP	N-methyl-2-pyrrolidone
ηsth	Solar-to-hydrogen conversion efficiency
OAS	Optical absorption
OC	Open circuit
OER	Oxygen evolution reaction
PbBr2	Lead(II) bromide
PbCl2	Lead(II) chloride
PbI2	Lead(II) iodide
PCBM	Phenyl-C_{61}-butyric acid methyl ester
PCE	Energy conversion efficiency
PEC	Perovskite solar cell
PEDOT:PSS	Poly(3,4-ethylenedioxythiophene) polystyrene sulfonate
PEM	Proton exchange membrane
PET	Polyethylene terephthalate
PL	Photoluminescence
P_{max}	Maximum power point
Pos	Position
PSC	Photo-electrochemical cell
Pt	Platinum
PTAA	Poly(triaryl amine)
PV	Photovoltaic
q	Charge of the carrier
QDs	Quantum Dots
QDSC	Quantum dot solar cells
R_a	Roughness
RBMs	Radial breathing modes
RGO	Reduced graphene oxide
RHE	Reversible hydrogen electrode
rr-P3HT	Poly(3-hexylthiophene-2,5-diyl)
SBS	Sedimentation-based separation
SC	Short circuit
SEM	Scanning electron microscopy
SIB	Sodium-ion battery
SiC	Growth on silicon carbide
SLG	Single layers graphene
Spiro-OMeTAD	2,2',7,7'-tetrakis(N,N-di-p-methoxyphenylamine)-9,9'-spirobifluorene
SWCNT	Single walled carbon nanotube
T	Transmittance
TBP	Tert-butylpyridine

TCO	Transparent conductive oxide
TEM	Transmission electron microscopy
TiO2	Titanium dioxide
TMD	Transition metal dichalcogenides
TPV	Transient photovoltage measurements
UPS	Ultraviolet photoelectron spectroscopy
UV	Ultraviolet
VB	Valence band
VBM	Valence band maximum
V_{mpp}	Potential at maximum power point
Vo	Onset potential
V_{oc}	Open circuit voltage
WF	Work function
XPS	X-ray photoelectron spectroscopy
XRD	X-ray diffraction
Zn^{2+}	Zinc cations
ZnO	Zinc oxide
α	Absorption coefficient
Γ	Brillouin zone center
γ	Surface energy
ΔGH^0	Gibbs free energy
η_F	Current-to-hydrogen faradaic efficiency
λ	Wavelength
π	Bonding molecular orbital
π*	Antibonding molecular orbital
τ	Average scattering time
ϕsaved	Ratiometric power-saved efficiency

Introduction

In recent years the focus on renewable energy sources has been raised due to increasing oil prices and the growing concern for global warming. Currently, most of the world's energy consumption is fossil fuel based, but there is an increasing interest in replacing the fossil fuels with renewable resources. In this context, solar energy represents the most significant contribution of energy worldwide, which, although has low power density, could potentially satisfies the global energy demand on its own. However, several challenges must be overcome to make solar energy viable and competitive on a large scale. For example, enhancing the performance of solar energy conversion systems through increased efficiency and use of durable materials; reducing the cost of the material, fabrication and installation, so that these systems can be deployed on a large scale.

Hydrogen (H_2), as energy carrier, is one of the most promising long-term solutions for renewable energy, due to its low environmental impact and high energy density (between 120-140 MJ kg^{-1}). However, H_2 is mostly produced from fossil fuels, which are limited in supply and create harmful CO_2 emissions. Photo-electrochemical (PEC) water splitting, a process in which H_2O is split into H_2 and O_2 using the energy from sunlight, is a promising technology for renewable hydrogen production. Efficient, inexpensive and electrochemically stable materials must be developed to make viable and widespread PEC water splitting devices implementation. However, essential barriers such as the creation of active catalysts, corrosion prevention strategies, and techniques for successfully integrating all required components of the PEC device must be overcome. Essential barriers also remain standing in the pathway of photovoltaic energy conversion efficiency. The continuous development of novel device concepts, materials, and fabrication processes has overcome these obstacles partially, contributing to decreasing the cost of solar power. Recently, perovskite solar cells (PSCs), considered as a promising direction for low-cost and highly efficient energy conversion, have shown a rapid growth of efficiency from 3.8% to 22.7 %. PCSs absorbers possess several distinctive features including broad light absorption from the visible to the near-infrared region, a high extinction coefficient, large charge carrier diffusion lengths, tunable optical properties and low-temperature solution processability. These aforementioned features are attracting considerable attention in the photovoltaic industry. However, further research in PSCs regarding the enhancement of their performance and stability,

lowering their fabrication costs, as well as developing environmentally benign perovskites is required.

In this scenario, graphene, a one-atom-thick planar sheet of carbon atoms densely packed in a honeycomb crystal lattice, has attracted great interest in recent years due to its high specific surface area and the excellent mechanical, electrical, optical and thermal properties. The advantage of these unique features has been exploited using graphene as a component of advanced (opto)electronic devices (*e.g.,* high-frequency devices, touch screens, flexible and wearable devices, ultrasensitive sensors/photodetectors, light emitting diodes and ultrafast lasers), as well as novel energy storage and conversion systems, including batteries, supercapacitors, as well as solar and photo-electrochemical (PEC) cells. However, graphene is a material without an electronic bandgap, making it deemed unfavorable as active component in application requiring semi-conductive properties. Therefore, other 2D semiconducting materials have been sought-after. In particular, transition metal dichalcogenides (TMDs), group III and IV compounds, and graphene analogues such as boron nitride (BN), typically exhibit strong in-plane covalent bonding and weak out-of-plane van der Waals interactions through the interlayer gap. These features, together with the quantum confinement and surface effects, are the reason for many interesting layering-dependent properties found in atomically thin 2D materials nanosheets but no on their bulk counterparts. For example, some bulk materials are semiconductors with indirect band gaps, while their single-layer nanosheets are semiconductors with direct band gaps, resulting in dramatic changes of their properties such as the enhancement of photoluminescence. The physical and chemical properties of 2D materials can also be related to the interlayer distance which triggers a series of regulations in the band gap, conductivity, thermoelectric and photovoltaic properties and superconductivity. In particular, varying the interlayer distance of 2D materials, it is possible to obtain novel heterostructures properties, which may not be achieved in the initial materials. A larger interlayer spacing also means further active sites, an ion-accessible surface in the interlayer space, accessible for catalysis. The latter will considerably enhance the performance of 2D materials in energy storage devices (*e.g.,* lithium-ion battery (LIB), sodium-ion battery (SIB) and supercapacitor), and energy conversion devices (*e.g.,* solar cells, fuel cells).

My Ph.D. research aimed to design and synthesize 2D materials for the production of high performance 2D materials-based (opto)electronic devices. Firstly, I produced graphene and 2D-TMDs from their parent bulk crystals in suitable liquids to yield dispersions by liquid phase

exfoliation (LPE) or chemical methods (Li-intercalation). This allowed the formulation of functional inks, which can be processed by large-scale, cost-effective solution processed techniques reaching high-electrocatalytic performance (η_{10} of 100 mV and cathodic current density > 100 mA cm^{-2} at η inferior to 200 mV) compatible with high-throughput industrial implementation focused on developing high-volume liquid-phase and chemical exfoliation for a wide variety of layered materials. These techniques have been optimized to control the flake size and to increase the edge-to-surface ratio, which is crucial for optimizing electrode performance in the final applications.

At the next step, I widened my activity towards the implementation of novel 2D materials-based (photo)electrochemical cell and solar cell platforms. In fact, the development of novel, sustainable methods for scalable and efficient hydrogen (H_2) production, as well the increase of the efficiency and the stability of the PSCs represented the main challenges of my activity. In order to attempt this, I exploited 2D materials as electro catalysts for H_2 evolution reaction and hole selective layers (HSLs) in organic H_2-evolving photocathodes. In detail, I designed solution-processed hybrid heterostructures based on carbon nanomaterials and 2D-TMDs, Which showing high PEC activity in different pH conditions, *i.e.,* ranging from acid to basic. Afterward, by tuning the electrochemical properties of 2D materials, I exploited graphene derivatives and 2D-TMDs as HSL for boosting the efficiency and the durability of PEC. The 2D material-based interface engineering avoids the recombination loss by preventing recombination defects between the different interface layers. Using 2D materials as interlayer permitted to achieve record high performances concerning all-solution-processed photocathodes (*i.e.*, photocurrent at 0 V *vs.* RHE ($J_{0V\ vs\ RHE}$) of -6.01 mA cm^{-2}, onset potential (V_o) of 0.6 V *vs.* RHE, ratiometric power-saved efficiency (ϕ_{saved}) of 1.11% and operational activity of 20 hours). Moreover, the photocathodes are demonstrated to be effective in different pH environment ranging from acid to basic, showing $J_{0V\ vs\ RHE}$ exceeding 1 mA cm^{-2}. This is pivotal for their exploitation in tandem configurations, where photoanodes operate only in restricted electrochemical conditions. Lastly, I demonstrated the up-scaling feasibility of the as-produced devices by fabricating a large-area (9 cm^2) flexible (onto ITO-PET substrate) photocathodes, with remarkable ϕ_{saved} of 0.31%.

In parallel, I exploited 2D material-based interface engineering also for improving the photovoltaic performance of the PSC. In particular, I successfully introduced 2D MoS_2 film in between the traditional hole transport layer, *i.e.,* 2,2',7,7'-tetrakis(N,N-di-p-methoxyphenylamine)-9,9'-

spirobifluorene (spiro-OMeTAD), and the perovskite absorber, *i.e.*, $CH_3NH_3PbI_3$ (known as $MAPbI_3$), to enhance the efficiency of PSCs. Besides the high power conversion efficiency value achieved (>20%), the addition of 2D-MoS_2 film significantly improved the stability of encapsulated PSCs, setting the state of the art for lifetime tests. Such superior device stability is ascribed to the twofold beneficial role of MoS_2, inhibiting both interface and structural aging pathways. Moreover, I also demonstrated the beneficial role of 2D-MoS_2 in the scaling up of this technology, by realizing large-area cells (>1 cm^2). Therefore, my work paves the way towards high efficiency, large-area and ultra-stable PSCs with lifetimes approaching the industrial standards.

In summary, the research work in my Ph.D. aimed to address the following objectives:

(a) Design, synthesis and characterization of 2D materials, *e.g.*, graphene and TMDs

(b) Integration of the as-produced 2D materials in (photo)electrochemical devices and PSCs.

A summary of the principal studies includes: *i)* Optimization of solution-based exfoliation processes for the synthesis of 2D materials. *ii)* Morphological, optical, electrical and electrochemical characterization of the as-produced 2D material dispersions and inks by different techniques, such as optical absorption (OAS), Raman spectroscopy, transmission electron microscopy (TEM) and atomic force microscopy (AFM). *iii)* Evaluation of 2D materials as electrocatalysts for hydrogen (H_2) evolution reaction (HER). *iv)* Exploitation of 2D materials as novel HSL in organic photoelectrochemical cells. *v)* 2D material-based interface engineering PSCs.

The following dissertation is organized in different chapters, whose content is summarized below.

Chapter 1 provides an overview of 2D materials and their applications. In fact, I underline the morphological, optical, electrical and electrochemical properties of 2D materials, providing a comparison with their bulk counterparts, and how such properties make them suitable for the design and realization of “next-generation” (opto)electronics and energy devices.

Chapter 2 presents the solution-based exfoliation methods, which I developed and used for the production of the 2D materials. A particular attention is paid to the LPE process, as it represents the main technique exploited for the production of 2D materials.

Chapter 3 reports the physicochemical, electrical and electrochemical characterization of the as-produced 2D material dispersions.

Chapter 4 shows the use of the as-produced 2D materials as electrocatalysts for HER. In particular, I investigated the impact of the morphology (lateral size and thickness), crystal structure (material phase), defects and chemical composition (impurity, doping) of 2D materials on the HER-electrocatalytic activity.

Chapter 5 reports the investigation of the use of 2D materials as novel HSL for H_2-evolving organic photocathodes, with a deep understanding on their role for increasing both the efficiency and the electrochemical stability of the devices.

Chapter 6 presents 2D material-based interface engineering for increasing the efficiency and the stability of the PSCs. In particular, it is reported the exploitation of the MoS_2 both as HTL (as replacement of the traditional Spiro-OMeTAD) or as active buffer layer between the perovskite active layer and the Spiro-OMeTAD.

Lastly, **Chapter 7** highlights the main results achieved during the completion of this Ph.D. program.

CHAPTER 1

CHAPTER 1: Two-Dimensional (2D) Material Families and Their Properties

1.1 Graphene

The building block of all organic materials is carbon, which can form a variety of hybridization states with the neighboring carbon atoms, such as sp, sp^2, sp^3. Indeed, due to their valence, the atoms of carbon can bond together in different ways forming the different carbon allotropes. Diamond (sp^3 hybridization) and graphite (sp^2 hybridization) are the best known allotropic forms because their different physical properties (*i.e.,* hardness, density, electrical and thermal conductivity and transparency). Many more allotropes and forms of carbon have been discovered and investigated in the last decades. Low dimensional carbon allotropes, *i.e*., nanoallotropes, include fullerenes (0-dimensional (0D)), carbon nanotubes (CNTs) (1-dimensional (1D)) and graphene (2D). Some of the carbon allotropes are presented in Figure 1.1.

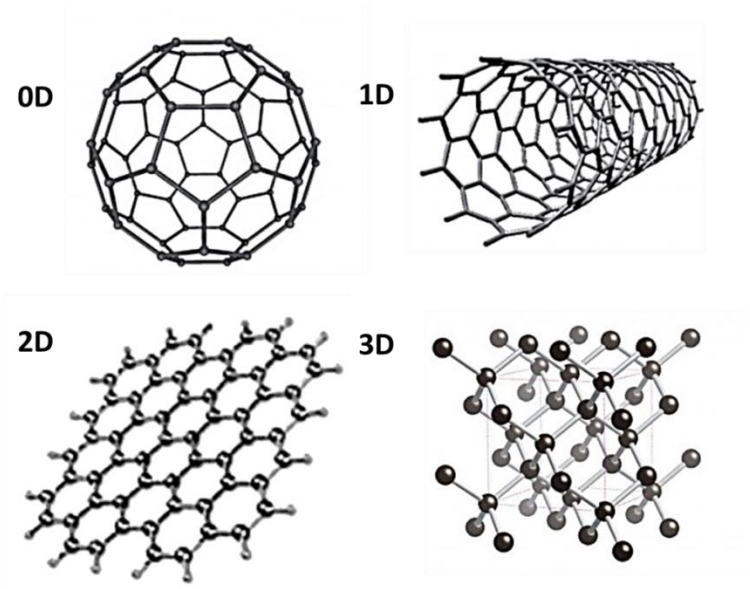

Figure 1.1. Representative allotropes of carbon: fullerenes (0D), carbon nanotubes (1D), graphene (2D) and diamond (3D). [1]

Typically, the properties of these carbon nanoallotropes (*e.g.,* surface area, electrical and thermal conductivity, mechanical strength, *etc.*) make them attractive for a wide range of applications. For example, fullerene represents the state-of-the-art acceptor component for organic photovoltaic, being also widely exploited as electron transport layer in different types of solar cells, selective dielectric films for chemical and bio sensors and *etc.*[2] Carbon nanotubes, probably one of the most

investigated materials in the past decade, have been exploited as electrode for batteries, supercapacitors, fuel cells, biomedical applications and *etc*.[3] Furthermore, the exceptional charge transport, electrical, optical properties of graphene have opened a new and exciting field of research and development of carbon-based electronic and optoelectronic devices, chemical sensors, nanocomposites and energy storage.[4]

Structurally, graphene consists of a two-dimensional honeycomb network of sp^2-hybridized carbon, with carbon-carbon bond distances of 0.142 nm (Figure 1.2).[5] Graphene was firstly studied theoretically in 1947 by P. R. Wallace, [6] who described the graphene as a zero gap semiconductor due to its lack of an electronic energy gap and its vanishing density of states at the K point, where the conduction and valence band meet. The qualitative description of the band structure of the graphene permitted to explain also the conductivity of graphite crystals.[6] The research of graphene grown slowly in the late 20th century hoping to observe superior electrical properties from thin graphite or graphene layers. Various attempts were performed to synthesize graphene including using the same approach for the growth of carbon nanotubes (producing graphite with hundred layers of graphene).[7] However, none of them provided perfect monolayer graphene. It was until 2004 that Andre Geim and Konstantin Novoselov used a successful method to isolate graphene, by mechanical exfoliation of graphite, i.e., "Scotch-Tape method. They obtained few layers graphene flakes. Following this approach, in 2005, they isolated the first-ever free-standing graphene flakes only one atom thick. [4,8] This was the starting point for the launch of a new research field that has brought them to receive the Nobel Prize in Physics in 2010 for groundbreaking experiments regarding the graphene,[9] including the studies of it electronic band structure.

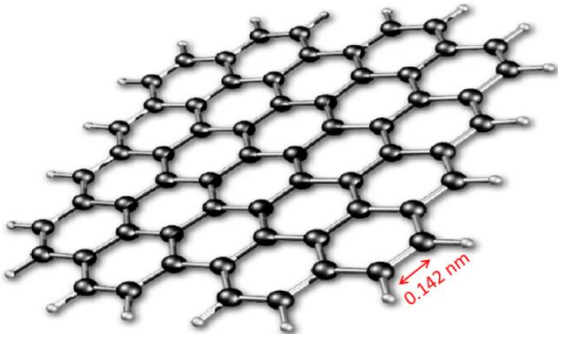

Figure 1.2. Honeycomb lattice structure of graphene with carbon-carbon bond distance.[10]

1.1.1 Electronic Properties

The band structure and therefore the electronic properties of graphene can be described by tight-binding Hamiltonian.[11] Because the bonding and anti-bonding σ-bands are well separated in energy (>10 eV at the Brillouin zone center Γ), they can be neglected in semi-empirical calculations, retaining only the two remaining π-bands.[12] The electronic wave functions from different atoms on the hexagonal lattice overlap.[13] However, the overlap between the $p_z(\pi)$ and the *s* or p_x and p_y orbitals is strictly zero by symmetry. Consequently, the p_z electrons, which form the π-bonds, can be treated independently from the other valence electrons. With one p_z electron per atom in the π–π* model (the s, p_x, p_y electrons fill the low-lying σ-band), the (–) band (Valence band (VB) π (bonding molecular orbital)) is fully occupied, whereas the (+) (conduction band (CB) π* -antibonding molecular orbital-) branch is totally empty. These occupied and unoccupied bands touch at the Dirac points (K points), see Figure 1-3a.[14] In single layer graphene, the unit cell consists of two carbon atoms - the A and B sublattices (see Figure 1-3b). The band structure of graphene exhibits two bands intersecting at two inequivalent points K and K' in the reciprocal space (see Figure 1-3b). Near these points, the electronic dispersion resembles that of relativistic Dirac electrons. For this reason, K and K' are commonly referred to as the "Dirac points". As the valence and conduction bands are degenerate at the Dirac points, graphene is a zero gap semiconductor.[15] Therefore, the Fermi level E_F is the zero energy reference, and the Fermi surface (*i.e.* an abstract boundary in reciprocal space) is defined by K and K'. The dispersion relation at K(K') yields the linear π- and π^*-bands for Dirac fermions:[11]

$$E^{\pm}(\kappa) = \pm \hbar v_F |\kappa| \qquad (1)$$

where $\kappa = k - K$ and v_F is the electronic group velocity, which is given by $v_F = \sqrt{3}\,\gamma_0 a/(2\hbar) \approx 10^6$ m s^{-1}. The linear dispersion given by the equation (1) is the solution to the following effective Hamiltonian at the K(K') point $H = \pm\hbar v_F (\sigma \bullet \kappa)$, where $\kappa = -i\nabla$ and σ are the pseudo-spin Pauli matrices operating in the space of the electron amplitude on the A–B sub-lattices of graphene.[16]

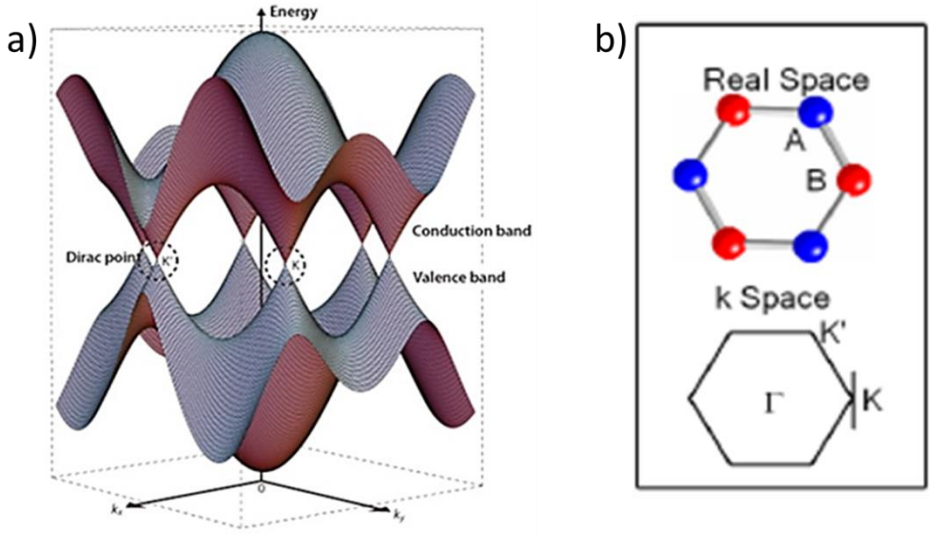

Figure 1.3. a) Schematic diagram of the linear energy band dispersion in graphene at the Dirac points.[17] b) Structure of graphene in the real and momentum space.

For a charge carrier moving through an electric field, mobility (μ) is inversely proportional to the carrier effective mass m*:[18]

$$\mu = \frac{q}{m^*}\tau$$

Where q is the charge of the carrier and τ is the average scattering time. Consequently, extremely high values of μ are expected for electrons in graphene, provided their behavior as massless Dirac fermions, hence free to move for micrometers without scattering at room temperature..[19] Such a low effective mass provides extremely high values of μ, which makes graphene an appealing candidate for many practical applications in electronic devices. As a matter of fact, experimental results at room temperature have shown mobility values around 15000-20000 $cm^2 V^{-1} s^{-1}$, [20] hence much higher compared with silicon, which has values in the order of 1000 $cm^2 V^{-1} s^{-1}$.[21]

1.1.2 Optical Properties

Although graphene is a single atom thick material,[22] it can be optically visualized[23] and its transmittance can be expressed in terms of the fine-structure constant.[24] The absorption spectrum of graphene is quite flat from ultraviolet (UV) to infrared (IR), with a peak at ~270 nm, due to the exciton-shifted van Hove singularity in the density of states.[25] This, in principle, allows graphene to be used over a broad wavelength range (*e.g.* from UV to THz).[26] In few layers graphene (FLG), other absorption features can be seen at lower energies, compared to single layer graphene, attributable to inter-band electronic transition from the unoccupied π* states.[27] The theoretical

transmittance (T) of a freestanding graphene can be derived by applying Fresnel equations, in the thin film limit, for a material with a fixed universal optical conductance ($G_0 = e^2/4\hbar \approx 6.08 \times 10^{-5}\ \Omega^{-1}$), [12] to give:

$$T = (1 + 0.5\,\pi\alpha)^{-2} \approx 1 - \pi\alpha \approx 97.7\ \%$$

where $\alpha = e^2/(4\pi\varepsilon_0\hbar c) = G_0/(\pi\varepsilon_0 c) \approx 1/137$ is the fine-structure constant.[24] The absorbance can be calculated as $A = 2 - \log_{10}\%T = \pi\alpha = 2.3\ \%$. Thus graphene reflect < 0.1 % of the incident light in the visible region[25] and it can be considered as a transparent material. Moreover, it is worth noting that its high T is almost independent from wavelength of the light,[28] due to the linear energy dispersion previously discussed. This is a key advantagecompared to traditional transparent conductors, such as the transparent conductive oxide (TCO) *e.g.,* ITO (Indium Tin Oxide) and fluorine-doped tin oxide (FTO).

1.1.3 Mechanical Properties

The remarkable mechanical properties of graphene are one of the reasons why graphene stands out as an individual material and as a reinforcing agent in composites. Graphene owes these exceptional mechanical properties to the sp^2 bonds that form the hexagonal lattice and opposes a variety of deformations in the plane[29]. In 2008, Hone and coworkers[30]measured, for the first time, the mechanical properties of free-standing atomically perfect nanoscale monolayer graphene by using nanoindentation in an atomic force microscope (AFM). The authors reported that Young's modulus of graphene is E= 1.0 ± 0.1 TPa and an intrinsic strength of 130 GPa. Since then, monolayer graphene known as the strongest material ever tested.

Different values of stiffness, probably arising from the inherent crumpling of graphene in the out-of-plane direction of the monolayer, have been reported[3132]. Crumpling of graphene is inevitable emerging from either out-of-plane flexural phonons or from static wrinkling. The latter is caused by the uneven stress at the boundary of the graphene produced, and it is responsible for the deterioration of the mechanical properties of the material. Another possible origin of crumpling of graphene is the presence of point defects at a finite distance, such as the Stone-Wales defects[33]. Crumpling and wrinkling are critical aspects of graphene, and both play a major role in the design of complex nanomechanical systems.

Another important mechanical property of graphene is its fracture toughness.[29] Zhang et al. determined the fracture toughness of CVD-synthesized graphene. They proved the fracture stress decreased with increasing crack length, and the critical strain energy release rate (G_C) was found to be 15.9 J m^{-2}. The fracture toughness of graphene was estimated as a critical stress intensity factor (K_C) of 4.0 ± 0.6 MPa. [34]

1.1.4 Thermal Properties

The heat flow direction in a two dimensional graphene can be divided into in-plane and out-of-plane directions. High in-plane thermal conductivity is due to covalent sp^2 bonding between carbon atoms, whereas out-of-plane heat flow is limited by weak van der Waals coupling.[35] Simulation work was first performed to predict the thermal conductivity of the monolayer graphene, showed the extremely high value of 6000 W $m^{-1}K^{-1}$ at room temperature,[36] especially if compared to graphite (2000 W $m^{-1}k^{-1}$) and diamond (2200 W $m^{-1}k^{-1}$).[35] Many work were later carried out to obtain the accurate thermal conductivity of the graphene, and it was reported to be 2000-4000 W $m^{-1}K^{-1}$ [35](when it was found in freely suspended samples). The upper end of this range is achieved for isotopically purified samples (0.01% ^{13}C instead of 1.1% natural abundance) with large grains, whereas the lower end corresponds to isotopically mixed samples or those with smaller grain sizes. Naturally, any additional disorder or even residue from sample fabrication will introduce more phonon scattering and lower these values further.[35] It can be seen that graphene presents an excellent thermal conductivity at room temperature which is highest among the any known materials such as diamond, graphite, CNT (3000 W $m^{-1}K^{-1}$ for Multi Walled Carbon Nanotubes (MWCNT)[37] and 3500 W m^{-1} K^{-1} in the case of single walled carbon nanotube (SWCNT).[38]) or metals (*i.e.,* silver (430 W m^{-1} k^{-1}) or copper (380 W m^{-1} k^{-1})). It is expected that thermal properties of graphene can be tuned and will be beneficial for thermoelectric applications.

1.2 Other 2D Materials

The amazing properties of graphene, such as excellent electrical and optical properties, [39] sparked a material revolution around the world. Despite the fascinating properties of graphene, the absence of an electronic bandgap limits its application as active material in logical circuits and in photovoltaics, where semiconducting properties are required. In fact, the very large off-current of graphene at room temperature, due to its zero bandgap, negatively influences the on/off ratio in

the transistor. Moreover, although graphene can absorb all the wavelength of the solar spectrum, the effects of thermal relaxation make challenging the use graphene as a light absorber in solar energy conversion devices. On one hand, researchers tried different methods to introduce a bandgap in graphene, including chemical functionalization[40] and nanostructuring,[41] However, these methods either sacrifice the high μ of graphene (for example, 150 meV bandgap causes the decrease of the μ down to 200 $cm^2V^{-1}s^{-1}$)[42] or require very high voltage (100 V opened a 250 meV bandgap in bilayer graphene)[34]. In fact, the opening of a band gap in graphene is not straightforward, mostly affecting the pristine properties of graphene.[43] On the other hand, new 2D materials have been sought-after. In particular, TMDs (*e.g.,* MoS_2,WS_2, and $NbSe_2$) represent a large family of layered materials with the formula MX_2, where M is a transition metal element from group IV (Ti, Zr or Hf), group V (V, Nb or Ta) or group VI (Mo, W), and X is a chalcogen atom (S, Se or Te) The monolayer TMDs are particularly interesting due to their direct energy band gaps and non-centrosymmetric lattice structure.[44,45] For example, MoS_2 exhibit tunable bandgaps that can undergo transition from an indirect band gap in bulk crystals to a direct band gap in monolayer nanosheets (Figure 1-4a).[46] Thus, the diverse 2D-TMDs have emerged as an exciting class of atomically thin semiconductors with tunable electronic structures (Figure 1-4b). The electronic structure of TMDs also exhibits special features except for general characteristics of common semiconductors. Electrons in 2D crystals that have a honeycomb lattice structure possess a pair of inequivalent valleys in the k-space electronic structure with an extra valley degree of freedom.[47] It is worth noting that a number of TMDs (MX_2 ,where M=Mo,W, and X = S, Se) exhibit nearly identical crystal structures and similar electronic structures, and will provide family of semiconducting atomic membranes for exploring the valley physics. Recent studies on exfoliated flakes of TMDs have shown exciting potential of these atomically thin materials, including the demonstration of atomically thin transistors,[48] vertical tunnelling transistors that may promise unprecedented switching speed,[49] vertical field-effect transistors (VFETs) that could enable 3D electronic integration,[50] as well as new types of optoelectronic devices such as tunable photovoltaic devices and light emitting devices.[51,52]

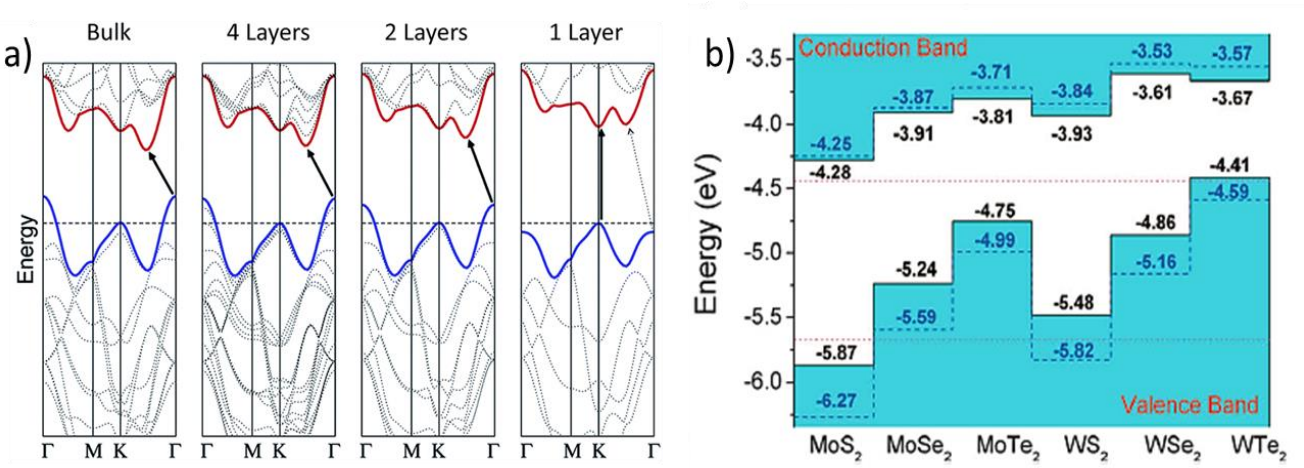

Figure 1.4. a) Energy dispersion in bulk, quadrilayer (4L), bilayer (2L) and monolayer (1L) MoS_2 from left to right. The horizontal dashed line represents the energy of a band maximum at the K point. The red and blue lines represent the conduction and valence band edges, respectively. The lowest energy transition increases with the decreasing layer and evolve from indirect to direct (vertical) transitions.[46]. b) The relative valence and conduction band edge of some common TMDs (monolayer).[48]

1.3 Production Techniques of 2D Materials

The successful exploitation of graphene and other 2D materials crucially depends on the development and optimization of the production methods.[53] In general, a large variety of approaches to produce graphene and 2D materials have been developed so far (see figure 1.5).[54] These can be roughly divided in two main typologies of production processes, *i.e.,* bottom-up and top-down.[54]

The bottom-up approach consists on the synthesis and growth of graphene/2D materials atom by atom (growth on silicon carbide (SiC), molecular beam epitaxy (MBE), precipitation from metals, chemical synthesis from benzene building block and chemical vapor deposition (CVD)).

The top-down approach for the production of graphene/2D materials consists in the exfoliation of a 3D bulk structure (mechanical cleavage (MC), anodic bonding , photoexfoliation, and liquid phase exfoliation (LPE)).

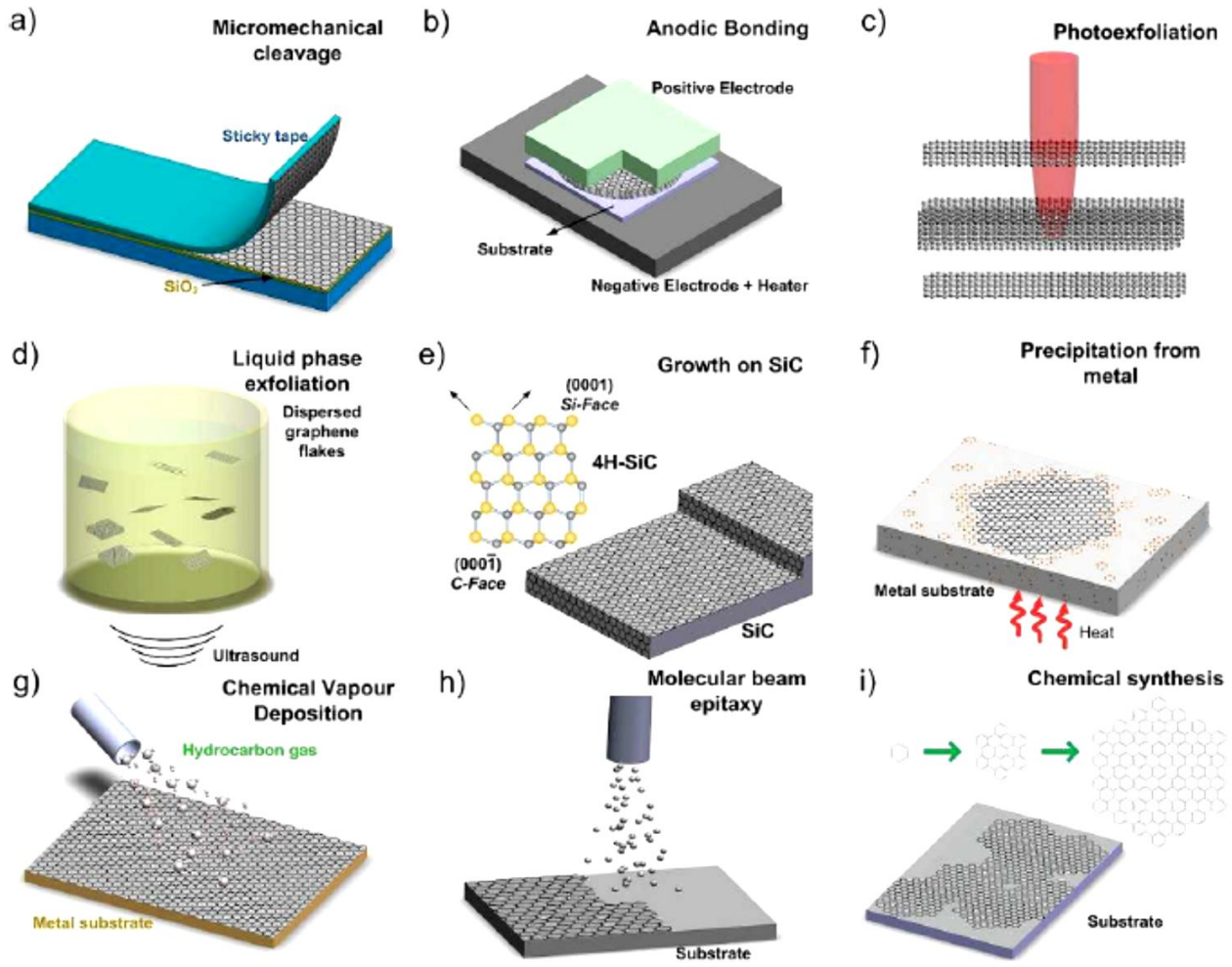

Figure 1.5. Schematic illustration of the main graphene production techniques. (a) Micromechanical cleavage. (b) Anodic bonding. (c) Photoexfoliation. (d) Liquid phase exfoliation.(e) Growth on SiC. Gold and grey spheres represent Si and C atoms, respectively. At elevated T, Si atoms evaporate (arrows), leaving a carbon-rich surface that forms graphene sheets. (f) Segregation/precipitation from carbon containing metal substrate. (g) Chemical vapor deposition. (h) Molecular Beam epitaxy. (i) Chemical synthesis using benzene as building block.[54]

In the following sections, I will provide further details about the use of SiC, CVD, MC, anodic bonding and LPE in the production of graphene.

1.3.1 Bottom-up Approach:

1.3.1.1 Growth of Graphene on Silicon Carbide (SiC):

The preparation of graphene by the thermal decomposition of SiC has been proposed as one of the viable routes for the synthesis of uniform and large-scale graphene layers.[55] The method of producing graphite from SiC is known as early as 1896, as reported by Acheson.[54] Actually, there is a considerable lattice mismatch between SiC (3.073Å) and graphene (2.46 Å) and, differently from

what happens in a traditional epitaxial growth process, in which Si is deposited on the SiC surface, in this growth technique the carbon rearranges itself in a hexagonal structure after the Si evaporation from the SiC substrate.[54] The procedure for the SiC thermal decomposition is theoretically simply and consists basically of two steps: firstly the samples cleaning is required to remove surface polishing damage, then the growth starts by thermal treatment of SiC.[55] For what concerns the second step, the annealing of the substrates results in the sublimation of the silicon atoms while the carbon-enriched surface undergoes reorganization and, for high enough temperatures, graphitization.[56] The typical range of annealing temperatures goes from 1300°C to 2000°C and the usual heating and cooling rates are 2-3°C/sec. This technique allows to obtain, to date, graphene domains up to 200 nm in size with mobility at room temperature up to 3·104 $cm^2V^{-1}s^{-1}$. The thermal decomposition, however, is not a self-limiting process and areas of different film thicknesses may exist on the same SiC crystal but the major short-coming regards the SiC wafers cost that blocks up the breakthrough of this method. A considerable advantage for the technological applications is that SiC, being an insulating substrate, can be simultaneously used as growth and election substrate without transferring the graphitic layers to another insulator substrate, avoiding all the drawbacks due to this process, as will be discussed later, for example, for the CVD technique.[54,55]

1.3.1.2 Chemical Vapor Deposition (CVD):

Chemical vapor deposition has been the workhorse for depositing several materials used in semiconductor devices for several decades. It has been widely used to deposit or grow thin films, crystalline or amorphous, from solid, liquid or gaseous precursors of many substances.[57] Chemical vapor deposition works combining gas molecules in a reaction chamber. While the combined gases come into contact with the substrate, which is heated at elevated temperatures under low pressure, a reaction takes place creating a material film on the substrate surface. The waste gases are then pumped out from the reaction chamber. Since the temperature of the substrate is a primary condition that defines the type of reaction that will occur, it is vital to set it rightly.

The deposition process can include two types of reactions: homogeneous gas phase reactions, which occur in the gas phase, and heterogeneous chemical reactions which occur on/near the vicinity of a heated surface leading to the formation of powders or films, in each case. During the

CVD process, the substrate is usually coated a very small amount, at a very slow speed, often described in microns of thickness per hour.

There exist many different types of CVD processes, including thermal, plasma enhanced (PECVD), cold wall and hot wall.[54] The kind of CVD to be used depends on the available precursors, the material quality, the thickness, and the structure needed.[54] The type of precursor is usually dictated by what is available, what yields the desired film, and what is cost-effective for the specific application. It must be noted that cost is an essential part of selecting a specific process. The principal advantages of using CVD are the high quality and high purity of the films created. This method has been employed as an inexpensive alternative to producing relatively high-quality and large-area graphene. During the CVD process to produce graphene, the gas species (commonly methane, ethylene, or acetylene) are fed into the reaction chamber and pass through the hot zone, where hydrocarbon precursors decompose to carbon radicals at the metal substrate surface and then, form single-layer and few-layer graphene. During the reaction, the metal substrate not only works as a catalyst but also determines the graphene deposition mechanism, which ultimately affects the quality of graphene. Finally, samples are cooled down in argon gas. During the cooling down process, carbon atoms diffuse out from the metal-C solid solution and precipitate on the metal surface to form graphene films.

Another crucial point in the production of graphene by CVD is the selection of the proper metal substrate. In 1966, Karu and Beer demonstrated that Ni substrates, exposed to methane at T = 900 °C, can be used to form thin graphite[58].Later, in 1984, Kholin et al. performed what may be the first CVD graphene growth on a metal surface[59]. The authors selected iridium (Ir) as the metal substrate to study the catalytic and thermionic properties of the metal in the presence of carbon[60]. Since then, other groups exposed metals, such as single crystal Ir[61,62], to carbon precursors and studied the formation of graphitic films in ultra-high vacuum (UHV) systems. It was after 2004 when the focus of the scientific community shifted to the actual growth of graphene. It was found that low-pressure chemical vapor deposition (LPCVD) on Ir(III) single crystals, using an ethylene precursor, yields graphene structurally coherent even over the Ir step edges[61]. However, the transfer of graphene to other substrates is a complicated process, influenced mainly because of the chemical inertness of this metal. Additionally, Ir is also very expensive. For this reason, the growth of graphene by CVD by using less costly metals such as Ni[63] and Co[64,65], compatible also with Si processing, has been studied. The use of these metals also

poses a different challenge since few layer graphene are usually grown, and single layer graphene grow non-uniformly. The process is, in fact, carbon precipitation, not yielding uniform single layer graphene, but rather few layer graphene, and not CVD growth as many papers claim [54,60,62.]

The first CVD growth of uniform, large area (~cm^2) graphene on a metal surface was in 2009[66]. The authors grew graphene on polycrystalline Cu foils, exploiting the thermal catalytic decomposition of methane and low carbon solubility. During the CVD process, the growth mostly ends as soon as the Cu surface is entirely covered with graphene[67]. Large area graphene growth was enabled principally by the low C solubility in Cu[68], and the Cu mild catalytic activity[69]. Indeed, the solubility of carbon in transition metal along with CVD conditions plays an important role in determining growth mechanism and ultimately controls the number of graphene layers. The growth mechanism depends on the nature of the catalyst.[70] The difference in the growth kinetics and mechanism between metal substrates was first ascribed to the different carbon solubility. However, the mechanism is more complicated. Carbon atoms, after decomposition from hydrocarbons, nucleate on Cu, and the nuclei grow into large domains.[71,72] The nuclei density depends on T and pressure. In fact, at low precursor pressure, mTorr, and T > 1000 °C, very large single crystal domains, ~0.5 mm, are observed.[70] However, once the Cu surface is fully covered, the films become polycrystalline. This can be associated with the fact that the nuclei are not registered.[70] For example, the cores are incommensurate to each other, even on the same Cu grain. The latter could be attributed to the low Cu-C binding energy[73]. It would be desirable to have substrates (*e.g.,* Ru) with higher binding energy with C.[72] However, while Ru is compatible with Si processing[74], oriented Ru films may be challenging to grow on large diameter (300 – 450 mm) Si wafers, or transferred from other substrates.

The surface roughness of the metal substrate is another issue to take into consideration. Commercial Cu foils have been used for the graphene synthesis to reduce the overall cost of fabrication process but these foils have strongly corrugated surface due to cold rolling process during manufacture. The surface roughness is known to produce graphene thickness variation on Cu[75]. Since graphene growth on copper is surface-limited, the smoothness of the chosen metal surface is critical for obtaining monolayer coverage across the entire surface of the substrate.[76] Another major problem with CVD is that graphene is obtained on top of a metal surface, thus often requiring a transfer process onto the substrate necessary for the specific

application (*i.e.,* insulating substrates). Moreover, inevitable structural damage occurs to graphene during the transfer process, which can thus degrade its properties.[77]

1.3.2 Top-Down Approach:

1.3.2.1 Mechanical Cleavage (MC):

The mechanical cleavage or exfoliation can be regarded as the mother of all techniques for the graphene production, since it was the way that allowed Geim and co-workers at Manchester University in 2004, to isolate the first single-layer samples from graphite.[78]

It consists basically in the exfoliation of a graphite block, highly oriented pyrolytic graphite (HOPG) or other types, through the adhesive tape so that the method has been universally known as "the scotch-tape technique". Then, the first piece of tape is repeatedly cleaved by other sticky pieces down to obtain an almost invisible powder on the starting tape. The number of the exfoliations ranges from 10 to 20 but,[79] a trade-off between this number, namely the flake thickness, and the mean size needs to be reached. Finally, at the end of the exfoliation process, the tape is transferred onto the election substrate that usually is silicon dioxide on Si (SiO_2/Si).[14]

Ideally, the single-layer graphene can be obtained making thinner and thinner the thickness of the graphite block. However, transferring the adhesive tape to the SiO_2/Si implicates that also glue residues can be released on the substrate. Besides eliminating the glue residues, was able to increase the mean flake size from ten up to hundreds of microns.[80] Although MC is impractical for large scale applications, it is still the method of choice for fundamental studies. Indeed, the vast majority of basic results and prototype devices were obtained using MC flakes. Thus, MC remains ideal to investigate both new physics and new device concepts.[54]

1.3.2.2 Anodic bonding

Anodic bonding is widely used in the microelectronics industry to bond Si wafers to glass, to protect them from humidity or contaminations. When employing this technique to produce single layer graphene, graphite is first pressed onto a glass substrate, and a high voltage of few KVs (0.5-2 kV) is applied between the graphite and a metal back contact, and the glass substrate is then heated (~200 °C for~ 10-20 mins). If a positive voltage is applied to the top contact, a negative charge accumulates in the glass side facing the positive electrode, causing the decomposition of

Na_2O impurities in the glass into Na^+ and O^-_2 Ions. Na^+ moves towards the back contact, while O^-_2 remains at the graphite-glass interface, establishing a high electric field at the interface. A few layers of graphite, including single layer graphene, stick to the glass by electrostatic interaction and can then be cleaved off; temperature and applied voltage can be used to control the number of layers and their size. Anodic bonding has been reported to produce flakes up to about a millimeter in width.[54]

1.3.2.3 Liquid Phase Exfoliation (LPE)

Liquid-phase exfoliation of graphite is based on exposing powdered graphite to special solvents or surfactants that favor an increase in the total area of graphite crystallites. Solvents ideal to disperse graphene are those that minimize the interfacial tension [mN/m] between the liquid and graphene flakes, *i.e.* the force that minimizes the area of the surfaces in contact.[54] The solvents that mainly match this requirement are N-methyl-pyrrolidone (NMP), Dimethylformamide (DMF).[81]

The second step of the procedure consists in the ultra-sonication aimed to favor the splitting of graphite into individual platelets. Finally, a "purification" step is required to separate the unexfoliated flakes from the thinner ones, constituting the so called surnatant phase of the suspension. Thicker flakes can be removed by different strategies based on ultra-centrifugation in a uniform medium or in a density gradient medium.[54] (see figure 1.6)

In this context, in the first step, the choice of the solvent for the exfoliation process is crucial. In fact, suitable solvents are those that minimize the interfacial tension between the liquid and the flakes in solution. In general, interfacial tension plays a key role when a solid surface is immersed in a liquid medium. If the interfacial tension between solid and liquid is high, there is poor dispersibility of the solid in the liquid. In the case of graphitic flakes in solution, if the interfacial tension is high, the flakes tend to adhere to each other and the work of cohesion between them is high (i.e. the energy per unit area required to separate two flat surfaces from contact), hindering their dispersion in liquid.[54] For example, graphene flakes have surface energy (γ) of ~ 40 mN m^{-1}, thus suitable solvents are NMP and DMF. However, these solvents are toxic and have high boiling point, *i.e.,* more than 150 °C. A possible solution to this issue relies on the tuning of γ parameter of lower boiling point solvents, such as acetone and ethanol, by adding stabilizing agents, such as surfactants or polymers. However, their residual can increase the inter-flake contact resistance.

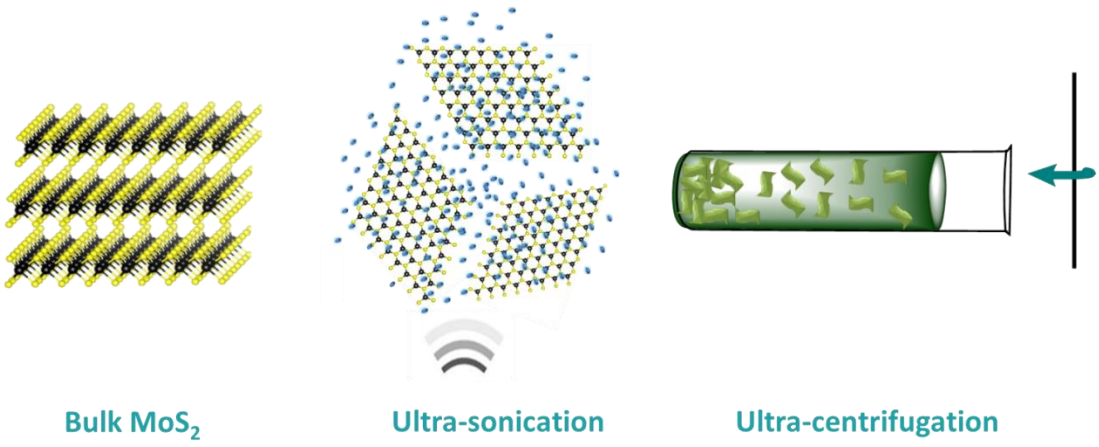

Figure 1.6. Liquid phase exfoliation of natural MoS_2 and size selection procedure by SBS.

The second step is the exfoliation of graphitic flakes, assisted by ultrasonication: bath ultrasonicator provides ultrasound excitations that are transmitted to the sample. Energy necessary to separate the graphitic layers is transferred via cavitation, namely the process through which bubbles and voids grow in the liquid and collapse; it is worth noting that excessive sonication can lead to structural destruction of the layers. To optimize the sonication process, the solution is put in small sealed vials of 60 mL and temperature of water is maintained under 40 ^{o}C: the reason is that, for NMP, γ ~ 40 mN m^{-1} at 20^{o}C is ideal to assist exfoliation of graphite, but drops to 35 mN m^{-1} at 40^{o}C, making exfoliation ineffective for T>40^{o}C.[82]

However, since the exfoliation process of layered materials produces dispersions with a heterogeneous composition, containing both un-exfoliated bulk material and very thin flakes. Thus, after the ultra-sonication process, a purification step is required. The most common purification procedure is the sedimentation-based separation (SBS), based on ultra-centrifugation in a uniform medium. The sedimentation-based separation separates flakes on the basis of their sedimentation rate in response to a centrifugal force acting on them. This process is described by the Svedberg equation:

$$s = \frac{m(1 - \vartheta'\rho)}{f} \qquad (1)$$

In which: s is the sedimentation coefficient (the time needed for flakes to sediment); ϑ' is the partial specific volume (the volume that each gram of the solute occupies in solution); ρ is the

density of the solvent; *f* is the frictional coefficient due to the motion through the solvent towards the bottom of the ultracentrifuge tube.

As expressed by equation (1), the sedimentation of flakes depends on their mass and frictional coefficient. Thick and large sheets, *i.e.* having larger mass, sediment faster with respect to small and thin sheets (having smaller mass), which are thus maintained in dispersion during the SBS process. By tuning the centrifugal forces, it is possible to obtain dispersions with flakes of different lateral sizes.

The as-produced dispersions of exfoliated and purified flakes can be further processed by exploiting several coating and printing strategies (*i.e.* ink-jet printing and screen-printing). However, in the large majority of cases, the as-produced dispersion itself cannot serve directly as an ink. In fact, the composition of inks is functional to the type of coating/printing process. In this context, the critical parameter is the rheology control of the 2D material inks. The rheological properties of inks are dependent on the flakes morphology (*i.e.* viscosity (η)) and can be further tailored using additives and/or γ modifiers.

1.4 Applications of 2D Materials

The wide class of 2D materials, the possibility of creating and designing hybrid structures with "on-demand" properties by means of spin-on processes, or layer-by-layer assembly opened up an ever-growing number of applications, including composite materials,[83] sensors,[84] flexible optoelectronics,[85] and energy storage [86]and conversion. [100] As previously mentioned, the advances achieved in the 2D material production methods, and, more in detail, the ability to formulate functional inks with tuned rheological and morphological properties, *i.e.,* lateral size and thickness of the dispersed 2D materials, is a step forward toward the development of industrial-scale, reliable, inexpensive printing/coating processes, a boost for the full exploitation of such nanomaterials. Consequently, graphene has been proposed as large-area flexible electrode for solar cells, replacing both metal collector and TCO.[87] Moreover, it has also been used as nanofiller in polymer to make polymer nanocomposite with enhanced mechanical properties, as well additional electrical features.[88] For example, the incorporation of graphene (with a very low filler content) into insulating polymers permitted to realize electrically conductive nanocomposites widely used in electrostatic dissipation devices and electromagnetic interference shielding which require electrical conductivity at the range of about 10^{-6} S m^{-1}.[89] Recently it has been proved that

the 2D materials can be used as interlayer in organic photovoltaics, increasing both the efficiency and the stability of both organic solar cell and PSCs. Graphene and other 2D material-based supercapacitors have been demonstrated for use in touch screen for smart phone and flexible display,[53] as well high-power application like Transistors[90]. The combination of thermal conductivity and electrical insulating property of h-BN are promising for potential applications in fabricating die attachments, encapsulation of electric wire, and electronic packaging materials.[91] The most typical existing TMDs (*i.e.,* MoS_2 , $MoSe_2$, WS_2) have evolved into a vast studying topic, gradually finding their applications in many related areas, such as transistors,[92] light-emitting diodes,[93] sensor, [94]solar cells,[95] Li-ion batteries,[96] photosensitizers,[100] catalyst[97] and gas storage[98]. However, due to the limitations in intrinsic structures, one simple material is highly difficult to satisfy all basic properties and functional performance in practical applications. For instance, graphene owns outstanding electrical performance, while fails in switch control due to its gapless band structure. On the contrary, MoS_2 could realize band engineering with the modulation of its number of layers, whereas its electron mobility is incomparable to that of graphene, making it impossible to act as transparent electrodes.

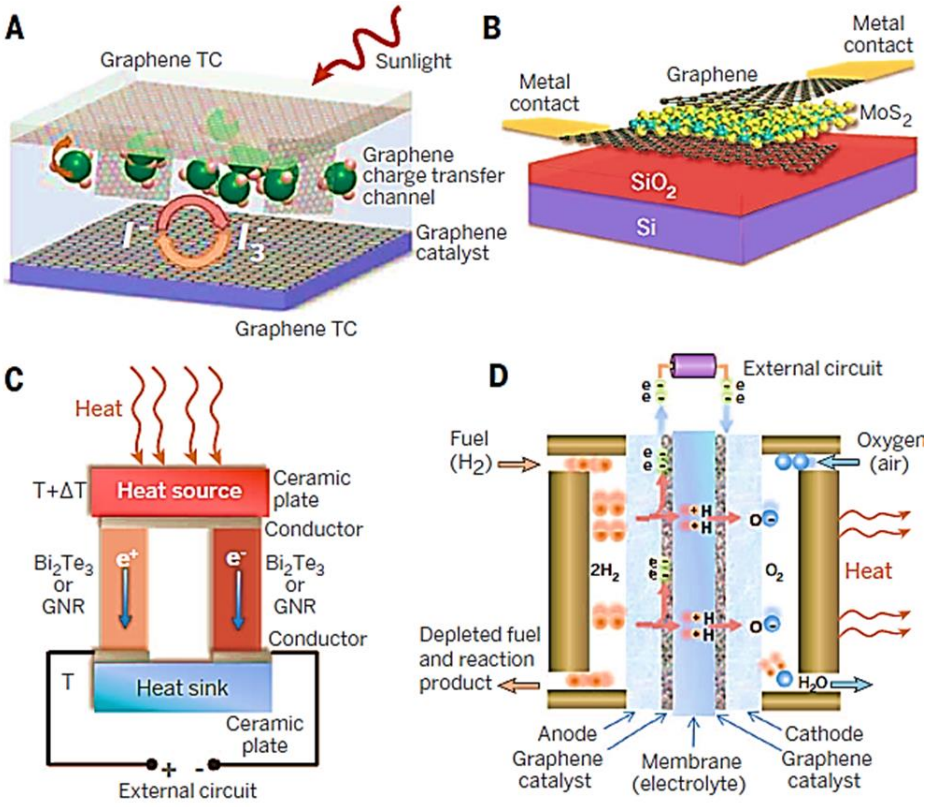

Figure 1.7. Energy conversion devices. A) Schematic of a dye-sensitized solar cell (DSSC) with graphene used in several components. B) Heterostructure (graphene/MoS_2/graphene) photovoltaic device. C) Schematic illustration of power generation in a thermoelectric device based on LM Bi_2Te_3 or graphene. D) Proton exchange membrane fuel cells.[99]

Therefore, fabrication of hybrid structures based on 2D materials by taking advantages of the individual component is one of latest research trends.[100] Figure 1.7. shows some of the most representative energy conversion applications for graphene and other 2D materials.

CHAPTER 2

CHAPTER 2: Experimental Methods

2.1 Materials Production

This chapter describes the experimental procedures I have exploited for the synthesis of 2D materials. In particular, I report here the details of the production of single-/few- layer 2H-MoS_2, 2H-$MoSe_2$ and graphene flakes by LPE, and the production of 1T-MoS_2 flakes by Li-intercalation method. Afterward, I report on the preparation of 2H-MoS_2 Quantum Dots (QDs) derived from 2H-MoS_2 flakes by solvothermal method. Hummer method is described for the production of graphene oxide (GO), while modified hydrothermal is reported for the synthesis of reduced graphene oxide (RGO). Lastly, I describe the different post-synthesis functionalization of the aforementioned produced materials in order to make them suitable for their end-application, which are reported in the last three chapters of my Thesis.

2.1.1 Preparation of Single-/Few-Layer 2H-MoS_2, 2H-$MoSe_2$ and Graphene Flakes Dispersion by LPE

Semiconducting 2H phase of MoX_2 (X= S, Se) flakes (2H-MoS_2 and 2H-$MoSe_2$ flakes) and graphene flakes are produced in form of dispersion by LPE[101,102] of their bulk counterpart in 2-Propanol (IPA) and NMP, respectively. The exfoliation process is followed by a purification step carried out in a centrifugal field by exploiting sedimentation-based separation (SBS).[103,104,105] Briefly, 30 mg of MoX_2 (X= S, Se) bulk crystal are added to 50 mL of IPA and then sonicated ((Branson® 5800 cleaner, Branson Ultrasonic) for 6 h. The resulting dispersion is ultra-centrifuged (Optima™ XE-90 ultracentrifuge, Beckman Coulter) for 60 min at 2700 g in order to separate un-exfoliated and thick MoX_2 (X= S, Se) crystals (collected as sediment) from the thinner MoX_2 (X= S, Se) flakes that remain in the supernatant. Afterward, 80% of the supernatant is collected by pipetting, obtaining MoX_2 (X= S, Se) flakes dispersion.[106] The graphene flakes are produced by LPE, followed by SBS, in NMP. Experimentally, 1 g of graphite (+100 mesh, ≥75% min, Sigma Aldrich) is dispersed in 100 ml of NMP (99.5% purity, Sigma Aldrich) and ultra-sonicated in a bath sonicator (Branson® 5800 cleaner, Branson Ultrasonic) for 6 h. The resulting dispersion is then ultra-centrifuged (Optima™ XE-90 ultracentrifuge, Beckman Coulter) at 17000 g for 50 min at 15 °C, to exploit SBS. Finally, the 80% of the supernatant is collected by pipetting, obtaining graphene flakes dispersion[107].

2.1.2 Chemical Exfoliation of Single-/Few-Layer 1T-MoS_2 Flakes Dispersion by Li- Intercalation Method

Metallic 1T phase of MoS_2 flakes (1T-MoS_2 flakes) are prepared by a Li- intercalation method.[108] Experimentally, 0.3 g of MoS_2 bulk powder (Sigma Aldrich) is dispersed in 4 mL of 2.0 M n-butyl lithium (n-BuLi) in cyclohexane (Sigma Aldrich). The dispersion is kept stirring for two days at room temperature under an Ar atmosphere. The Li-intercalated material (Li_xMoS_2) is separated by suction filtration under Ar. Li_xMoS_2 is washed with anhydrous hexane to remove non-intercalated Li ions and organic residues. Li_xMoS_2 powder is then exfoliated by ultra-sonication (Branson® 5800 cleaner, Branson Ultrasonic)) in deionized (DI) water for 1 h. The obtained dispersion is then ultra-centrifuged (Optima™ XE-90 ultracentrifuge, Beckman Coulter) at 7450 g for 20 min to remove Lithium hydroxide (LiOH) and the un-exfoliated material. Finally, the precipitate is filtered and re-dispersed in IPA (absolute alcohol, without additive, $99.8%, Sigma Aldrich), in order to accurately control the concentration of the final dispersion.

2.1.3 One-step Synthesis of 2H-MoS_2 QDs by Solvothermal Method

2H-MoS_2 quantum dots (2H-MoS_2 QDs) are produced through a one-step solvothermal method starting from 2H-MoS_2 flakes, produced by LPE of bulk MoS_2 crystals in IPA followed by SBS (see Figure 2.1). The resulting dispersion is refluxed in air under stirring for 24 h at 140 °C and subsequently ultra-centrifuged for 30 min at 24600 g. Afterward, the supernatant is collected by pipetting. The synthesis of QDs starting from 1T-MoS_2 flakes leads to 2H-MoS_2 QDs, as indicated by X-ray photoelectron spectroscopy (XPS) analysis (see Chapter 3). This can be ascribed to the intrinsic metastable nature of 1T-MoS_2 flakes, which relax, during the solvothermal treatment, toward the thermodynamically favored 2H phase.[109,110] To be noted, 1T-MoS_2 QDs cannot be obtained by exploiting the aforementioned procedure.

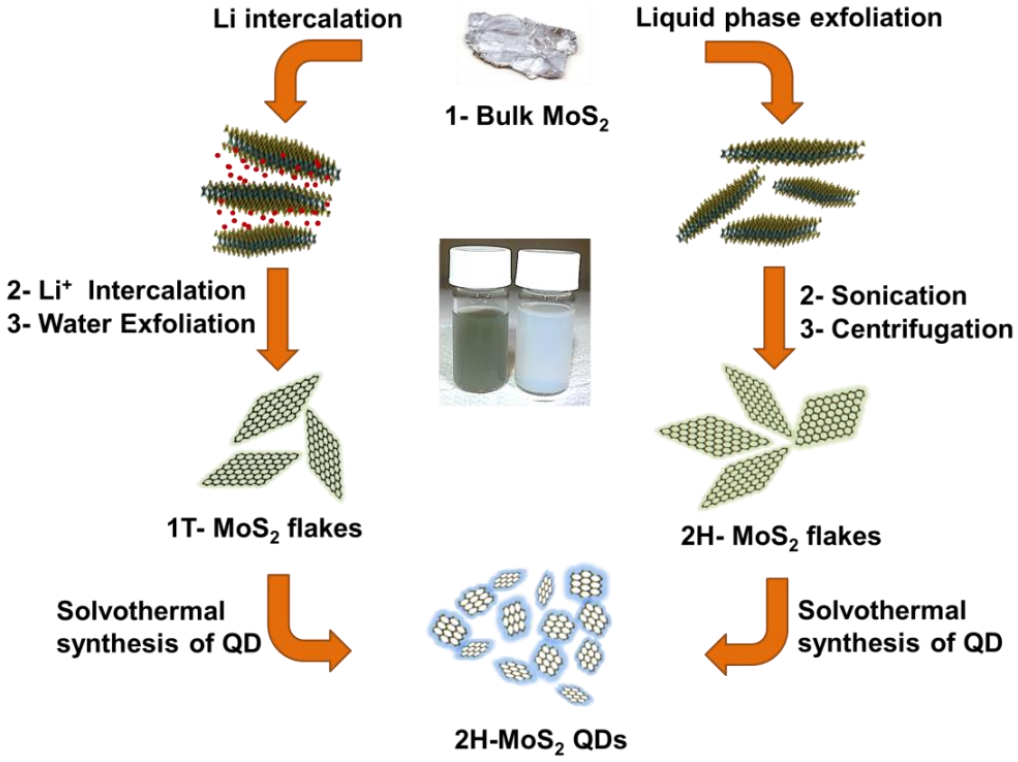

Figure 2.1. Solvothermal synthesis of MoS_2 QDs from 2H-MoS_2 and 1T-MoS_2 flakes in IPA.

2.1.4 Preparation of GO by Modified Hummer's Method

Graphene oxide (GO) is synthesized from graphite flakes (Sigma Aldrich, +100 mesh ≥75% min) using a modified Hummer's method.[111] Briefly, 1 g of graphite and 0.5 g of Sodium nitrate ($NaNO_3$) (Sigma Aldrich, reagent grade) are mixed, followed by the dropwise addition of 25 mL of Sulfuric acid (H_2SO_4) (Sigma Aldrich). After 4 h, 3 g of Potassium permanganate ($KMnO_4$) (Alpha Aesar, ACS 99%) is added slowly to the above solution, keeping the temperature at 4 °C with the aid of an ice bath. The mixture is let to react at room temperature overnight and the resulting solution is diluted by adding 2 L of distilled water under vigorous stirring. Finally, the sample is filtered and rinsed with H_2O.

2.1.5 Preparation of RGO by Modified Hydrothermal Method

Reduced graphene oxide (RGO) is produced by thermal annealing in a quartz tube (120 cm length and 25 mm inner diameter) passing through a three zones split furnace (PSC 12/--/600H, Lenton, UK). Gas flows are controlled upstream by an array of mass flow controllers (1479A, mks, USA). Under a 100sccm flow of Ar/H_2 (90/10 %), 100 mg of GO are heated to 100 °C for 20 min to

remove the presence of water residuals. Subsequently, a ramp of 20 °C/min is used to reach 1000 °C, and stabilized at this temperature for 2 h. Finally, the oven is left to cool to room temperature.

2.1.6 Debundling of SWNTs

Single-wall carbon nanotubes (SWNTs) (> 90% purity, Cheap Tubes) are used as received, without any purification step). The SWNT dispersions are produced by dispersing SWNTs in NMP at a concentration of 0.2 g L^{-1} and using ultra-sonication-based de-bundling.[112,113] Briefly, 10 mg of SWNTs powder is added to 50 mL of IPA in a 100 mL open top, flat bottomed beaker. The dispersion is sonicated using a horn probe sonic tip (Vibra-cell 75185, Sonics) with vibration amplitude set to 45% and a sonication time of 30 min. The sonic tip is pulsed for 5s on and 2s off to avoid damage to the processor and reduce any solvent heating. Ice bath around the beaker during sonication is used in order to minimize heating effects.

2.1.7 Functionalizations of 2D Materials Films

2.1.7.1 $HAuCl_4$-Chemical Doping-of MoS_2 Flakes Films

In this section is described a controllable chemical p-doping technique of a MoS_2 film by Doping Chloroauric acid ($HAuCl_4$) reducing agent. The MoS_2 dispersion is deposited onto the previously treated FTO by spin coating (Laurell Tech. Corp. Spin coater) using a single step spinning protocol with a rotation speed of 3000 rpm for 60 s. Post-thermal annealing in an Ar atmosphere at 150 °C for 30 min is performed for the MoS_2 films. The latter are subsequently doped by spin casting $HAuCl_4(3H_2O)$ (Sigma Aldrich) in methanol solution as p-doping agents on top, by using the same single step spinning protocol of the MoS_2 deposition. The doped films are subsequently dried for 30 min under an Ar atmosphere (see Chapter 5 for more details). [108]

2.1.7.2 Thermal Texturization of $MoSe_2$ Flakes Films

Pristine $MoSe_2$ are produced in form of dispersion by LPE in IPA, as described in Section 2.1.1, and 0.5 mg mL^{-1} of the resulting dispersion are deposited by drop costing on top of glassy carbon (GC) substrate. Thermal treatment of GC/$MoSe_2$ is carried out in a quartz tube (120 cm length and 25 mm inner diameter) passing through a three zones split furnace (PSC 12/--/600H, Lenton, UK). The electrodes are heated at 600 or 700 or 800 °C with a ramp of 12 °C/min, and stabilized at this temperature for 5 hours under a 100 sccm flow of Ar/H_2 (90/10 %). Gas flows are controlled

upstream by an array of mass flow controllers (1479A, mks, USA). Finally, the oven is cooled down to room temperature.

2.1.7.3 Chemical Treatment-induced Phase Conversion of $MoSe_2$ Flakes Films

Hybrid electrodes are fabricated by depositing SWNTs and $MoSe_2$ flakes (SWNT/$MoSe_2$) on the nylon membranes with size pore of 0.2 µm (Whatman® membrane filters nylon, Sigma Aldrich) through sequential vacuum filtration processes of the as-prepared SWNT and $MoSe_2$ dispersions (mass loading of 2 mg cm^{-2} for all materials). Chemical treatment of SWNTs/$MoSe_2$ is obtained by bathing them in 5 ml of n-butyllithium (Sigma Aldrich) in a sealed vial at room temperature under N_2 atmosphere. After 12 hours, electrodes are washed with deionized water to remove the remaining Li present in the form of lithium cations (Li^+) and then cleaned with IPA and blow dried with compressed N_2 gas.

2.1.7.4 Transition Metal Choride-Chemical Doping of the $MoSe_2$ Flakes

The transition metal chloride (MCl_2)-chemical doping of the $MoSe_2$ flakes is obtained by mixing MCl_2 solution in anhydrous IPA, where MCl_2 dissociate in M^{2+} and $2Cl^-$ (MCl_2 solution concentration here adopted, *i.e.,* 0.4 g L^{-1} inferior to solubility limit of MCl_2 in alcohol, >> 1 g L^{-1}),[114] with the $MoSe_2$ dispersion, thus obtaining $MoSe_2$:MCl_2 dispersions in IPA (1:1 molar ratio). These undergo an ultra-sonication treatment, during which hypothesized "cascade reaction" occurs as follow:

step 1: a) $MoSe_2 + M^{2+} + 2Cl^- \rightleftarrows MoSe_2^{2+} + M_0\downarrow + 2Cl^-$ and/or

b) $MoSe_2 + 2M^{2+} + 4Cl^- \rightleftarrows MoSe_2^{2+} + M_0\downarrow + MCl_4^{2-}$

step 2: a) $MoSe_2^{2+} + 2Cl^- \rightleftarrows MoSe_2{-}2Cl$ and/or

b) $MoSe^{2+} + MCl_4^{2-} \rightleftarrows MoSe_2{-}MCl_4$

The doping mechanism starts from an electron transfer from $MoSe_2$ to M^{2+} (*step 1*), which is caused by the high electronegativity of the latter, being theoretically estimated in aqueous solution-phase as 2.636, 2.706, 2.891, 2.952, 2.796 and 2.660 Pauling units for Fe^{2+}, Co^{2+}, Ni^{2+}, Cu^{2+}, Zn^{2+} and Cd^{2+}, respectively.[115] These values agree with the Irving-Williams order of transition metal complexes[116] and have to be considered as underestimation with respect to those corresponding to IPA-solution because of the higher polarity of H_2O (~10.2)[117], whose solvation weakens the electron-accepting power of general cations,[115] with respect to that of IPA (~3.9).

Similar initiating doping mechanism has been proposed for MCl_2- and MCl_3-doped graphene[118] and CNTs[119] (actually, MCl_3 doping has been supposed to start with $2MoSe_2 + 2MCl_3 \rightleftarrows 2\ MoSe_2^{+} + MCl_2^{-} + MCl_4^{-}$ followed by $3MCl_2^{-} \rightleftarrows 2M^0\downarrow + MCl_4^{-} + 2Cl^{-}$).[117] Lastly, neutralization of the charged species ($MoSe_2^{2+}$, MCl_4^{2-} and Cl^{-}) occur by the creation of $MoSe_2$–2Cl and $MoSe_2$–MCl_4 complexes (*step 2*). These show net charge displacement: in fact, the electron cloud is shifted toward the Cl-based centers, while $MoSe_2$ is p-type doped.[115]

2.1.7.5 Post-synthesis Silane Functionalization of GO and RGO

The silane functionalization of GO and RGO is carried out based on the covalent linking of silane groups to the GO and RGO oxygen functionalities.[120] Briefly, 0.5 mg mL^{-1} GO and RGO dispersions in ethanol (absolute alcohol, ≥99.8%, without additive, Sigma Aldrich) are sonicated for 30 min and subsequently functionalized by adding 250 µL of (3-mercaptopropyl)trimethoxysilane (MPTMS) (95%) (Sigma Aldrich) per mg of GO and RGO, refluxing at 60 ^{o}C for 15 h. The final product is obtained by subsequent washing with ethanol to remove the unreacted silane and precipitating the material by centrifugation. The functionalized GO and RGO are re-dispersed in ethanol by sonication at different concentrations.

2.2 Characterization Techniques and Instrumentation:

The optical absorption spectroscopy (OAS) of the diluted dispersions of 2D crystal in IPA or NMP is carried out by using a Cary Varian 5000UV-Vis spectrometer. The absorption spectrum is acquired using a 1 mL quartz glass cuvette. The solvent baseline is subtracted to the recorded spectrum. The steady-state photoluminescence (PL) emission measurements are performed using an Edinburgh Instruments FLS920 spectrofluorometer. The PL spectra are collected exciting the samples at different wavelengths ranging from 280 to 500 nm at a step of 20 nm, using a Xe lamp coupled to a monochromator. Dispersions are contained in a quartz glass cuvette with a path length of 1cm. To discard any contribution from the solvent, blank (control) measurement is carried out in the same experimental conditions used for the characterization of the aforementioned samples.

Raman measurements are carried out with a Renishaw 1000 using a 50× objective, by focusing laser radiation with a wavelength of 532 nm and an incident power of 1 mW on the sample. The different peaks of the Raman spectra of the investigated samples are fitted with Lorentzian

functions. For each sample 30 spectra are collected For statistical analysis which is carried out by means of software Origin 8.1 (OriginLab).

X-ray photoelectron spectroscopy (XPS) analysis is carried out using a Kratos Axis Ultra spectrometer on each flakes drop cast onto 50 nm-Au sputtered coated Si wafers from the 0.1 mg mL^{-1} dispersion in IPA. The XPS spectra are acquired using a monochromatic Al Ka source operated at 20 mA and 15 kV. High-resolution spectra are collected with pass energy of 10 eV and energy step of 0.1 eV over a 300 mm X 700 mm area. The Kratos charge neutralizer system is used on all specimens. Spectra are charge-corrected to the main line of the C 1s spectrum set to 284.8 eV, and analyzed with Casa XPS software (version 2.3.17).

The crystal structure is characterized by X-ray diffraction (XRD) using a PANalytical Empyrean with CuKa radiation. The samples for XRD are prepared by drop-casting of the dispersions on a silicon wafer and dried under vacuum.

Transmission electron microscopy images (TEM) are taken on a JEM 1011 (JEOL) transmission electron microscope, operating at 100 kV. 0.01 mg ml^{-1} of 2D crystal dispersions in IPA or NMP are drop-casted onto carbon coated Cu TEM grids (300 mesh), rinsed with DI water and subsequently dried under vacuum overnight. The lateral dimensions of the flakes are measured using ImageJ software (Java). Statistical TEM analysis is carried out by means of software Origin 8.1 (OriginLab).

Scanning electron microscopy (SEM) analysis is carried out with a FEI Helios Nano lab field-emission scanning electron microscope. The samples are imaged without any metal coating or pre-treatment. Atomic force microscopy (AFM) images are obtained using a commercial AFM instrument MFP-3D (Asylum Research), with NSG30/Au (NT-MDT) probes in tapping mode in air. These golden silicon probes have a nominal resonance frequency and spring constant of 240–440 kHz and 22–100 Nm^{-1}, respectively. The tip is a pyramid with 14–16 mm length and ~20 nm apex diameter. The images are processed with the AFM company software Version-13, based on IgorPro 6.22 (Wavemetrics). Statistical analysis of the height profiles is carried out by means of software Origin 8.1 (OriginLab).

Ultraviolet photoelectron spectroscopy (UPS) analysis is performed on drop-cast films of each 2D materials sample deposited onto Si wafer, to estimate the position of the valence band maximum (VBM) of the materials under investigation and the effect of illumination on it. The measurements are carried out with a Kratos Axis UltraDLD spectrometer using a He I (21.22 eV) discharge lamp.

The analyses are performed on an area of 55 µm in diameter, at pass energy of 5 eV and with a dwell time of 100 ms. The work function (*i.e.*, the position of the Fermi level with respect to vacuum level) is measured from the threshold energy for the emission of secondary electrons during He I excitation. A −9.0 V bias is applied to the sample in order to precisely determine the low kinetic energy cut-off. Then, the position of the valence band maximum *vs.* vacuum level is estimated by measuring their distance from the Fermi level, according to the previous reported graphical method.[121,122]

CHAPTER 3

CHAPTER 3. Characterization of 2D Material Dispersions

3.1 Graphene Flakes

3.1.1 Optical Absorption Spectroscopy Analysis

Figure 3.1. reports the UV-Vis absorption spectrum of the as-produced graphene flakes dispersion in NMP (1:10 diluted). The peak at ~265 nm is a signature of the van Hove singularity in the graphene density of states[123]. The concentration of graphene flakes in dispersion is determined from the optical absorption coefficient at 660 nm, using A = αlc where l [m] is the light path length, c [g L^{-1}] is the concentration of dispersed graphitic material, and α [L g^{-1} m^{-1}] is the absorption coefficient. In accordance with previous studies, α is assumed equal to 1390 L g^{-1} m^{-1} at 660 nm.[124] The extrapolated concentrations for the as-produced graphene flakes dispersion is 0.32 g L^{-1}.

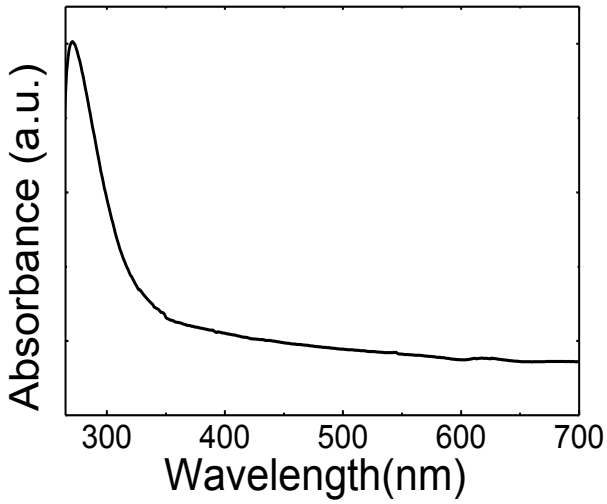

Figure 3.1. UV-Vis absorption spectrum of the graphene flakes dispersion (1:10 diluted) in NMP.

3.1.2 Raman Spectroscopy Analysis

The as-produced graphene flakes are characterized by means of Raman spectroscopy. A typical Raman spectrum of defect-free graphene shows, as fingerprints, G and D peaks.[125] The G peak corresponds to the E_{2g} phonon at the Brillouin zone center.[126] The D peak is due to the breathing modes of sp^2 rings and requires a defect for its activation by double resonance.[127,128] The 2D peak is the second order of the D peak, being a single peak in monolayer graphene, whereas it splits in

four in bilayer graphene, reflecting the evolution of the band structure.[125] The 2D peak is always seen, even in the absence of D peak, since no defects are required for the activation of two phonons with the same momentum.[129] Double resonance can also happen as intra-valley process, *i.e.*, connecting two points belonging to the same cone around K or K'. This process gives rise to the D' peak for defective graphene.[129] The D+D' is the combination mode of D and D' while the 2D' is the second order of the D'.[129] As in the case of 2D, 2D' is always seen even when the D' peak is not present.[129] Previous studies on graphene flakes produced by LPE have shown that these defects are predominantly located at the edges, while the basal plane of the flakes is defect-free. This is demonstrated by the absence of correlation between I(D)/I(G) and Full width at half maximum (FWHM)(G).[130,131,132] Figure 3.2a reports a representative Raman spectrum of the as-produced graphene flakes, showing all the bands above described. The statistical analysis of the position of G (Pos(G)) (Figure 3.2b), the full width half maximum of G (FWHM(G)) (Figure 3.2c), the position of 2D (Pos(2D)) (Figure 3.2d), the full width half maximum of 2D (FWHM(2D)) (Figure 3.2e), the intensity ratio between the 2D and G peaks (I(2D)/I(G)) (Figure 3.2f) and the intensity ratio between the D and G peaks (I(D)/(IG)) (Figure 3.2g) give useful quantitative information on the structural properties of the graphene flakes. In particular, the Pos(2D) is at ~2700 cm^{-1} (Figure 3.2d) while the FWHM(2D) ranges from 60 to 75 cm^{-1} (Figure 3.2e). These values are ascribed to few-layer graphene flakes.[133,134] The I(2D)/I(G) varies from 0.6 to 1.2 (Figure 3.2f), as expected from a combination of single- and few-layer graphene flakes.[135] The presence of D and D' indicates the defective nature of the graphene flakes. Figure 3.2g shows the statistical analysis of I(D)/I(G), which varies between 0.3 and 0.7, while Figure 3.2h does not show any correlation between I(D)/I(G) and FWHM(G), thus proving defect-free basal planes of the as produced graphene flakes, in accordance with previous studies.

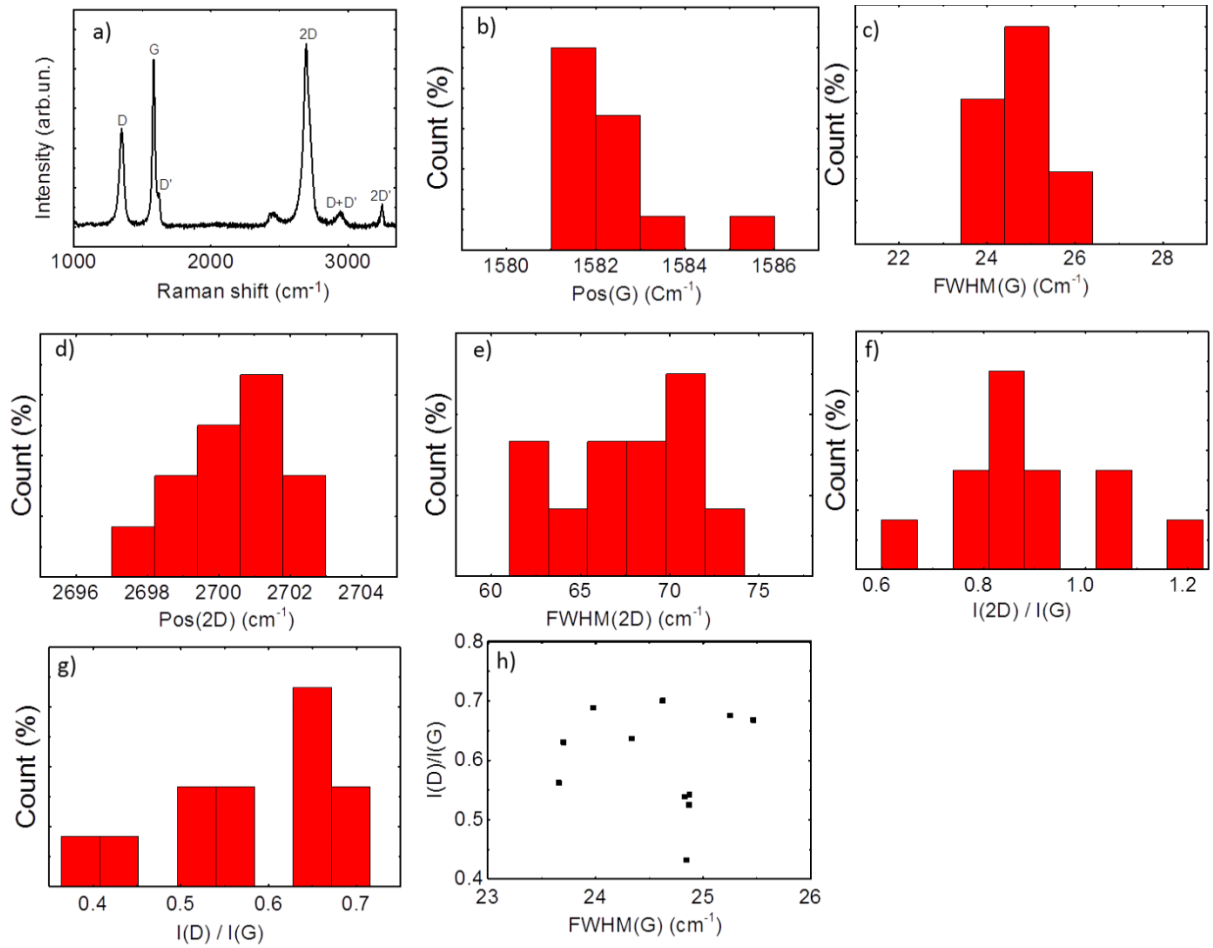

Figure 3.2. a) Representative Raman spectrum of the single-/few-layer graphene flakes produced by LPE in NMP. The D, G, D', 2D, D+D' and 2D' bands are also denoted. b) Statistical Raman analysis of the Pos (G), c) FWHM(G), d) Pos(2D), e) FWHM(2D), f) I(2D)/I(G), g) I(D)/I(G) and h) I(D)/I(G) *vs.* FWHM(G) plot.

3.1.3 Morphological Characterization

The morphology of the as-produced graphene flakes is characterized by means of TEM and AFM. Figure 3.3a shows a representative TEM image of graphene flakes, which have irregular shape and rippled morphology. Statistical TEM analysis of the flakes lateral dimension indicates values distributed in the range of 200-1500 nm and an average value of ~450 nm (Figure 3.3b).

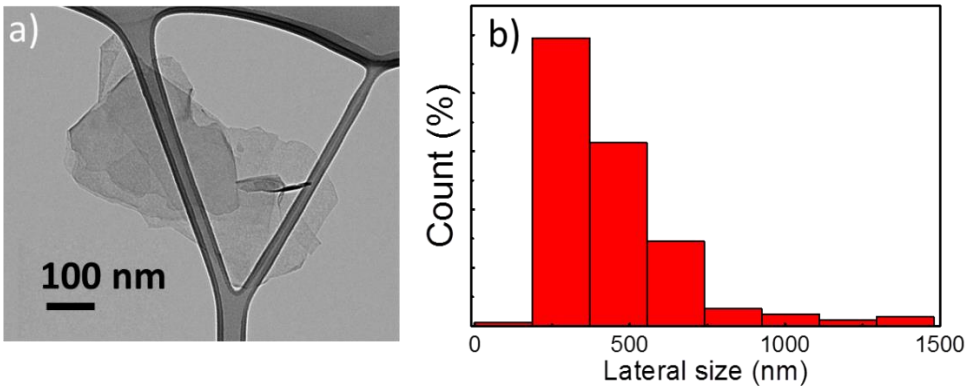

Figure 3.3. a) TEM images of the as-produced graphene flakes and b) TEM statistical analysis of their lateral dimension.

Figure 3.4a shows a representative AFM image of graphene flakes. The main thickness distribution is in the 0.5-4 nm range (Figure 3.4b), with the presence of few thicker flakes (> 5 nm). Thus, the sample is mostly composed by a combination of single- and fe-layer graphene flakes, in agreement with Raman spectroscopy analysis (see Section 3.1.2).

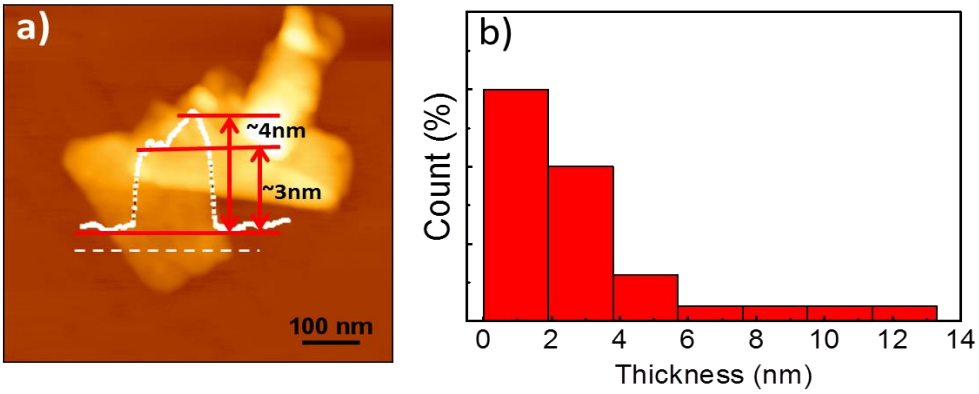

Figure 3.4. a) AFM images of the as-produced graphene flakes and b) AFM statistical analysis of their lateral dimension.

3.1.4 X-ray Photoelectron Spectroscopy Analysis

X-ray Photoelectron Spectroscopy (XPS) measurements are carried out on as-produced graphene flakes to ascertain their chemical composition. The results are shown in Figure 3.5. The C_{1s} spectrum of the graphene flakes (Figure 3.5a) shows the presence of oxidized C-O and C=O groups at binding energies 286.4 eV and 288.3 eV, respectively.[136] The percentage content (%c) of C=O and C-O is ~8%. However, these groups are also attributed to the presence of residual solvent molecule of NMP. In fact, N_{1s} spectrum (Figure 3.5b) indicates a %c of NMP ~3.5%. Taking into account the NMP contribution in the %c of the oxidized groups, these results confirm that high-

quality graphene flakes (%c >95%) are obtained by LPE in NMP, in agreement with previous studies.[137]

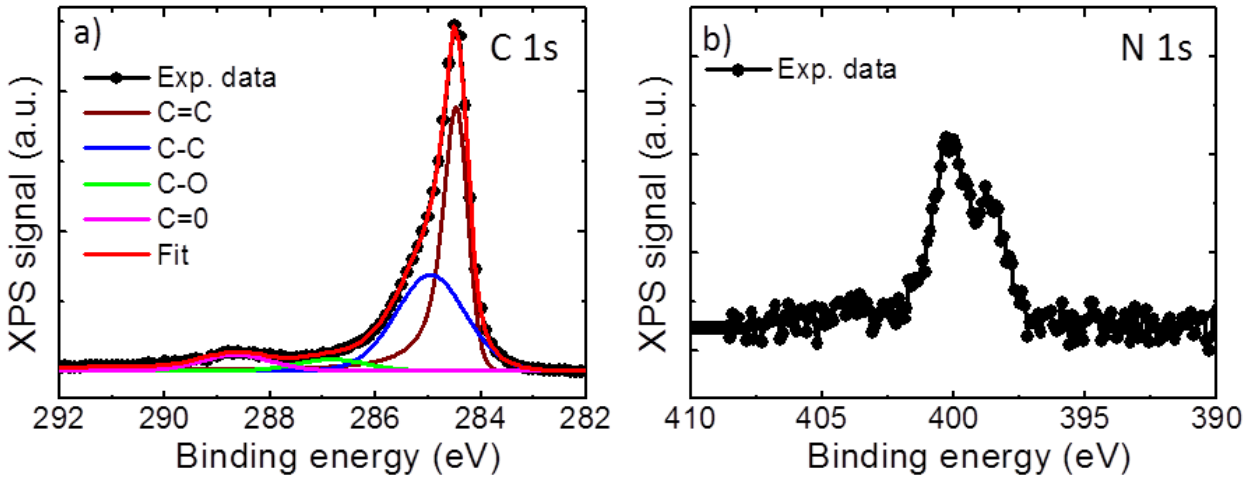

Figure 3.5. a) C 1s and b) N_{1s} XPS spectra of the graphene flakes sample produced by LPE of graphite in NMP. The deconvolution of C 1s XPS spectra is also shown, indicating the contribution of C=C (purple), C-C (blue), C-O (green), C=O (magenta).

3.2 Graphene Oxide RGO Flakes:

3.2.1 Optical Absorption Spectroscopy Analysis

Figure 3.6 shows the UV-Vis absorption spectra of GO and RGO dispersions in ethanol. The GO spectrum reports a characteristic maximum at ~240 nm; this maximum is assigned to π-π* transition of C-C bonds. The broad shoulder between 290-300 nm is as attributed to the π-π* transition of C=O bonds.[138,139,140,141] In the RGO spectrum, the maximum peak shifts to 275 nm and the absorption in the visible region (400-700 nm) increases with respect to GO. This is linked with the restoration of the π-conjugation of sp^2 carbon atoms in the aromatic rings upon thermal reduction.[142] Moreover, the peak attributed to C=O bonds is significantly attenuated and red-shifted of ~20 nm with respect to the GO spectrum. This indicates the removal of oxygen-containing functional groups in the RGO.[142,143,144]

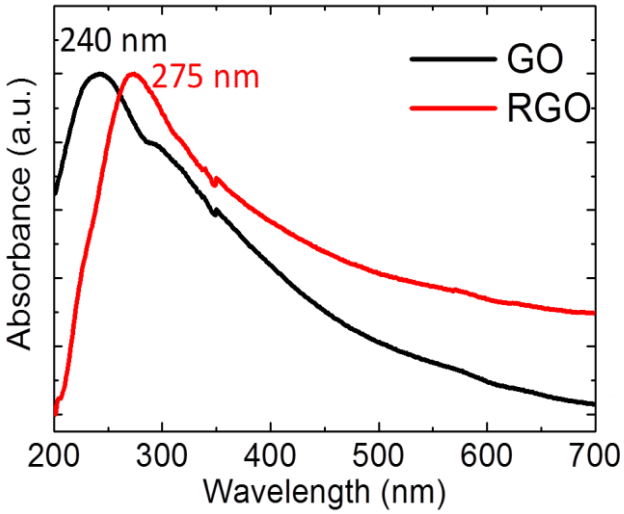

Figure 3.6. UV-Vis absorption spectra of GO (black line) and RGO (red line) dispersions in ethanol. The maximum absorption peaks (~240 nm for GO and ~275 nm for RGO), related to the π–π* transition of aromatic C–C bonds, are also evidenced.

3.2.2 Raman Spectroscopy Analysis

The structural properties of GO and RGO are also investigated by Raman Spectroscopy, whose spectra are reported in Figure 3.7. The Raman spectrum of GO reveals two main peaks located at 1352 and 1591 cm^{-1}, corresponding to D and G bands, respectively.[126,127]

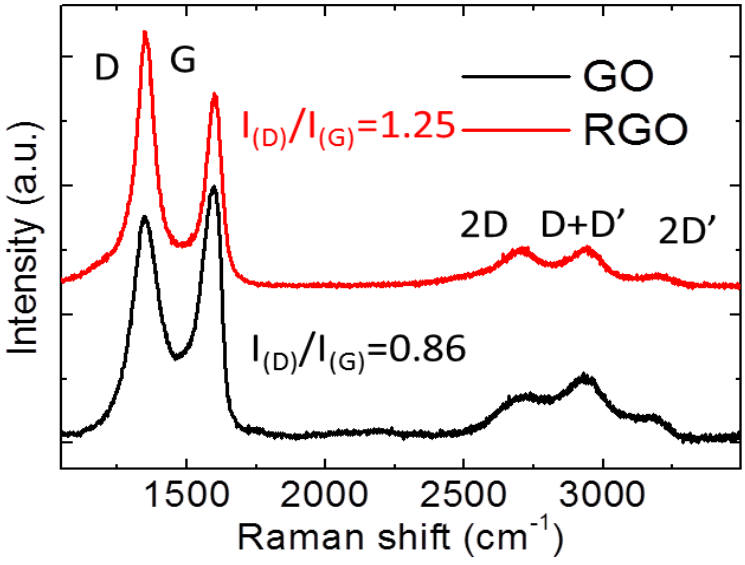

Figure 3.7. Raman spectra of GO (black line) and RGO (red line) deposited onto a Si wafer with 300 nm thermally grown SiO_2. The main peaks G and D, the overtones 2D and 2D' and the combination mode D+D' are also evidenced, together with the I(D)/I(G) (~0.86 for GO, and ~1.25 for RGO).

The 2D peak, is located at ~2700 cm^{-1}.While the D' band, being located at ~1600 cm^{-1} in presence of high-density defects, is merged with the G band. The 2D' peak is located at ~3200 cm^{-1},[129] while D+D', positioned at ~2940 cm^{-1} is the combination mode of D and D'.[129] These overtones show a low intensity and a very broad line shape due to electronic scattering,[145]. The FWHM(D) is 127 cm^{-1}, while FWHM(G) is 79 cm^{-1}. The FWHM(G) always increase with disorder and, indeed, it is much larger than pristine graphene (FWHM(G) < 20cm^{-1}) and edge-defected graphene flakes (FWHM(G)~25cm^{-1}, in accordance with Raman spectroscopy analysis in Section 3.1.2)[146,147] The increase of I(D)/I(G) (~0.86) and FWHM(D) (~125cm^{-1}) with respect to the those of graphene flakes (I(D)/I(G) (0.3-0.7) and FWHM(D) (37 cm^{-1})) is due to the presence of both structural defects (due to the oxidation process) and covalent bonds (*e.g.*, C–H, C–O), both contributing to the D peak. In the case of RGO, Pos(D) is at 1352 cm^{-1}, Pos(G) is at 1597 cm^{-1}, FWHM(G) is 64 cm^{-1} and FWHM(D) is 83 cm^{-1}. The softening of the G band with respect to that of GO could be ascribed to the presence of defected regions as consequence of thermal stresses upon annealing.[148] FWHM(D) and FWHM(G) are narrower with respect to those of GO, indicating a restoration of the sp^2 rings. The I(D)/I(G) for RGO (~1.25) is considerable higher with respect to the GO one (~0.86). The I(G) is constant as a function of disorder because it is related to the relative motion of sp^2 carbons, while an increase of I(D) is directly linked to the presence of sp^2 rings. Thus, an increase of the I(D)/I(G) ratio means the restoration of sp^2 rings.[Error! Bookmark not defined.,Error! Bookmark not defined.] Raman statistical analysis of the Pos(D), Pos(G), FWHM(D), FWHM(G) and the I(D)/I(G) is reported in Figure 3.8.

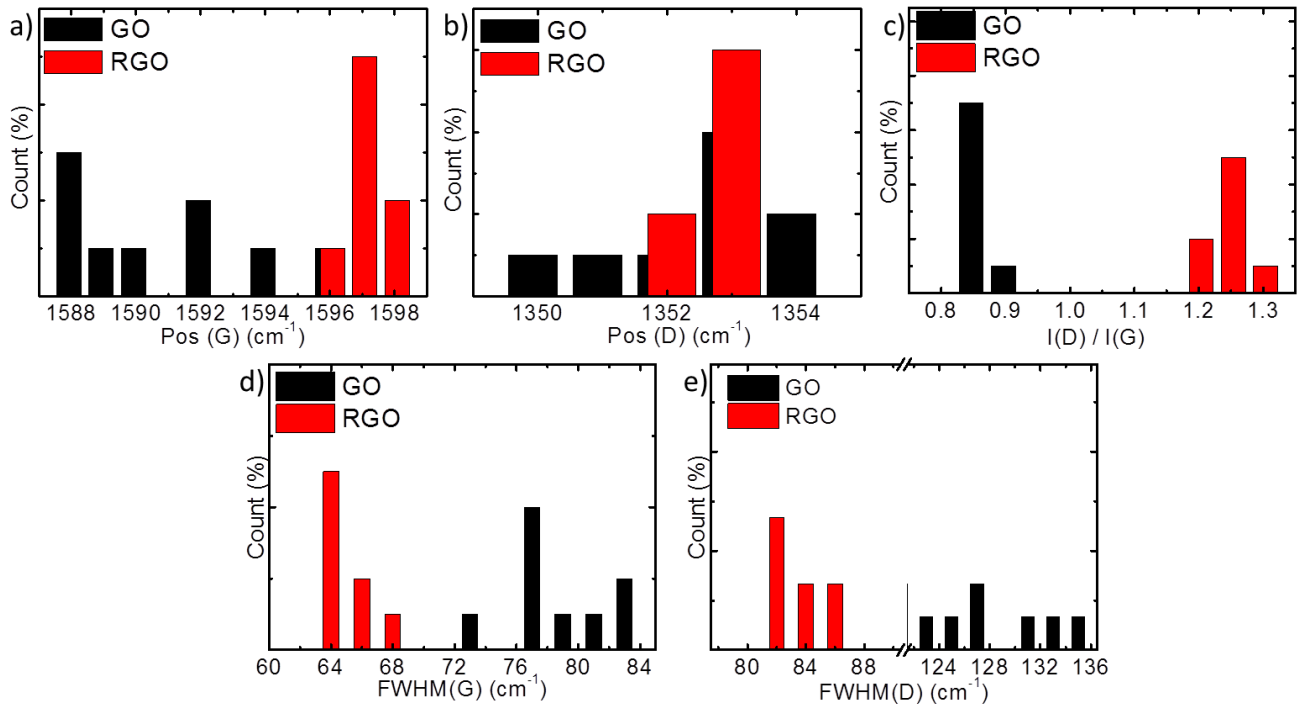

Figure 3.8. Statistical Raman analysis of the GO (black histograms) and RGO flakes (red histograms) for a) Pos(G), b) Pos(D), c) I(D)/I(G), d) FWHM(G) and e) FWHM(D), calculated on 20 spots measured. The GO and RGO flakes are deposited from their respective ethanol dispersions onto a Si wafer with 300 nm thermally grown SiO_2.

3.2.3 Morphological Characterization

The lateral size and thickness of the as-produced GO and RGO flakes is characterized by means of TEM and AFM, respectively. Figure 3.9a shows a representative TEM image of GO flakes, which have irregular shape and rippled morphology. Figure 3.9b shows the TEM image of RGO flakes, which have a more crumbled structure with respect to the GO ones. The TEM statistical analysis of the lateral size (Figure 3.9e) yields mean values of 2.8±1.6 μm for GO, and 1.7±0.8 μm for RGO. The changes of the RGO with respect to the GO are attributed to the thermal-induced stresses during the reduction treatment at high temperature (1000 °C).[149] Figure 3.9c,d show the AFM images of the GO and RGO flakes, respectively. Representative height profiles are also reported in Figure 3.9c,d (red lines), showing nano-edge steps between 0.6 and 1.6 nm indicating the overlap or few-layer structure of the flakes. The AFM statistical analysis (Figure 3.9f) gives an average thickness of 1.7±0.9 nm and 1.8±1.1 nm for GO and RGO flakes, respectively. This indicates the few-layer nature of the as-produced flakes (thickness of single-layer pristine graphene is ~0.34 nm).[150,151]

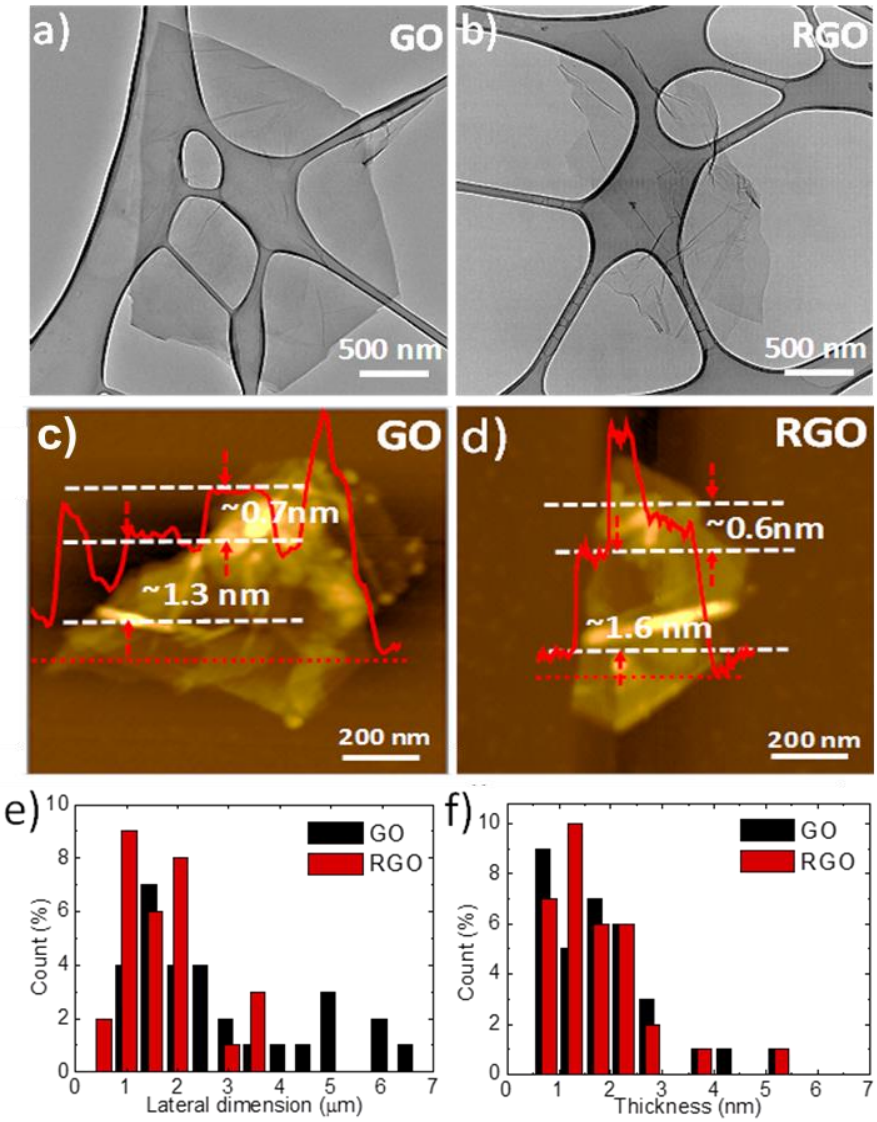

Figure 3.9. a) TEM images of the GO and b) RGO flakes drop casted onto carbon coated Cu TEM grids (300 mesh) from 0.01 mg mL^{-1} dispersions in ethanol. c) AFM images of GO and d) RGO flakes deposited onto a V1-quality mica substrate from 0.1 mg mL^{-1}. Representative height profiles of representative flakes are also shown (red line). e) TEM statistical analysis of the lateral dimension of GO (black histograms) and RGO flakes (red histograms), derived from different images and calculated on 50 flakes. f) AFM statistical analysis of the thickness of GO flakes (black histograms) and RGO flakes (red histograms), derived from different images and calculated on 50 flakes.

3.2.4 X-ray Photoelectron Spectroscopy Analysis

The C atomic network and the associated oxygen functional groups in the GO and RGO are evaluated by XPS measurements. Figure 3.10 shows that the C 1s spectrum of GO can be de-convoluted into four components[152]: the vacancies distorting the sp^2 network, the C-C bonds in the GO rings, the C-O groups, and the C=O groups, centered at (283.7±0.2), (284.7±0.2), (286.8±0.2) and (288.2±0.2) eV, respectively.[153,154,155] The corresponding atomic percentage contents (%c) show the prevalence of C-C (48.5%) and C-O bonds (41.5%). C=O bonds have still significant %c of

7.6%, while vacancies correspond to residual %c of 2.4%. These data indicate, as expected, the strong presence of the oxygen functionalities in GO. Different results are obtained for the C 1s spectrum of RGO, which is clearly dominated by C sp^2 (75.6%, peak centered at 284.5 eV), while the C-O peak, centered at (286.9±0.3) eV, is strongly reduced (6.9%) with respect to same peak of GO.[156,157] Vacancies-related and C=O bonds almost disappeared with respect to the GO case (indeed the reported fit is obtained with no vacancies and C=O contributions). Moreover, a residue of C sp^3 C is still present (peak centered at 285 eV, %c = 8.5%) as well as carboxylate carbon O–C=O bonds, represented by the peak at 290.0 eV with a %c of 3.8%. These results indicate that the delocalized π-conjugated structure is almost fully restored in RGO.[158,159]

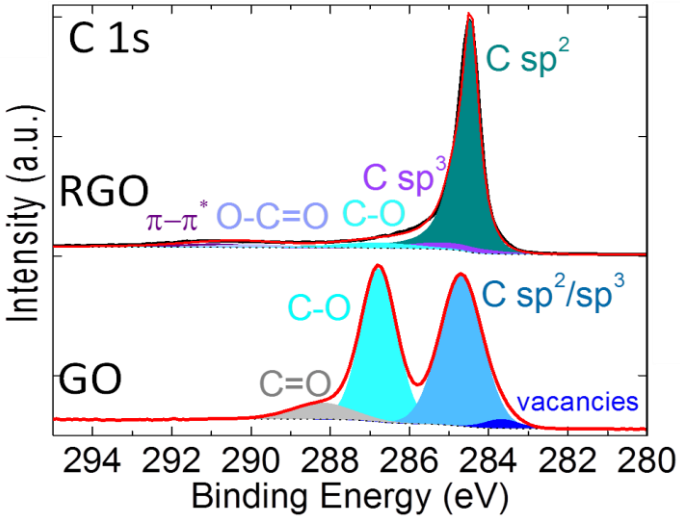

Figure 3.10. XPS spectra of C 1s peak of GO and RGO.

3.2.5 Ultraviolet Photoelectron Spectroscopy Analysis

Ultraviolet Photoelectron Spectroscopy (UPS) measurements are carried out to estimate the work function (WF), *thus* the position of the Fermi energy (E_F) *vs.* vacuum level, of GO and RGO flakes. Figure 3.11 shows the secondary electron cut-off (threshold) energies of the He-I (21.22 eV) UPS spectra of GO (~16.3 eV) and RGO (~16.7 eV). The corresponding WF values are 4.9 eV for GO and 4.4 eV for RGO. The higher WF of GO with respect to RGO is ascribed to the presence of surface dipole moments due to the oxygen functional groups, which disrupt the π-conjugation, as also evidenced by the XPS analysis,[160,161,162] The upper inset of Figure 3.11 shows the spectra region near the E_F, which are used for estimating the VB level of GO, ~6.7 eV, and RGO, ~4.4 eV (thus approaching its E_F level). The relative distance between the VB and E_F level of GO (~1.8 eV) indicates its insulating nature, while that of RGO (<0.1 eV) evidences its metal-like behavior.[163,164]

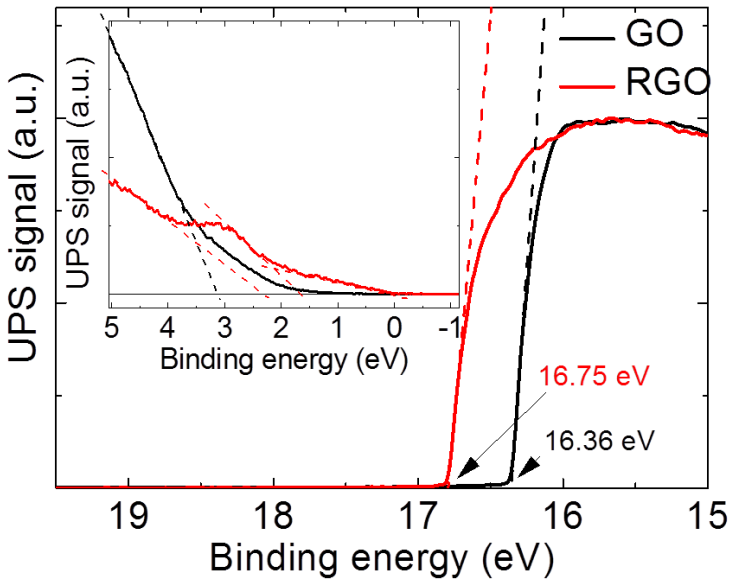

Figure 3.11. Secondary electron threshold region of He-I UPS spectra of GO (black line) and RGO (red line), which are used for estimating the WF values. The upper inset shows valence band region of He-I UPS spectra of GO and RGO which are used for estimating VB values.

3.3 Functionalized Graphene Oxide and f-RGO Flakes

3.3.1 Morphological Characterization

The effect of chemical modification with silane functionalities on the morphology of the f-GO and f-RGO flakes (see production details in Chapter 2, Section 2.1.7.5), with respect to the GO and RGO flakes, is investigated by means of TEM and AFM. Figure 3.12a and Figure 3.12b reports representative TEM images of f-GO and f-RGO flakes, respectively. Both cases present an irregular shape and rippled transparent paper-like morphology, with a more crumbled structure for the f-RGO with respect to that of GO. TEM statistical analysis of the lateral dimensions (Figure 3.12e) reports mean values of ~2.8±1.4 µm for f-GO, and ~1.7±0.9 µm for f-RGO. Figures 3.12c,d show the AFM images of f-GO and f-RGO flakes, respectively. Representative height profiles are also reported in Figures 3.12c,d (red lines), showing nano-edge steps between 0.6 nm-0.8 nm. This indicates the overlap or few-layer structure of the flakes, as observed for the native GO and RGO (see Section 3.2.3). AFM statistical analysis (Figure 3.12f) gives an average thickness of 2.0±1.1 nm for f-GO flakes and 1.7±0.9 nm for f-RGO flakes. The values of lateral dimension and thickness obtained for f-GO and f-RGO are comparable with the ones of GO and RGO, respectively (See Section 3.2.3). Thus, the TEM and AFM results indicate that the chemical modification of the flakes, with silane functional groups, does not affect the lateral dimension and thickness of the

flakes (mean values of 2.8±1.4 µm for f-GO (1.7±0.9 µm for f-RGO) and 2.0±1.1 nm for f-GO flakes (1.7±0.9 nm for f-RGO flakes), respectively).

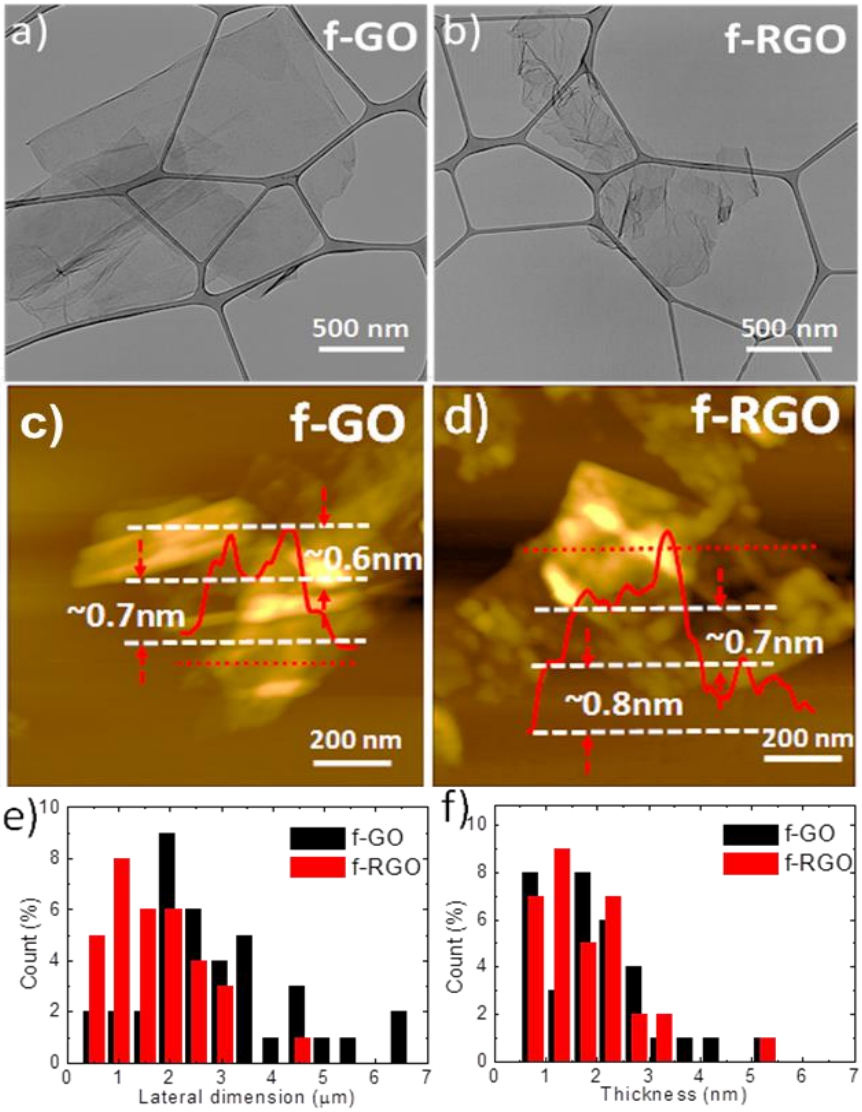

Figure 3.12. a) TEM images of the f-GO and b) f-RGO flakes drop casted onto carbon coated Cu TEM grids (300 mesh) from 0.01 mg mL^{-1} dispersions in ethanol. c) AFM images of f-GO and d) f-RGO flakes deposited onto a V1-quality mica substrate from 0.1 mg mL^{-1}. Representative height profiles of representative flakes are also shown (red line). e) TEM statistical analysis of the lateral dimensions of GO (black histograms) and RGO flakes (red histograms), obtained from different images and calculated on 50 flakes. f) AFM statistical analysis of the thickness of GO flakes (black histograms) and RGO flakes (red histograms), obtained from different images and calculated on 50 flakes.

High-resolution TEM images of f-GO (Figure 3.13a) and f-RGO (Figure 3.13b) show darker grey spots (different contrast with respect to the GO and RGO flakes) that are attributed to the presence of MPTMS molecules anchored over the flakes.

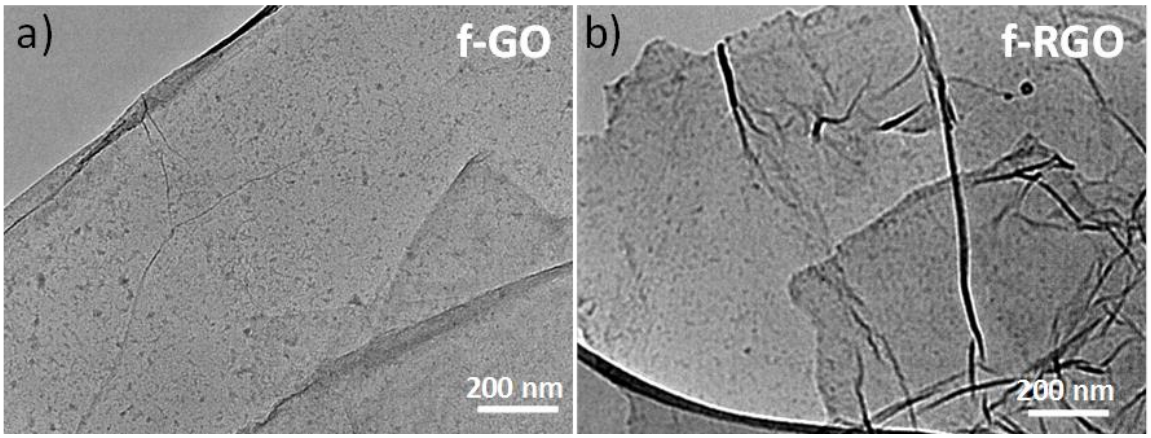

Figure 3.13. a) High-resolution TEM image of f-GO and b) f-RGO casted onto carbon coated Cu TEM grids (300 mesh) from 0.01 mg mL^{-1} dispersions in ethanol.

3.3.2 X-ray Photoelectron Spectroscopy Analysis

The extent of silane functionalization of GO and RGO flakes is evaluated by means of XPS measurements. In the Si 2s and S 2p spectra (Figure 3.14a), the appearance of the silane- and thiol-related peaks at (153.4±0.3) eV and 163.4±0.3) eV, respectively,[165,166] indicates the effectiveness of the MPTMS functionalization procedure, although sulfur oxidation is observed (peaks around ~168 eV and ~169 eV related to S 2p doublet of SO_4^{2-})[167,168] both in the f-GO and f-RGO samples. These oxidized S groups are either due to MPTMS molecules that interacted with oxygen moieties on the GO and RGO surfaces or, more likely, to a fraction of molecules that gets oxidized during the functionalization process itself. The oxidized S groups are the 33% and the 15% of the total S content for f-GO and f-RGO, respectively. The functionalization level is estimated from the ratio between the sum of the %c of SH free and S-S bonds related to the silane and that of C bonds (~0.06 and ~0.03 for f-GO and f-RGO, respectively). The functionalization level is estimated from the ratio between the %c of un-oxidized S and that of C (~0.02 and ~0.01 for f-GO and f-RGO, respectively). The lower level of functionalization for f-RGO with respect to the one of f-GO is related to its low content of oxygen functionalities (Figure 3.10), which act as anchor points for the silane groups,[169,170,171] Moreover, the XPS analysis evidences an interconnection between the MPTMS molecules in the f-RGO case, since a low intensity S 2p doublet related to S-S bonds (centered at ~164.5 eV, accounting for 10% of the total S content) is needed for fitting of the experimental data. The increase of the C sp^2 %c of f-GO (58.2%) with respect to that of GO (48.5%) is attributed to the slight heating during the functionalization process. For the case of f-RGO flakes, the C sp^2 %c (75.7%) is the same observed for RGO flakes. Thus, the π-conjugated structure of RGO is not affected by the functionalization process.[172]

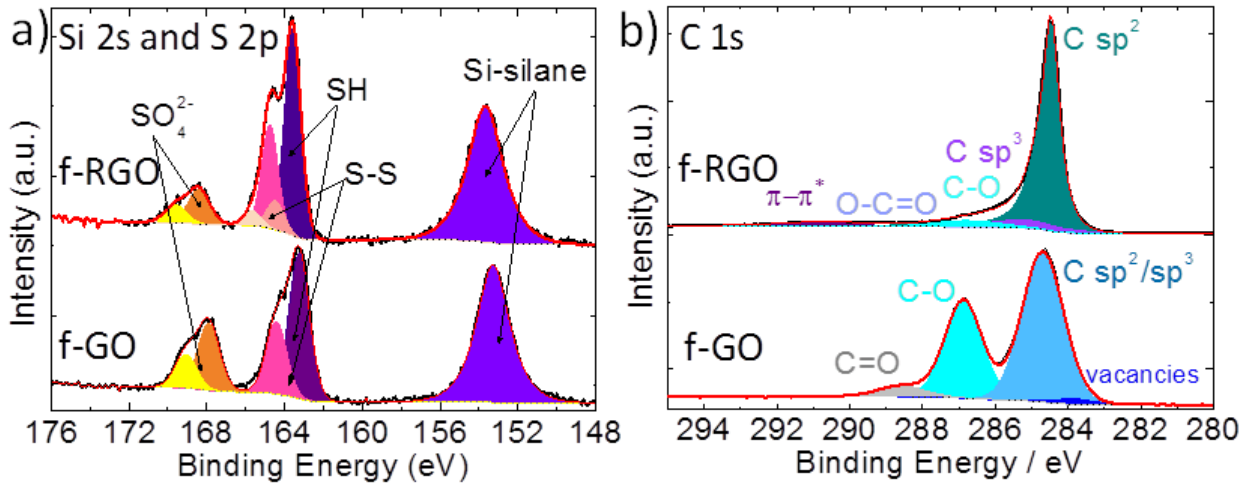

Figure 3-14. a) Si 2s and S 2p spectra of f-GO and f-RGO. Their deconvolution is also shown. b) C 1s spectra of GO and RGO. Their deconvolutions are also shown.

3.3.3 Ultraviolet Photoelectron Spectroscopy Analysis

Ultraviolet photoelectron spectroscopy (UPS) measurements of f-GO and f-RGO flakes are reported in Figure 3-15. The UPS data acquired for GO and RGO flakes (as previously shown in Figure 3.11) are also reported as comparison. The secondary electron cut-off energies of the He-I (21.22 eV) UPS spectra, as obtained by applying a bias of -9 V to the samples, of GO and f-GO is equal (~16.3 eV), while a slight difference of 0.1 eV is observed for RGO (~16.7 eV) with respect to f-RGO (~16.8 eV). The corresponding WF values are 4.9 eV for GO and f-GO, 4.4 eV for RGO and 4.3 eV for f-RGO. The higher WF of GO and f-GO with respect to that of RGO and f-RGO is attributed the presence of surface dipole moments attributable to the oxygen functional groups which disrupt the π-conjugation, as evidenced by the XPS analysis (Figures 3.10 and 3.14b). Importantly, the functionalization with silane molecules does not introduce significant changes. The inset of Figure 3.15 shows the spectra region near E_F, which are used for estimating the VB level of the materials (~6.7 eV for GO, ~6.9 eV for f-GO, and 4.4 for both RGO and f-RGO). These results indicate that the insulating behavior of GO is also confirmed for the f-GO, while the metal-like behavior of RGO is preserved by the f-RGO.

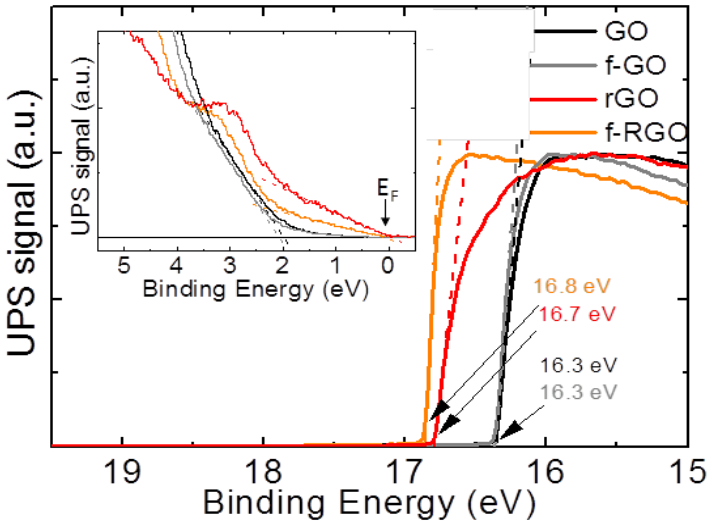

Figure 3.15. Secondary electron threshold region of He-I UPS spectra of GO (black line), f-GO (grey line), RGO (red line) and f-RGO (orange line). The upper inset shows valence band region of He-I UPS spectra of GO and RGO which are used for estimating VB values.

3.4 2H-MoS_2, 1T-MoS_2 Flakes and 2H-MoS_2 QDs

Layered TMD materials, depending on the arrangement of S atoms, present generally two different polymorph structures: 2H (trigonal prismatic D3h) and 1T (octahedral Oh) phases (Figure 3-16). The two phases are supposed to exhibit completely different electronic structures. The 2H phase is relatively stable, but semiconducting and of poor conductivity. The 1T phase is metastable at room temperature, but metallic and of better conductivity. Both phases can easily convert to each other through an intra-layer atomic plane glide, which involves a transversal displacement of one of the S-planes.[173]

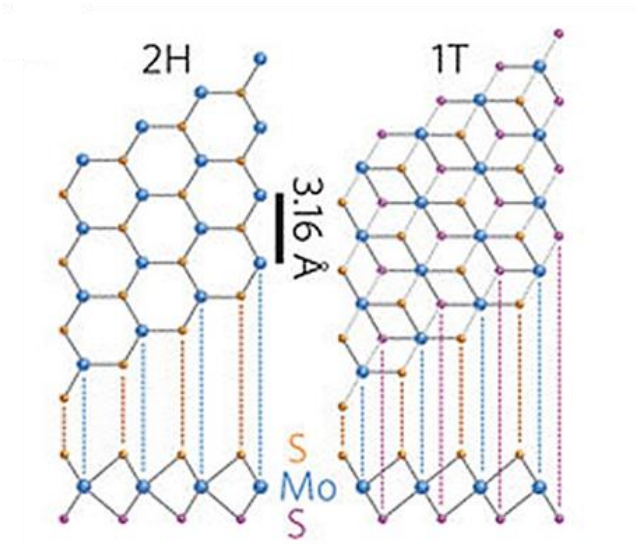

Figure 3.16. Schematic models of single-layered MoS_2 with 2H and 1T phases in basal plane. Mo, blue; top S, orange; bottom S', purple. [174]

3.4.1 Optical Absorption Spectroscopy Analysis

The UV-Vis absorption spectra of 2H-MoS_2 flakes and 2H-MoS_2 QDs dispersed in IPA are reported in Figure 3.17. For 2H-MoS_2 flakes, absorption peaks at ~670 nm and ~620 nm arise from the direct transitions from the valance band to the conduction band at the K-point of the Brillouin zone of layered MoS_2, known as the A and B transitions, respectively. The broad absorption band centered at ~400 nm arises from the C and D inter-band transitions between the density of state peaks in the valence and conduction bands.[175,176,177,178]

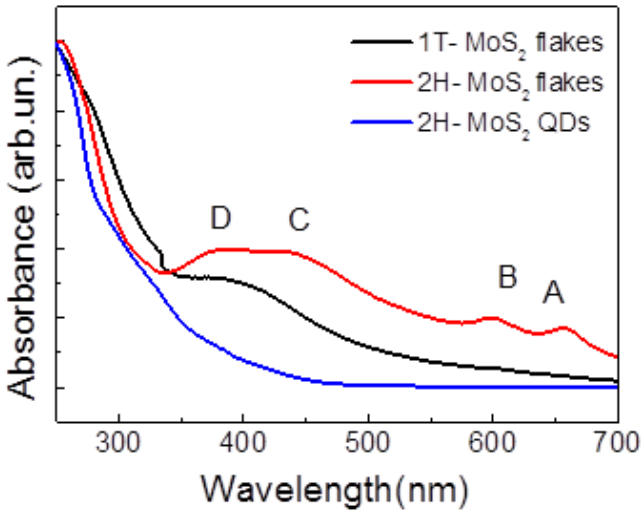

Figure 3-17. UV-Vis absorption spectra of 0.1 mg mL^{-1} 2H-MoS_2 flakes, 1T-MoS_2 flakes and 2H-MoS_2 QDs dispersion in IPA.

Differently from the 2H-MoS_2 flakes, the 2H-MoS_2 QDs do not show the typical excitonic peaks (A, B, C, D), and their absorption edge is shifted towards lower wavelength with respect to the flakes. This is a consequence of quantum confinements effects, which increases the gap energy of QDs with the decrease of their lateral size.[179,180,181]

3.4.2 Photoluminescence Characterization

The PL spectra of 2H-MoS_2 QDs dispersion in IPA, collected at different excitation wavelengths (from 280 to 500 nm) are reported in Figure 3.18a. The PL peaks are red-shifted with increasing excitation wavelength. This excitation-dependent PL emission is ascribed to quantum confinements and edge state emission effects. The sharp small features observed in the spectra are related to the IPA solvent, as observed in its blank PL spectrum[182] (Figure 3.18b). Both the 2H-MoS_2 and 1T-MoS_2 flakes does not shown any PL signal in the visible range, being their band gap

significantly reduced with respect to those of the 2H-MoS_2 QDs, in accordance with optical absorption spectroscopy analysis of the previous section.

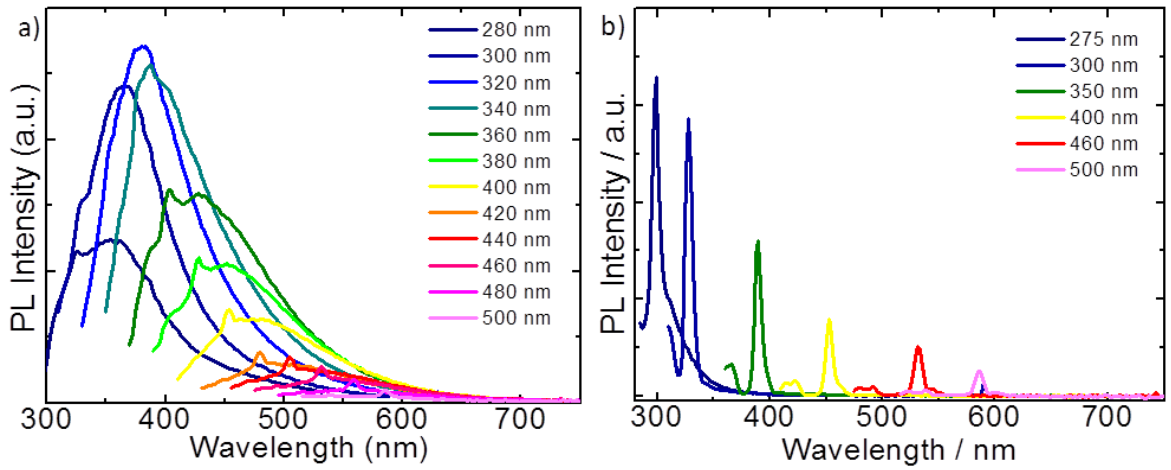

Figure 3.18. a) Photoluminescence spectra of the 2H-MoS_2 QDs at different excitation wavelength (*i.e.*, ranging from 280 to 500 nm). b) Blank (control) PL measurements of IPA at different excitation wavelength.

3.4.3 Raman Spectroscopy Analysis

Raman spectroscopy measurements are carried out to investigate the vibrational modes of 2H-MoS_2 ,1T-MoS_2 flakes and 2H-MoS_2 QDs with respect to those of bulk MoS_2 (Figure 3.19). According to group theory analysis, bulk TMDs are members of D_{6h} point group symmetry,[183] characterized by four Raman active modes, *i.e.*, three in-plane E_{1g}, E^1_{2g}, and E^2_{2g}, and one out-of-plane A_{1g}. Only two of those are typically accessible experimentally, namely E^1_{2g} and A_{1g},[184] since the E^2_{2g} mode is at very low frequencies (~30 cm^{-1}), and the E_{1g} mode is forbidden in backscattering geometry on a basal plane.[Error! Bookmark not defined.] The E^1_{2g} and A_{1g} modes involves the in-plane displacement of Mo and S atoms and the out-of-plane displacement of S atoms, respectively. Representative Raman spectra show the presence of $E_{2g}{}^1(\Gamma)$ (~379 cm^{-1} for 1T-MoS_2, 2H-MoS_2 flakes and 2H-MoS_2 QDs, and ~377 cm^{-1} for bulk MoS_2) and $A_{1g}(\Gamma)$ (~403 cm^{-1}). The $E_{2g}{}^1(\Gamma)$ mode of the 1T-MoS_2, 2H-MoS_2 flakes and 2H-MoS_2 QDs exhibits softening with respect to the one of the bulk MoS_2. The shift of the $E_{2g}{}^1(\Gamma)$ mode is explained by the dielectric screening of long range Coulomb MoS_2 interlayer interaction.[185,186] In additional, Raman spectra between 600-900 cm^{-1} do not reveal additional peaks related to molybdenum oxide species[187], such as the MoO_3 bands located at ~285 cm^{-1} (B_{2g}, B_{3g}), ~666 cm^{-1} (B_{2g}, B_{3g}) and ~820 cm^{-1} (Ag, B_{1g})[188] or the MoO_2 band located at ~203 cm^{-1}, ~228 cm^{-1}, ~345 cm^{-1}, ~363 cm^{-1}, ~461 cm^{-1}, ~495 cm^{-1}, ~571 cm^{-1}, ~589 cm^{-1} and ~744 cm^{-1}.[189] The peaks located at ~520 cm^{-1} and ~303 cm^{-1} are attributed to the

transverse optical (TO) and the second-order transverse acoustic (2TA) phonon modes of Si[190,191], (samples are deposited onto Si/SiO_2 substrates), respectively.

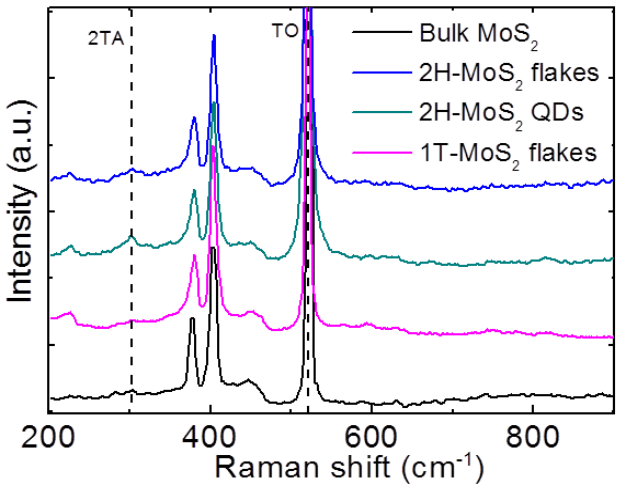

Figure 3.19. Raman spectra of the bulk MoS_2 (black), 1T-MoS_2 (magenta), 2H-MoS_2 flakes (blues) and 2H-MoS_2 QDs (cyan). The peaks located at ~520 cm^{-1} and 303 cm^{-1} are ascribed to the TO and the 2TA phonon modes of Si are indicated by black vertical dashed lines.

The FWHM of the $E_{2g}^1(\Gamma)$ and $A_{1g}(\Gamma)$ (FWHM($E_{2g}^1(\Gamma)$) and FWHM($A_{1g}(\Gamma)$), respectively) of 2H-MoS_2 flakes and 2H-MoS_2 QDs increases of ~3 cm^{-1} and ~2 cm^{-1}, respectively, compared to the corresponding modes of bulk MoS_2. The increase of FWHM($A_{1g}(\Gamma)$) for 2H-MoS_2 flakes and QDs is attributed to the variation of interlayer force constants between the inner and outer layers. Figure 3.20 shows the statistical Raman analysis of the peaks position difference of the $A_{1g}(\Gamma)$ and $E_{2g}^1(\Gamma)$ modes, *i.e.*, Pos(A_{1g}) - Pos(E_{2g}^1), FWHM(E_{2g}^1) and FWHM(A_{1g}) for 2H-MoS_2 flakes (panel a, b and c, respectively), 2H-MoS_2 QDs (panels d, e and f, respectively), 1T-MoS_2 flakes (panels g, h and i, respectively) and bulk MoS_2 (panels j, k and l, respectively).

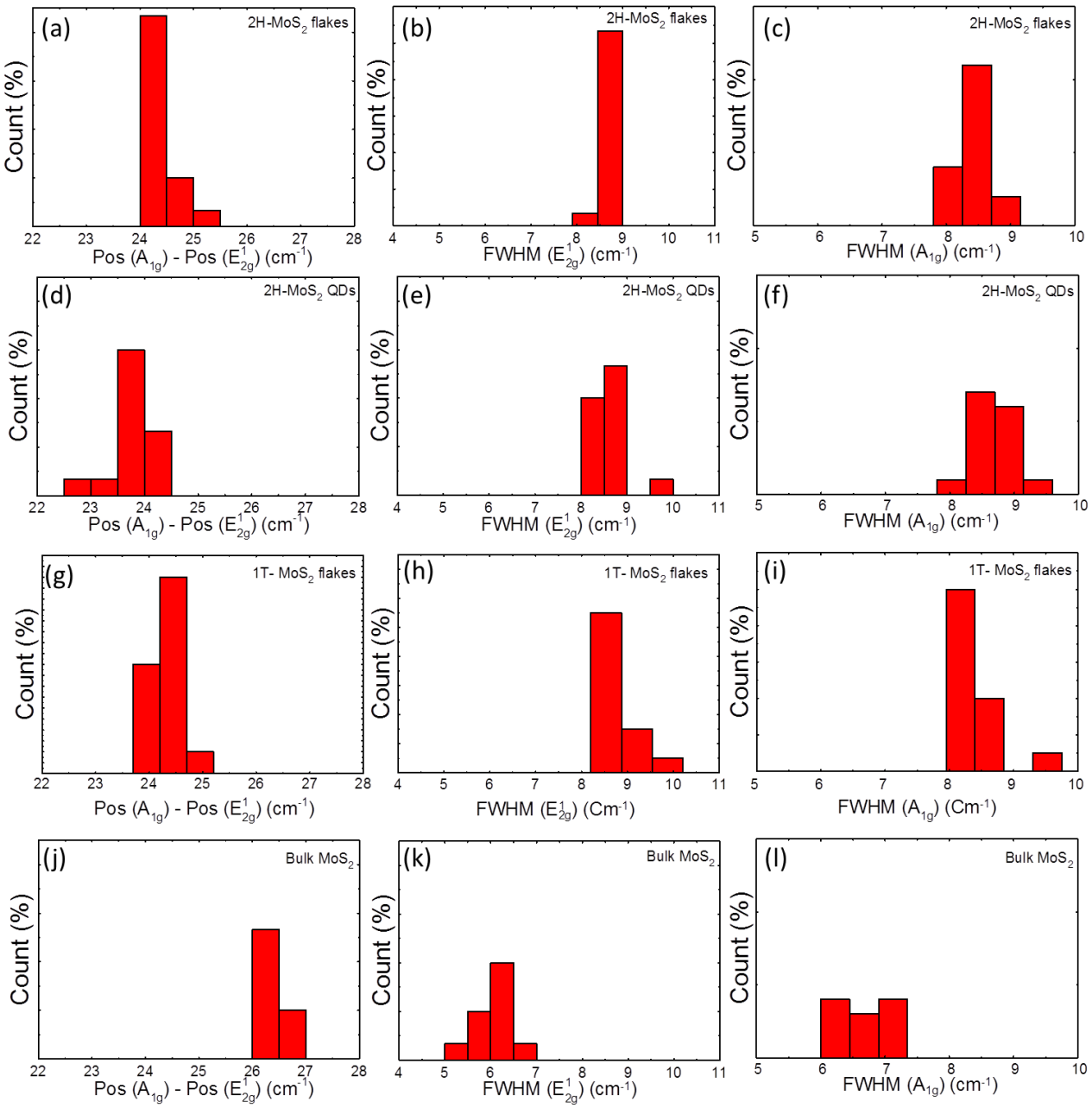

Figure 3.20. Statistical Raman analysis of a) Pos(A_{1g}) - Pos(E_{2g}^1), b) FWHM(E_{2g}^1) and c) FWHM(A_{1g}) for 2H-MoS_2 flakes; d) Pos (A_{1g}) - Pos(E_{2g}^1), e) FWHM(E_{2g}^1) and f) FWHM(A_{1g}) for 2H-MoS_2 QDs; g) Pos (A_{1g}) - Pos(E_{2g}^1), h) FWHM(E_{2g}^1) and i) FWHM(A_{1g}) and 1T-MoS_2 flakes; j) Pos (A_{1g}) - Pos(E_{2g}^1), k) FWHM(E_{2g}^1) and l) FWHM(A_{1g}) for bulk MoS_2.

3.4.4 Morphological Characterization

Figure 3.21a,b,c show representative TEM images of sample 2H-MoS_2 flakes, 2H-MoS_2 QDs and 1T-MoS_2 Flakes, respectively. 2H-MoS_2 and 1T-MoS_2 flakes are composed by irregularly shaped flakes with average lateral dimension of ~420 nm and ~250 nm, respectively (Figure 3.21 j,l), while 2H-MoS_2 QDs consists of QDs with average lateral dimension of ~6 nm (Figure 3.21k). Figure 3.21d,e,f show representative AFM images of 2H-MoS_2 flakes, 2H-MoS_2 QDs and 1T-MoS_2 flakes,

respectively. Height profiles (dashed white lines) indicate the presence of one- and two-layer flakes and QDs (the monolayer thickness between 0.7-0.8 nm).[192] The average thickness of both the 2H-MoS_2 flakes and 2H-MoS_2 QDs is ~2.7 nm (Figure 3.21m,n) while in case of 1T-MoS_2, the average thickness is ~0.7 nm (Figure 3.21p) .

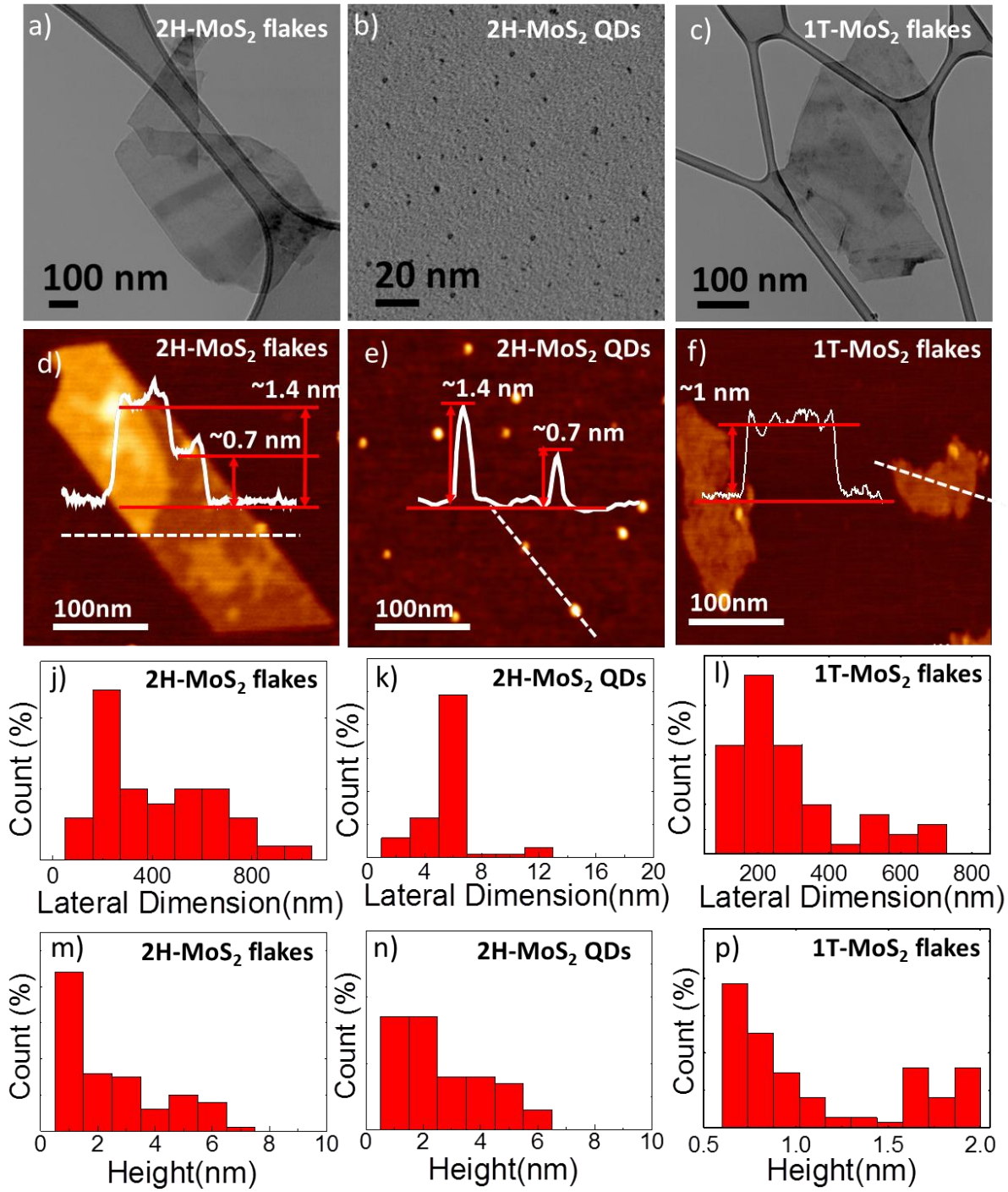

Figure 3.21. TEM images of the as-produced a) 2H-MoS_2 flakes , b) QDs and c) 1T-MoS_2 flakes.AFM images of representative as-produced d) 2H-MoS_2 flakes, e) QDs and f) 1T-MoS_2 flakes, deposited onto mica sheets. Representative height profiles (solid white lines) of the indicated sections (white dashed lines) are also shown. TEM statistical analysis of j) 2H-MoS_2 flakes, k) QDs and l) 1T-MoS_2 flakes . AFM statistical analysis of m) 2H-MoS_2 flakes, n) QDs and p) 1T-MoS_2 flakes.

3.4.5 X-ray Diffraction Measurements

X-ray diffraction (XRD) measurements are used to evaluate the crystal structure of 2H-MoS_2 flakes and 2H-MoS_2 QDs with respect to the bulk MoS_2 (Figure 3.22). Bulk MoS_2 exhibits the characteristic XRD peaks of hexagonal-structure polycrystalline films (JCPDS card no.77-1716).[193] The dominant (002) peak, centered at 14.4°, corresponds to the interlayer spacing (*d*) of 0.614 nm. In addition, various weak diffraction reflections are also observed at higher angles, e.g., the ones attributed to the (100), (103), (006), (105), and (008) planes, which are characteristic of polycrystalline MoS_2. For the 2H-MoS_2 flakes, the intensity of the (002) peak increases with respect to that of bulk MoS_2, indicating a preferential exposure of (002) basal planes,[194,195] while all the other diffraction reflections almost disappear, in agreement with the single crystal structure of the few-layered 2H-MoS_2 flakes. In the case of QDs, the intensity of (002) peak is strongly reduced with respect to the bulk material and the 2H-MoS_2 flakes. Similar to 2H-MoS_2 flakes, all the other diffraction peaks disappear.[193] These results indicate that the QDs have the same crystal structure of their native flakes.

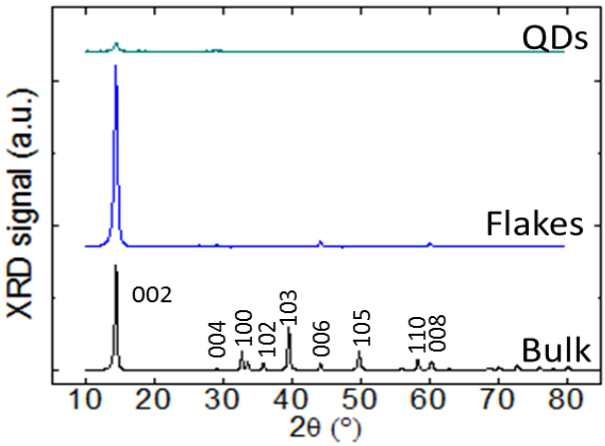

Figure 3-22. XRD spectra of bulk MoS_2, 2H-MoS_2 flakes and 2H-MoS_2 QDs.

3.4.6 X-ray Photoelectron Spectroscopy Analysis

The XPS measurements are carried out on both the as-produced 2H-MoS_2 flakes and 2H-MoS_2 QDs to determine their elemental composition and chemical phase. The S 2s and Mo 3d XPS spectra are shown in Figure 3.23 together with their deconvolution. Here, the peak at the lowest binding energy (~226 eV) is assigned to S 2s while the peak at ~229 eV is assigned to Mo $3d_{5/2}$ of 2H-MoS_2. The peak centered at ~232.5 eV can be fitted with two components. The first component (~232 eV) is assigned to Mo $3d_{3/2}$ of the 2H-MoS_2.[196] Instead, the second component (~233 eV), as well

as the low intensity peak centered at ~236 eV, are associated with the MoO_3 phase, usually produced as a byproduct of exfoliated MoS_2 flakes exposed to air.[197] However, the MoO_3-related peaks in both flakes and QDs spectra are negligible, indicating a transformation of only a small fraction of sulfide to oxide during the production of flakes and QDs from the bulk MoS_2. In fact, the percentage content (%c) of MoO_3 is <7% and <5% for flakes and QDs, respectively. These results prove that our production method produces 2H-MoS_2 flakes and QDs, overcoming the drawbacks of previous studies on MoS_2 flakes produced by LPE in NMP,[196] where oxidized species (%c between 40 and 60%, depending on processing) are present. Moreover, the solvothermal treatment does not change the chemical composition of the 2H-MoS_2 flakes, since there are no significant differences between the XPS spectra of flakes and QDs.

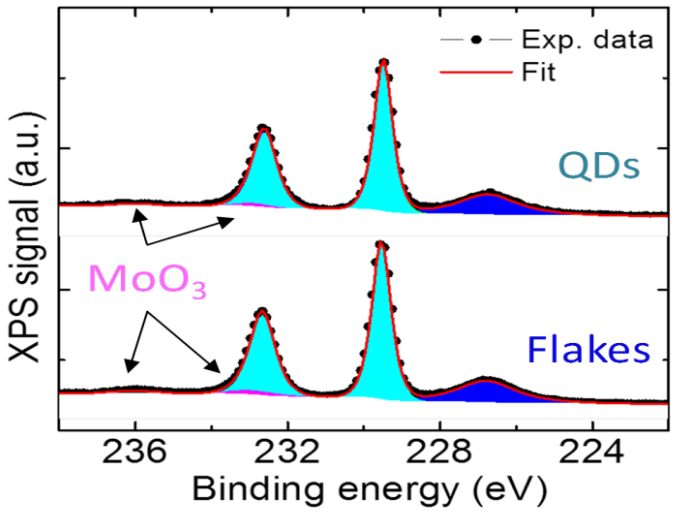

Figure 3-23. Mo $_{3d}$ and S $_{2s}$ XPS spectra for 2H-MoS_2 flakes and QDs. Their deconvolution is also shown, and the area of the MoS_2 related bands are colored in blue (S $_{2s}$) and cyan (Mo $_{3d}$). The bands attributed to the MoO_3 are colored in magenta.

Figure 3-24a reports the XPS spectra of the as produced 1T-MoS_2 flakes. As shown in Chapter 2, the 1T-MoS_2 flakes are obtained by chemical lithium intercalation method.[198] By this method, the resulting MoS_2 flakes are expected to be a mixture of both 2H and 1T phase. Nevertheless, previous studies showed that the metastable metallic 1T phase dominate the electro catalytic properties of the as-exfoliated material[199,200,201]. Notably, mild annealing (~100 ^{o}C) leaded to gradual restoration of the semiconducting phase.[202] Following these consideration, in the XPS spectrum of 1T-MoS_2 flakes, the peaks located at ~229 eV and at ~232 eV are assigned to Mo 3d and they are fitted by two components. These are attributed to the 2H (green line) and 1T phase (cyan line) of MoS_2, respectively. Figure 3.24b shows the XPS spectra of MoS_2 QDs produced

starting from the 1T-MoS_2 flakes. Clearly, the 1T phase contribution is reduced with respect to the one observed in 1T-MoS_2 flakes, indicating that the solvothermal treatment causes a 1T-to-2H phase conversion.[182] These results prove that it is challenging to produce 1T-MoS_2 QDs from 1T-MoS_2 flakes because of the intrinsic metastable nature of the latter.

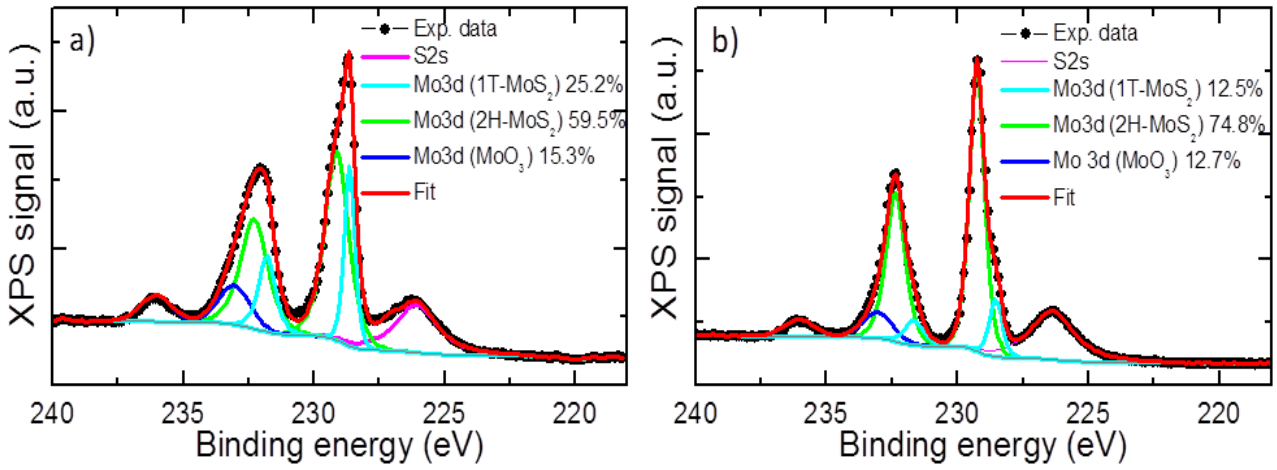

Figure 3-24. Mo 3d and S 2s XPS spectra for a) 1T-MoS_2 flakes and b) the MoS_2 QDs derived from 1T-MoS_2 flakes. Their deconvolutions are shown, indicating the contribution of both 1T and 2H phase of MoS_2 for Mo 3d peaks (solid cyan and green lines, respectively). The S 2s band of MoS_2 and Mo 3d bands of MoO_3 are also evidenced (solid magenta and blue lines, respectively). The percentage contents of Mo $_{3d}$ bands attributed to 2H-MoS_2, 1T-MoS_2 and MoO_3 are also reported in the figure legends.

3.5 2H-$MoSe_2$ Flakes

In the following sections, 2H-$MoSe_2$ flakes, as derived by LPE in IPA (see Chapter 2) will be simply denoted by $MoSe_2$ flakes, being the 1T-$MoSe_2$ flakes not investigated in this dissertation.

3.5.1 Optical Absorption Spectroscopy Analysis

The UV-Vis absorption spectrum of $MoSe_2$ flakes dispersion in IPA is reported in Figure 3.25. Absorption peaks around 810 nm (1.53 eV) and 708 nm (1.75 eV) correspond to the A and B excitonic peaks. These peaks arise from the direct inter band transitions at the K-point of the Brillouin zone of the 2H-phase $MoSe_2$,[203] as originated from the energy split of valence-band formed from the Mo atom, and spin-orbital coupling due to the in-plane confinement of the electron and atomic mass of Mo,[204] The shoulder in the absorption spectra around ~410 nm is attributed to the C and D inter-band transitions between the density of state peaks in the valence and conduction bands of the 2H-phase of $MoSe_2$,[205] Thus, the origin of these band resembles that of MoS_2, as reported in see Section 3.4.1.

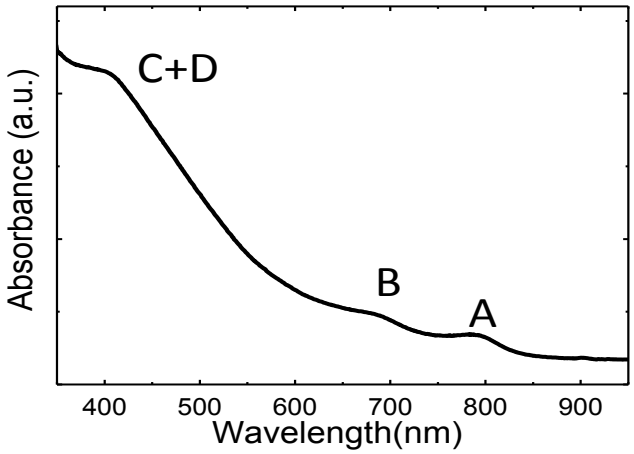

Figure 3.25. UV-Vis absorption spectrum of 2H-$MoSe_2$ flakes dispersions in IPA. The excitonic peak peaks (A and B) and the inter-band transitions (C and D) are also indicated.

3.5.2 Raman Spectroscopy Analysis

Raman spectroscopy is carried out on both $MoSe_2$ bulk and $MoSe_2$ flakes in order to investigate their different topological structure. As previously explained in Section 3.4.3., $MoSe_2$ belong to the D_{6h} point group symmetry, characterized by three in-plane E_{1g}, E^1_{2g}, and E^2_{2g}, and one out-of-plane A_{1g}. Only two of those are typically accessible experimentally, namely E^1_{2g} and A_{1g},[184] since the E^2_{2g} mode is at very low frequencies (~30 cm^{-1}), and the E_{1g} mode is forbidden in backscattering geometry on a basal plane.[184] Additionally, when the number of layers decreases below a certain threshold, the interlayer vibrational mode B_{2g} becomes active, because of the breakdown of translational symmetry.[206] This mode is present only in few-layer flakes, while it is absent in single-layer $MoSe_2$.[207] Representative spectra of $MoSe_2$ bulk and $MoSe_2$ flakes are reported in Figure 3.26. The A_{1g} mode is located at ~241 cm^{-1} for the $MoSe_2$ bulk, while it is red-shifted to ~239 cm^{-1} for the 2H-$MoSe_2$ flakes, in agreement with the softening of the vibrational mode accompanied by the reduction in flake thickness. The in-plane E^1_{2g} mode is observed at ~287 cm^{-1} for both samples.[207] For the case of 2H-$MoSe_2$ flakes, the E^1_{2g} peak position (Pos(E^1_{2g})) and intensity (I(E^1_{2g})) are estimated by simultaneously fitting the E^1_{2g} and the nearby (partially overlapped) Si peaks. [208]

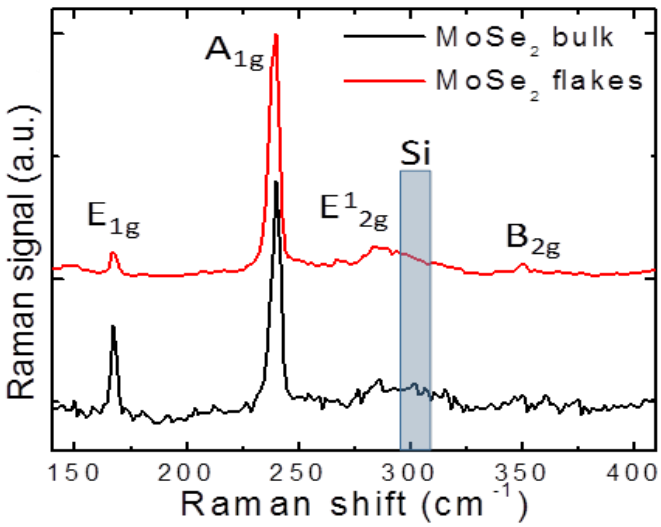

Figure 3.26. Raman spectra of $MoSe_2$ bulk (black) and as-produced $MoSe_2$ flakes deposited on Si/SiO_2 substrates. The main peaks, *i.e.*, the in-plane modes E_{1g}, E^1_{2g}, and E^2_{2g}, the out-of-plane mode A_{1g} and the breathing mode B^1_{2g} are named in the graph.

This procedure is not applied for $MoSe_2$ bulk because of its lower $I(E^1_{2g})$ with respect to that of $MoSe_2$ flakes. The intensity ratio between the A_{1g} and E^1_{2g} modes ($I(A_{1g})/I(E^1_{2g})$) for $MoSe_2$ flakes is ~21. This value agrees with those reported for few-layer $MoSe_2$ flakes.[209] The in-plane E_{1g} mode is observed at ~167 cm^{-1} in both $MoSe_2$ bulk and $MoSe_2$ flakes. The activation of the mode E_{1g} is due by a resonance-induced symmetry breaking effect.[210] Moreover, the energy of this mode, being independent on the number of layers, does not change between the $MoSe_2$ bulk and exfoliated flakes. Finally, the B_{2g} mode, inactive for $MoSe_2$ bulk, is present at ~352 cm^{-1} for the $MoSe_2$ flakes, confirming their few-layers morphology.[211] Statistical Raman analysis is reported in Figure 3.27

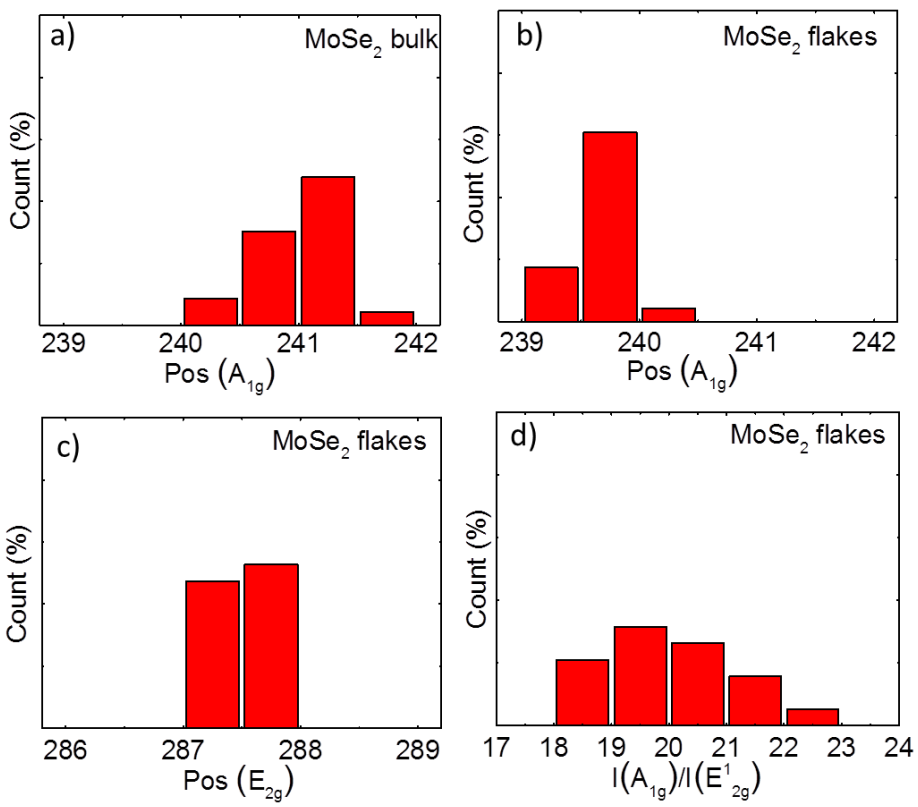

Figure 3.27. Statistical Raman analysis of: a) Pos (A_{1g}) of $MoSe_2$ bulk; b) Pos(A_{1g}), c) Pos(E_{2g}) and I(A_{1g})/I(E_{2g}) of $MoSe_2$ flakes.

3.5.3 Morphological Characterization

Figure 3.28a shows the TEM image of $MoSe_2$ flakes, displaying crumpled paper-like structure. Statistical TEM analysis (Figure 3.28b) indicates a lateral size of the flakes in the 10-170 nm range (log normal distribution peaking at ~29 nm). A representative AFM image of the exfoliated 2H-$MoSe_2$ flakes is shown in Figure 3-28c, together with the height profile of a single $MoSe_2$ flake (white line in Figure 3-28c), showing a nano-edge steps (i.e., flake thickness) of ~1 nm. Statistical AFM analysis (Figure 3-28d) evidences the presence of single- to few-layer $MoSe_2$ flakes (thickness of a $MoSe_2$ monolayer lies generally between 0.6 nm and 1 nm)[212], with a log normal distribution peaking at ~3 nm.

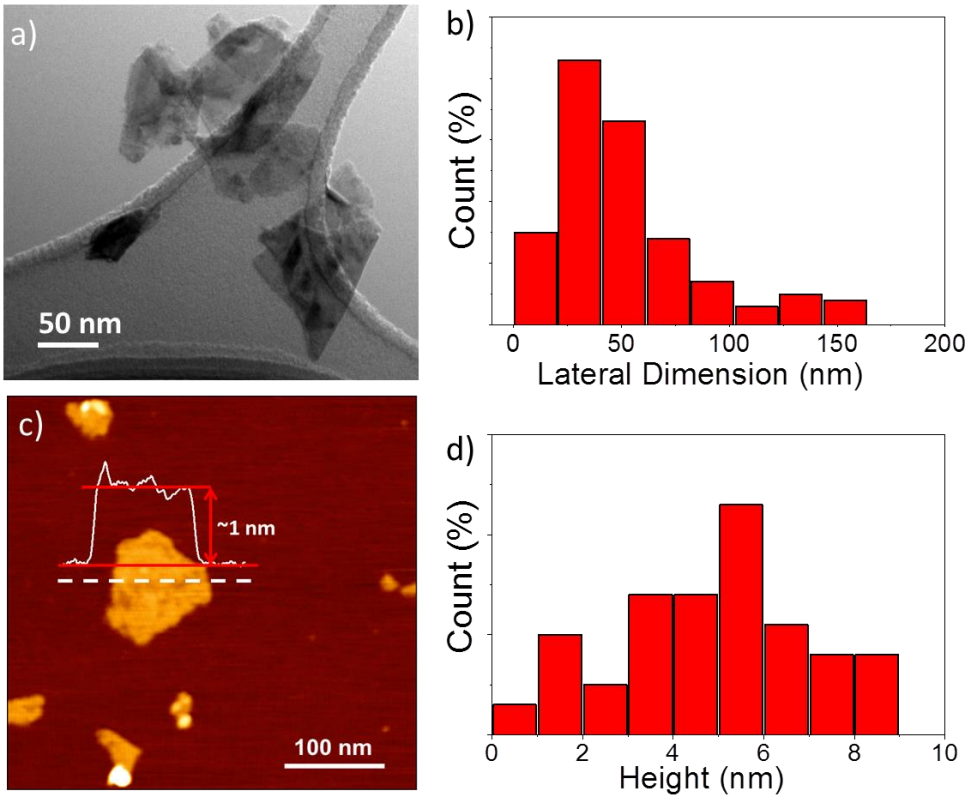

Figure 3-28. a) TEM images of the 2H-$MoSe_2$ flakes and b) the statistical analysis of their lateral dimension (calculated on 80 flakes). c) AFM images of $MoSe_2$ flakes deposited onto a mica sheet. The height profile of a representative flake is also shown (white line). d) Statistical analysis of the thickness of the $MoSe_2$ flakes (calculated on 80 flakes from different AFM images).

3.5.4 X-ray Diffraction Measurements

The crystallinity of the $MoSe_2$ flakes is investigated through XRD measurements. Figure 3.29 show the XRD pattern obtained for $MoSe_2$ flakes, together with that of the $MoSe_2$ bulk. The latter can be indexed with JCPDS Card No. 29-0914 of the hexagonal phase of $MoSe_2$ (*i.e.*, 2H-$MoSe_2$), in agreement with several reports in literature.[213,214] For the case of $MoSe_2$ flakes, the (002) peak is clearly broadened (see inset to Figure 3-29) and the other peaks, although retaining the same position of the native bulk, almost disappear. This indicates the exfoliated nature along the c-axis of the $MoSe_2$ flakes without phase changes. The data also indicate the purity of the materials, since they do not reveal additional peaks assigned to Se powder and oxidized species.

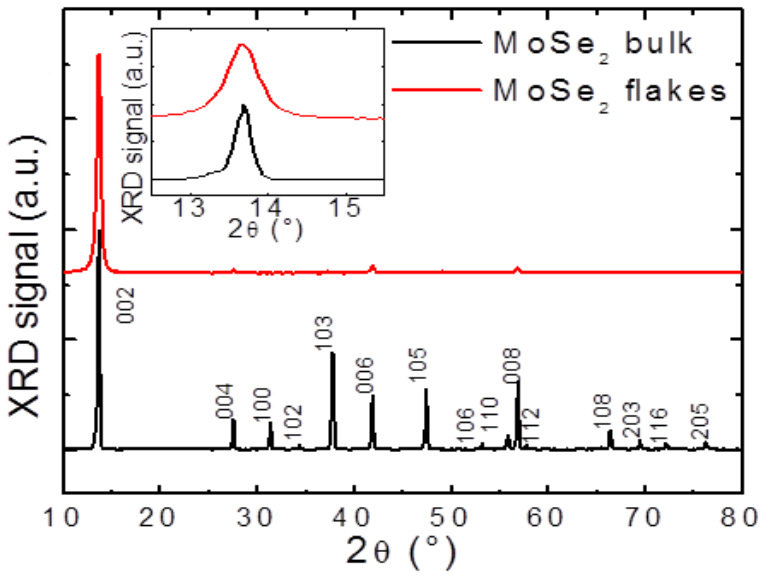

Figure 3.29. XRD spectra of the $MoSe_2$ bulk (black) and $MoSe_2$ flakes. The diffraction peaks of the hexagonal phase of $MoSe_2$ (2H-$MoSe_2$) are also indicated over the XRD spectrum of the $MoSe_2$ bulk. The inset panel shows the broadening of the (002) peak of the $MoSe_2$ flakes with respect to that of the $MoSe_2$ bulk.

3.5.5 X-ray Photoelectrons Spectroscopy Analysis

The XPS measurements are carried out on $MoSe_2$ bulk and $MoSe_2$ flakes to further study the chemical composition and states. Mo 3d and Se 3d XPS spectra are shown in Figure 3.30a,b respectively, together with their deconvolution. In Figure 3.30a, the two peaks located at (229.3±0.2) eV and (232.4±0.2) eV correspond to Mo $3d_{5/2}$ and Mo $3d_{3/2}$ peaks of Mo(IV) state in $MoSe_2$, in agreement with literature reports for MoS_2 and $MoSe_2$.[215,216] The additional peaks at binding energies of (232.5±0.2) eV and (235.7±0.2) eV are assigned to the Mo(VI) state and are related to MoO_3 residues.[217] The compositional analysis indicates that the percentage content (%c) of MoO_3 (defined as $MoO_3/(MoO_3+MoSe_2)$) is ~11% in the $MoSe_2$ flakes case, consistent with the one recorded for $MoSe_2$ bulk (~6%). This result proves that LPE of $MoSe_2$ bulk crystal in IPA produces $MoSe_2$ flakes without the drawbacks of TMD flakes produced by LPE in NMP, which gives oxidized species at significantly higher contents (%c between 40-60%, depending on the exfoliation processing).[218] In Figure 3-30b, the peaks at (54.9±0.2) eV and (55.7±0.2) eV are attributed to the Se $3d_{5/2}$ and Se $3d_{3/2}$ peaks, respectively, of the selenide moiety of $MoSe_2$.[219] The compositional analysis shows that the Mo:Se atomic ratio is higher than 1:1.9 for both $MoSe_2$ bulk and $MoSe_2$ flakes, almost in agreement with the theoretical stoichiometry of $MoSe_2$ (1:2).

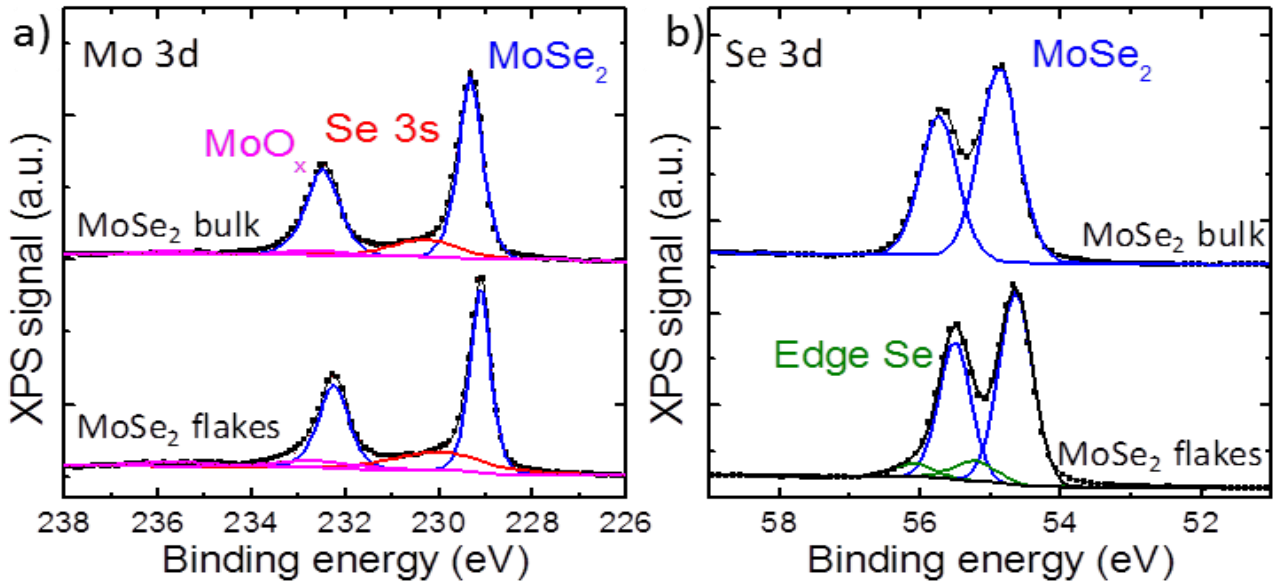

Figure 3.30. a) Mo 3d and b) Se 3d XPS spectra for $MoSe_2$ bulk (top curves) and $MoSe_2$ flakes (bottom curves). Their deconvolution is also shown, evidencing the band ascribed to: $MoSe_2$ (blue curves); Se 3s band (red curve), overlapping the Mo 3d XPS spectrum; oxidized species (MoO_x) (magenta curves); Edge (elemental) Se (green curves).

3.6 SWCNTs

3.6.1 Optical Absorption Spectroscopy Analysis

Figure 3.31 reports the UV-Vis/NIR absorbance spectrum of SWCNT dispersions in NMP. As predicted by theory, the absorbance spectrum of SWCNTs is expected to be dominated by a series of relatively sharp inter band transitions, at energies denoted as E_{11}, E_{22}, etc., associated with the van Hove singularities.[220] The latter are correlated with the electronic structure of SWCNTs. In fact, the quasi 1D nature of SWCNTs, including semiconducting versus metallic character, cause the electronic density of states to have a series of sharp van Hove maxima at energies dependent on tube diameter (d) and the chiral wrapping angle describing its construction from a graphene sheet.[221,222] The spectrum shown in Figure 3.31 is consistent with this expectation, with the first van Hove transitions (E_{11}) of the direct band gap semiconducting tubes falling in the 900-1300 nm wavelength range, while their subsequent van Hove transition (E_{22}) are located between 550 and 900 nm. The lowest energy van Hove transitions of the metallic SWCNTs also appear between 400 and 600 nm. All of the transitions are in good accordance with the diameter distribution from 0.8 to 1.2 nm. [221,222]

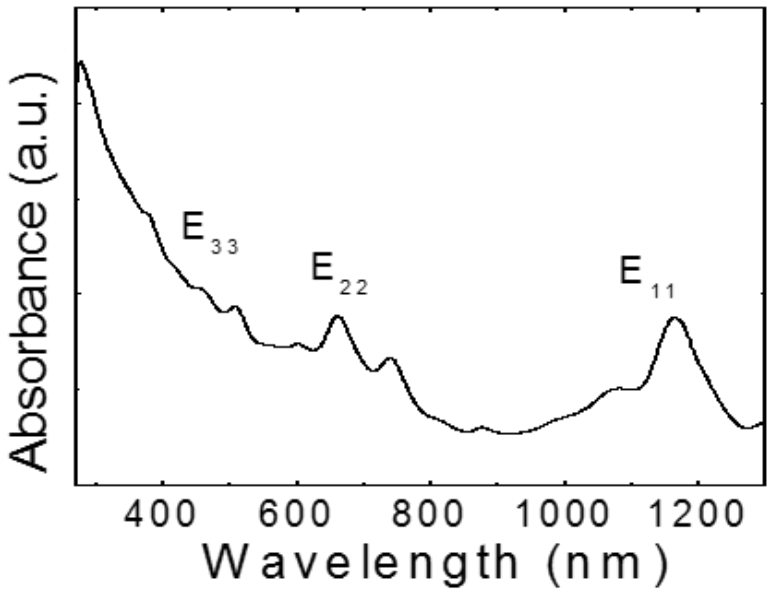

Figure 3.31. UV-Vis/NIR absorbance spectrum of SWCNT dispersions in NMP. The van Hove transitions are indicated.

3.6.2 Raman Spectroscopy Analysis

Raman spectroscopy is a useful tool for studying the structure of SWCNTs. The main features of the Raman spectrum of SWCNTs are the radial breathing modes (RBMs),[223] as well as the D, G^+ and G^- and 2D peaks. The Pos(RBM), is inversely related to SWCNT diameter (d)[224] as given by Pos(RBM)= $C_1/d + C_2$. In this study we use the C_1=214.4 cm^{-1} nm and C_2=18.7 cm^{-1}, in accordance with previous studies.[225] Raman spectroscopy also probes possible damage, i.e., the presence of defects, via the D peak.[226] The D peak is due to the breathing modes of sp^2 rings and requires a defect for its activation by double resonance.[227] The G^+ and G^- bands are located between 1500-1600 cm^{-1}. These originate from the longitudinal (LO) and tangential (TO) modes, respectively, derived from the splitting of the E_{2g} phonon of graphene at the Brillouin zone center.[228] The positions of the G^+ and G^- peaks, Pos(G^+), Pos(G^-), are diameter dependent and their separation increases with decreasing diameter.[229] In metallic SWCNTs, the FWHM (G^-) is larger and Pos(G^-) down-shifted with respect to the semiconducting SWCNTs.[230] Thus, a wide, low frequency G^- is a fingerprint of metallic SWCNTs. The Raman spectrum of our SWCNTs acquired at 532 nm excitation wavelength is shown in Figure 3-32 The spectrum shape indicates the presence of metallic SWCNTs, while the analysis of the Pos(RBM) indicates d <1 nm. A weak D peak is also observed, I(D)/I(G) <0.15, indicating the presence of a small number of defects.[231]

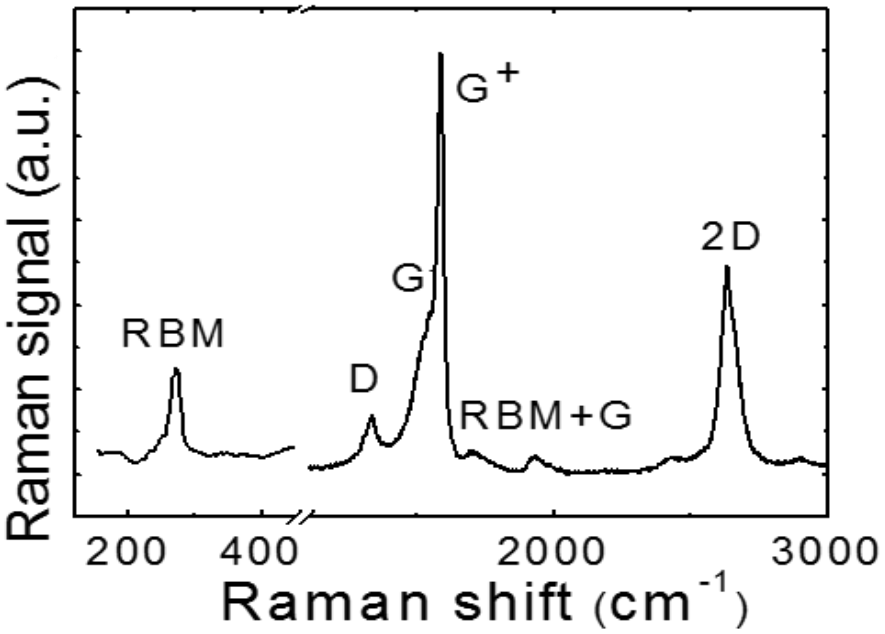

Figure 3.32. Raman spectrum of SWCNTs. The main mode are evidenced.

3.6.3 Morphological Characterization

Figure 3.33a,b shows representative TEM images of bundled SWCNTS. The length of the SWCNTs is between 5-30 µm (Figure 3-33a), in accordance with their datasheet provided from the supplier company. Amorphous carbon is not evidenced at the highest magnification of Figure 3-33b, agreeing with the declared quality of the SWCNTs (amorphous carbon content < 3%).

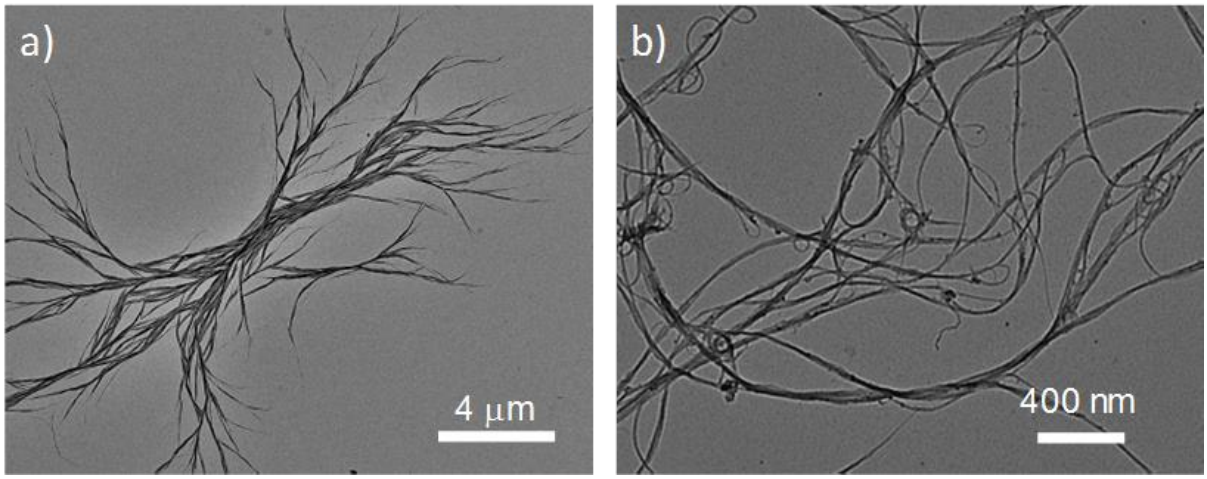

Figure 3.33. TEM images of bundled SWCNTs at different magnification: scale bar of a) 4 µm and b) 400 nm.

CHAPTER 4

CHAPTER 4: Transition Metal Dcihalcogenides for Hydrogen Evolution Reaction (HER)

4.1 Fundamentals of HER

Hydrogen, as a clean, efficient, and durable energy carrier, has been intensively pursued to address the issues of severe global energy shortage and environmental deterioration.[232,233] Toward this end, an effective approach to hydrogen production is based on environmentally friendly electrocatalytic water-splitting,[234,235] which involves the HER[236] and the oxygen evolution reaction (OER).[237]

The electrocatalytic production of hydrogen via water splitting is composed of two half reactions:

Anode : $2H_2O \leftrightarrow O_2 + 4H^+ + 4e^-$ (oxygen evolution reaction, OER) Ea = 1.23V − 0.059 · pH (V vs. normal hydrogen electrode ,NHE)

Cathode: $4H^+ + 4e^- \leftrightarrow 2H_2$ (hydrogen evolution reaction, HER) Ec = 0V − 0.059 ·pH (V vs. NHE) (see Figure 4.1a).

In fact, 1.23 V is the lowest limit voltage we need to split water into hydrogen and oxygen.

The HER in acid solution is assumed to proceed by an initial discharge of the hydronium ion (H_3O^+) and the formation of hydrogen intermediated, *i.e.*, atomic hydrogen adsorbed (H_{ads}), in the so-called Volmer step ($H_3O^+ + e^- \rightleftarrows H_{ads} + H_2O$), followed by either the electrochemical Heyrovsky step ($H_{ads} + H_3O^+ + e^- \rightleftarrows H_2 + H_2O$) or the chemical Tafel recombination step ($2H_{ads} \rightleftarrows H_2$). In alkaline conditions, the H_{ads} is formed by the discharge of H_2O ($H_2O + e^- \rightleftarrows H_{ads} + OH^-$). Then, either the Heyrovsky step ($H_2O + H_{ads} + e^- \rightleftarrows H_2 + OH^-$) or the chemical Tafel recombination step ($2H_{ads} \rightleftarrows H_2$) occur. Currently, Pt-group metals are the most efficient electrocatalysts for HER, but the high price and low availability of Pt-group metals hinder their widespread commercialization. Thus, the ongoing search for Pt-free catalysts with highly catalytic activity, high durability in both acid and alkaline conditions and low cost for the HER has attracted much attention.[238] Recent work showed that the 2D-TMD semiconductors are promising and attractive electrocatalysts for the HER.[239] Two general types of surface sites are present on 2D-crystal: terrace sites on the basal planes and edge sites on the side surfaces. However after theoretical calculation, the edge sites are found to be active for HER, but not the terrace sites. That is the reason why for example bulk MoS_2 and $MoSe_2$

are not an active catalyst for HER. The basal surface of these material, which were previously believed to be inert towards the HER, can be converted into HER active species via appropriate structural engineering, which included phase and morphological transformation, metal doping, defect site generation. Since increasing the number of active sites would enable high – performance 2D-catalyst for HER, Engineering the TMD electrocatalysts is therefore one of the major frontiers of the HER research.[240]

4.1.1 Overpotential, Tafel Slope, Exchange Current Density and Faradaic Efficiency

The Figures of Merit (FoM) to assess the HER-activity of an electrocatalysts are: 1) the overpotential at 10 mA cm^{-2}-cathodic current density (η_{10}); 2) the Tafel Slope (b); 3) the exchange current (i_0) and 4) the Faradaic Efficiency (FE).[241,242] More in details, b and i_0 are extracted from the linear portion of the Tafel plots, which show the relation between the overpotential and the current density of the electrodes, in accordance with the Tafel equation[241,243]

$$\eta = a + b\ log|i|$$

In this equation, η is the applied overpotential, i is the measured current a is A is the intercept of the linear regression and b is the Tafel slope. More in detail, this equation can be derived by simplifying the Butler-Volmer equation:[245]

$$\eta = -\frac{RT}{anF}\ Ln\ (i_0) + \frac{RT}{anF}\ Ln\ (i)$$

Here, R is the ideal gas constant, T is the absolute temperature, α is the transfer coefficient, n is the number of electrons transferred, F is the faraday constant, and i_0 is the exchange current. This equation can be simplified to yield the version written above by making the following substitutions:

$$b = \frac{2.3RT}{anF}$$

Experimentally, b have often been used to identify the HER mechanism and its rate-determining step (r.d.s.). In particular, for[241,244,245]

Volmer reaction: $b = \frac{2.3\ RT}{aF} \approx 120\ mV$

Heyrovsky reaction, $b = \frac{2.3\ RT}{(1+a)F} \approx 40\ mV$

Tafel reaction, $b = \frac{2.3\ RT}{2F} \approx 30\ mV$

While these values can be used as a guide for identifying HER mechanisms, one should keep in mind that those calculations are based on a strict set of assumptions that do not universally hold. For instance, the value of α of the elementary steps can vary for different materials and experimental conditions, as well surface coverage of adsorbed H might change as a function of η . Multiple pathways can also occur in parallel with one another. Thus, identifying the HER mechanism based on Tafel slope analysis alone is not always clear, even on well-de fined and thoroughly investigated materials such as Pt.[246]

The i_0 is positively correlated to the number of the available HER-electrocatalytic sites and their HER-kinetics.[241,242] i_0 The value of i_0 is determined experimentally by extrapolating the linear portion of the Tafel plot to the y-axis (Figure 4.1b). When i_0 is normalized on the geometric area of the electrodes (A_{geom}), the exchange currenty density (j_0) is obtained (*i.e.*, $j_0 = i_0/A_{geom}$). Notably, the overall electrochemical performances will be strictly related to the all aforementioned FoM, *i.e.,* η_{10}, b and i_0 (see Figure 4.1.).

Laslty, the FE denotes the efficiency with which electrons are transferred from electrode to the electrolyte facilitating the desired electrochemical reaction, *i.e.*, the HER. In agreement with faraday's law,[247] it can be simply described by the following equation:

$$FE = \frac{\text{mol of } H_2}{\frac{1}{2}\ \frac{\int_0^{\Delta t} i\ dt}{F}}$$

Where: *i* is the measured currnet, *t* is the time and *F* is Faraday constant (96485 C mol^{-1}); mol of H_2 is the number of H_2 moles evolved over the interval time *Δt.* Experimentally, mol of H_2 can be measured by gas chromatography instrumentation.[248]

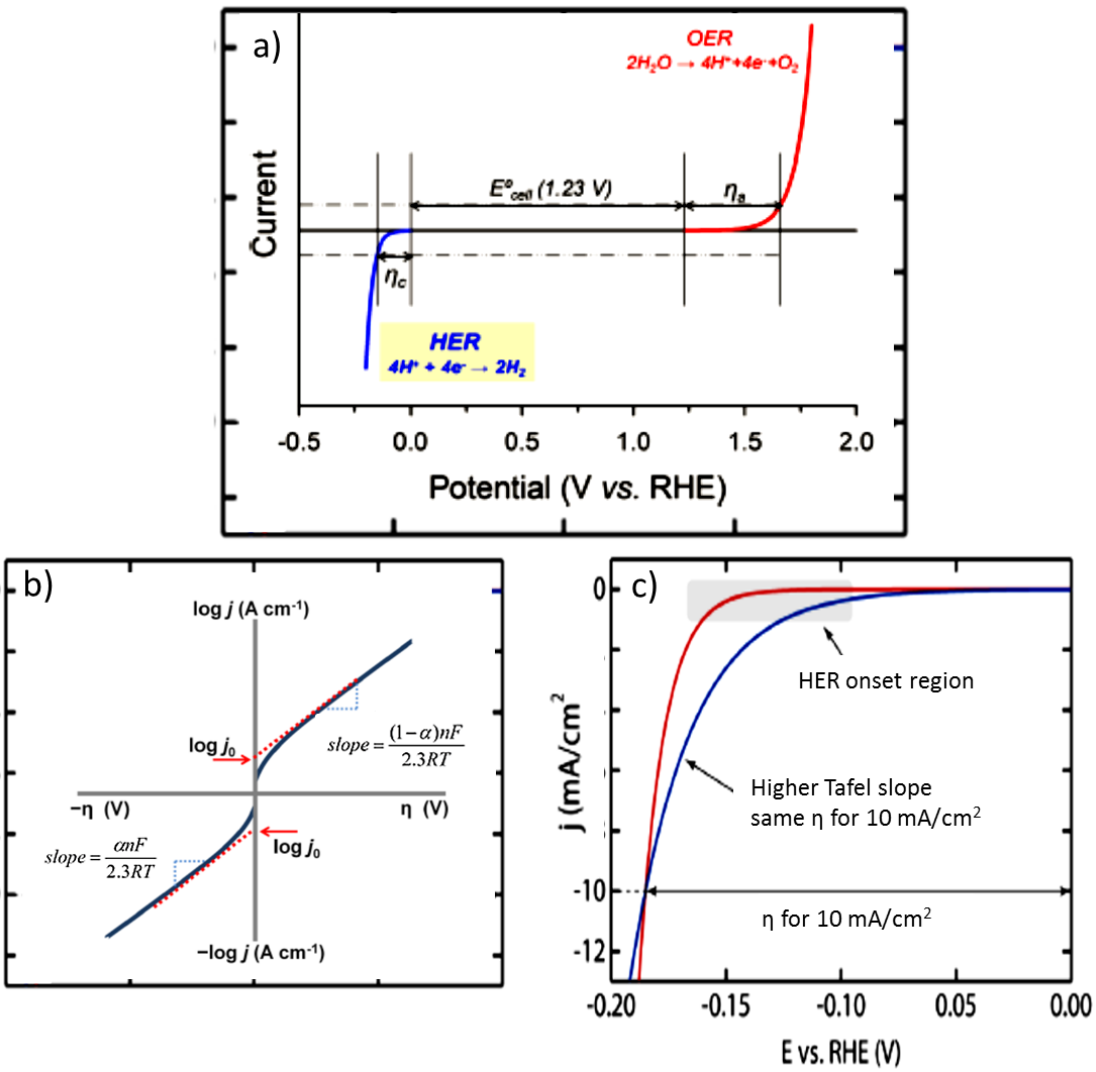

Figure 4.1. a) I-V curve for the full water splitting reaction. b) Key features of anodic and cathodic Tafel plots. c) Current density as a function of potential for two theoretical catalysts.[249]

4.1.2 Electrochemical Measurements

Electrochemical measurements on the as-prepared electrodes are carried out at room temperature in a flat-bottom fused silica cell under a three-electrode configuration using CompactStat potentiostat/galvanostat station (Ivium), controlled via Ivium's own IviumSoft. A Pt wire is used as the counter-electrode and saturated KCl Ag/AgCl is used as the reference electrode. Measurements are carried out in 200 mL 0.5 M H_2SO_4 (99.999% purity, Sigma Aldrich) (pH 1) or 1 M KOH (≥ 85% purity, ACS reagent, pellets, Sigma Aldrich). Oxygen is purged from electrolyte by flowing N_2 gas throughout the liquid volume using a porous frit for 30 minutes before starting the measurements. A constant N_2 flow is maintained afterwards for the whole duration of the experiments, to avoid re-dissolution of molecular oxygen in the electrolyte.

Potential difference between the working electrode and the Ag/AgCl reference electrode is converted to the reversible hydrogen electrode (RHE) scale via the Nernst equation[250]:

$$E_{RHE}=E_{Ag/AgCl}+0.059\ pH+E^{0}_{Ag/AgCl}$$

where E_{RHE} is the converted potential versus RHE, $E_{Ag/AgCl}$ is the experimental potential measured against the Ag/AgCl reference electrode, and $E^{0}_{Ag/AgCl}$ is the standard potential of Ag/AgCl at 25 °C (0.1976 V). Polarization curves are acquired at a 5 mV/s scan rate. Polarization curves from all catalysts are iR-corrected, ($E_{iR\text{-}corrected} = E_{applied} - iR$)[251] where $E_{applied}$ is the applied potentials, i is the current and the R is the series resistance arising from the substrate and electrolyte resistances. R is measured by electrochemical impedance spectroscopy (EIS) at open circuit potential and at frequency of 104 Hz. The linear portions of the Tafel plots are fit to the Tafel equation as explain in section 4.1.1 The j_0 is the current calculated from the Tafel equation by setting η equal to zero. Stability tests are carried out by chronoamperometry measurements (j-t curves), *i.e.,* by measuring the current in potentiostatic mode at -0.5 V vs. RHE in 0.5 M H_2SO_4 over time (200 min).

4.2 Electrodes Fabrication and Electrochemical Characterizations:

This chapter of describes the fabrication of TMD-based electrodes exploited as electrocatalyst for HER. The TMDs reported in the previous two chapters are here used. These include 2H- and 1T-MoS_2 flakes, 2H-MoS_2 QDs and 2H-$MoSe_2$ flakes (simply denoted as $MoSe_2$ flakes). The engineering of the electrocatalytic active sites of TMDs trough thermal, chemical methods and the coupling between TMDs and graphene flakes/SWCTNs in heterostructures are investigated to improve intrinsic HER-activity of the TMDs. Indeed, the following sections describes the works performed for creating innovative TMD-based technologies capable to compete with state-of-the-art solutions in terms of HER-FoM, costs and scalability.

4.2.1 Hybrid Graphene Flake/2H-MoS_2 QDs Heterostructures for Efficient Electrochemical HER

In the last years, MoS_2 has been extensively explored as a HER electrocatalyst. Indeed, theoretical and experimental studies have identified that the unsaturated S atoms located at the edges of thermodynamically 2H- MoS_2 can absorb H^+ with a small Gibbs free energy ($\Delta GH^0 \approx 0.08$ eV),[252] acting as active site for HER.[253] In addition, the electronic structure of the 2H-MoS_2 edge is dominated by metallic one-dimensional states,[254] differently from the semiconducting states in

bulk MoS_2 and in basal planes of 2H-MoS_2 flakes,[254] where electrons transport is limited by hopping transport mechanisms.[254] Recent advances have shown that the HER activity of MoS_2 flakes can be significantly enhanced when the semiconducting 2H phase is converted into metallic 1T phase via chemical exfoliation using Li or organo-Li compounds.[255,261] However, the 1T-MoS_2 phase is thermodynamically metastable with a relaxation energy of ~1.0 eV[299] for the conversion to the stable 2H phase.[256] This limits the exploitation of 1T-MoS_2 for HER applications. In order to overcome this drawback, extensive efforts are currently devoted toward the development of 2H-MoS_2 nanostructures to maximize the number of active edge sites and/or to tailor the edge structure itself to reach enhanced HER kinetics.[257] Among different strategies proposed to advance the HER kinetics, the exploitation of graphene-based scaffolds/substrates have been recently demonstrated to be a promising route to improve the electronic conductivity of 2H-MoS_2 flakes.[258] Moreover, graphene-based scaffolds represent freestanding flexible supports, meeting the mechanical requirements for innovative energy conversion technologies, and, at the same time, offering interconnected porosities for the transport of evolved H_2.[259] In this context, flexible graphene flake/2H-MoS_2 QD heterostructures should offer a 2-fold benefit. On one hand, the QDs provide higher number of catalytic and conductive edge sites with respect to their native 2H-MoS_2 flakes.[260] On the other hand, flexible graphene-based conducting scaffold enables the electrons to access the active surface of QDs, thus favoring the HER kinetics.[244] On the basis of this rationale, the following sections reports the design solution-processed flexible hybrid graphene flake/2H-MoS_2 QD heterostructures, showing enhanced electrocatalytic activity for HER with respect to their native individual components. As described in Chapter 2, 2H-MoS_2 QDs are produced through a scalable, environmentally friendly one-step solvothermal approach from MoS_2 flakes obtained by LPE of the bulk counterpart in IPA. This materials synthesis avoids the use of high boiling point and/or toxic solvents typical of traditional methods. The electrocatalytic performance of the 2H-MoS_2 flakes and 2H-MoS_2 QDs, as well the corresponding heterostructures, are compared to that of the 1T-MoS_2 flakes, produced by lithium intercalation method (see Chapter 2), being a consolidated benchmark in term of HER-electrocatalytic activity.[261,262]

4.2.1.1 Fabrication of the Electrodes:

Dispersions of 2H-MoS_2 flakes, 2H-MoS_2 QDs, and 1T-MoS_2 flakes are deposited on GC sheets (Sigma Aldrich) (GC/2H-MoS_2 flakes, GC/2H-MoS_2 QDs and GC/1T-MoS_2 flakes, respectively) by drop-casting (mass loading of 0.5 mg/cm^2). Flexible hybrid heterostructures of graphene flakes

(graphene), graphene flakes/2H-MoS_2 flakes (graphene/2H-MoS_2 flakes) and graphene flakes/2H-MoS_2 QDs (graphene/2H-MoS_2 QDs) or 1T-MoS_2 flakes (graphene/1T-MoS_2 flakes) are fabricated by sequentially depositing graphene flakes and MoS_2 flakes or QDs dispersions onto nylon membranes with size pore of 0.2 μm (Whatman membrane filters nylon, Sigma Aldrich) through a vacuum filtration process (MoS_2 mass loading of 0.5 mg/cm^2). All the electrodes are dried overnight at room temperature before their electrochemical characterization. Notably, this solution-processed fabrication of heterostructures is scalable and compatible with high-throughput industrial processes.

4.2.1.2 Electrodes Characterization:

The morphology of the different flexible heterostructures, fabricated by the sequential deposition of graphene and MoS_2 dispersions on nylon membranes, is analysed by using AFM. Figure 4.2 shows the representative 1.5×1.5 μm^2 AFM topographies of the graphene, graphene/2H-MoS_2 flakes, and graphene/2H-MoS_2 QDs flexible electrodes (Figure 4.2a,d,g), as well as, their respective AFM phase images (Figure 4.2b,e,h) and AFM 3D images (Figure 4.2c,f,i). The analysis of the roughness derived from Figure 4.2a,dg reveal the lowest roughness (R_a = 10 nm; RMS = 15nm) in the case of graphene/2H-MoS_2 QDs where the presence of graphene flakes is not observed. In the other two cases, the uniform coverage of the surface with layered material reported roughness of: R_a = 16 nm; RMS = 20nm and R_a = 25 nm; RMS = 31 nm for graphene and graphene/2H-MoS_2 flakes electrodes, respectively. The homogeneous coverages of the layered material, for graphene and graphene/2H-MoS_2 flakes, and QDs or QDs aggregates in the case of graphene/2H-MoS_2 QDs heterostructures is also confirmed by the AFM phase images displayed in Figure 4.2b, Figure 4.2e and Figure 4.2h, respectively. In fact, these images show the domains of the different overlay materials of the electrodes over the entire imaged areas (1.5×1.5 μm^2).

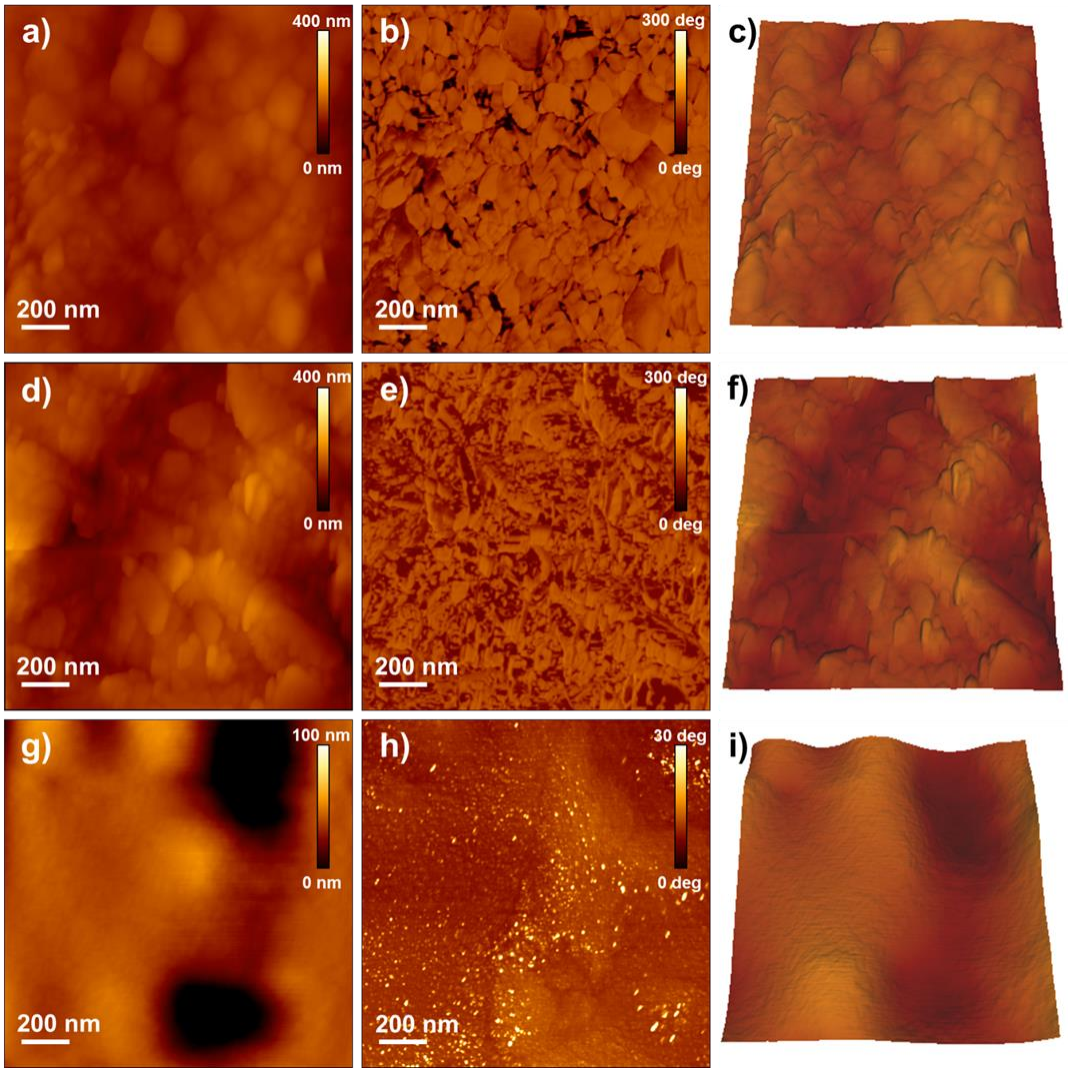

Figure 4.2. AFM characterization of the a-c) graphene, d-f) graphene/2H-MoS_2 flakes, and g-i) graphene/2H-MoS_2 QDs flexible electrodes. The AFM topography images of a) graphene, d) graphene/2H-MoS_2 flakes, and g) graphene/2H-MoS_2 QDs flexible electrodes show layered material in the first two cases, while in the case of graphene/2H-MoS_2 QDs it is observed a smoother surface covered by the presence of QDs. The AFM phase images of b) graphene, e) graphene/2H-MoS_2 flakes and h) graphene/2H-MoS_2 QDs flexible electrodes. Thethe AFM3D images are shown of c) graphene, f) graphene/2H-MoS_2 flakes and i) graphene/2H-MoS_2 QDs flexible electrodes.

4.2.1.3 Electrochemical Characterization:

The HER electrocatalytic activity of the heterostructures is investigated in 0.5 M H_2SO_4. The 2H-MoS_2 flakes and QDs are also deposited and tested on a GC electrode in order to provide their individual electrocatalytic properties on a flat inert conductive substrate. GC/1T-MoS_2 flakes and graphene/1T-MoS_2 flakes are also fabricated and tested as benchmark for HER. Figure 4.3a displays the iR-corrected polarization curves for the different MoS_2 based electrodes. The GC/2H-MoS_2 QDs electrode shows ~60 mV lower η_{10} (~312 mV) with respect to that of the GC/2H-MoS_2 flakes (~372 mV). The HER activity increases remarkably in the case of the heterostructures (η_{10} of

~175 and ~136 mV for the graphene/2H-MoS_2 flakes and graphene/2H-MoS_2 QDs, respectively), with respect to that obtained on GC. Moreover, the η_{10} of graphene/2H-MoS_2 QDs is lower with respect to those of GC/1T-MoS_2 flakes (~235 mV) and graphene/1TMoS_2 flakes (~151 mV). The obtained Tafel slopes are ~145, ~98 and ~78 mV dec^{-1} for GC/2H-MoS_2 flakes, GC/2H-MoS_2 QDs and GC/1T-MoS_2 flakes, respectively. These values suggest that the HER is limited by the Volmer reaction(theoretical Tafel slope is equal to 120 mV cm^{-1}) for GC/2H-MoS_2 flakes. In fact, for this configuration, the limited number of edges slows down the hydrogen adsorption rate. Differently, for the case of GC/1T-MoS_2 flakes, the Volmer–Heyrovsky mechanism (Tafel slope varying between 120 and 40 mV cm^{-1}) occurs for HER process. The observed behavior is in agreement with previous works reported in literature on 2H-MoS2 QDs,[263,264] where the reaction kinetics are not limited by the number of catalytic edge sites as for the 2H-MoS_2 flakes and, therefore, the Volmer-Heyrovsky mechanism is thus facilitated.[264] The Tafel slopes for graphene/2H-MoS_2 flakes, graphene/2H-MoS_2 QDs and graphene/1T-MoS_2 flakes are ~163, ~141 and ~82 mV cm^{-1}, respectively. These values show an increase of ~0.13%, 0.44% and 0.05% with respect to those for GC/2H-MoS_2 flakes, GC/ 2H-MoS_2 QDs and GC/1T-MoS_2 flakes, respectively. This could be ascribed to the presence of large H_{ads} coverage for the range of η where the Tafel slope has been extrapolated, in agreement with theoretical simulations of HER kinetics in acidic conditions.[265] The current densities (between 1.5 and 6.5 mA cm^{-2}) measured in the 0.10–0.05 V *vs.* RHE scale range suggest the presence of an intermediate step, ascribable to the Volmer reaction, preceding the H_2 evolution. Moreover, the j_0 values for graphene/2HMoS_2 flakes and graphene/2H-MoS_2 QDs (~0.97 and ~1.31 mA cm^{-2}, respectively) are significantly increased with respect to the one obtained for GC/2H-MoS_2 flakes and GC/2H-MoS_2 QDs (~0.03 mA cm^{-2}).

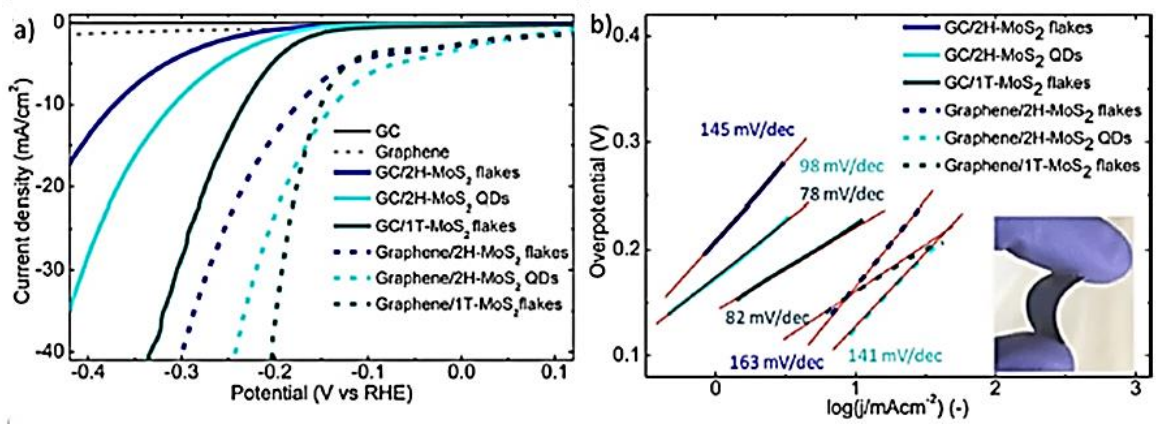

Figure 4.3. a) Polarization curves of 2H-MoS_2 flakes, 2H-MoS_2 QDs, 1T-MoS_2 flakes, on GC electrode (solid lines), and graphene/2H-MoS_2 flakes, graphene/2H-MoS_2 QDs and graphene/1T-MoS_2 flakes (dashed lines). Polarization curves of GC and graphene flakes are also shown for comparison. b) Tafel plots of the same MoS_2-based electrodes shown in

panel (a). Linear fits (red lines) and the corresponding Tafel slope values are reported. Inset: photograph of a representative flexible hybrid graphene flakes/2H-MoS_2 QDs electrode.

The electrocatalytic stability of the graphene/2H-MoS_2 QDs in HER-condition is evaluated by chronoamperometry measurements (j–t curves) at −0.5 V *vs*. RHE (Figure 4.4). The graphene/2H-MoS_2 QDs show a progressive HER activation, with a ~10% increase of j after 200 min, whereas the current density of graphene/2H-MoS_2 flakes decreases by ~4% with respect to the starting values. These results suggest the catalytic edge sites of 2H-MoS_2 QDs are more resistant toward oxidative/degradation processes, which passivate the HER catalytic sites, compared to those of 2H-MoS_2.[264] In fact, density functional theory calculation have shown that oxidation energies for MoS_2 flakes depend on the local competition of binding energy of the covalent bonds at the edge sites,[266] whose nature can be different for 2D and 0D nanostructures.[267]

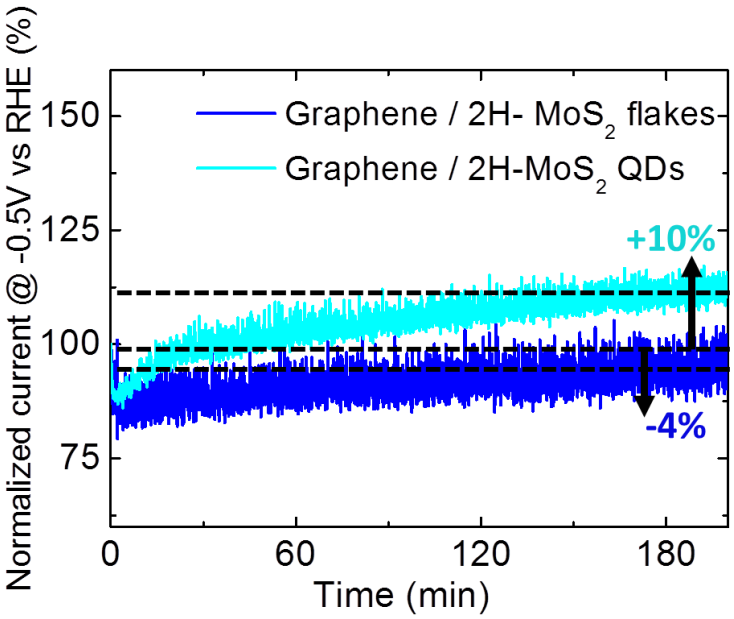

Figure 4.4. Chronoamperometry measurements (j-t curves) at -0.5 V *vs*. RHE of the graphene/2H-MoS_2 flakes (blue lines) and graphene/2H-MoS_2 QDs (cyan line), over 200 min.

4.2.2 Engineered $MoSe_2$-based Heterostructures for Efficient Electrochemical HER:

As discussed in Section 4.2.1, the development of nanostructured TMD electrodes with preferentially exposed edge sites is essential for achieving state-of-the art HER-electrocatalytic activity in the frame of noble metal-free electrocatalysts.[268] In this context, thermo-induced texturization processes in H_2 environment have been reported for activating the TMD basal planes by creating chalcogen-vacancies and form edge-like sites, *i.e.,* high HER-electrocatalytic activity, across various morphologies, including bulk minerals, few-layer microflakes (lateral dimension of

2–5 μm) and nanoflakes (lateral dimension of ~200 nm). In the previous sections, self-standing graphene substrate are demonstrated to effectively enhance the HER-electrocatalytic activity of ~1 μm-thick MoS_2 flakes-based films (0.5 mg cm^{-2} mass loading) with respect to the ones based on GC as substrate. Indeed, these results suggest the existence of a HER-assisting HER electrochemical coupling between graphene substrate and TMD flakes overlay over a spatial range up to μm-scale. However, clear experimental and theoretical evidences of these "long-range" (*i.e.*, μm-scale) phenomena have not been reported yet, differently from the "short-range" (nm-scale) phenomena occurring in hybrid composite materials. Taking into account the aforementioned consideratons, this section report solution-processed hybrid heterostructures made of either graphene flakes or SWCNTs and $MoSe_2$ flakes (in the following named as graphene/$MoSe_2$ and SWCNTs/$MoSe_2$, respectively) for HER. Amongst the TMDs, $MoSe_2$ is opted for its higher intrinsic electrical conductivity (~10^{-1} Ω^{-1} cm^{-1}) with respect to those of the other TMDs (*e.g.*, ~10^{-2} Ω^{-1} cm^{-1} for the most studied case of MoS_2), and low ΔG_H^0 at its edges sites (<0.1 eV). As described in Chapter 2, $MoSe_2$ and graphene flakes are produced in form of dispersion by LPE of their bulk counterpart in IPA and NMP, respectively. The SWCNT dispersions are produced by firstly dispersing SWCNTs in NMP followed by an ultrasonication-based de-bundling process. Subsequently, graphene/$MoSe_2$ or SWCNTs/$MoSe_2$ heterostructures are fabricated by depositing sequentially the as-formulated dispersions on nylon membranes through vacuum filtration, thus adopting the methodology of the graphene fake/2H-MoS_2 QD heterostructures studied in Section 4.2.1. The optimization of the $MoSe_2$ flakes mass loading (up to 5 mg cm^{-2}) as well the electrode assembly *via* monolithic stacking of different heterostructures permit to achieve remarkable HER-electrocatalytic activity (*i.e.*, η_{10} of 100 mV and cathodic current density > 100 mA cm^{-2} at η less than 200 mV). Differently from HER-electrocatalysts based on 2D-TMDs/carbon-based material compounds, the as-produced heterostructures have μm-thick bilayer-like structure. Moreover, electrode thermal annealing in H_2 environment and chemical bathing in n-butyllithium are exploited for texturizing the $MoSe_2$ flakes basal planes (through Se-vacancies creation), and to achieve in situ semiconducting-to-metallic phase conversion, respectively (*i.e.*, activating new electrocatalytic sites). The as-engineered electrodes show accelerated HER-kinetics with respect to that of untreated electrode, as evidenced by Tafel plot analysis (~4.8-fold enhancement of the exchange current density and a decrease of the Tafel slope from 63 to 54 mV dec^{-1} after electrode chemical and thermal treatment, respectively). To sum up, the following sections reports new methods and guidelines for producing and engineering TMDs-based electrodes compatibly with

scalable manufacturing (*i.e.*, solution-based processing) and competing with current noble metal-free technologies.

4.2.2.1 Fabrication of the Electrodes

$MoSe_2$ flakes are deposited on GC sheets (Sigma Aldrich) (GC/$MoSe_2$) by drop-casting the as-produced $MoSe_2$ flakes dispersion (see Chapter 2) (mass loading of 2 mg cm^{-2}). Solution-processed hybrid heterostructured electrodes (*i.e.*, graphene/$MoSe_2$ and SWCNTs/$MoSe_2$) are produced by depositing sequentially the as-produced material dispersions (see Chapter 2) on nylon membranes with size pore of 0.2 µm (Whatman® membrane filters nylon, Sigma Aldrich) through vacuum filtration. A mass loading of 2 mg cm^{-2} (electrode area of 3.14 cm^2) is firstly adopted for all the materials (graphene flakes, SWCNTs and $MoSe_2$ flakes). Afterward, the mass loading of the $MoSe_2$ flakes is increased to 5 mg cm^{-2} in order to increase the overall number of active sites via the control of the electrode thickness, as recently observed for liquid phase exfoliated TMD-based electrodes.[269] The electrodes are dried overnight at room temperature before their electrochemical characterization. Electrodes made of graphene flakes or SWCNTs only (here named as graphene and SWCNTs, respectively), *i.e.*, without the $MoSe_2$ flakes deposition, are also produced as references. Thermal treatment of GC/$MoSe_2$ and SWCNT/$MoSe_2$ is carried out in a quartz tube (120 cm length and 25 mm inner diameter) passing through a three zones split furnace (PSC 12/--/600H, Lenton, UK). The electrodes are heated at 600 or 700 or 800 °C with a ramp of 12 °C min^{-1}, and stabilized at this temperature for 5 hours under a 100 sccm flow of Ar/H_2 (90/10%). Gas flows are controlled upstream by an array of mass flow controllers (1479A, mks, USA). Finally, the oven is cooled down to room temperature. Chemical treatment of SWCNTs/$MoSe_2$ is obtained by bathing them in 5 ml of n-butyllithium (Sigma Aldrich) in a sealed vial at room temperature under N_2 atmosphere. After 12 hours, electrodes are washed with deionized water to remove the remaining Li present in the form of lithium cations (Li^+) and then cleaned with IPA and dried with compressed N_2 gas.

4.2.2.2 Electrodes Characterization

4.2.2.2.1 Graphene/$MoSe_2$ and SWCTNs/$MoSe_2$ heterostrcutures

The surface morphology of the as-prepared electrodes is characterized by SEM and AFM. Figures 4.5a-d show the top-view SEM images of the electrodes. The surface of graphene electrode has a

crumpled, wrinkled and flake-like structure, while the one of SWCNT electrode consists of a mesoporous network given by a bundle-like morphology. The surface of the hybrid electrodes ($MoSe_2$ flakes mass loading = 2 mg cm^{-2}) is clearly modified by the $MoSe_2$ flakes addition with respect to the bare graphene and SWCNT electrodes. For the graphene/$MoSe_2$ electrode, the $MoSe_2$ flakes uniformly cover the underlying graphene flakes. Differently, for SWCNTs/$MoSe_2$, the underlying mesoporous network of the SWCNTs is still observed, thus indicating the penetration of $MoSe_2$ flakes into the SWCNTs.

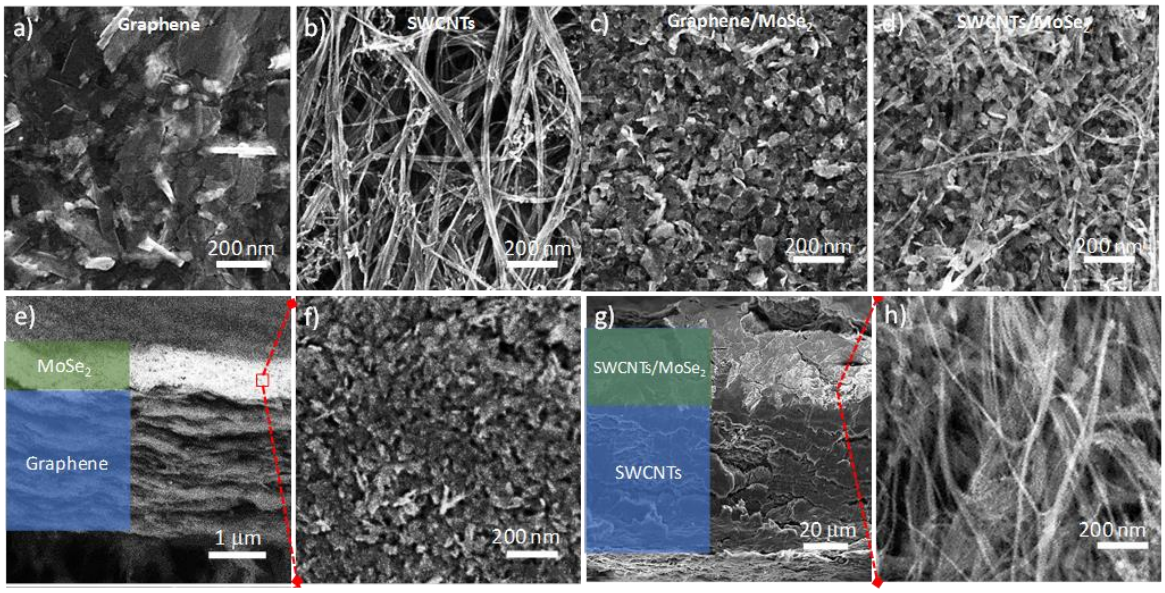

Figure 4.5. Top-view SEM images of a) graphene, b) SWCNTs, c) graphene/$MoSe_2$ and d) SWCNTs/$MoSe_2$. Cross-sectional SEM images of e-f) graphene/$MoSe_2$ and g-h) SWCNTs/$MoSe_2$. Panel f) and h) resolve the structures of the top-layers for the corresponding hybrid electrodes. The materials mass loading is 2 mg cm^{-2}.

Figure 4.6 reports the AFM images of the electrode surfaces, evidencing morphologies similar to those observed by SEM. The R_a values are ~46.2 nm and ~103 nm for graphene and SWCNT electrodes, respectively. This values decrease to ~21 nm and 70 nm, respectively, for the corresponding hybrid electrodes, indicating that $MoSe_2$ flakes deposition flattens the electrode surfaces. For graphene/$MoSe_2$, the flattening of the electrode surface is attributed to the smaller lateral dimension of the $MoSe_2$ flakes (10-170 nm) with respect to that of graphene flakes (200-1500 nm), leading to a more compact (*i.e.,* more dense) overlayer with respect to the graphene flakes film. For the SWCNTs/$MoSe_2$, the surface flattening is a consequence of the $MoSe_2$ flakes filling and coverage of SWCNTs mesoporous network. Figure 4.5e-h show the high-resolution cross-sectional SEM images of representative graphene/$MoSe_2$ and SWCNTs/$MoSe_2$. For graphene/$MoSe_2$, a well-defined bilayer structure is observed (Figure 4.5e,f). $MoSe_2$ flakes are deposited as a homogeneous porous overlayer (see high-magnification image, Figure 4.5f) because

of the filter-like behavior of the graphene flakes.[270, 271] The estimated layer thickness is ~2.5 µm and ~0.8 µm for graphene and $MoSe_2$ flakes layer, respectively. Considering that the graphene and $MoSe_2$ flakes have identical mass loading, these values indicate that the $MoSe_2$ flakes film is denser with respect to that of graphene flakes, in accordance with the corresponding R_a values measured by AFM (Figure 4.6). For SWCNTs/$MoSe_2$, the high-magnification SEM image (Figure 4.5g) reveals that the $MoSe_2$ flakes penetrate within the mesoporous SWCNTs network (commonly referred as bucky-paper).[272,273]

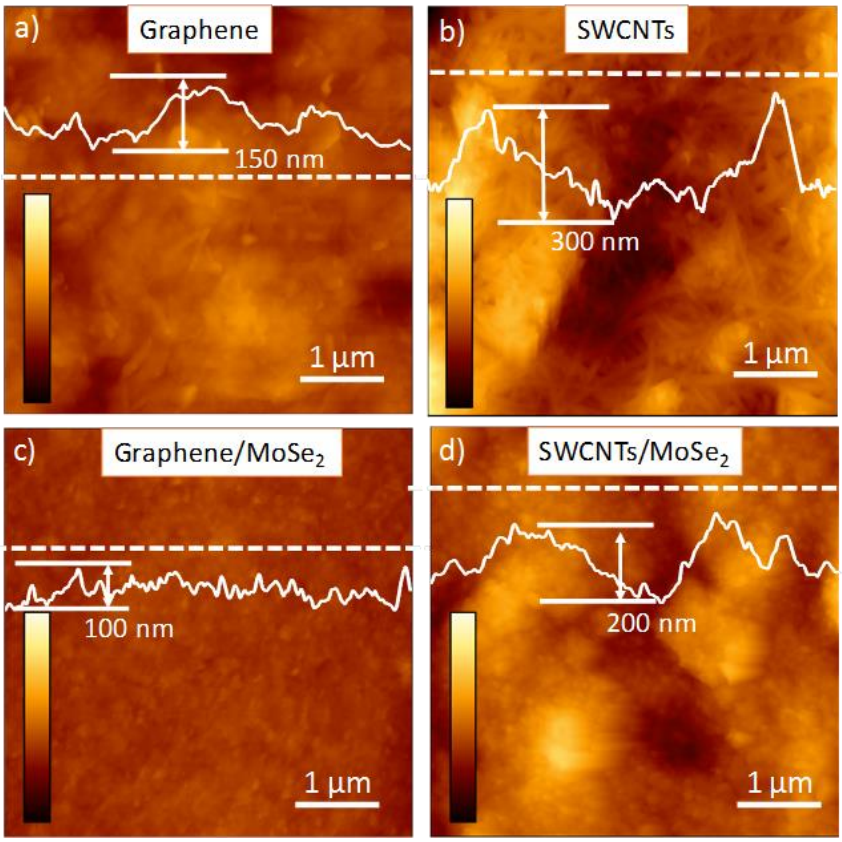

Figure 4.6. AFM images of a) graphene, b) SWCNTs, c) graphene/$MoSe_2$ and d) SWCNTs/$MoSe_2$. Height profiles along representative cross sections (white dashed lines) are also shown. The z-scale bar is 1 µm.

However, a bilayer structure is still observed, as also confirmed by EDX analysis of cross-sectional SEM images of SWCNTs/$MoSe_2$ (Figure 4.7). Moreover, the thickness of the whole electrode exceeds 100 µm, thus indicating low-density bucky-paper formation. High-magnification cross-sectional SEM image of the SWCNTs/$MoSe_2$ (Figure 4.5h) reveals that the $MoSe_2$ flakes penetrate within the SWCNTs network.

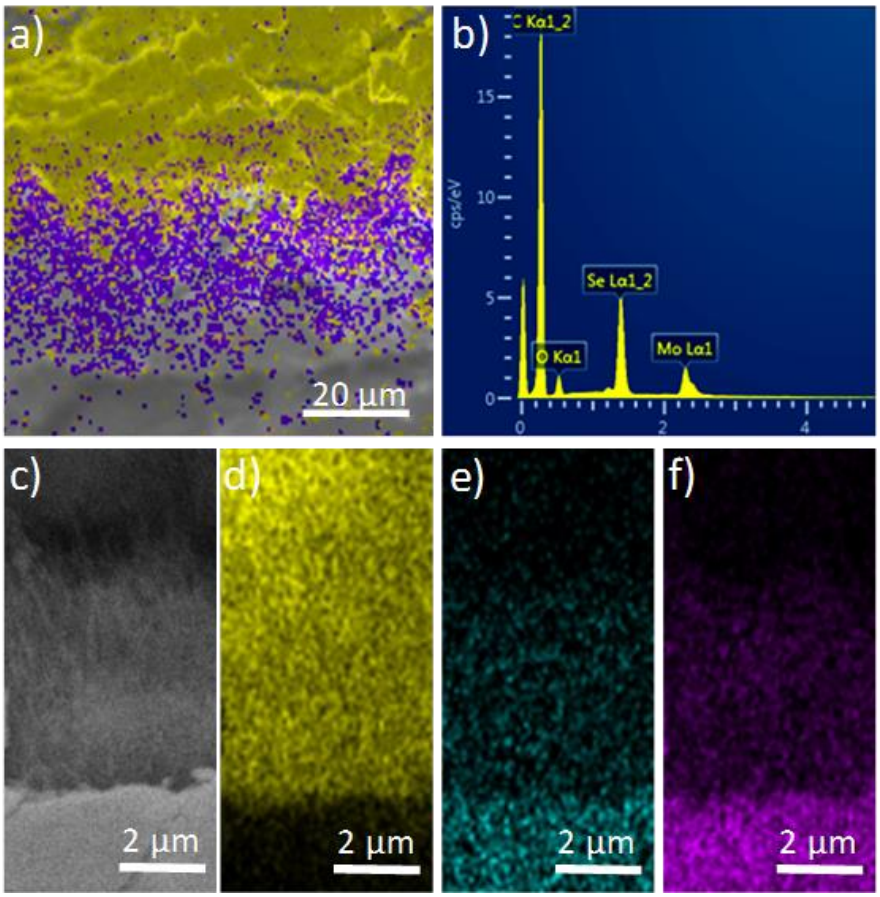

Figure 4.7. a) EDX analysis of a representative cross-sectional image of SWCNTs/$MoSe_2$ with b) the corresponding mass spectrum. c) Cross-sectional SEM images of a magnified region of the image of panel a), and the corresponding EDX analysis for d) C, e) Mo and f) Se atoms. Atom color code: yellow C; cyan Mo; violet Se.

Figure 4.8 shows the Raman spectra of the graphene/$MoSe_2$ and SWCNTs/$MoSe_2$, focusing in the spectral region between 140-410 cm^{-1} where the Raman peaks of $MoSe_2$ flakes are located (see Chapter 3, Figure 3.26). The comparison with the Raman spectrum of the $MoSe_2$ flakes does not reveal significant differences, thus indicating that no structural modifications of the as-produced $MoSe_2$ flakes occur during their film deposition through vacuum filtration of their dispersions.

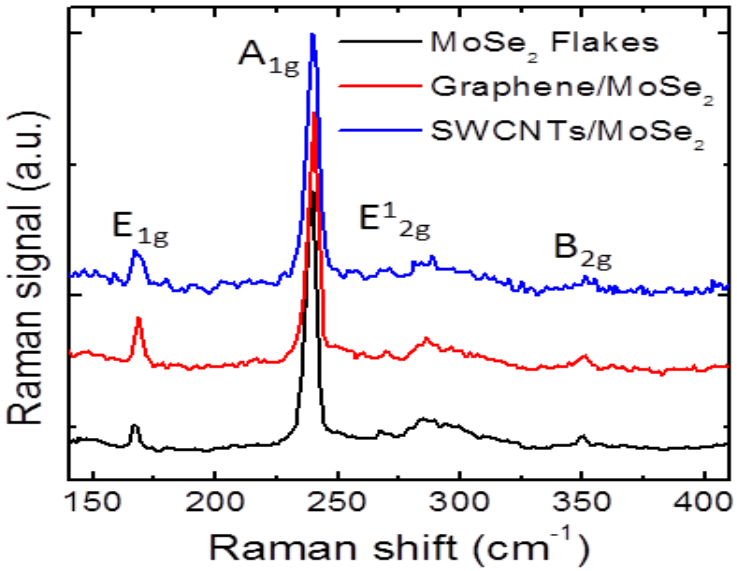

Figure 4.8. Raman spectra of $MoSe_2$ flakes (black) deposited on Si/SiO_2 substrates and the as-produced herostructures (graphene/$MoSe_2$ flakes (red) and SWCNTs/$MoSe_2$ (blues)) ($MoSe_2$ flakes mass loading of 2 mg cm^{-2}). The main peaks of the $MoSe_2$ flakes, *i.e.,* the in-plane modes E_{1g}, E^1_{2g}, and E^2_{2g}, the out-of-plane mode A_{1g} and the breathing mode B^1_{2g} are named in the graph.

Similar conclusion are also derived from XPS measurements on the heterostructures (Figure 4.9), where not significant changes are observed in the Mo 3d and Se 3d spectra with respect to those of as-produced $MoSe_2$ flakes. In particular, Mo 3d XPS spectra (Figure 4.9a) show the two Mo $3d_{5/2}$ and Mo $3d_{3/2}$ of Mo(IV) state in $MoSe_2$ peaks [274,275] (see Chapter 3, Figure 3.30a) (located at: (229.2±0.2) eV and (232.3±0.2) eV for graphene/$MoSe_2$; (229.1±0.2) eV and (232.2±0.2) eV for SWCNTs/$MoSe_2$). The additional peaks (located at: (233.1±0.2) eV and (236.2±0.2) eV for graphene/$MoSe_2$; (232.9±0.2) eV and (236.0±0.2) eV for SWCNTs/$MoSe_2$) are assigned to the Mo(VI) state and are related to MoO_3 residues,[276,277] The compositional analysis indicates that the percentage content (%c) of MoO_3 (defined as $MoO_3/(MoO_3+MoSe_2)$) is ~12% for graphene/$MoSe_2$ and ~17% for SWCNTs/$MoSe_2$. The %c of MoO_3 increase of 9% for graphene/$MoSe_2$ and 54% for SWCNTs/$MoSe_2$ with respect to that of as-produced $MoSe_2$ flakes (~11%, see Chapter 3). However, it is still comparable between the heterostructures and the as-produced $MoSe_2$ flakes. Se_{3d} spectra (Figure 4.9b) show the Se $3d_{5/2}$ and Se $3d_{3/2}$ peaks of the diselenide moiety of $MoSe_2$ [278,279](see Chapter 3, Figure 3.-30d) (located at: (54.8±0.2) eV and (55.6±0.2) eV for graphene/$MoSe_2$; (54.6±0.2) eV and (55.5±0.2) eV for SWCNTs/$MoSe_2$. For both Mo 3d and Se 3d spectra, a slight downshift shift of the binding energy (~0.1 eV for graphene/$MoSe_2$ and ~0.2 eV for SWCNTs/$MoSe_2$) is observed with respect to those of as-produced $MoSe_2$ flakes (see Chapter 3,

Figure 3.30). The changes might be ascribed to the µm-spatial range electrochemical coupling between $MoSe_2$ flakes and the low-dimension carbon-based substrates.

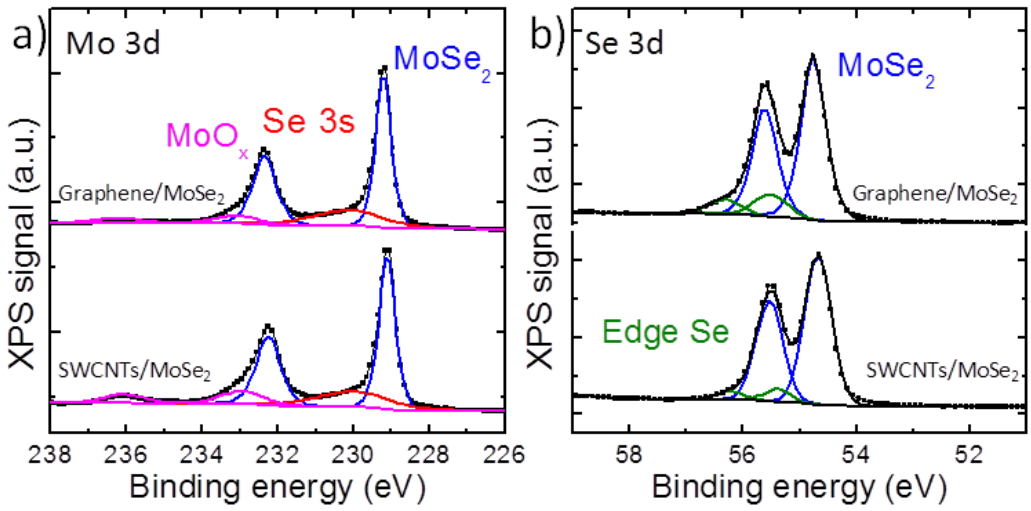

Figure 4.9. a) Mo 3d and b) Se 3d XPS spectra for graphene/$MoSe_2$ (top curves) and SWCNTs/$MoSe_2$ (bottom curves). Their deconvolution is also shown, evidencing the band ascribed to: $MoSe_2$ (blue curves); Se_{3s} band (red curve), overlapping the Mo 3d XPS spectrum; oxidized species (MoO_x) (magenta curves); Edge (elemental) Se (green curves).

4.2.2.2.2 Engineering of the Electrode:

In order to improve the HER-electrocatalytic activity of the $MoSe_2$ flakes, and in general that of all 2D-TMDs, is essential to activate their basal planes,[280,281] *i.e.*, the predominant inert (0001) surface plane,[282] as well to increase their electrical conductivity.[283] Thus, two treatments are investigated (Figure 4.10): 1) thermo-induced texturization by flakes annealing in H_2 environment; 2) in situ semiconducting (2H-$MoSe_2$)-to-metal (1T-$MoSe_2$, MoO_x and elemental atoms) phase conversion by flakes chemical bathing in organo-lithium compound.

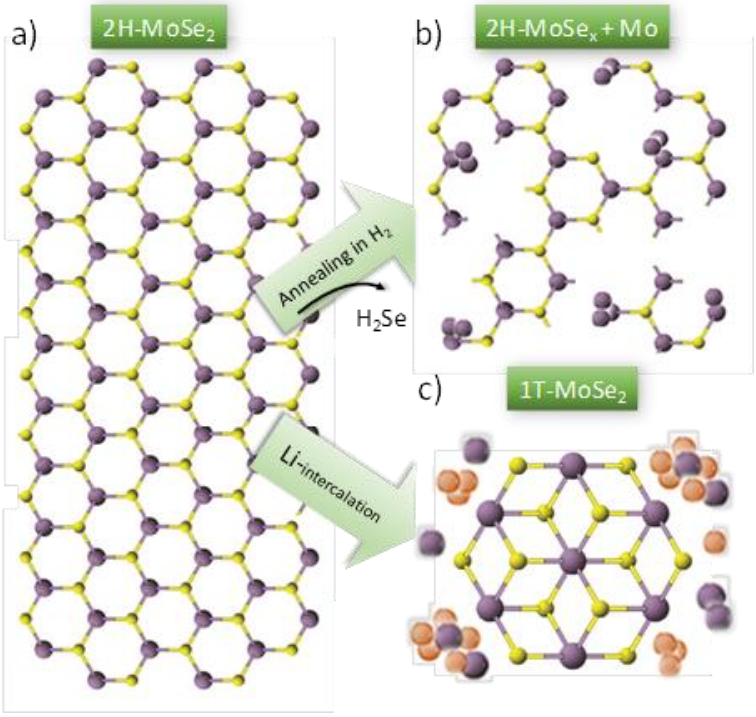

Figure 4.1. Schematic illustration of the treatment adopted on $MoSe_2$ flakes for increasing their HER-electrocatalytic activity. a) as-produced 2H-$MoSe_2$ flake; b) Se-vacancy engineered 2H-$MoSe_2$ flake produced by thermo-induced flakes texturization in H_2 environment; c) 1T-$MoSe_2$ flake, MoO_x and elemental atoms produced by in situ semiconducting)-to-metallic phase conversion (as obtained by chemical bathing in n-buthyllithium). Atom colour code: purple, Mo; yellow, Se.

In the first process, Se atoms in defect-free $MoSe_2$ flakes (Figure 4.10a) are expected to be removed as H_2Se gas leading to the formation of Se-vacancies and edges in the (0001) plane. Simultaneously, the excess Mo could form metal clusters on the $MoSe_2$ flakes (Figure 4.10b). Similar treatment has been reported for MoS_2, where HER-electrocatalytic activity has been improved by increasing the edge site intensity on the surface and by making the flake conductive through the generation of metallic Mo cluster.[284] The second treatment is expected to induce the 2H-to-metallic (1T-$MoSe_2$, MoO_x and elemental atoms) phase conversion of the $MoSe_2$ (Figure 4.10c). Similar approach has been applied on MoS_2 monolayer-based field-effect transistors (FETs) in order to locally induce the 2H-to-1T phase conversion of the MoS_2.[285] This phase engineering decreased the high-resistance contacts (0.7 kΩ µm-10 kΩ µm) of 2H-MoS_2 to 200-300 Ω µm, thus optimizing the carrier injection into the channel.[285] In this case, the phase conversion of $MoSe_2$ flakes is expected to increase their electron conductivity as well to enhance the surface reactivity of their basal plane toward atomic H binding (*i.e.*, to decrease ΔG_H^0). Figure 4.-11 reports the AFM images of the annealed $MoSe_2$ flakes films deposited on Si substrate, in comparison with that not annealed. The results show a progressive size reduction of the $MoSe_2$ flakes, with consequent

smoothing of their films, with increasing the annealing temperature up to 700 °C. In fact, the R_a value reduces from 22 nm for not annealed film, to 12 nm for the film annealed at 600 °C and 11 nm for the one annealed 700 °C. Contrariwise, once the temperature is further increased to 800 °C, the formation of aggregates is noticed due to excessive removal of Se and Mo cluster assembling, which consequently determine a R_a increase up to 20 nm.

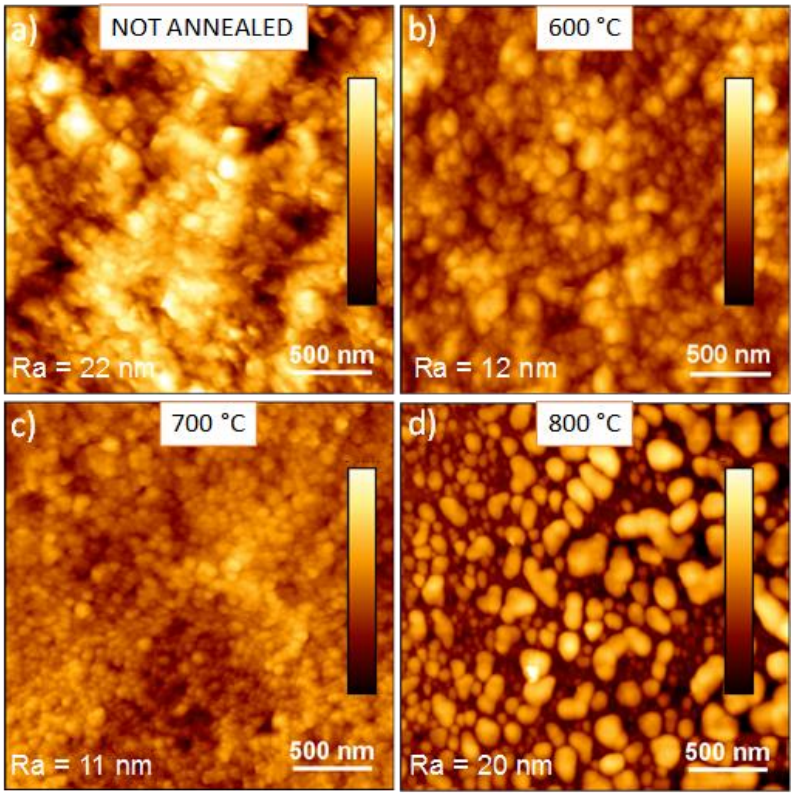

Figure 4.11. AFM images of $MoSe_2$ flakes films deposited onto Si substrate. a) untreated sample; a-c) samples annealed at 600 °C (panel b) , 700 °C (panel c) and 800 °C (panel d) in Ar/H_2 (90/10%) for 5 h. The z-scale bar is 145 nm.

Figure 4.12 shows the XPS measurements on $MoSe_2$ flakes film deposited on Si substrate and annealed at different temperature (*i.e.*, 600, 700 and 800 °C) in Ar/H_2 (90/10%) for 5 h. The Mo 3d XPS spectra confirm the progressive formation of elemental Mo (0) with increasing the annealing temperature. More in detail, the %c of Mo (0) and total Se is > 10% and < 20%, respectively, for annealing temperature ≥ 700 °C. In these conditions, Mo (VI) is also observed with %c > 50% and it might be attributed to the subsequent oxidation of elemental Mo under air exposure.[286]

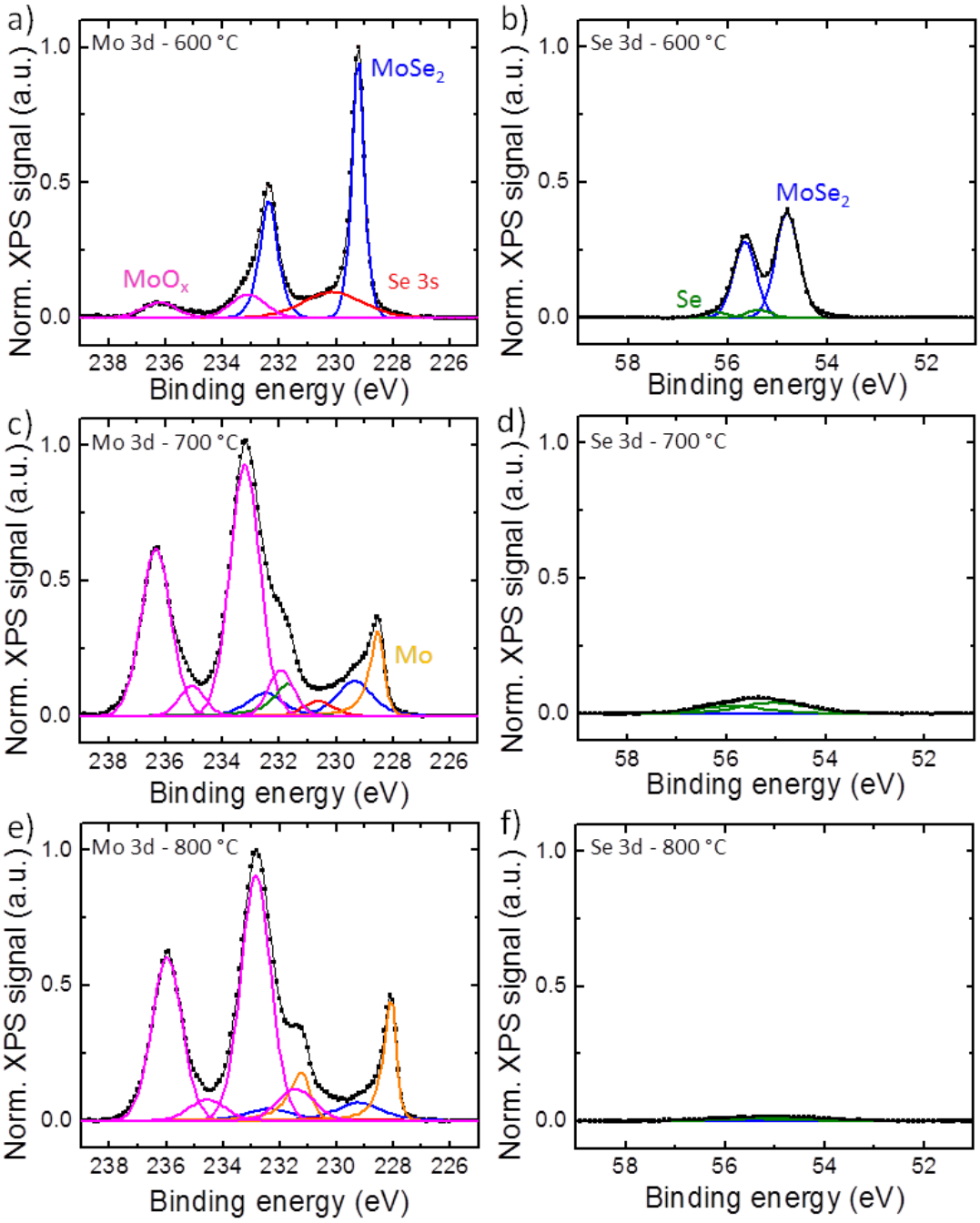

Figure 4.12. a) Mo 3d and b) Se 3d normalized XPS spectra for $MoSe_2$ flakes annealed at 600 °C in Ar/H_2 (90/10 %) for 5 h. c) Mo 3d and d) Se 3d normalized XPS spectra for $MoSe_2$ flakes annealed at 700 °C in Ar/H_2 (90/10 %) for 5 h. e) Mo 3d and f) Se 3d normalized XPS spectra for $MoSe_2$ flakes annealed at 800 °C in Ar/H_2 (90/10 %) for 5 h.Their deconvolution is also shown, evidencing the band ascribed to: $MoSe_2$ (blue curves); Se 3s band (red curve), overlapping the Mo 3d XPS spectrum; oxidized species (MoO_x) (magenta curves); elemental Mo (orange curves); edge/elemental Se (green curves).

Figure 4.13 shows the XPS spectra of $MoSe_2$ flakes films after chemical treatment, *i.e.,* 12 h-chemical bathing in n-butyllithium. The results confirm the modification of the surface chemistry of $MoSe_2$. The spectra evidence the formation of different metallic phases, *e.g.*, MoO_x and Mo) and additional elemental atoms (Se and residual Li-species), contributing/overlapping to Mo 3d and Se 3d spectra of $MoSe_2$ flakes (Li-species 1s XPS spectrum peaks between 50-60 eV),

respectively. The $MoSe_2$-related XPS bands might be attributed to both the semiconducting (2H) and metallic (1T) phases.

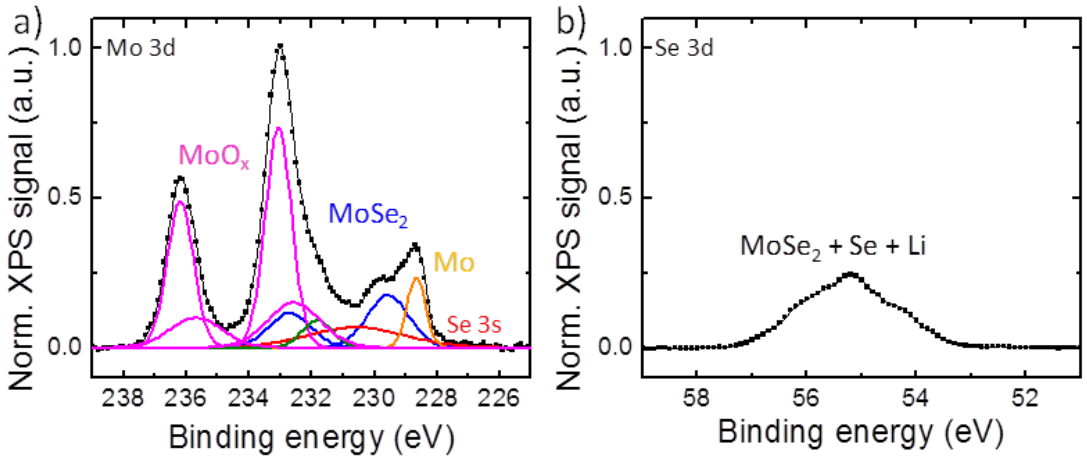

Figure 4.13. a) Mo 3d and b) Se 3d normalized XPS spectra for $MoSe_2$ flakes bathed in n-butyllithium for 12 h. The deconvolution of Mo 3d XPS spectrum is also shown, evidencing the band ascribed to: $MoSe_2$ (blue curves); Se 3s band (red curve), overlapping the Mo 3d XPS spectrum; oxidized species (MoO_x) (magenta curves); elemental Mo (orange curves).

4.2.2.3 Electrochemical Characterization:

The HER-electrocatalytic activity of the as-produced electrodes is evaluated in 0.5 M H_2SO_4 (pH 1). Acid condition are specifically evaluated because of giving an higher $MoSe_2$ flakes HER-electrocatalytic activity with respect to that expressed in alkaline condition (1M KOH, pH 14). Actually, the kinetic energy barrier of the initial Volmer step and the strong adsorption of the formed OH- on the surfaces of $MoSe_2$ flakes (and, more in general, of the 2D-TMDs) are held responsible for the sluggish HER kinetics in alkaline solutions. Figure 4.14 shows the comparison between the $MoSe_2$ flakes HER-electrocatalytic activity in acid (0.5 M H_2SO_4) and alkaline (1 M KOH) solutions. The η_{10} are 0.34 V and 0.37 V in acid solution and alkaline solutions, respectively. The higher η_{10} observed in alkaline solution with respect to the acid solution has been attributed to the kinetic energy barrier of the initial H_2O discharge and H_{ads} formation, as well as to the strong adsorption of the formed OH^- on the surfaces of $MoSe_2$ flakes..[287,288]

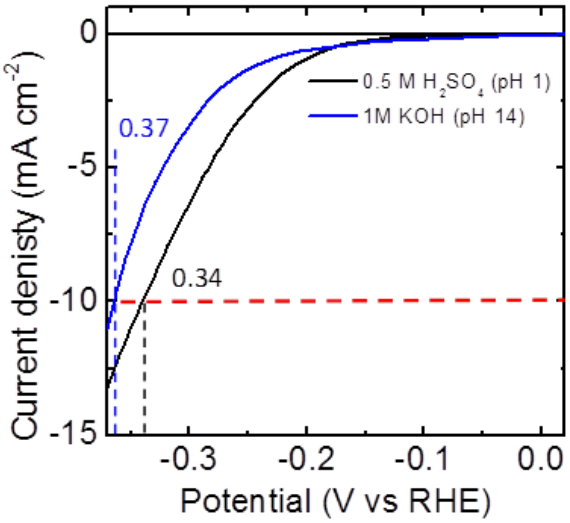

Figure 4.14. Polarization curves of GC/$MoSe_2$ in acid (0.5 M H_2SO_4, pH 1) (black line) and alkaline solution (1 M KOH, pH 14). The η_{10} values are indicated for each curve.

The $MoSe_2$ flakes are also deposited and tested on GC electrode (*i.e.*, GC/$MoSe_2$) in order to test their native electrocatalytic properties on flat inert conductive substrate. Figure 4.15a displays the *iR*-corrected polarization curves for the different electrodes. Clearly, the graphene/$MoSe_2$ and SWCNTs/$MoSe_2$ show higher current density with respect to the GC/$MoSe_2$. The η_{10} decreases from 0.34 V for GC/$MoSe_2$ to 0.18 and 0.17 V for graphene/$MoSe_2$ and SWCNTs/$MoSe_2$, respectively. The Tafel slopes are 88, 80, and 67 mV dec^{-1} for GC/$MoSe_2$, graphene/$MoSe_2$ and SWCNTs/$MoSe_2$, respectively. These values agree with the Volmer-Heyrovsky HER-mechanism for all the electrodes, in agreement with previous studies..[289,290] However, the decrease of the Tafel slope values observed for graphene/$MoSe_2$ and SWCNTs/$MoSe_2$ with respect to that observed for GC/$MoSe_2$ indicates that the HER-electrocalytic activity of the electrode is less limited by the Volmer reaction step. The j_0 values are 5, 56 and 29 µA cm^{-2} for GC/$MoSe_2$, graphene/$MoSe_2$ and SWCNTs/$MoSe_2$. The value obtained for GC/$MoSe_2$ agrees with those reported in literature for 2D-TMDs with similar mass loading.[291,292] The values obtained for SWCNTs/$MoSe_2$ are comparable to those reported for $MoSe_2$ flake/SWCNT compounds (in the order of 10^2 µA cm^{-2}).[292] Notably, the highest j_0 value is measured for graphene/$MoSe_2$ which is a bilayer-like heterostructures consisting of graphene flakes film covered by an homogeneous layer of $MoSe_2$ flakes (see SEM analysis, Figure 4-5 e,f). This indicates two-fold HER-assisting properties of the heterostructures: 1) the $MoSe_2$ flakes electrical conductivity guarantees the electron accessibility to the HER-electrocatalytic sites in film with µm-thickness scale; 2) the overall kinetics of the $MoSe_2$ flakes are accelerated with respect to the GC/$MoSe_2$ by the favorable electrochemical coupling with

graphene flakes- or SWCNTs substrates, which turns out a decrease of $MoSe_2$ flakes ΔG_H^0. Notably, this electrochemical coupling is effective for ~µm-thick layer of $MoSe_2$ flakes, differently to the short-spatial range (nm-scale) coupling expressed by hybrid graphene/ or CNTs/TMDs.[293,294] In addition, for the SWCNTs/$MoSe_2$, the porosity of the $MoSe_2$ flakes overlay, as observed by SEM analysis (Figure 4.5g-h), also support the H_{ads} surface coverage, thus reducing even more ΔG_H^0 (*i.e.,* the Tafel slope) with respect to that for graphene/$MoSe_2$. Lastly, the interpenetration between SWCNTs and $MoSe_2$ flakes for the SWCNTs/$MoSe_2$ (see SEM analysis, Figure 4.5g,h) is expected to increase the electron accessibility to the HER-electrocatalytic sites, being the electrode conductivity enhanced by the SWCNTs addition.[291,292,293]

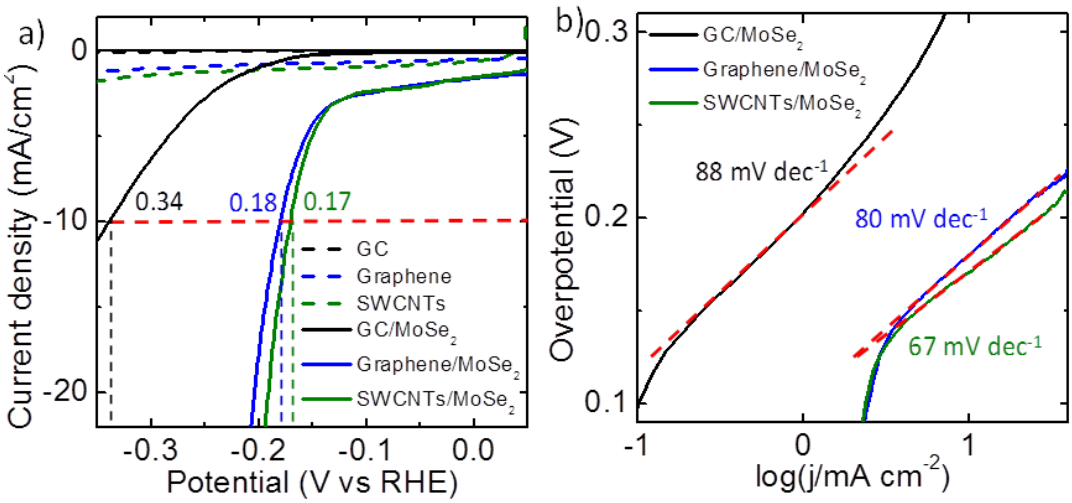

Figure 4.15. a) Polarization curves of GC/$MoSe_2$ (solid black line), graphene/$MoSe_2$ (solid blue line), SWCNTs/$MoSe_2$ (solid green line). Polarization curves of GC (dashed black line), graphene (dashed blue line) and SWCNTs (dashed green line) are shown for comparison. b) Tafel plots of the GC/$MoSe_2$ (solid black line), graphene/$MoSe_2$ (solid blue line) and SWCNTs/$MoSe_2$ (solid green line). Linear fits (dashed red lines) and the corresponding Tafel slope values are reported.

Taking into account the aforementioned experimental results and observations, the increase of $MoSe_2$ flakes mass loading (up to 5 mg cm^{-2}) (Figure 4.16, left sketch) in SWCNTs/$MoSe_2$ is intended for fully exploit the HER-assisting properties of the heterostructures. In addition, monolithic stacking of different heterostructures (SWCNTs/$MoSe_2$) (Figure 4.16, right sketch) is also proposed as a smart electrode assembly for achieving state-of-the art competing areal HER-perfomance (e.g., cathodic current density > 100 mA cm^{-2} at overpotential less than 0.2 V).[295]

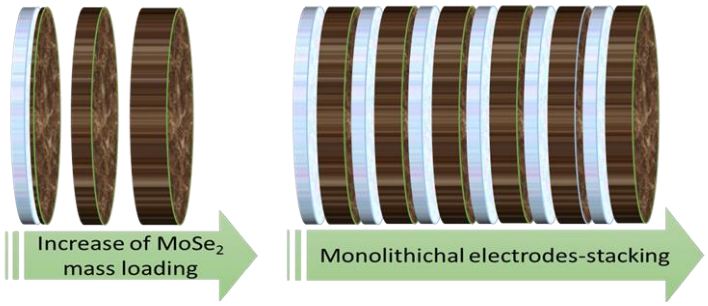

Figure 4.16. Sketch of the electrodes obtained by increasing $MoSe_2$ flakes mass loading and by monolithical stacking of different electrodes.

As reported in Figure 4.17 a-b, the as-produced electrodes show remarkable HER-electrocatalytic activity, *i.e.,* η_{10} values of 0.15, 0.12 and 0.10 V for 1, 2 and 6 monolithically stacked SWCNTs/$MoSe_2$, each one with $MoSe_2$ flakes mass loading of 5 mg cm^{-2} (*i.e.,* total electrode mass loading: 5, 10, 30 mg cm^{-2}, respectively). The η_{10} reduction is explained by Tafel plot analysis, which evidences an increase of j_0 with increasing the mass loading of the $MoSe_2$ flakes (from 2 to 5 mg cm^{-2}) and the increase of the number of stacked electrodes (form 1 to 6), meaning an effective increase of the HER-electrocatalytic active sites of $MoSe_2$ flakes. The j_0 values are 64, 165 and 203 µA cm^{-2} for the electrode with $MoSe_2$ flakes mass loading of 5 mg cm^{-2}, and for those obtained by stacking 2 and 6 electrodes, respectively. It is worth to note that the j_0 values of 203 µA cm^{-2} is one of the highest value reported in literature for TMDs,[291,292] overcoming also those usually reported for 1T-TMDs (*e.g.,* 167 µA cm^{-2} for 1T-MoS_2 nanoparticles).[296,297] Tafel slope values, instead, are similar for all the electrodes, thus suggesting the same HER-mechanism (Volmer-Heyrovsky) for all the electrodes.

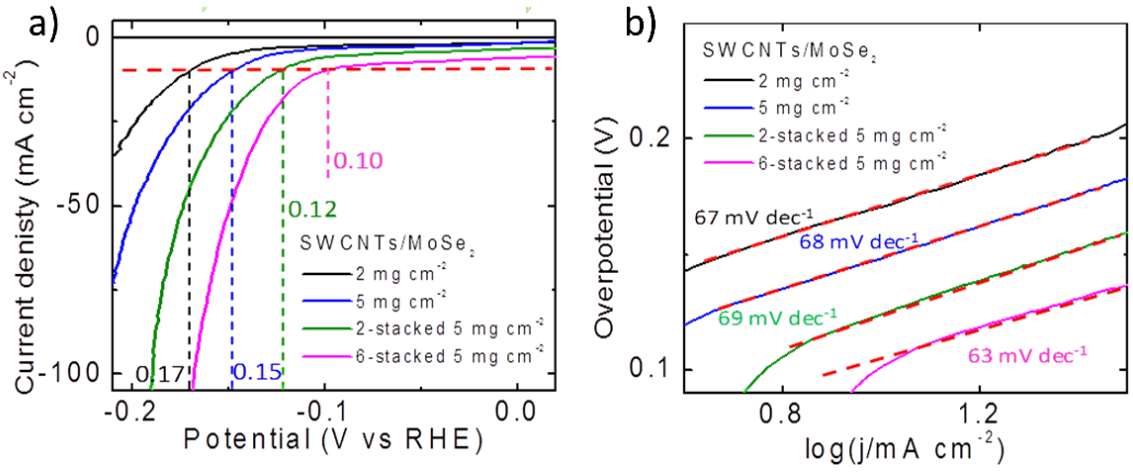

Figure 4.17 a) Polarization curves of SWCNT/$MoSe_2$ with $MoSe_2$ flakes mass loading of 2 mg cm^{-2} (solid black line), 5 mg cm^{-2}, (solid blue line), and the electrode obtained by the monolithical stacking of 2 and 6 SWCNTs/$MoSe_2$ with

$MoSe_2$ flakes mass loading of 5 mg cm^{-2} (solid green and magenta lines, respectively). b) Tafel plots of SWCNT/$MoSe_2$ with $MoSe_2$ flakes mass loading of 2 mg cm^{-2} (solid black line), 5 mg cm^{-2}, (solid blue line), and the electrode obtained by the monolithical stacking of 2 and 6 SWCNTs/$MoSe_2$ with $MoSe_2$ flakes mass loading of 5 mg cm^{-2} (solid green and magenta lines, respectively)Linear fits (dashed red lines) and the corresponding Tafel slope values are reported.

Figure 4.18 reports the polarization curves measured for the electrode annealed at 600, 700 and 800 °C in Ar/H_2 (90/10 %) for 5 h, in comparison to that obtained for the untreated electrode. The results evidence that the HER-electrocatalytic activity of the electrodes annealed at 600 and 700 °C are clearly enhanced with respect to the untreated electrode. In particular, the η_{10} decreases from 0.34 V in untreated electrode to 0.29 and 0.26 V in the electrodes annealed at 600 and 700 °C, respectively. A further increase of the temperature up to 800 °C cause a deterioration of the HER-electrocatalytic activity, whose η_{10} (0.44 V) increases of 0.1 V with respect to that of the untreated electrode. The Tafel slope values are also positively affected by the thermal treatment at 600 and 700 °C, for which they result to be 86 and 74 mV dec^{-1}, respectively. For the treatment at 800 °C, the lowest Tafel slope is observed (~144 mV dec^{-1}). The exchange current density (j_0) values increase for all temperature, being 19.09, 11.48 and 9.6 μA cm^{-2} for 600, 700 and 800 °C. These results are explained by considering the thermo-induced texturization of the basal plane of $MoSe_2$ flakes film (See Figure 4-11, and 4-12). More in detail, Se-vacancies, *i.e.,* HER-electrocatalytic sites, are formed due to H_2Se gas evolution during the thermal treatment in H_2 environment. However, at the highest temperature of 800 °C, an excessive removal of Se could be disadvantageous for the HER-electrocatalytic activity due to the disappearance of the $MoSe_2$ phase.

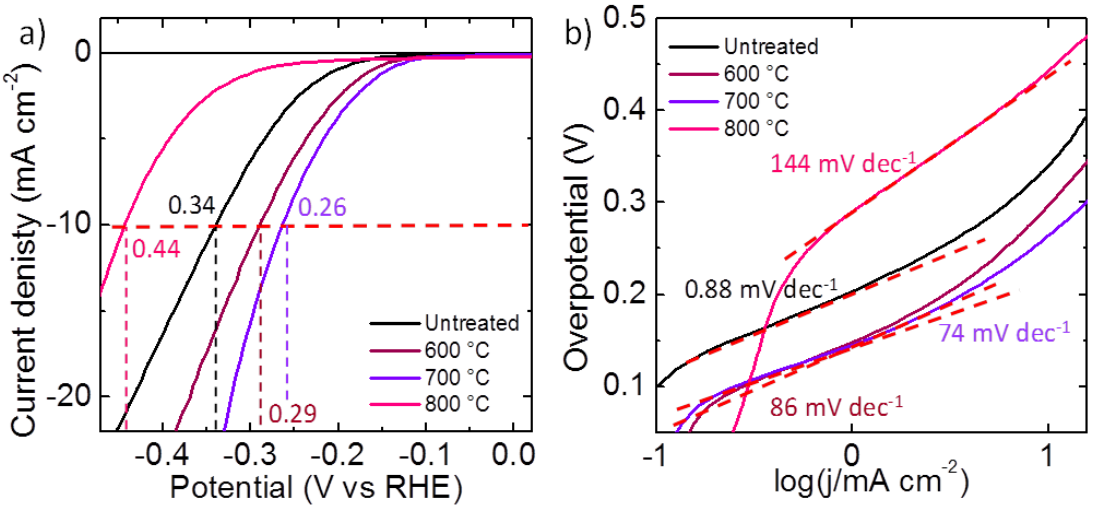

Figure 4.18. a) Polarization curves of untreated GC/$MoSe_2$ (solid black line) and GC/$MoSe_2$ annealed at 600 °C (solid purple line), 700 °C (solid violet line) and 800 °C (solid magenta line). The η_{10} values are also indicated for each curve.

b) Tafel plots of untreated GC/$MoSe_2$ and GC/$MoSe_2$ annealed at 600 °C (solid purple line), 700 °C (solid violet line) and 800 °C (solid magenta line). Linear fits (dashed red lines) and the corresponding Tafel slope values are reported.

On the basis of the aforementioned results obtained on GC/$MoSe_2$, SWCNTs/$MoSe_2$ heterostructres are also thermal or chemically treated (annealing in H_2 at 700 °C or 12 h-chemical bathing in n-butyllithium). Figure 4.19a displays the polarization curves obtained for the treated electrodes in comparison to that of the untreated one ($MoSe_2$ flakes mass loading of 2 mg cm^{-2}). Clearly, both chemical and thermal treatments enhance the HER-electrocatalytic activity of the electrode. More in detail, the η_{10} decrease from 0.17 V for the untreated electrode to 0.15 and 0.13 V for the Li-intercalated and annealed in H_2 electrodes, respectively. The Tafel slope and j_0 values are 83 mV dec^{-1}, and 167 µA cm^{-2}, respectively, for chemically treated electrode, while they are 54 mV dec^{-1} and 55 µA cm^{-2}, respectively, for the thermally treated electrode. Notably, the treated electrodes show a remarkable increase of j_0 (479% and 90% after chemical and thermal treatments, respectively) with respect to that of the untreated electrode (j_0 = 29 µA cm^{-2}). This indicates an increase of the number of the HER-electrocatalytic sites because of the semiconducting-to-metallic phase conversion of the $MoSe_2$ flakes or the Se-vacancies addition in their basal planes.[298] Moreover, the thermal treatment also decreases the Tafel slope values (from 67 mV dec^{-1} to 54 mV dec^{-1}), thus providing an effective method for accelerating the overall HER-kinetic (Figure 4.19b).

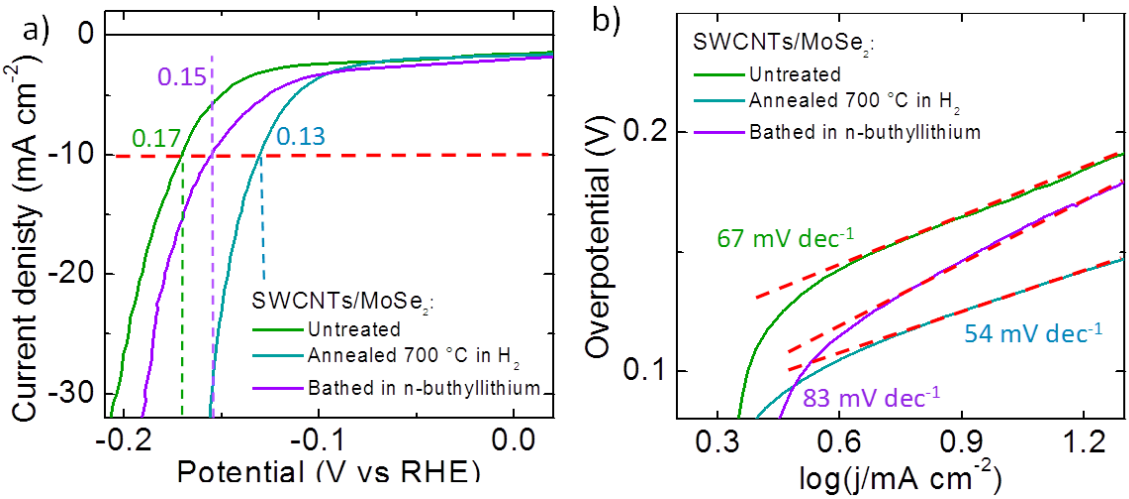

Figure 4.19 a) Polarization curves of untreated SWCNTs/$MoSe_2$ (solid green line), SWCNTs/$MoSe_2$ annealed at 700 °C in Ar/H_2 (90/10%) for 5 h (solid dark cyan line), SWCNTs/$MoSe_2$ chemically treated in n-butyllithium for 12 h (solid violet line). b) Tafel plots of the SWCNTs/$MoSe_2$ (solid green line), SWCNTs/$MoSe_2$ annealed at 700 °C in Ar/H_2 (90/10%) for 5 h (solid dark cyan line), SWCNTs/$MoSe_2$ bathed in n-buthyllithium for 12 h (solid violet line). Linear fits (dashed red lines) and the corresponding Tafel slope values are reported.

The electrochemical stability of the untreated graphene/$MoSe_2$, SWCNTs/$MoSe_2$ and the treated electrodes is evaluated by chronoamperometry measurements (j-t curves). For all cases, a constant η is applied in order to give equal starting current density of -30 mA cm^{-2}, *i.e.,* similar operative HER-condition. As shown in Figure 4.20, the electrodes retain a steady HER-electrocatalytic activity over a period of 40000 s (*i.e.,* > 11 h). In particular, for the SWCNTs/$MoSe_2$ chemically treated in n-butyllithium, the current density decreases of ~28%. The HER-electrocatalytic activity degradation might be caused by the thermodynamically metastable nature of the 1T-phase, which could be converted back to the native 2H-phase,[299] as well by the dissolution of soluble MoO_x species in acid.[300] Differently, for the untreated graphene/$MoSe_2$ and SWCNTs/$MoSe_2$ and the SWCNTs/$MoSe_2$ annealed at 700 °C in H_2 environment, only slight current density fluctuations are observed, which might be caused by the consumption of H^+ or the accumulation of H_2 bubbles on the electrode surface, hindering the reaction.[301,302] Thus electrochemical stability is demonstrated for these cases as expected from the natural 2H-phase of $MoSe_2$.[299,303]

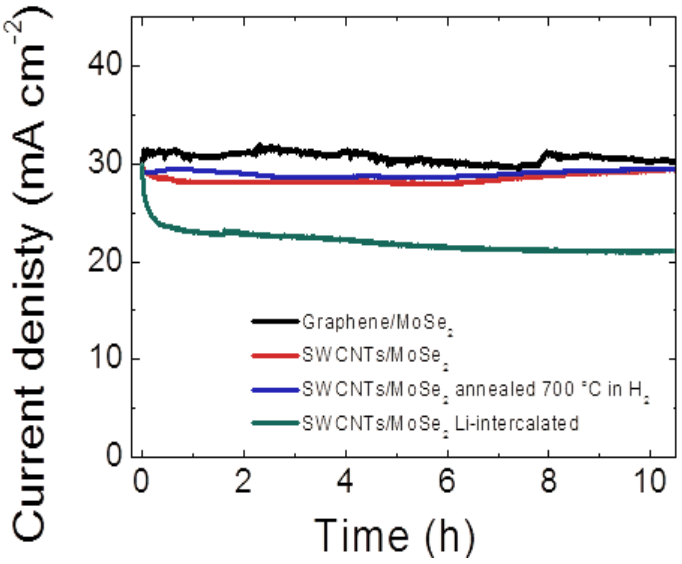

Fig.ure 4.20. Chronoamperometry measurements (j-t curves) of the heterostructured electrodes: graphene/$MoSe_2$ (black line), SWCNTs/$MoSe_2$ (red line), SWCNTs/$MoSe_2$ annealed at 700 °C in H_2 environment (blue line) and SWCNTs/$MOSe_2$ Li-intercalated (*i.e.,* chemically treated in n-butyllithium) (cyan line).

4.2.3 Non-Noble Metal Chloride Charge-Transfer Doping of $MoSe_2$ Flakes for Efficient PH-Universal Electrochemical HER.

Despite of these progresses achieved in the previous section on TMDs for electrochemical HER, it is still challenging to provide scalable and cost-effective pH-universal TMD-based electrocatalysts

capable to compete with cathode materials found in current large-scale hydrogen production technologies[304,305] (*e.g.,* Ni alloy[306,307] or high surface area noble metal coated-Ni[308] for chloro-alkaline or alkaline zero gap water[309] electrolysis units, and Pt nanoparticles supported on carbon black (Pt/C) for proton exchange membrane (PEM) electrolysis.[310,311,312] Indeed, the following sections report the design of pH-universal efficient HER-electrocatalysts based on single/few layer $MoSe_2$ flakes produced by cost-effective LPE[313,314,315] of the bulk counterpart in IPA and non-noble 3*d* metal (Fe, Co, Ni, Cu, Zn, Cd) chloride (MCl_2)-chemical doping.[316,317,318] The rigorous understanding of the HER-pathways in our electrodes by first-principles calculations is not straightforward, and at this stage lies beyond the scope of the present discussion. However, HER-assisting role of both the MCl_2-doping is explained by considering multiple functional effects, *i.e.,* 1) the modulation of the electronic state of $MoSe_2$ flakes; 2) the Cl^{-} or MCl_4^{2-} induced triggering of new HER-active sites; **Error! Bookmark not defined.,Error! Bookmark not defined.** 3) the facilitated production of H_{ads} and (for alkaline condition) H_2O discharge due the local upward band-bending emergence at p-doped/undoped regions of $MoSe_2$ flakes; 4) (for alkaline solution) the promotion of H_2O discharge due to the electrocatalytic activity of metal hydroxyl-oxides clusters formed after air exposure or under HER-operative electrochemical condition. Taking into account the results of the Section 4.2.2 and 4.2.3, the HER-assisting electrochemical coupling between SWCNTs and MCl_2-doped $MoSe_2$ flakes ($MoSe_2$:MCl_2) is then exploited for achieving for achieving current density *vs*. η requirements targeted in pH-universal large-scale hydrogen production.

4.2.3.1 Fabrication of the Electrodes

The $MoSe_2$ flakes and their MCl_2-doped counterparts (*i.e.,* $MoSe_2$:MCl_2) are deposited on GC sheets (Sigma Aldrich) (electrodes labelled as $MoSe_2$ and $MoSe_2$:MCl_2) by drop-casting the as-produced dispersion (mass loading of 0.2 mg cm^{-2} referred to exfoliated $MoSe_2$). The SWCNTs/$MoSe_2$ (or SWCTNs/ $MoSe_2$:MCl_2) are fabricated by depositing the SWCTN and $MoSe_2$ (or $MoSe_2$:MCl_2) dispersion onto nylon membranes (Whatman® membrane filters nylon, 0.2 µm pore size, Sigma Aldrich) *via* vacuum filtration process. The fabrication protocol of the heterostructures resemble that reported for the heterostructures studied in Section 4.2.1 and 4.2.2 The mass loading of the materials is 0.64 mg cm^{-2} for both SWCNTs and $MoSe_2$ (for $MoSe_2$:MCl_2 this values is referred to the exfoliated $MoSe_2$). The electrode area is 3.14 cm^2. The electrodes are dried overnight at room temperature before their electrochemical characterization.

4.2.3.2 Electrodes Characterization

Figures 4-21a,b report the top-view SEM images of the SWCNT paper (SWCNT mass loading: 0.64 mg cm^{-2}) and SWCNTs/ $MoSe_2$ (SWCTNs mass loading: 0.64 mg cm^{-2}; $MoSe_2$ mass loading: 0.64 mg cm^{-2}). The surface of SWCNT paper consists of a mesoporous network with bundle-like arrangement (Figure 4.21a). The surface of SWCNT paper is clearly modified by the $MoSe_2$ overlay (Figure 4-21b), which is characterized by the flaked nature of the $MoSe_2$, in agreement with the $MoSe_2$ morphology derived by TEM and AFM analysis (see Chapter 3). The AFM images of the electrode surfaces (Figure 4.21c) evidence morphologies similar to those observed by SEM. The R_a values are ~103 nm and ~70 nm for SWCNT paper and SWCNTs/ $MoSe_2$ surfaces, respectively. These values indicate that $MoSe_2$ deposition flattens the SWCNT paper. The top-view SEM image of a representative SWCNTs/ $MoSe_2$:MCl_2 (M = Ni) (Figure 4.21d) does not evidence significant surface changes with respect to SWCNT/ $MoSe_2$. The cross-sectional SEM images of SWCNTs/ $MoSe_2$:$NiCl_2$ (Figure 4.21e) shows bilayer-like architecture with the thickness of the MoSe2:$NiCl_2$ overlay of ~1 μm. Figures 4.21 f,g show a top-view and side-view photographs of SWCNTs/ $MoSe_2$:$NiCl_2$. In Figures 4.21g, SWCNTs/ $MoSe_2$:$NiCl_2$ is manually bended for illustrating its mechanical flexibility, which can enable versatile designs for advanced solar fuel devices, including flexible PEC cells[319,320] and hydrogen storage system[321,322]. Moreover, the porosity and flexibility properties of the as-produced heterostructures enable their sequential stacking (here extended up to achieve 4-stacked heterostructures) (Figure 4.21h) for scalable targeting the areal performance requirements in energy renewable buffer units.

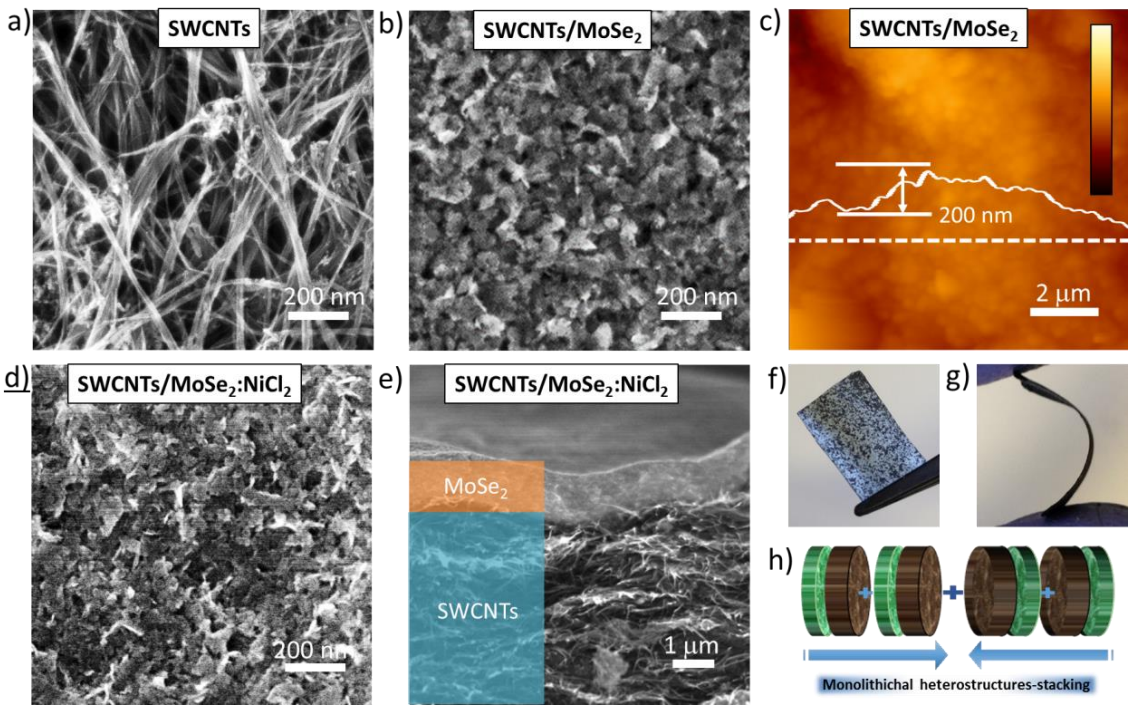

Figure 4.21. Solution-processed, flexible and self-standing heterostructured electrodes between SWCNTs and SWCNTs/ $MoSe_2$:MCl_2 prepared via sequential vacuum filtration of the material dispersions. a,b) Top-view SEM images of SWCNTs bucky paper and SWCNTs/ $MoSe_2$:$NiCl_2$. c) AFM images SWCNTs/ $MoSe_2$. Height profile along representative cross section (white dashed lines) is also shown. The z-scale bar is 1 µm. d)Top-view and e) cross-sectional SEM images of SWCNTs/ $MoSe_2$:$NiCl_2$. f) Top-view and g) side view photographs of SWCNTs/ $MoSe_2$:$NiCl_2$ (electrode area: 0.8x1.5 cm^2. In panel g the electrode is manually bended in order to show its mechanical flexibility. h) Sketch of the monolithical heterostructures-stacking (up to 4-stacked heterostructures).

Energy-dispersive X-ray (EDX) spectroscopy analysis of top view SEM image of SWCNTs/$MoSe_2$:$NiCl_2$ (Figure 4.2) shows the Ni is uniformly distributed onto the heterostructure surface, thus indicating that $NiCl_2$-doping of the $MoSe_2$ is uniform.

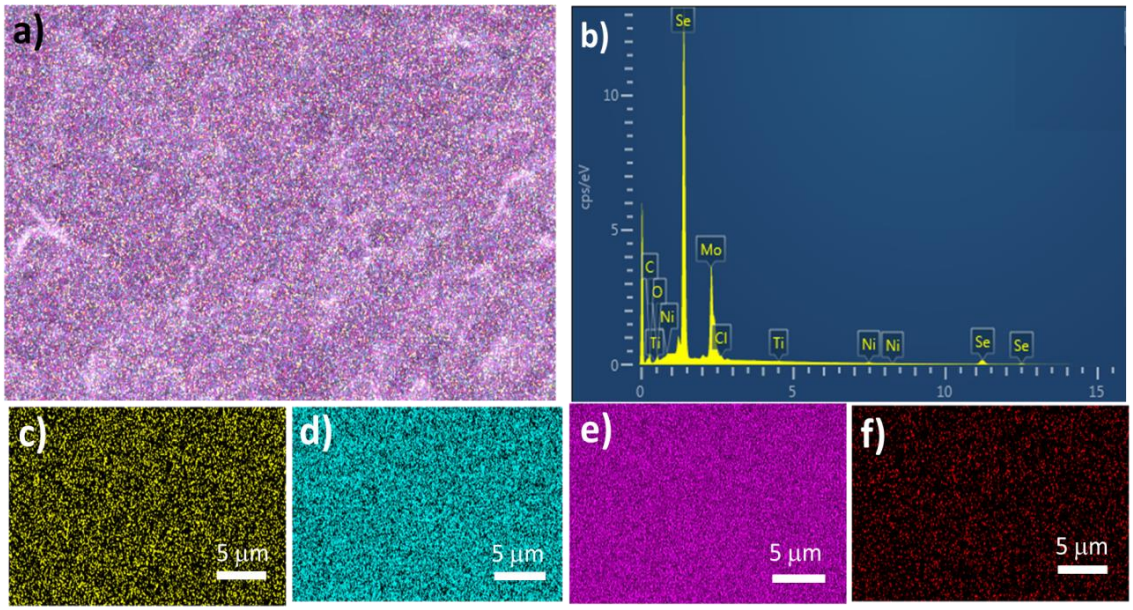

Figure 4.22. EDX analysis of the surface of SWCNTs/ex-$MoSe_2$:$NiCl_2$. a) Elemental mapping on a representative top-view SEM image of SWCNTs/ $MoSe_2$:$NiCl_2$. b) The mass spectrum of the EDX analysis of the SEM image of panel a. c-f) EDX analysis of the SEM image showed in panel a for the single element: c) C, d) Mo, e), Se and f) Ni. atom color code: yellow C; cyan Mo; violet Se; red Ni.

However, EDX analysis of cross-sectional SEM image of SWCNTs/$MoSe_2$:$NiCl_2$ (Figure 4.23) reveals that Ni is distributed uniformly also along the vertical direction of the heterostructure, including SWCNT paper. This means that during deposition of the $MoSe_2$:MCl_2, the elemental metal (*i.e.*, $M^0\downarrow$) and, eventually, MCl_2 residuals infiltrate into SWCNT paper. Thus, the formation of metal oxides (MO or M_2O_3) or metal hydroxyl-oxides ($M(OH)_2$, $M(OH)_3$ or M(OH)O) into SWCNT paper, and the MCl_2-doping of the latter occur during the fabrication of the heterostructures. It is worth noting that p-doping of the SWCNT is beneficial for enhancing the electron transfer from SWCTN paper to the active sites of $MoSe_2$:MCl_2, agreeing with experimental observations on high-sensitive, fast response (< 15 µs) gate-tuneable p-n heterojunction diode-photodetector using SWCNTs and single-layer MoS_2 as p-type and n-type semiconductors.[323]

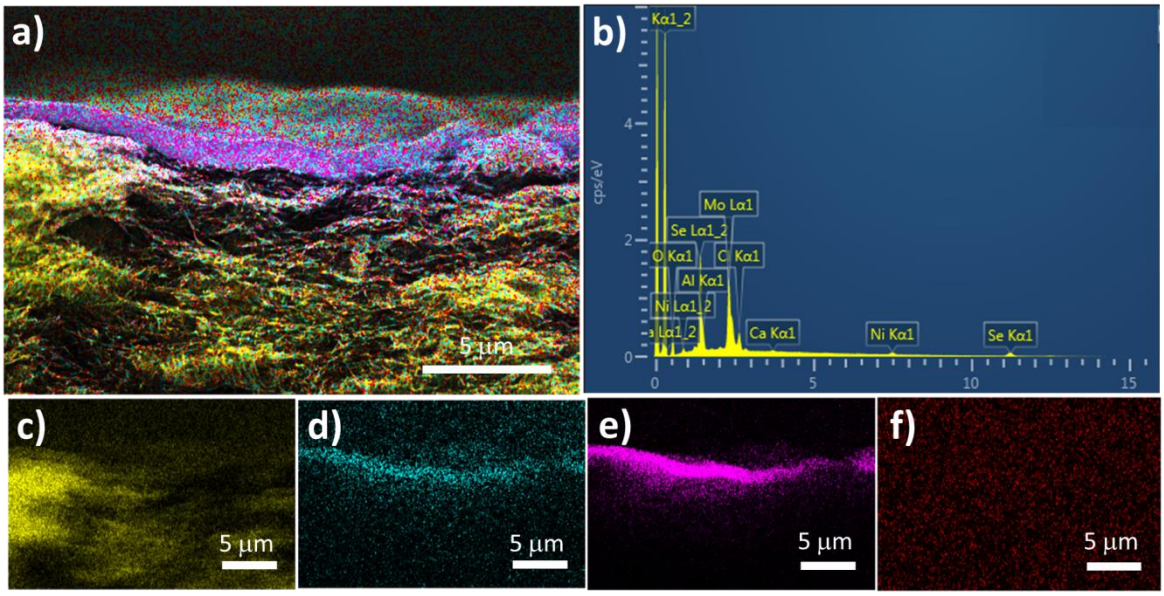

Figure 4.23. EDX analysis of the cross-section of SWCNTs/ $MoSe_2$:$NiCl_2$. a) Elemental mapping on a representative cross-sectional SEM image of SWCNTs/ $MoSe_2$:$NiCl_2$. b) The mass spectrum of the EDX analysis of the SEM image of panel a. c-f) EDX analysis of the SEM image showed in panel a for the single element: c) C, d) Mo, e), Se and f) Ni. atom color code: yellow C; cyan Mo; violet Se; red Ni.

Raman spectroscopy measurements are carried out on $MoSe_2$ and $MoSe_2$:MCl_2, as well on the $MoSe_2$ bulk counterpart, in order to investigate their structural topological properties. The characteristic Raman mode are of $MoSe_2$ are described in Chapter 3-Representative spectra of $MoSe_2$ bulk, $MoSe_2$ and $MoSe_2$:MCl_2 are reported in Figure 4.24. The A_{1g} mode is located at ~241 cm^{-1} for the $MoSe_2$ bulk, while it is red-shifted to ~239 cm^{-1} for the $MoSe_2$, in agreement with the softening of the vibrational mode accompanied by the reduction in flake thickness.[324,325] The in-plane E^1_{2g} mode is observed at ~287 cm^{-1} for both samples[336] The intensity ratio between the A_{1g} and E^1_{2g} modes ($I(A_{1g})/I(E^1_{2g})$) (~21) and the presence of the B_{2g} mode (located at ~352 cm^{-1}) in $MoSe_2$ spectra agrees with its few-layer flake structure.[326,327] The activation of the mode E_{1g} is due by a resonance-induced symmetry breaking effect.[328] Moreover, the energy of this mode, being independent on the number of layers,[329] does not change between the $MoSe_2$ bulk and $MoSe_2$.

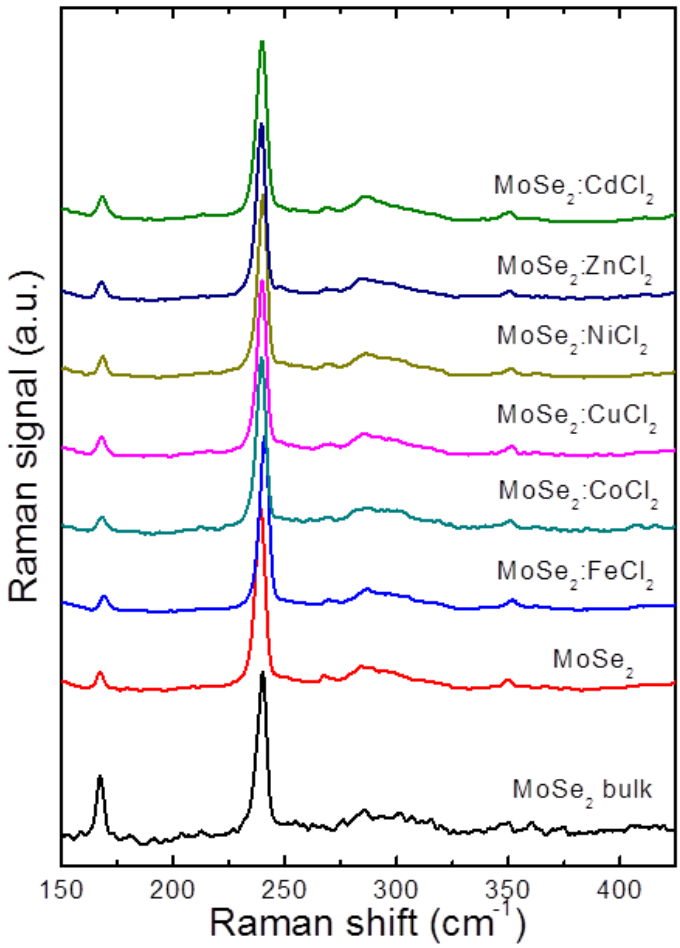

Figure 4.24. Raman spectra of $MoSe_2$ bulk (black curve), $MoSe_2$ (red curve), $MoSe_2$:$FeCl_2$ (blue curve), MoSe2:CoCl2 (cyan curve), MoSe2:CuCl2 (magenta curve), $MoSe_2$:$NiCl_2$ (dark yellow curve), $MoSe_2$:$ZnCl_2$ (Navy curve) and $MoSe_2$:$CdCl_2$ (olive curve), as deposited on Si/SiO_2 substrates. The main peaks, *i.e.,* the in-plane modes E_{1g}, E^1_{2g}, and E^2_{2g}, the out-of-plane mode A_{1g} and the breathing mode B^1_{2g} are named in the graph.

After MCl_2-doping, Raman peaks of $MoSe_2$ are still observed, thus indicating that the crystal structure of $MoSe_2$ is preserved. These observations agree with the formation of van deer Waals complexes between $MoSe_2^{2+}$ and Cl^- or MCl_4^{2-}, as resulting by the neutralization through physisorption and/or chemisorption of the charged species created during the MCl_2-doping of $MoSe_2$ (*step 2*).[330,331]

X-ray photoelectron spectroscopy measurements are used for evaluating the chemical and electronic state within the exposed surfaces of MCl_2-doped $MoSe_2$ ($MoSe_2$:MCl_2). In particular, the Mo 3d and Se 3d XPS spectra of $MoSe_2$:MCl_2 (except for M = Cu) show uniform shift (0.1-0.4 eV range) towards lower binding energy compared to those of the as-produced $MoSe_2$ (Figure 4.25). The downshift agrees with the lowering of the Fermi level upon the p-type MCl_2-doping of the $MoSe_2$ and the upward band-bending emergence localized at doped/undoped regions

interface.[332,333] In the Mo 3d spectra, in addition to the two peaks located at ~229 eV and ~232 eV corresponding to Mo $3d_{5/2}$ and Mo $3d_{3/2}$ peaks of Mo(IV) state in $MoSe_2$, [334,335] the peaks at higher binding energies at ~232 eV and ~236 eV are assigned to the Mo(VI) state, as attributed to MoO_3 residues in pristine materials. Binding energy peak of Cl 2*p* at ~198 eV is also detected in the $MoSe_2$:MCl_2, together with the distinct binding energy peaks associated with the M 2p or 3d doublets (Fe $2p_{3/2}$ at 711 eV (satellite features at 720 eV) and Fe $2p_{1/2}$ at 725 eV; Co $2p_{3/2}$ at 882 eV (satellite feature at 887 eV) and Co $2p_{1/2}$ at 798 eV (satellite feature at 803 eV); Ni $2p_{3/2}$ at 856 eV (satellite feature at 863 eV) and Ni $2p_{1/2}$ at 874 eV (satellite feature at 881 eV); Ni $2p_{3/2}$ at 856 eV (satellite feature at 863 eV) and Ni $2p_{1/2}$ at 874 eV (satellite feature at 881 eV); Cu $2p_{3/2}$ at 932 and 935 eV (satellite features between 942 and 946 eV) and Cu $2p_{1/2}$ at 952 and 955 eV (satellite features around 963 eV); Zn $2p_{3/2}$ at 1023 eV and Zn $2p_{1/2}$ at 1046 eV; Cd $3d_{5/2}$ at 406 eV and Cd $3d_{3/2}$ at 413 eV. All the peaks refer to oxidized states of M (*i.e.*, Fe(III), Co(II), Ni(II), Cu(I) or Cu(II), Zn(II) and Cd(II)), which can be attributed to both MCl_2 residuals and oxidized species formed by the reaction between $M^0\downarrow$ and O_2 or H_2O, after ambient exposure of the $MoSe_2$:MCl_2. The oxidized species can be either metal oxide (*e.g.*, MO for M(II), M_2O_3 for M(III)) or metal hydroxyl-oxides (*e.g.*, $M(OH)_2$ for M(II) or $M(OH)_3$ and M(OH)O for M(III). For the case of Cu, the additional peaks observed at 932 and 952 eV are ascribed to the Cu $2p_{3/2}$ and Cu $2p_{1/2}$ of Cu(I) species (*e.g.*, Cu_2O). It is worth noting that the formation of interfacial dipole complexes between $MoSe_2$ and oxidized species of M could also alter the electronic surface states of the $MoSe_2$,[336] turning out to a different level of oxidation for Mo in $MoSe_2$ and formed complexes. In particular, chemical composition analysis evidences that the percentage content (%c) of Mo(VI) increases from 23% in $MoSe_2$ to 75%, 26%, 42%, 25%, 47%, 58% after doping with $FeCl_2$, $CoCl_2$, $NiCl_2$, $CuCl_2$, $ZnCl_2$ and $CdCl_2$, respectively. Notably, $FeCl_2$-doping leads to the highest level of oxidation of $MoSe_2$. Furthermore, only for this case, the ratio between the %c of Cl and that of M is lower than 1. This is tentatively explained by taking into account the evolution of HCl, which is formed when residual $FeCl_2$ reacts with O_2 or H_2O to form metal hydroxyl-oxide (*i.e.,* $4MCl_2 + 6H_2O + O_2 \rightleftarrows 4\ M(OH)O + 8HCl$)[337,338] or metal hydroxyl-chloride (*i.e.*, $MCl_2 + H_2O \rightleftarrows M(OH)Cl + HCl$)[337] , respectively, during the drying in air of $FeCl_2$-doped $MoSe_2$ deposited on onto Si/SiO_2 substrate.

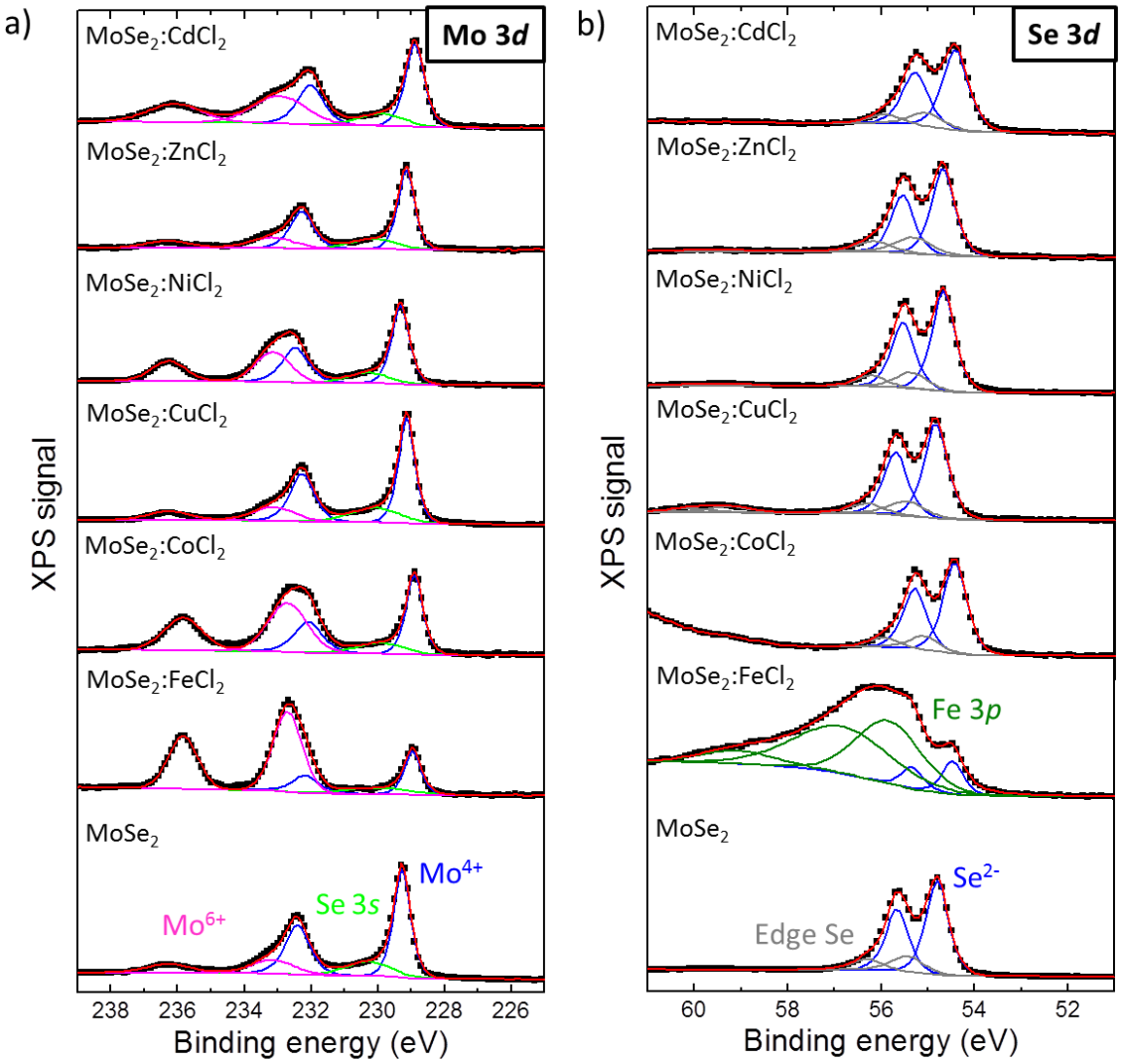

Figure 4-25. a,b) *Mo 3d and* Se *3d* XPS spectra of $MoSe_2$ and $MoSe_2$:MCl_2. Their deconvolutions are also shown, evidencing the band ascribed to: Mo(IV) and Se(II) ($MoSe_2$) (blue curves); Se 3s band (red curve), overlapping the Mo 3d XPS spectrum; Mo(VI) (MoO_3) (magenta curves); Se(0) (edge Se) (grey curves); Fe 3p band (olive curve), overlapping the Se 3s XPS spectrum.

4.2.3.3 Electrochemical Characterization

The HER-activities of $MoSe_2$ and $MoSe_2$:MCl_2, deposited on GC electrode ($MoSe_2$ mass loading: 0.2 mg cm^{-2}), are evaluated both in acid (0.5 M H_2SO_4) and alkaline (1 M KOH) solutions (Figure 4.26). Figure 4.26a,b show LSV curves of $MoSe_2$ and $MoSe_2$:MCl_2, in acid and alkaline solutions, respectively, while Figure 4.26c,d reports the corresponding Tafel plots. The extrapolated FoM are reported in Figure 4.26e-g. The results evidence that the HER-activity of $MoSe_2$ is affected by the MCl_2-doping. In acid solution, the $MoSe_2$ doped with $CdCl_2$, $ZnCl_2$, $CuCl_2$ and $NiCl_2$ show higher cathodic current densities with respect to that of pristine case, while the $CoCl_2$- and $FeCl_2$-doping decrease the HER-activity. Thus, η_{10} decreases from 0.31 V for the $MoSe_2$ to 0.23 V for most active case of $MoSe_2$:$CdCl_2$, while it increases to 0.44 V for the $MoSe_2$:$FeCl_2$. Tafel slope of $MoSe_2$:$NiCl_2$ significantly decreases from 0.102 V dec^{-1} in the $MoSe_2$ to 0.065 V dec^{-1}, while it is marginally affected for $CoCl_2$-, $CuCl_2$-, $ZnCl_2$- and $CdCl_2$- doping (0.094, 0.116, 0.101 and 0.106 V dec^{-1}, respectively) and it increases for $FeCl_2$-doping (0.175 V dec^{-1}). Similarly, the j_0 is significant affected by $NiCl_2$-doping, without evidencing remarkable variation for the others MCl_2-dopings. In alkaline solution, $CoCl_2$ and $NiCl_2$ are the most effective dopants for increasing the HER-activity of the $MoSe_2$. The corresponding η_{10} are 0.31 V and 0.27 V, respectively, which are lower with respect to that of the $MoSe_2$ (0.36 V). $CdCl_2$ and $ZnCl_2$ dopants do not significantly affect the $MoSe_2$ HER-activity, which decreases for both $MoSe_2$:$CuCl_2$ and $MoSe_2$:$FeCl_2$. Similarly to the acid conditions, $NiCl_2$ is the most effective dopant for decreasing the Tafel slope of the $MoSe_2$ (from 0.147 to 0.114 V dec^{-1}). Comparable j_0 are instead obtained for all the $MoSe_2$:MCl_2 with respect to the $MoSe_2$, showing values in the 10-30 $\mu A\ cm^{-2}$ range (with the only exception of $MoSe_2$:$CuCl_2$ which shows an higher j_0 value around 70 $\mu A\ cm^{-2}$). The results show that MCl_2-doping offers a strategy to enhance the HER-activity of $MoSe_2$ in both acid and alkaline solutions. Once experimentally established the effect of the MCl_2-doping on HER-electrocatalytic activity of $MoSe_2$, flexible, self-standing and hybrid heterostructures between commercial single-walled carbon nanotubes (SWCNTs) and $MoSe_2$ (SWCNTs/$MoSe_2$:MCl_2), produced via sequential vacuum filtration of the SWCNT and $MoSe_2$ (or $MoSe_2$:MCl_2), are investigated as flexible HER-active electrodes compatible with high-throughput scalable industrial manufacturing. The rationale of the choice of these heterostructures is based on my recent work[339] where I experimentally demonstrated long-range ($\geq 1\mu m$) electrochemical coupling between TMDs and graphene or SWCNT paper (substrates)[340,341]

for increasing the HER-activity of TMDs, without resorting the synthesis of hybrid TMDs/carbon materials compounds.[342]

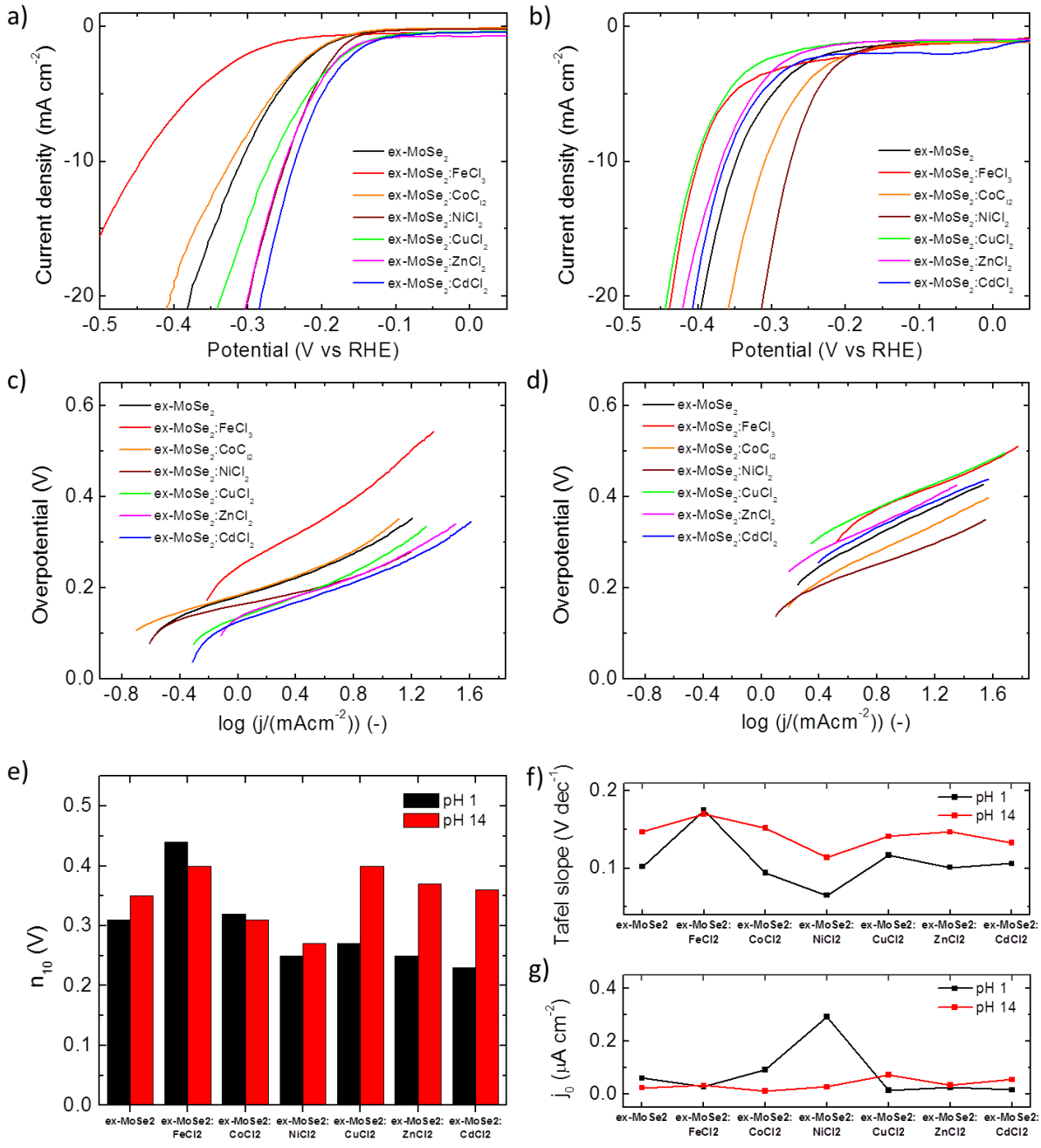

Figure 4.26. Electrochemical characterization of the HER-activity of $MoSe_2$ and $MoSe_2$:MCl_2 in acid and alkaline solutions. a,b), LSV curves for $MoSe_2$ and $MoSe_2$:MCl_2 in 0.5 M H_2SO_4 (pH 1) and 1 M KOH (pH 14), recorded during initial potential sweeps. c,d) Corresponding Tafel plots of the LSV curves in a and b. e-g) Comparison between FoM assessing the HER-activities of $MoSe_2$ and $MoSe_2$:MCl_2 in acid and alkaline solutions.

Figures 4.27a,b reports the *iR*-corrected LSV curves of the SWCNTs/$MoSe_2$:$CdCl_2$ and SWCNTs/ $MoSe_2$:$NiCl_2$ in acid and alkaline solutions, respectively, together with those obtained for 2- and 4-

stacked corresponding heterostructures (labeled as: 2-SWCNTs/ $MoSe_2$:$CdCl_2$ and 2-SWCNTs/ $MoSe_2$:$NiCl_2$; 4-SWCNTs/ $MoSe_2$:$CdCl_2$, and 4-SWCNTs/ $MoSe_2$:$NiCl_2$). The $CdCl_2$ and $NiCl_2$-chemical doping are evaluated because of the higher HER-activity expressed by $MoSe_2$:$CdCl_2$ and $MoSe_2$:$NiCl_2$ in acid and alkaline solutions, respectively, with respect to the other $MoSe_2$:MCl_2 (Figure 4.27a,b). LSV curves of SWCNTs/$MoSe_2$:$NiCl_2$ and SWCNTs/$MoSe_2$:$CoCl_2$ in acid solution and alkaline solution, respectively, are also reported for comparison (being $MoSe_2$:$NiCl_2$ and $MoSe_2$:$CoCl_2$ the second most HER-active $MoSe_2$:MCl_2 in the aforementioned solutions). These results show that the most HER-active hybrid heterostructures are those based on $MoSe_2$:$CdCl_2$ and $MoSe_2$:$NiCl_2$, in acid and alkaline solutions, respectively, thus proving a synergic effect of the MCl_2- doping and the electrochemical coupling between SWCTNs and $MoSe_2$ for increasing the HER-activity of the $MoSe_2$. Notably, the 4-stacked heterostructures yield current densities higher than 100 mA cm^{-2} at overpotential lower than 0.2 V, both in acid and alkaline conditions. A fully rigorous kinetic analysis of the HER , *i.e.,* the establishment of Tafel slope and the j_0, is not reported here because of the unambiguous results which derives in presence of high-surface area poor HER-active SWCNT paper, giving capacitive current density also for low LSV sweep voltage rate (≤ 5 mV s^{-1}).[343] Thus, the trend of the HER-activity is expressed only by the analysis if η_{10} as extrapolated for LSV measurements (Figure 4.27c,d). In acid condition, η_{10} is 0.13 V and 0.16 V for SWCNTs/ $MoSe_2$:$CdCl_2$ and SWCNTs/ $MoSe_2$:$NiCl_2$, respectively. After stacking SWCNTs/$MoSe_2$:$CdCl_2$ heterostructures, η_{10} decrease from 0.13 V to 0.11 V and 0.08 V for 2-SWCNTs/$MoSe_2$:$CdCl_2$ and 4-SWCNTs/$MoSe_2$:$CdCl_2$. In alkaline condition, η_{10} is 0.14 V and 0.22 V for SWCNTs/ $MoSe_2$:$NiCl_2$ and SWCNTs/ $MoSe_2$:$CoCl_2$, respectively. After stacking SWCNTs/ $MoSe_2$:$NiCl_2$, η_{10} decrease from 0.14 V to 0.11 V and 0.06 V for 2-SWCNTs/$MoSe_2$:$NiCl_2$ and 4-SWCNTs/$MoSe_2$:$NiCl_2$. Notably, the heterostructures stacking, together with MCl_2 doping and SWCNTs/ $MoSe_2$ coupling, are effective to reach state-of-the-art η_{10} at in both acid and alkaline conditions. Although efficient TMD-based HER-electrocatalysts in acid solution have been already reported in recent literature,[344,345,346] the corresponding HER kinetics in alkaline electrolytes usually suffers from a high overpotential (η_{10} > 0.22 V).[347] The high kinetic energy barrier of the initial Volmer step and the strong adsorption of the formed OH^- on the surfaces of TMDs are held responsible for the sluggish HER kinetics in alkaline solutions.[348,349]

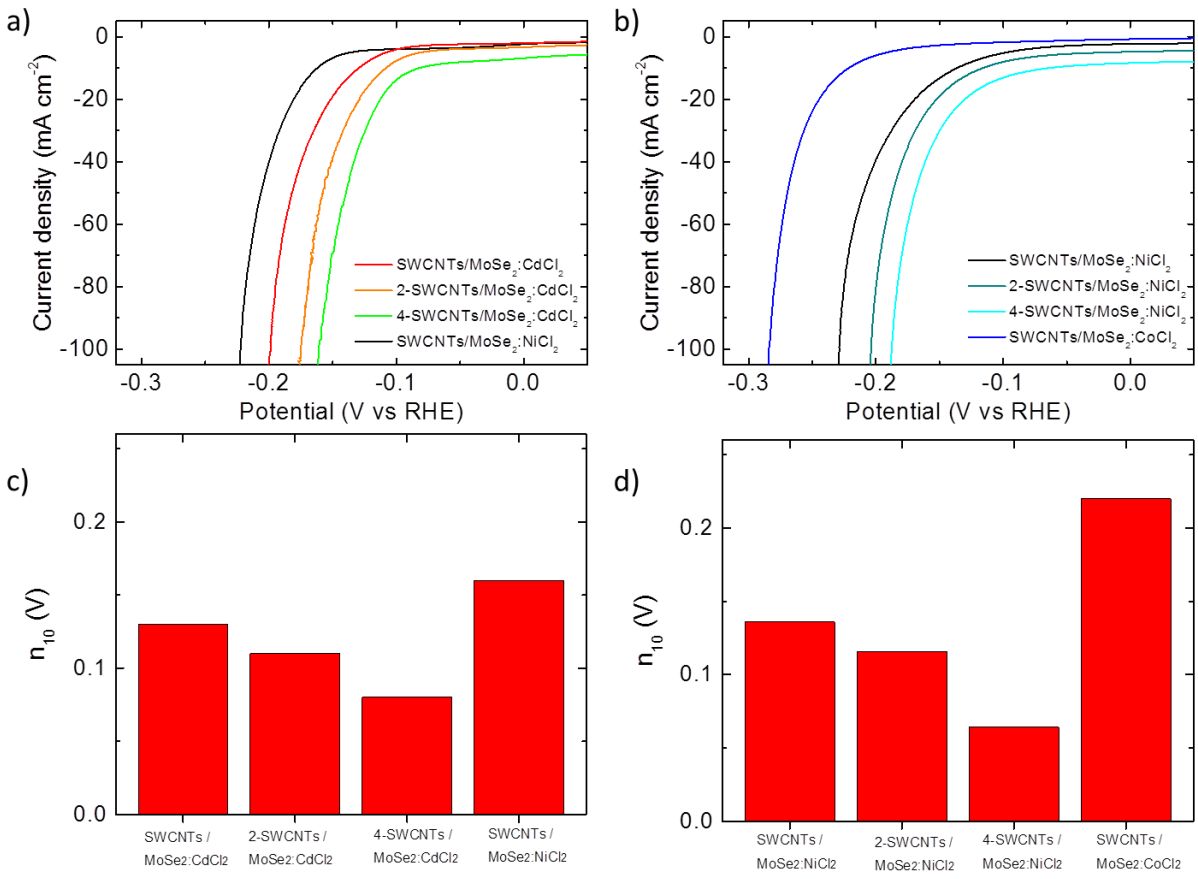

Figure 4.27. a) LSV curves for SWCNTs/ $MoSe_2$:$CdCl_2$, 2-SWCNTs/$MoSe_2$:$CdCl_2$, 4-SWCNTs/$MoSe_2$:$CdCl_2$ and SWCNTs/$MoSe_2$:$NiCl_2$ in 0.5 M H_2SO_4 (pH 1). b) LSV curves for SWCNTs/$MoSe_2$:$NiCl_2$, 2-SWCNTs/$MoSe_2$:$NiCl_2$, 4-SWCNTs/$MoSe_2$:$NiCl_2$ and SWCNTs/$MoSe_2$:$CoCl_2$ in 1 M KOH (pH 14). c,d) Comparison between the n_{10} corresponding to LSV curves in a and b.

Beyond the HER-activity, the electrocatalytic stability is another important criterion for attempting commercial purpose of an electrocatalyst. Figures 4.28a,b show the chronoamperometry measurements at fixed overpotential of -0.18 V vs. RHE for SWCNTs/ $MoSe_2$:$CdCl_2$ and SWCNTs/ $MoSe_2$:$NiCl_2$ in acid condition, and SWCNTs/ $MoSe_2$:$NiCl_2$ and SWCNTs/ $MoSe_2$:$CoCl_2$ in alkaline condition. In acid condition (Figure 4-28a) the SWCNTs/ $MoSe_2$:$CdCl_2$ and the SWCNTs/ $MoSe_2$:$NiCl_2$ slightly degrade, retaining ~86% and ~84% of the current densities. In basic condition, the SWCNTs/ $MoSe_2$:$NiCl_2$ and the SWCNTs/ $MoSe_2$:$CoCl_2$ show catalytic activation which increases the current densities of 13% during the first 50 min. After, the SWCNTs/ $MoSe_2$:$NiCl_2$ continue to manifest activation effects, reaching an overall increase of the current density of ~20% after 1000 min, while the SWCNTs/ $MoSe_2$:$NiCl_2$ slightly degrades retaining ~99% of the initial current densities. Notably, similar degradation and activation trends are observed for the $MoSe_2$:MCl_2 deposited on glassy carbon, as illustrated in the Figure 4-28c,d.

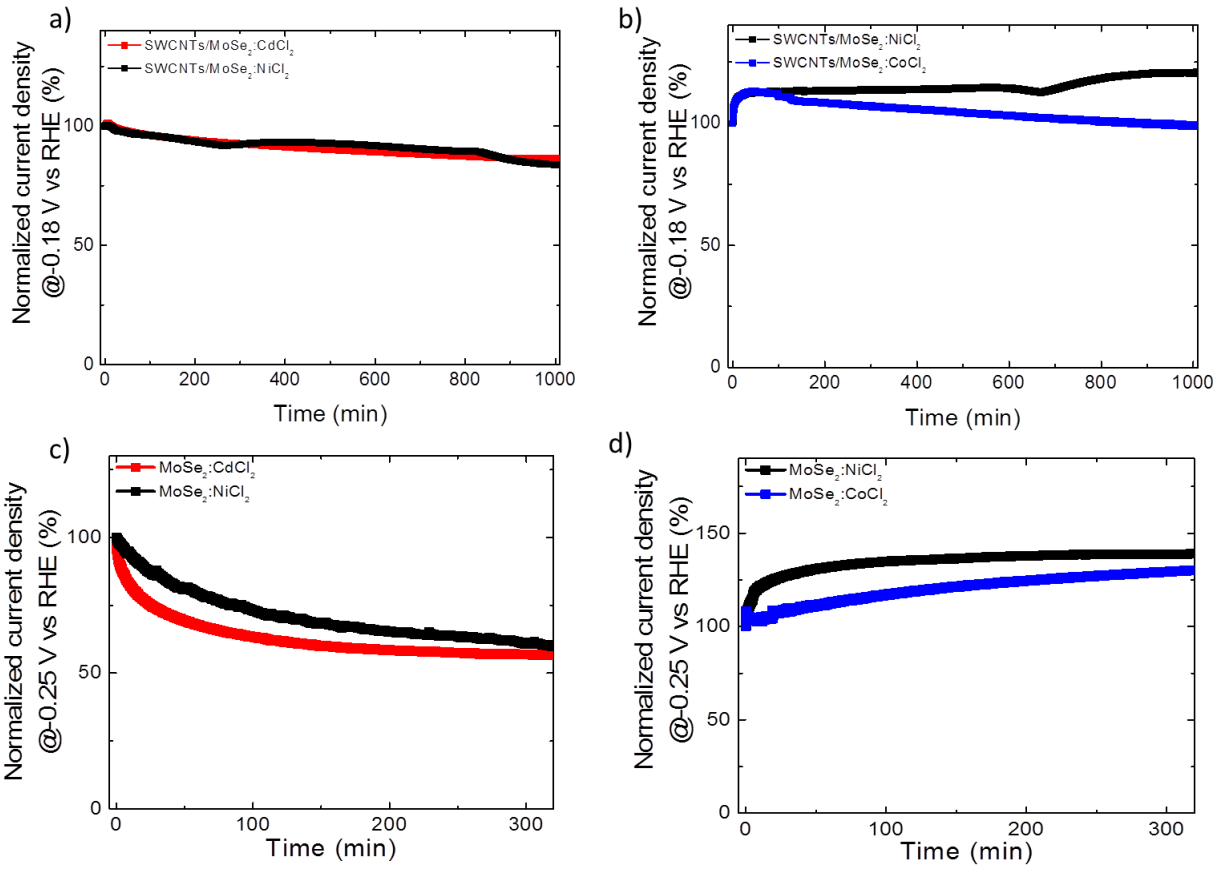

Figure 4.28. a,b) Chronoamperometry measurements (j-t curves) at fixed potential of -0.18 V *vs.* RHE for: a) SWCNTs/ $MoSe_2$:$CdCl_2$ and SWCNTs/ $MoSe_2$:$NiCl_2$ in 0.5 M H_2SO_4 . b) SWCNTs/$MoSe_2$:$NiCl_2$ and SWCNTs/ $MoSe_2$:$CoCl_2$ in 1 M KOH. c) chronoamperometry measurements of $MoSe_2$:$CdCl_2$ and $MoSe_2$:$NiCl_2$ deposited on glassy carbon in 0.5 H_2SO_4; d) $MoSe_2$:$NiCl_2$ and $MoSe_2$:$CoCl_2$ deposited on glassy carbon in 1 M KOH.

4.3 Summary:

In this chapter I reported the design and the engineering of advanced TMD-based electrodes. In particular, Section 4.2.1. shows that solution-processed flexible graphene flake/2H-MoS_2 QD heterostructures yield remarkable and stable HER electrocatalytic activity, overwhelming the one of GC/2H-MoS_2 flakes and GC/2H-MoS_2 QDs, respectively. The 2H-MoS_2 QDs, produced by an environmentally friendly solvothermal process in IPA, show average diameter of 6 nm, crystallinity retention, and low percentage content (<5%) of oxidized byproducts. The hybrid graphene flakes/2H-MoS_2 QDs heterostructure enables to reach a lower η10 (~136 mV) with respect to that of both graphene flakes/2H-MoS_2 flakes (175 mV) and GC/1T-MoS_2 flakes heterostructures (~235 mV) as well as graphene flakes/1T-MoS_2 flakes (~151 mV) heterostructure. These HER electrocatalytic performances approach those of several MoS_2-based catalyst reported in literature, overcoming the ones of recent MoS_2 flakes or MoS_2 QDs recently synthesized by

scalable routes. Section 4.2.2 reports the engineering of solution-processed heterostructures between $MoSe_2$ flakes and graphene flakes or SWCNTs as advanced HER-electrocatalysts. Compatibly with scalable material synthesis and electrode manufacturing, multiple insights and methods are exploited synergistically to target state-of-the-art-competing HER-electrocatalysts. These include: 1) μm-spatial range HER-assisting electrochemical coupling between $MoSe_2$ flakes and low-dimension carbon-based materials (*i.e.*, graphene flakes and SWCNTs); 2) thermo-induced texturization of the planes of $MoSe_2$ flakes; 3) wet-chemical 2H-to-1T phase conversion of the $MoSe_2$ flakes; 4) monolithic heterostructure stacking. In particular, a remarkable an η_{10} of 100 mV and cathodic current density > 100 mA cm^{-2} at η inferior to 200 mV are achieved by optimizing the $MoSe_2$ flakes mass loading on SWCNTs and by electrode assembly via monolithic stacking of multiple heterostructures. The so-optimized heterostructures show a ~4.8-fold enhancement of the j_0 (from 29 to 167 μA cm^{-2}) after chemical bath in n-butyllithium, and ~20% decrease of the Tafel slope (from 67 to 54 mV dec^{-1}) after thermal annealing at 700 °C in Ar/H_2 (90/10%). Moreover, the engineered heterostructures fully retain steady HER-electrocatalytic activities over more than 11 h, thus addressing practical durability requirements. Finally, Section 4.2.3 reports MCl_2-doping of $MoSe_2$ flakes and the heterostructures between SWCNTs and $MoSe_2$:MCl_2 as an effective toolkit for designing pH-universal HER-electrocatalysts. In particular, by adopting $MoSe_2$ flakes produced by cost-effective LPE of the bulk counterpart in IPA, MCl_2-chemical doping and solution-processed manufacturing of the heterostructured electrodes permit to achieve the key-requirements targeted in pH-universal large-scale H_2 production. Further optimization of the heterostructure design (*e.g.,* material mass loading and layer thickness), heterostructure-stacking (*i.e.,* number of heterostructures) and MCl_2-doping (*i.e.,* $MoSe_2$:MCl_2 molar ratio of the $MoSe_2$:MCl_2 dispersion, MCl_2-doping of SWCNT paper) are promising for a rapid and straightforward enhancement of the current HER-activity here achieved (η_{10} decreases from 0.31 V for the $MoSe_2$ flakes to 0.23 V for most active case of $MoSe_2$:$CdCl_2$ and 0.08 V for SWNT/$MoSe_2$:$CdCl_2$ in acid condition). To sum up, our TMD-based electrode technologies effectively offer low-cost alternative to the current state-of-the-art for electrocatalytic production of H_2 in both alkaline and acid electrolysers.

CHAPTER 5

CHAPTER 5: Solar Water Splitting

5.1 Photoelectrochemical (PEC) Cells

Photoelectrochemical (PEC) cells convert sunlight into H_2 and O_2 by water splitting. Generally, a PEC device comprises a semiconductor photoelectrode and a counter electrode immersed in an aqueous electrolyte.[350] Semiconductor photoelectrode absorbs the light photogenerating electrical charges.[351] The latter are needed to perform the redox chemistry of the HER, *i.e.*, $4H^+ + 4e^- \rightarrow 2H_2$ and OER, *i.e.,* $2H_2O \rightarrow O_2 + 4H^+ + 4e^-$.[352,353] The electrochemical potential of the bottom of the photoelectrode CB must be more negative than the H^+/H_2 redox level ($E°(H^+/H_2) = 0$ V *vs*. RHE, while the one of the top of the photoelectrode VB must be more positive than the O_2/H_2O redox level ($E°(O_2/H_2O) = 1.23$ V *vs*. RHE).[354,355] These thermodynamic constraints limit the choice of the semiconductor materials to the ones having band gap exceeding 1.23 V.[356,357,358] Consequently, these single semiconductor absorbers cannot harvest a significant portion of the solar spectrum and therefore their potential solar-to-hydrogen conversion efficiency (η_{STH}) is intrinsically limited (in agreement with the Shockley-Quiesser limit)[359,360] (see details in Section 5.2). However, tandem PEC cells based on two vertically stacked absorbing materials with different band gap can simultaneously optimize the solar light harvesting[361] and increase the photovoltage,[362] which in turn enhances the photocurrent values.[363,364] Currently, tandem cells with η_{STH} up to 18% have been demonstrated,[365] mainly using compound III-V semiconductors.[366,367,368] However, the manufacturing cost of these materials is significantly higher (*e.g*., PV-module cost are > 2 USD/W_p, where W_p states for watt peak)[369] than *e.g.*, Si (PV-module cost between 0.5-1 USD/W_p).[370] Recently, η_{STH} >10% has been demonstrated by using cheaper materials[365] such as Si,[371] CIGS [372] and halide perovskites.[373] Despite these results, the main obstacles for the commercialization of water splitting PEC devices include the use of expensive and not scalable deposition techniques (such as atomic layer deposition,[374] ion layer adsorption and reaction,[375] sputtering[376] and evaporation of metal/metal oxide protective layers),[377] and limited lifetime of devices in contact with aqueous electrolytes.[378] The latter, in particular, is challenging for the implementation of monolithically integrated devices fully immersed in water.[379] To overcome this issue, encapsulation strategies of the photoactive semiconductors have been proposed, with the result of increasing the overall fabrication

costs.[380,381,382] Thus, the discovery of new photoelectrode materials is needed to further improve the water splitting efficiency and long term stability with respect to the current technology.[383] Therefore, this chapter describes the use of organic conjugated polymers as candidate photocathode materials due to their low costs (potential PV module costs ~1 USD/W_p)[384] and compatibility with high-throughput production techniques[385] (solution-processed roll-to-roll and large-area deposition processes). Moreover, 2D material are exploited for engineering the interface between organic photoactive materials and the metal collector/electrocatalyst, permitting the realization of state-of-the-art photoelectrochemical solution-processed organic photocathodes.

5.2 Solar-to-hydrogen Conversion Efficiency (η_{STH}):

The overall thermodynamic efficiency of the solar water splitting (*i.e.*, η_{STH}) is the most important FoM of a PCE cell.[386] This quantity is defined as the amount of chemical energy stored in the form of H_2 divided by the amount of sunlight energy striking the device, as shown in the following equation:

$$\eta_{\mathrm{STH}} = \left[\frac{\mathrm{J_{SC}} \times 1.23 \times \eta_{\mathrm{F}}}{\mathrm{P}}\right]_{\mathrm{AM\ 1.5\ G}}$$

where j_{sc} is the short-circuit photocurrent density, η_F is the faradaic efficiency for hydrogen evolution, and P is the incident illumination power density, measured under standard solar illumination conditions (AM1.5G).[386] This FoM directly depends on the photophysical properties of the semiconductor photoelectrodes, such as light absorption and exciton formation, as well as charge carrier separation and transport.[387,388,389] The photogenerated electrons and holes have to overcome energetic constraints, corresponding to the thermodynamic potential of the HER and OER processes, respectively., as aforementioned in the previous section.[390,391]

Many studies in the field of PEC water splitting focus on individual device components or un-optimized systems which are not capable of splitting water without an externally applied bias. In these cases, other FoM are typically used to express the photoelectrochemical perfomances,[392] *i.e.*: 1) the cathodic photocurrents at 0 V *vs.* RHE ($J_{0V\ vs\ RHE}$); 2) the onset potential (V_o) (defined as the potential at which the photocurrent related to the HER is observed); 3) the maximum power point (V_{mpp}) (defined as d(JV)/dV=0) V_{mpp}, the fill factor (FF) (defined as the ratio of maximum obtainable

power to the product of the $J_{0V\ vs\ RHE}$ and V_o ($J_{mpp}xV_{mmp}/J_{0V\ vs\ RHE}xV_o$, where J_{mpp} is the current density at V =V_{mpp}); 4) the ratiometric power-saved relative to a non-photoactive (NPA) dark

electrode with an identical catalyst (C) ($\Phi_{saved,NPA,C}$) and the ratiometric power-saved relative to an ideally non-polarizable reversible hydrogen electrode, *i.e.,* the RHE, ($\Phi_{saved,ideal}$). $\Phi_{saved,NPA,C}$ is calculated by the following Equation:

$$\Phi_{saved,NPA,C} = \eta_F \times |j_{photo,m}| \times [E_{light}(J_{photo,m}) - E_{dark}(J_{photo,m})]/P_{in} = \eta_F \times |j_{photo,m}| x V_{photo,m}/P_{in}$$

where η_F is the current-to-hydrogen faradaic efficiency, P_{in} is the power of the incident illumination and $j_{photo,m}$ and $V_{photo,m}$ are the photocurrent and photovoltage at the V_{mpp}, respectively. j_{photo} is obtained by calculating the difference between the current under illumination of a photocathode and the current of the corresponding catalyst. The photovoltage V_{photo} is the difference between the potential applied to the photocathode under illumination (E_{light}) and the potential applied to the catalyst electrode (E_{dark}) to obtain the same current density. The subscript "m" stands for "maximum". $\Phi_{saved,NPA,C}$ reflects the photovoltage and photocurrent of a photocathode independently from the over-potential requirement of the catalyst. It is assumed that the catalyst film deposited on FTO is identical to the one deposited on TiO_2. $\Phi_{saved,ideal}$ is simply obtained by considering RHE as catalyst electrode, *i.e.,* setting E_{dark} = 0 V *vs.* RHE in the previous equation.

5.3 Hybrid Organic H_2-evolving Photocathode:

As previously mentioned in the introductory section, organic conjugated polymers are promising as candidate photocathode materials[393],[394,395] due to their low costs[396] (and compatibility with high-throughput production techniques (solution-processed roll-to-roll and large-area deposition processes).[397] In the field of photovoltaics, they have been established materials to address mechanical flexibility and low-cost power production of next-generation photovoltaic technologies. Recently, regio-regular poly(3-hexylthiophene-2,5-diyl) (rr-P3HT) has been also exploited in bulk heterojunction (BHJ) configuration with phenyl-C_{61}-butyric acid methyl ester (PCBM) for photocathodes reaching $J_{0V\ vs\ RHE}$ of 8 mA cm^{-2} and V_o of 0.7 V vs.[398] RHE. Actually, regio-regular rr-P3HT, the most studied photoactive polymer in organic photovoltaics, has a direct bandgap of 1.9 eV,[399] thus close to the optimum value for a PEC tandem device ($\eta_{\_STH}$ of 21.6% is predicted stacking 1.89 eV and 1.34 eV energy band gap semiconductors).[364] Moreover, the lowest unoccupied molecular orbital (LUMO) level of PCBM, the organic molecule typically adopted as

electron acceptors in BHJ configuration adopting rr-P3HT as electron donor, is several hundreds of millivolts more negative than the E° H^+/H_2 potential ($LUMO_{PCBM}$ – E° H^+/H_2> -0.5 V),[400] thus photogenerated electrons possess the energy enabling the HER process.[401] Furthermore, the optoelectronic properties of rr-P3HT, such as light absorption and charge photo-generation, are fully retained in aqueous environments.[402]

Indeed, the most successful architecture of organic photocathodes consists of rr-P3HT:PCBM BHJ sandwiched between two charge-selective layers (CSLs), and a thin electrocatalyst (EC) layer.[386] Specifically, the HSL is deposited between a transparent conductive oxide (TCO) *e.g.*, indium tin oxide (ITO) or fluorine-doped tin oxide (FTO), and the rr-P3HT:PCBM, while the electron-selective layer (ESL) is deposited on top of the rr-P3HT:PCBM. The device is completed by depositing an EC for HER (e.g., Pt[395,403] or free-metal catalysts[386,395]), giving the overall structure TCO/HSL/rr-P3HT:PCBM/ESL/EC. TiO_2 and its sub-stoichiometric phases have demonstrated to be consolidated ESL materials,[395, 404] the choice for the HSL counterpart has been a more complex task. In fact, although efficient HSL materials have been identified (e.g., MoO_3,[405] WO_3,[403] NiO,[404] CuI[51], PEDOT:PSS[394]) their intrinsic electrochemical degradation under HER-working conditions limited the lifetime of the photocathodes, lasting from several minutes to about few hours (up to 10 hours in the case of WO_3).[406] Moreover, the operational activity of the most efficient structures has been demonstrated only in acidic conditions,[404] with only a few examples showing remarkable cathodic $J_{0V\ vs\ RHE}$ of 1.2 mA cm^{-2} at neutral pH.[394] The possibility to design a photocathode able to operate in a larger pH window is beneficial for the development of tandem architectures operating at neutral or alkaline solutions.[407] In these conditions, the photoanodes (having complementary electrochemical properties) of the tandem architecture usually exhibit lower overpotential loss for OER.[408] In addition, the possibility to operate at near-neutral pH aqueous conditions is of utmost interest, *i.e.*, permitting the use of sea and river water as easy-available and non-hazardous/corrosive electrolyte.[409] This relaxes the stability constraints of practical photoactive and catalyst components.[410]

5.4 Photoelectrochemical Measurements:

Photoelectrochemical measurements are carried out at room temperature in a flat-bottom fused silica cell under a three electrode configuration using a Compact Stat potentiostat/ galvanostat station (Ivium), controlled via Ivium's own Ivium- Soft. A Pt wire is used as the counter-electrode

and sat. KCl Ag/ AgCl is used as the reference electrode. Measurements are performed in 50 mL aqueous solution of 0.5 M H_2SO_4 (99.999% purity, Sigma Aldrich) at pH 1. Oxygen is purged from electrolyte solutions by flowing nitrogen gas throughout the liquid volume using a porous frit at least 30 minutes before starting measurements. A constant, slight nitrogen flow is maintained afterwards for the whole duration of experiments, to avoid re-dissolution of molecular oxygen in the electrolyte. Potential differences between the working electrode and the reference electrode are reported with respect to the RHE scale using the Nernst equation. A 300 W Xenon light source LS0306 (Lot Quantum Design), equipped with AM1.5G filters, is used to simulate solar illumination (1 sun) at the glass substrate side of the samples inside the test cell. Linear Sweep Voltammetry (LSV) is used to evaluate the response of devices in the dark and under 1 sun illumination. Voltage is swept starting from the V_{oc} of the photocathodes to a negative potential of -0.3 V vs. RHE at a scan rate of 10 mV s^{-1}. The stability test is performed by recording in time the J_0 V vs. RHE under continuous illumination (1 sun) at 0 V vs. RHE.

5.5 Two Dimensional (2D) Materials Interfaces Engineering:

The research of novel HSL materials for rr-P3HT:PCBM-based photocathodes has recently involved 2D materials, including graphene derivatives[404] and TMDs.[386] The advantage of using the 2D materials is linked with the possibility of creating and designing layered artificial structures with on-demand electrochemical properties[411] by means of large-scale, cost-effective solution processed production methods.[412] In fact, the possibility to produce 2D materials from the exfoliation of their bulk counterpart in suitable liquids, as described in Chapter 2, permits to formulate functional inks.[413] The latter can then be deposited on different substrates by established printing/coating techniques.[413] So far, the durability of the graphene/TDMs-based photocathodes has been tested over no more than 1 hour-period.[404] Indeed, further investigations on these classes of 2D materials as CSLs for PEC application are of great interest for the community searching new solution for PEC H_2 production. The next sections discuss the novel use of 2D materials for organic photocatohdes, providing new insight and guidelines for approaching concrete applications.

5.5.1 MoS_2 Flakes as a HSL for Solution-Processed Hybrid Organic H_2-Evolving Photocathodes

This section reports the potentiality of 2D material interface engineering by using few-layer MoS_2 flakes as a HSL in organic PEC cells. In particular, MoS_2 flakes, as produced by Li-intercalation of

the bulk counterpart (see Chapter 2), are proposed as an efficient atomic-thick HSL for rr-P3HT:PCBM-based photocathodes. P-type chemical doping of the MoS_2 flakes is carried out to tune on-demand the MoS_2 Fermi level. This permits to match the HOMO level of the rr-P3HT, thus easing the hole collection at the electrode. The optimized p-doped MoS_2-based photocathodes reach $J_{0v\ vs\ RHE}$ of 1.21 mA cm $^{-2}$ V_o of 0.56 V *vs.* RHE and a $\Phi_{saved,NPA,C}$ of 0.43%, showing an increase with respect to pristine MoS_2-based photocathodes, under simulated 1 SUN illumination. The electrochemical performance reached by MoS_2-based photocathodes approach the state-of-the-art values of 0.47% for solution-processed rrP3HT:PCBM-based photocathodes,[386]

5.5.1.1 Architecture of MoS_2-based Organic Photocathode

Photocathodes are fabricated according to the architecture FTO/HSL/rr-P3HT:PCBM/TiO_2/MoS_3, where few-layer MoS_2 flakes are used as the HSL. Complementary architectures without the HSL are also fabricated. FTO coated soda-lime glass substrates (Dyesol, sheet resistance 15 Ω sq^{-1}) are cleaned according to the following protocols: sequential sonication baths in DI water, acetone, and IPA each lasting for 10 minutes and plasma cleaning in an inductively coupled reactor for 20 minutes (100 W RF power, excitation frequency 13.56 MHz, 40 Pa of O_2 gas process pressure, background gas pressure 0.2 Pa). The MoS_2 dispersion is deposited onto the previously treated FTO by spin coating (Laurell Tech. Corp. Spin coater) using a single step spinning protocol with a rotation speed of 3000 rpm for 60 s. Concentrations of the dispersions of 0.05, 0.1 and 0.4 mg mL^{-1} are tested. Post-thermal annealing in an Ar atmosphere at 150 °C for 30 min is performed for the MoS_2 films. The latter are subsequently doped by spin casting $HAuCl_4.3H_2O$ (≥ 99.9% trace metals basis, Sigma Aldrich) in methanol (ACS reagent, ≥99.8%, Sigma Aldrich) solution as p-doping agents on top, by using the same single step spinning protocol of the MoS_2 deposition. Doping concentrations of 5, 10, and 20 mM are tested. All doping solutions are sonicated for 10 minutes before deposition. The doped films are subsequently dried for 30 min under an Ar atmosphere. The organic polymer film used in all the architectures consists of a blend of rr-P3HT, as the donor component, and PCBM, as the acceptor component (rr-P3HT:PCBM). rr-P3HT (electronic grade, M_n: 15 000-45 000, Sigma Aldrich) and PCBM (99.5% purity, Nano C) are separately dissolved in chlorobenzene (ACS grade, Sigma Aldrich), at 1:1 wt ratio and 25 mg mL^{-1} on a polymer basis. Polymer blend solution is stirred at 40 °C for 24 hours before use. Blend thin films are obtained by spin casting the rr-P3HT:PCBM solution using the following set of parameters: two step spinning protocol with rotation speeds of 800 rpm for 3 s followed by 1600 rpm for 60 s, respectively. This

spin casting protocol produced a rr-P3HT:PCBM blend layer 200±20 nm thick, as measured by means of a Dektak XT profilometer (Bruker) equipped with a diamond-tipped stylus (2 mm) selecting a vertical scan range of 25 mm with 8 nm resolution and a stylus force of 1 mN, on an area of 0.25 cm^2. TiO_2 precursor solution is prepared in IPA and subsequently deposited by spin casting on top of the rr-P3HT:PCBM film as the ESL. Subsequently, during 12 h in air at room temperature, the precursor converted to TiO_2 by hydrolysis. A three step spinning protocol with rotation speeds of 200 rpm for 3 s, 1000 rpm for 60 s and 5000 rpm for 30 s is used. Post-thermal annealing in an Ar atmosphere is carried out at 130 °C for 10 min for all the devices before catalyst deposition. The devices are completed by a layer of MoS_3 nanoparticles (Alfa Aesar) acting as the catalyst for the HER process. The catalyst layer is obtained by spin casting a 3.8 mg mL^{-1} water: acetone: NaOH (1M) 1:2:0.2 dispersion on top of the TiO_2. The dispersion is stirred overnight at room temperature and sonicated for 10 minutes before its use. The spinning protocol is identical to the one adopted for the TiO_2 deposition.

5.5.1.2 Working Principles of MoS_2-based Organic Photocathode

Figure 5.1 shows the representative energy band edge positions of the semiconductors of the hybrid photocathode together with the redox levels of the HER and OER. MoS_2, as the HSL, is expected to extract the photogenerated holes towards the back conductive substrate (FTO) while the TiO_2 (as ESL) transports the photogenerated electrons towards MoS_3 (EC). Here, aqueous protons are reduced to H_2, which evolves from the photocathode surface.[394,406] In order to provide the electrical driving force for the holes' collection, MoS_2 films are doped by gold nanoparticles on top of them,[414] thus increasing the WF values of the films (see details in next section).

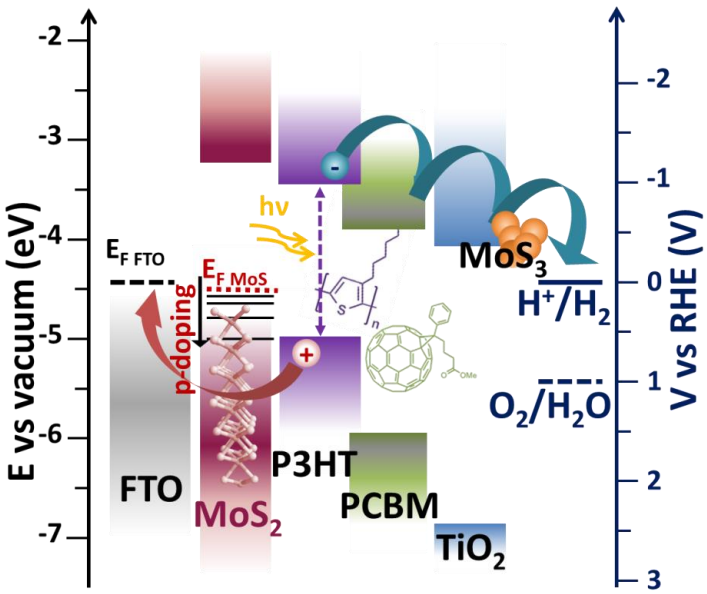

Figure 5.1. Typical energy band edge position of materials assembled in the hybrid solution-processed photocathode. The rr-P3HT:PCBM layer, in BHJ configuration, efficiently absorbs light and generates charges. MoS_2 and TiO_2 act as hole- and electron- selective layers (HSL and ESL), respectively, driving the holes towards the FTO substrates and the electrons towards the MoS_3 nanoparticles, acting as the EC layer for the HER. Redox levels of both the hydrogen evolution reaction (HER) (blue solid line) and oxygen evolution reaction (OER) (blue dashed line) are also shown.

5.5.1.3 Characterization of MoS_2-based Organic Photocathode:

The effects on the surface morphology of the FTO after the MoS_2 flake deposition are microscopically investigated by AFM. Figure 5.2a reports the AFM image of the bare FTO, while Figure 5.2b shows one of the FTO/MoS_2. FTO/MoS_2 shows nano-step height modulations on the grained FTO (grain size >100 nm).[415] Representative height profiles of the AFM images are reported in Figure 5.2c and d for FTO and FTO/MoS_2, respectively. For the case of FTO/MoS_2, the edge steps of the zoomed height profile (as defined by the blue dashed rectangle) are in the 1–1.5 nm range, in agreement with the flake thickness (2.3 ± 1.6 nm) measured by AFM (Figure 3-21 f).

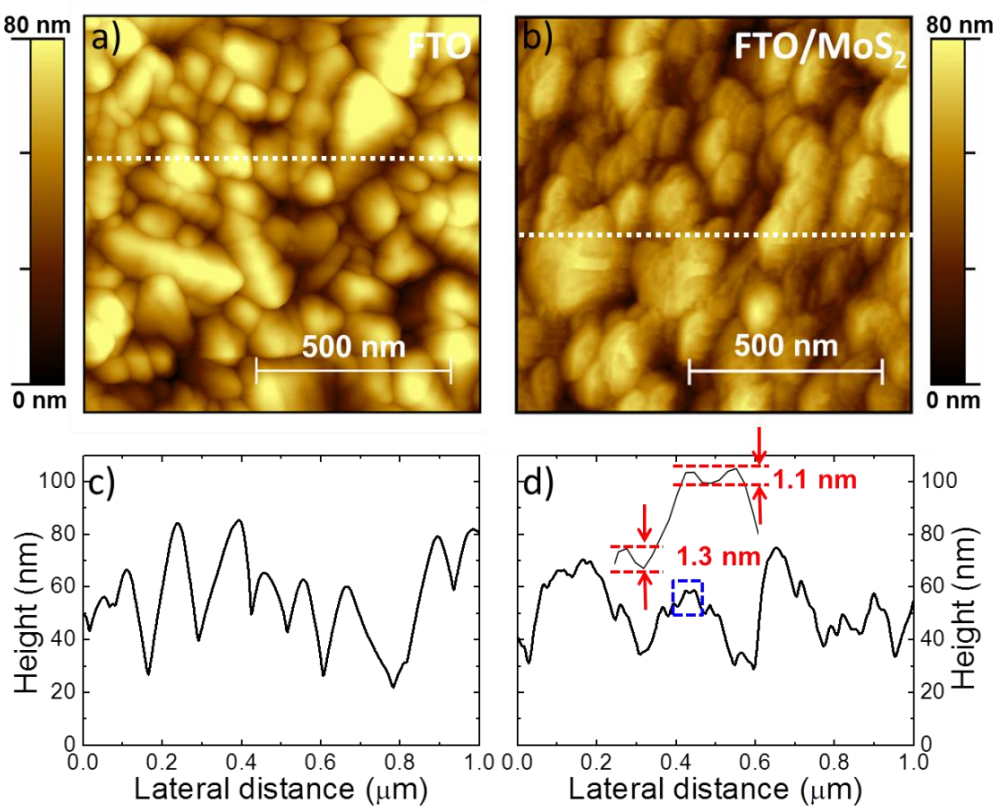

Figure 5.2. a) AFM images of FTO and b) FTO/MoS_2. The MoS_2 films are deposited from a 0.1 mg mL^{-1} MoS_2 dispersion in IPA. Representative height profiles of c) FTO and d) FTO/MoS_2 (the corresponding profile positions are shown by the dashed lines in a) and b), respectively). In d), the zoom of the height profile defined by the blue dashed rectangle, showing nano-edge steps, is reported.

MoS_2 flakes deposited onto FTO, are subsequently doped by spin coating $HAuCl_4$ methanol solution on top of the flakes themselves. The doping process is a consequence of the positive reduction potential of the $HAuCl_4$, which is then prone to accept electrons from MoS_2 carrying out the reduction of Au^{3+} to Au^0 species.[414] As a consequence, the electrical properties of the MoS_2 film, *i.e.*, the conductivity and the WF value, are significantly affected. The doping level is modulated by varying the concentration of $HAuCl_4$ solutions. Values of concentration of 5, 10, and 20 mM are investigated, giving the MoS_2-based films here named as p-MoS_2 (5 mM), p-MoS_2 (10 mM) and p-MoS_2 (20 mM), respectively. The WF value of MoS_2, (Table 5.1), is 4.6 eV, thus similar to the one measured for FTO (4.7 eV). After doping, the WF values of the p-MoS_2 (5 mM) (4.9 eV) and p-MoS_2 (10 mM) (5.1 eV) increase by 0.3 and 0.5 eV, respectively, compared to the one shown by the pristine MoS_2 film. Further increase of the doping level up to 20 mM does not reflect an additional rise of the WF value.

Table 5.1. WF values of FTO, MoS_2 and p-MoS_2 (5, 10, 20 Mm)

Material	Work function (eV)
FTO	**4.7**
MoS_2	**4.6**
p-MoS_2 (5 mM)	**4.9**
p-MoS_2 (10 mM)	**5.1**
p-MoS_2 (20 mM)	**5.1**

Figure 5.3 reports the AFM images of the FTO/p-MoS_2 (10 mM), which shows no differences in surface morphology with respect to the un-doped case (FTO/MoS_2). The roughness average (R_a) values are reported in Table 5-2, showing a decrease of about 2 nm for both FTO/MoS_2 and FTO/p-MoS_2 (10 mM) (R_a values of 11.6 nm and 11.9 nm, respectively) if compared with the value of the bare FTO (R_a=13.8). Thus, the FTO roughness is reduced by the overlayer of MoS_2 flakes, which could be linked with their planarity and face-on arrangement.

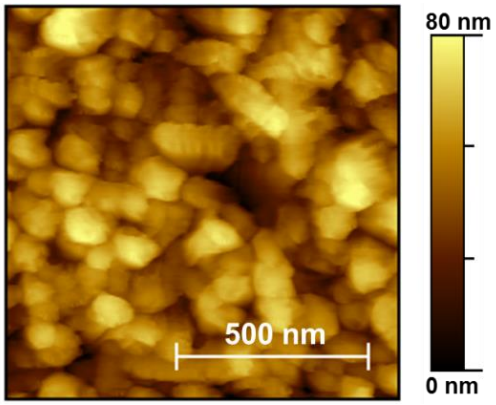

Figure 5.3. AFM images of FTO/p-MoS_2 (10 mM). The MoS_2 films are deposited from a 0.1 mg mL^{-1} MoS_2 dispersion in IPA. The calculated R_a is 11.9 nm.

Figure 5.4 reports the top SEM images of the FTO, FTO/MoS_2, FTO/p-MoS_2 (10 mM) and FTO/p-MoS_2 (20 mM) samples. No modifications of the FTO surface are observed after the MoS_2 flake deposition and doping treatment, i.e., 10 mM $HAuCl_4.3H_2O$, in agreement with the AFM data, *i.e.*, R_a values reported in Table 5.2. The increase of the doping level to 20 mM $HAuCl_4.3H_2O$ determines the formation of some aggregates, thus affecting the surface's homogeneity, as revealed by Figure 5.4d. These aggregates are attributed to the precipitation of Au and MoO_3 clusters after Au ion reduction and Mo(IV) to Mo(VI) conversion processes.[416] In fact, for the doping level exceeding 10 mM, more electrons are needed to reduce the increased number of Au

ions, and thus Mo(IV) can be converted into Mo(VI), resulting in the formation of Au nanoparticles and MoO_3.[414,416]

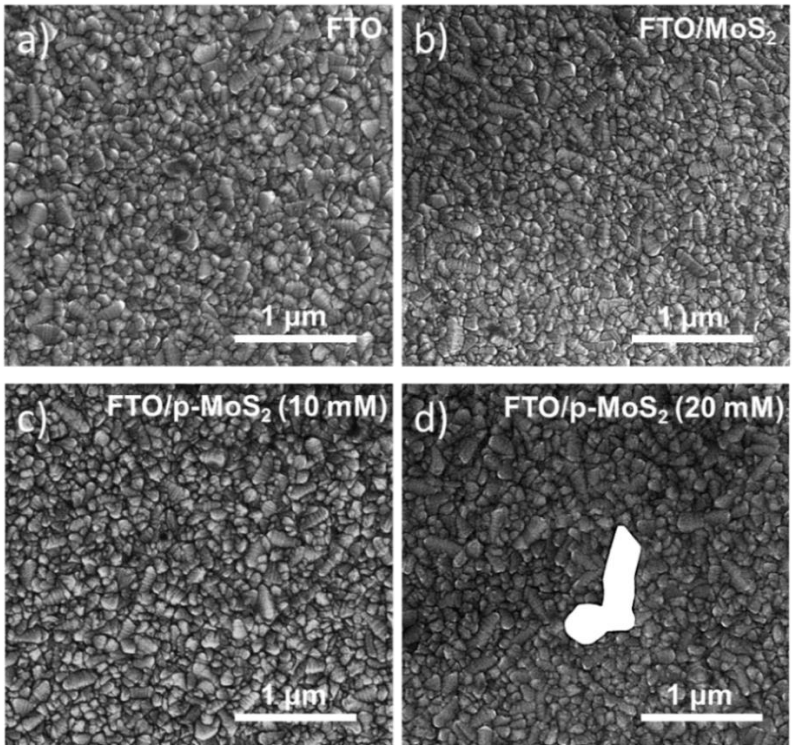

Figure 5-4 . Top view SEM images of the a) bare FTO, and b) FTO/MoS_2, c) FTO/p-MoS_2 (10 mM) and d) FTO/p-MoS_2 (20 mM) films. The MoS_2- based films are deposited from a 0.1 mg mL^{-1} MoS_2 dispersion in IPA.

Table 5.2. Roughness average (R_a) values of the FTO, FTO/MoS_2 and FTO/p-MoS_2 (10 mM). The MoS_2 films are deposited from a 0.1 mg mL^{-1} MoS_2 dispersion in IPA.

Sample	**R_a (nm)**
FTO	**13.8**
FTO/MoS_2	**11.6**
FTO/ p-MoS_2 (10 mM)	**11.9**

5.5.1.4 Photoelectrochemical Characterization:

The photocathodes are characterized by LSV in H_2SO_4 solution at pH=1. The results for MoS_2 and p-MoS_2 (10 mM) deposited from 0.1 mg mL^{-1} MoS_2 dispersion in IPA are reported in Figure 5.5a, where they are compared with the responses of a HSL-free photocathode and the current-potential curve of the MoS_3 EC (deposited directly onto FTO).

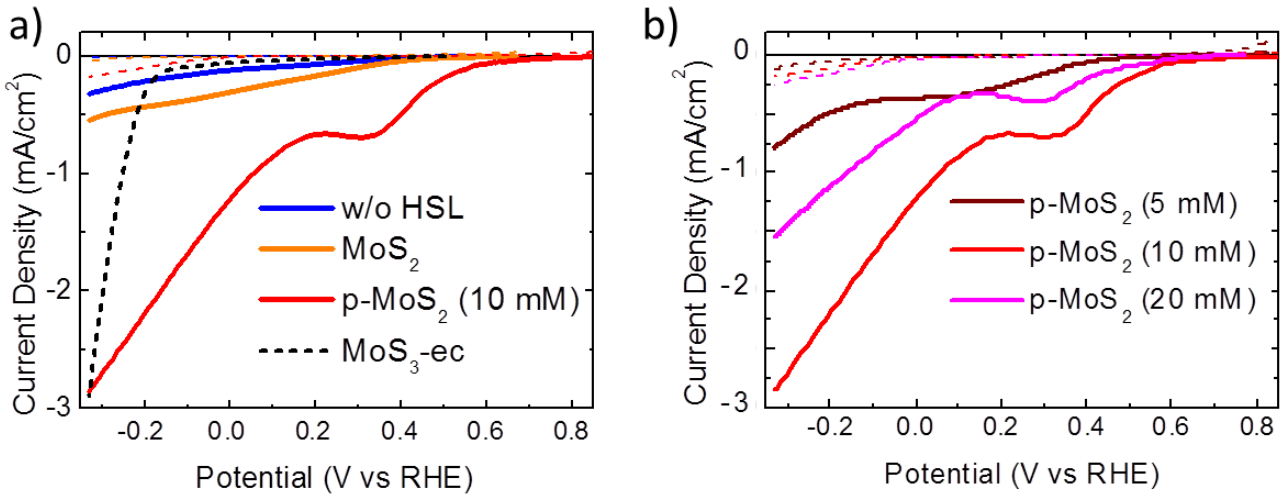

Figure 5.5. a) LSVs recorded for the photocathodes using MoS_2 (orange lines) and p-MoS_2 (10 mM) (red lines) as HSLs measured in 0.5M H_2SO_4 solution at pH=1, under dark (dashed lines) and AM 1.5 light illumination (100 mW cm^{-2}) (solid lines) MoS_2 films are deposited by 0.1 mg mL^{-1} MoS_2 dispersion in IPA. The photoelectrochemical responses of the photocathode without any HSL (blue lines) and the current–potential curve of the MoS_3 electrocatalyst (deposited directly on FTO) (short dashed black line) are also shown. b) LSVs recorded for p-MoS_2-based photocathodes obtained with different levels of doping (purple, red and magenta lines for 5, 10 and 20 mM $HAuCl_4.3H_2O$ methanol solution, respectively), under the same previous conditions.

The MoS_3 EC reveals activity for the HER, with an onset over potential of 180 mV with respect to the RHE potential.[417] The voltammograms of the photocathodes show a photocurrent that increases when the potential is swept towards negative values. The photocurrents are positively affected by the presence of MoS_2 films, thus confirming their role as the HSL. The dependence on the doping level of the p-MoS_2-based photocathodes is shown in Figure 5.5b.

Although the value of the main FoM of the undoped MoS_2- based photocathode ($J_{0\ V\ vs.\ RHE}$ = 0.3 mA cm^{-2}, V_{oc} = 0.3 V vs. RHE, $\Phi_{saved,NPAC}$ = 0.070%) increases with respect to the ones of the HSL-free photocathode ($J_{0\ V\ vs.\ RHE}$ = 0.12 mA cm^{-2}, V_o = 0.07 V vs. RHE, $\Phi_{saved,NPAC}$ = 0.015%), significant photocurrents are observed only using p-MoS_2 (above 1 mA cm^{-2} for potential <0.06 V vs. RHE for a doping level of 10 mM). For p-MoS_2 (10 mM) and p-MoS_2 (20 mM), the presence of a photoreduction peak, located at ~0.33 V vs. RHE, is also observed. Its origin is attributed to the chemical reduction of the MoS_3 EC towards more electrocatalytically active MoS_{2+x} species for the HER.[418]

Table 5.3. FoMs of photocathodes fabricated without the HSL and with MoS_2 and p-MoS_2 (5, 10 and 20 mM) as HSL: the current density taken at 0 V vs. RHE ($J_{0\ V\ vs.\ RHE}$), the onset potential (V_o), defined as the potential at which a photocurrent density of 0.1 mA cm^{-2} is reached, and the power-saved FoM $Ø_{saved,NPAC}$

HSL	$J_{0\ V\ vs.\ RHE}$ (mA cm^{-2})	V_o (V vs. RHE)	$Φ_{saved,NPAC}$ (%)
-	0.12	0.07	0.015
MoS_2	0.30	0.30	0.070
p-MoS_2 (5 mM)	0.36	0.35	0.095
p-MoS_2 (10 mM)	1.21	0.55	0.423
p-MoS_2 (20 mM)	0.54	0.49	0.192

In the case of p-MoS_2 (10 mM), $J_{0\ V\ vs.\ RHE}$, V_o and $Φ_{saved,NPAC}$ are 1.21 mA cm^{-2}, 0.56 V vs. RHE and 0.423%, respectively. Photocathodes based on p-MoS_2 (20 mM) (highest doping level) and p-MoS_2 (5 mM) (lowest doping level) report $J_{0\ V\ vs.\ RHE}$ of 0.54 and 0.36, thus decreasing by 56% and 70% with respect to the case of p-MoS_2 (10 mM), respectively. Concerning p-MoS_2 (5 mM), also in this case there is a decrease of the V_o (V_o = 0.35 V *vs*. RHE) of 200 mV with respect to the values observed for p-MoS_2 (10 mM). Moreover, we noted a decrease of 60 mV of the V_o for the p-MoS_2 (20 mM) if compared with the p-MoS_2 (10 mM) photocathode. The values of $Φ_{saved,NPAC}$ calculated for p-MoS_2 (5 mM) and p-MoS_2 (20 mM) are 0.095% and 0.192%, respectively. These values correspond to a decrease of 77.5% and 54.6% with respect to that of p-MoS_2 (10 mM), respectively. The obtained results highlight the importance of the WF tuning of the MoS_2 films by p-doping treatment for their full exploitation as highly performant HSLs. Figure 5.6 shows the MoS_2 doping level dependence of the photocathodes' FoM, as gathered from Table 5.3. In agreement with the SEM characterization reported in Figure 5.4d, the decrease of the $J_{0\ V\ vs.\ RHE}$ for the p-MoS_2 (20 mM) case could be ascribed to charge recombination pathways, i.e., leakage currents, in the presence of blend-uncovered Au and MoO_3 clusters. Although these surface alterations of the MoS_2 films negatively affect the photocurrents, the V_o value is similar to the one recorded for p-MoS_2 (10 mM). Differently, for the case of p-MoS_2 (5 mM), we observed a decrease of both the $J_{0\ V\ vs.\ RHE}$ and the V_o with respect to the p-MoS_2 (10 mM) case.

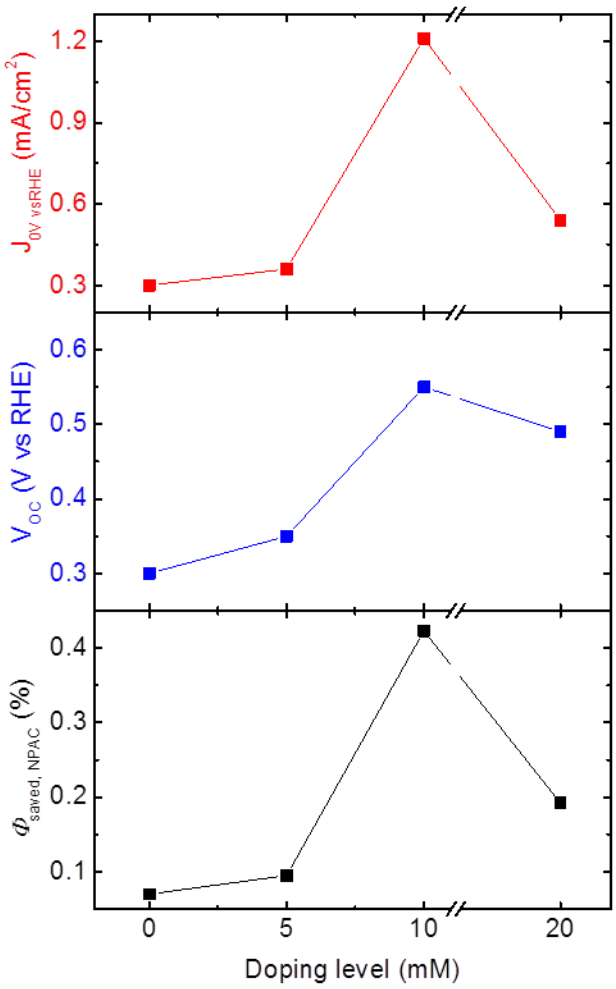

Figure 5.6. Dependence of the photocatodes' FoMs (red, blue and black colours for $J_{0\ V\ vs.\ RHE}$, V_o and $\Phi_{saved,NPAC}$, respectively) on the $HAuCl_4$ doping level (from 0 to 20 mM) of the p-MoS_2 films.

This result could be linked with differences (homogeneity) of the MoS_2 film doping, as suggested by the lower WF value of p-MoS_2 (5 mM) film (4.9 eV) if compared with the ones of p-MoS_2 (10 mM) and p-MoS_2 (20 mM) films (5.1 eV). As a consequence, the main characteristics of the p-MoS_2 (5 mM)-based photocathode (V_o ~ 0.35 V vs. RHE, $J_{0\ V\ vs.\ RHE}$ ~ 0.36 mA cm^{-1} and $\Phi_{saved,NPAC}$ ~ 0.095) are similar to those recorded for the undoped MoS_2-based photocathode (V_o ~ 0.30 V vs. RHE, $J_{0\ V\ vs.\ RHE}$ ~ 0.30 mA cm^{-1} and $\emptyset_{saved,NPAC}$ ~ 0.070). To sum up, V_o seems to be linearly correlated with the WF values of the different films, while the $J_{0\ V\ vs.\ RHE}$ turns out also to be affected by the film surface morphology. The combination of these effects explain the behaviour of the $\Phi_{saved,NPAC}$, whose best value of 0.423% is reached for the p-MoS_2 (10 mM)-based photocathode. The stability test under potentiostatic conditions is performed for p-MoS_2 (10 mM) case, recording in time the $J_{0\ V\ vs.\ RHE}$ under continuous illumination (Figure 5.7). The data show an average initial photocurrent value of 1.36 mA cm^{-2} followed by a steep decrease in performance down to 0.77 mA cm^{-2} during the first 5

minutes (photocurrent loss of 50.7%). After 30 minutes of continuous operation, the photocurrent density reaches 0.49 mA cm^{-2} (photocurrent loss of 63.2%). Thus, the photocurrent mainly decreases at the beginning of the illumination process. The quick, initial performance degradation being attributed to the irreversible MoS_3 detachment from the surface of the electrodes.[Error! Bookmark not defined.] After more than 5 min, a progressive stabilization is observed. Notably, there is no delamination of the film during the measurements, suggesting the electrochemical stability of the FTO/p-MoS_2/ P3HT:PCBM under-layers.

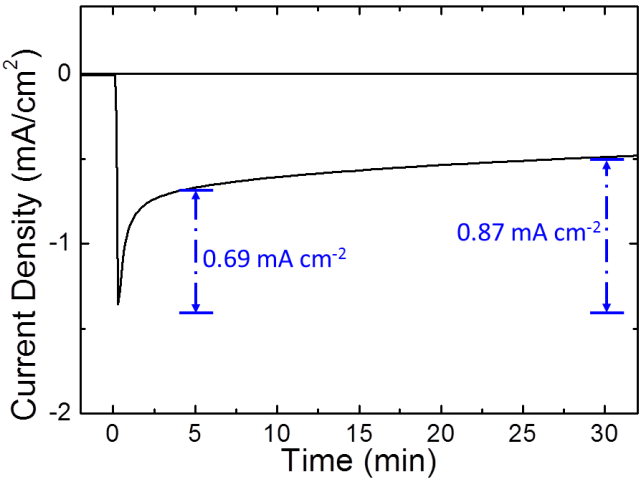

Figure 5.7. Potentiostatic stability test of the photocathode fabricated with p-MoS2 (10 mM) at pH 1 and 0 V vs. RHE under continuous illumination (1 sun). The blue lines mark the losses of the photocurrent after 5 and 30 min.

5.5.2 Graphene-Based HSL for High-Efficiency and Flexible, H_2-Evolving Organic Photocathodes:

This section reports the use of solution-processed graphene derivatives as HSL to boost efficiency and durability of rr-P3HT:PCBM-based photocathodes. To increase the efficiency and the durability of the photocathodes, two different strategies are used. The first one relies on the fabrication of hydrogen-bonded FTO/graphene-based HSL/rr-P3HT:PCBM structures through the chemical functionalization of GO/RGO (compounds here named as f-GO and f-RGO, respectively), with MPTMS in an ethanol solution. The second one is the implementation of solution-processed conductive and catalytic Pt on carbon-tetrafluoroethylene-perfluoro-3,6-dioxa-4-methyl-7-octenesulfonic acid copolymer blend (Pt/C-Nafion) overlay. The optimization of the proposed architectures allowed to achieve a record-high efficiency for solution-processed rr-P3HT:PCBM-based photocathodes, extending their operational activity up to 20 h. Moreover, the designed photocathodes are effectively working in different pH environments ranging from acid to basic.

This is pivotal for their exploitation in tandem configurations, where photoanodes operate only in restricted electrochemical conditions.

5.5.2.1 Architecture of Graphene Derivative-based Organic Photocathodes

Photocathodes are fabricated according to the architecture FTO/HSL/rr-P3HT:PCBM/TiO_2/Pt, where GO, RGO, f-GO and f-RGO films are used as HSL. Architectures without HSL are also fabricated. FTO coated soda-lime glass substrates (area 1×1.5 cm^2, sheet resistance 15 Ω/□, Dyesol) are cleaned according to the protocols which already explained in 5.4.1.1 section.

Graphene oxide, RGO, f-GO and f-RGO are dispersed in ethanol by sonication at different concentration (0.5, 1 and 1.5 mg mL^{-1}) and deposited onto the previously treated FTO by spin coating ((WS-650Mz-23NPPB Laurell Tech. Corp. Spin coater) using a single step spinning protocol with rotation speed of 2000 rpm for 60 s. Post thermal annealing in Ar atmosphere at 150 °C for 10 min. is performed for the GO and RGO films. The organic polymer film used in all the architectures consisted in a blend of rr-P3HT, as the donor component, and PCBM, as the acceptor component (rr-P3HT:PCBM). rr-P3HT (electronic grade, Mn 15000-45000, 99.995% trace metals basis, Sigma Aldrich) and PCBM (>99.5%, Nano C) are separately dissolved in chlorobenzene (ACS grade, 99.8%, Sigma Aldrich), at a weigth ratio 1:1 and 25 mg mL^{-1} on a polymer basis. Polymer blend solution is stirred at 40 °C for 24 h before use. Blend thin films are obtained by spin coating the rr-P3HT:PCBM solution using the following set of parameters: two step spinning protocol with rotation speeds of 800 rpm for 3 s followed by 1600 rpm for 60 s, respectively. This spin coating protocol produced a rr-P3HT:PCBM blend layer of 200 ±20 nm thick, as measured with a Dektak XT profilometer (Bruker) equipped with a diamond-tipped stylus (2 mm) selecting a vertical scan range of 25 mm with 8 nm resolution and a stylus force of 1 mN, on an area of 0.25 cm^2. TiO_2 paste (Ti-Nanoxide T-L/SC formulation, anatase particle size 15-20 nm, 3% wt, Solaronix) is deposited on top of rr:P3HT:PCBM by spin casting. Before its deposition rr:P3HT:PCBM films are treated by oxygen plasma for 30 s (20 W RF power, excitation frequency 13.56 MHz, 40 Pa of O_2 gas process pressure, background gas pressure 0.2 Pa) in order to increase their wettability by the TiO_2 dispersion. A three step spinning protocol with rotational speeds of 200 rpm for 3 s, 1000 rpm for 60 s and 5000 rpm for 30 s is used. Subsequently, the samples are dried for 12 h in air at room temperature. Post thermal annealing in a N_2 atmosphere is performed at 130 °C for 10 min for all the devices before catalyst deposition. The devices are completed by the deposition of a layer of

Pt nanoparticles (>99.97% trace metals basis) (Sigma Aldrich) or Pt/C (20% Pt on Vulcan XC72, Sigma Aldrich) blended with Nafion (Nafion® 117 solution, 5% in a mixture of lower aliphatic alcohols and water, Sigma Aldrich) (Pt/C-Nafion) as catalyst for HER. The Pt catalyst layer is obtained by spin coating 1 mg mL^{-1} Pt nanoparticles dispersion in DI water on top of the TiO_2. The Pt/C-Nafion layer is deposited by spin coating 5 mg mL^{-1} Pt/C dispersion in DI water with the addition of 80 µL of Nafion dispersion. The dispersions are stirred overnight at room temperature and sonicated for 10 minutes before their use. Spinning protocols are identical to the one adopted for the TiO_2 deposition.

5.5.2.2 Working Principles of Graphene Derivative-based Organic Photocathodes

The full structure of a photocathode based on solution-processed organic semiconductors comprises a transparent conductive substrate /HSL/photo-active layer/ ESL/EC. The operations of HSL/ESL concern: 1) charge extraction, *i.e.,* the energy alignment between the conduction/valence bands of the HSL/ESL with respect of the highest occupied molecular orbital (HOMO)/LUMO levels of the organic active material, in order to create barrier-free potential and high-quality ohmic junctions that separate and inject the photogenerated charges; 2) charge selectivity, depending by the relative position of the HSL CB with respect to the LUMO of the PCBM and that of the ESL VB of the rr-P3HT HOMO (*i.e*., $CB_{HSL} > LUMO_{PCBM}$ and $VB_{ESL} < HOMO_{P3HT}$),in order to reduce electron and hole recombination, respectively; 3) optical transparency in the spectral range of absorption of the organic material, in order to avoid losses in the incident photonic flux; 4) surface smoothness, in order to improve the quality of the contacts with the active layer;[419,420,421] 5) photoelectrochemical stability in aqueous electrolytes in HER-working conditions.[**Error! Bookmark not defined.**,403] Here solution-processed graphene-derivatives, *i.e*., GO and RGO, are exploited as HSL candidates. Figure 5.8 shows the representative energy band edge positions of the photocathode materials together with the redox levels of the HER (-4.44 eV/0 V *vs*. vacuum level/HER) and OER (-5.67 eV/1.23 V *vs*. vacuum level/HER). The work function of GO (See Chapter 3) shows better alignment with the HOMO level of rr-P3HT (~5 eV) if compared with the one of RGO. However, the metal-like behavior of the RGO could, in principle, boost the holes transport towards the FTO.

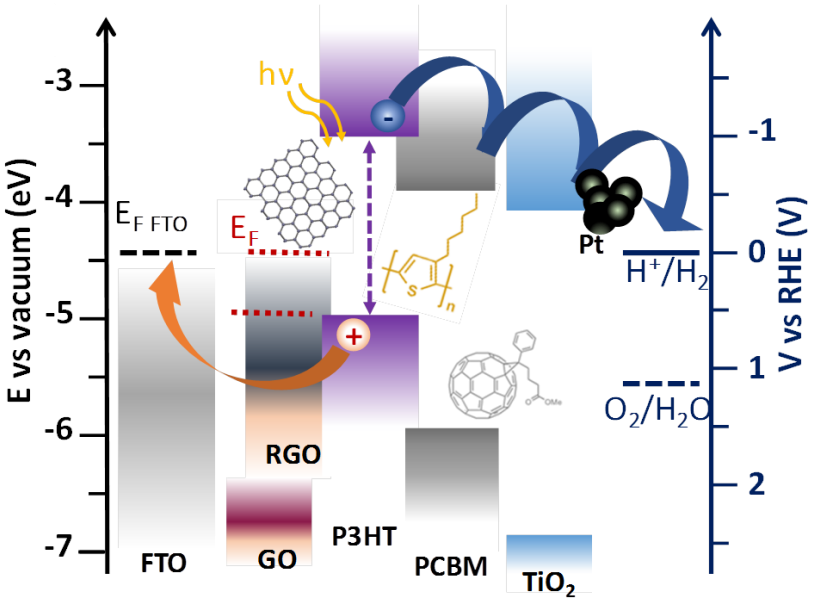

Figure 5.8. Scheme of the energy band edge position of the materials assembled in the solution-processed organic photocathode. The graphene-based layer and TiO_2 act as HSL and ESL, respectively, driving the holes towards the FTO substrates and the electrons towards the Pt nanoparticles, acting as EC layer for the HER process. Redox levels of both HER (blue solid line) and OER (blue dashed line) are shown.

5.5.2.3 Characterization of Graphene Derivative-based Organic Photocathode

Top-view SEM images of FTO/GO (Figure 5.10a and Figure 5.10b) and FTO/RGO (Figures 5.10c, d) films provide a detailed for characterization of the HSL surface topography. Clearly, FTO crystal grains, as evidenced by SEM image of pristine FTO (Figure 5.9) are visible on a sub-µm scale (Figures 5.10a,c), indicating that no significant changes of the substrate surface occur after the GO and RGO deposition. Brighter regions, delimitated by red dashed lines, could be attributed to areas with low GO and RGO coverage. However, low-magnification SEM images (Figures 5.10b,d) evidence the presence of flakes aggregates. On the other hand, for the case of RGO the substrate topography is clearly altered by the inhomogeneous film properties of the RGO (Figure 5-10d), which have been previously observed in rr-P3HT:PCBM based OSCs.[422,423] In order to confirm that atomic-thick HSLs effectively cover the FTO substrates, EDX analysis is performed on FTO/GO (Figures 5.10e-h) and on FTO/RGO (Figures 5.10i-n). Carbon atoms in the mass spectrum of Figures 5.10f,l are unambiguously attributed to the GO and RGO, and the C mapping in Figures 5-10g,m shows the homogeneity of C content onto the surface of FTO, identified by the Sn mapping (Figures 5.10h,n). In the case of RGO, an area with higher C content (delimited by dashed red line in Figure 5.10m) is ascribed to the presence of flakes aggregates, as evidenced by red dashed line in Figure 5.10i. The aggregation of RGO flakes is attributed to the low dispersibility of RGO in polar solvents, such as ethanol used here. This is a consequence of the limited content of oxygen

functionalities (%c of C-O 6.9%) (see previous XPS analysis in Chapter 3, Figure 3.10), *i.e.*, loss of surface polarity, which determine a hydrophobic behavior.[424,425] Thus, while GO dispersions are stable, we observed sedimentation of RGO dispersion as consequence of the poor hydrogen-bonding capability of the flakes.

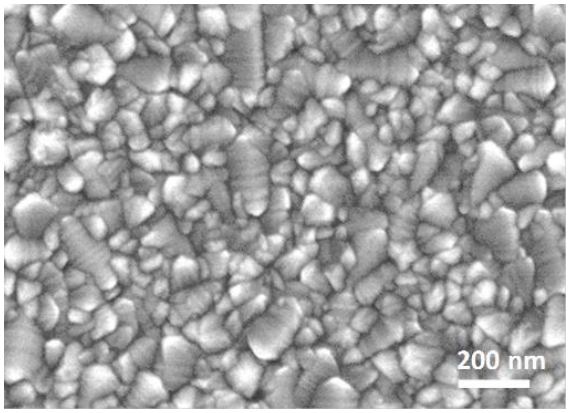

Figure 5.9. SEM images of FTO substrate

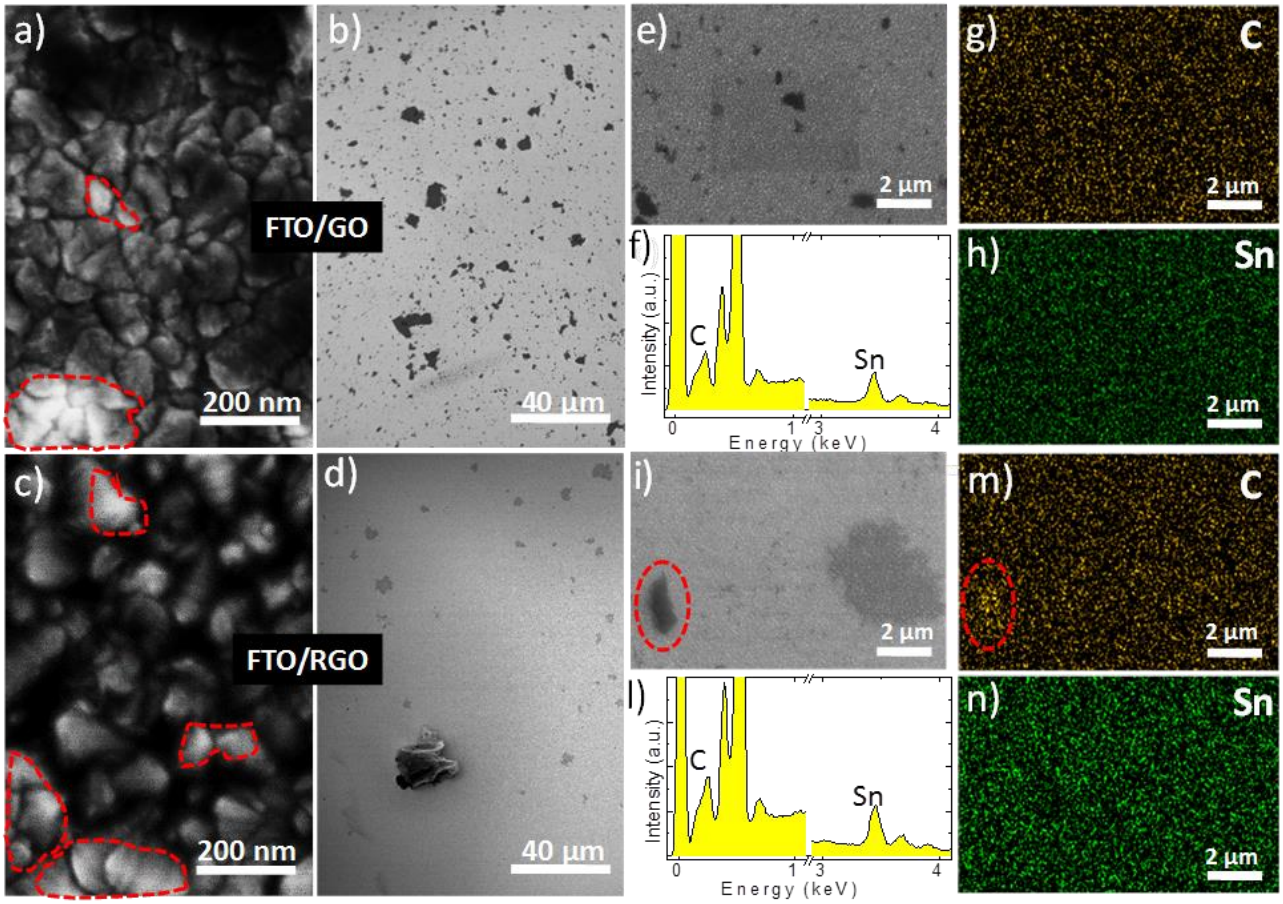

Figure 5.10. Top-view SEM images of a-b) GO and c-d) RGO film deposited on top of the FTO substrate from 1 mg mL^{-1} ethanol dispersion. In a) and c) the bar scale is 200 nm, while b) and d) show a larger area (bar scale is 40 µm). e) Top-view SEM images of FTO/GO, on which elemental EDX analysis is performed. f) EDX spectrum of FTO/GO. g) C and h) Sn mapping corresponding to the EDX analysis of FTO/GO. i) Top-view SEM images of FTO/RGO, on which elemental

EDX analysis is performed. l) EDX spectrum of FTO/RGO. m) C and n) Sn mapping corresponding to the EDX analysis of FTO/RGO. The areas delimitated by red dashed lines in a) and c)) indicate regions with lower level of GO and RGO coverage, respectively. The area delimitated by red dashed lines in i) and m) evidences the abundance of C due to the presence of GO and RGO flakes' aggregate.

EDX analysis of FTO/f-GO and FTO/f-RGO (Figure 5.11) indicates that C and Si atoms, which are attributed to the f-GO and f-RGO flakes, are homogeneously distributed over the FTO, as already shown for GO and RGO layers (Figure 5.10). It is worth noting that, while RGO deposition determined the formation of large aggregates (Figure 5.10d), the deposition of f-RGO is not altering the characteristic morphology of the FTO (FTO grains are still visible on the high-magnification image (Figure 5.11b). This is a consequence of the improved dispersion in ethanol in presence of MPTMS groups, which decreases the surface energy of RGO (~46.1 mN/m in ethanol) and enhance its compatibility with polar solvents such as ethanol, increasing the dispersion stability, and avoiding the flakes aggregation during film deposition.

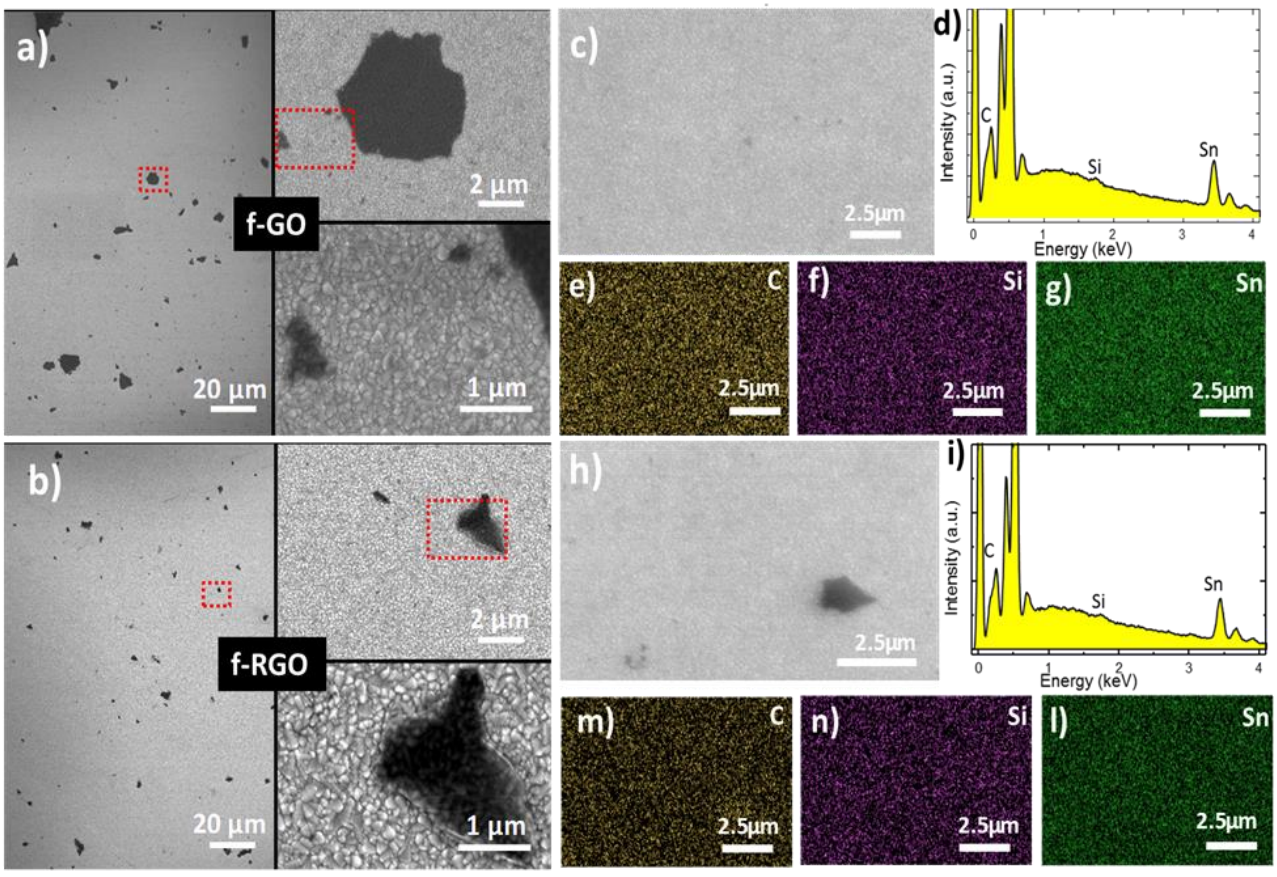

Figure 5.11. a) Top-view SEM images of f-GO layer deposited atop the FTO substrate from a 1 mg mL^{-1} ethanol solution. Three panels show images with different magnification (20 µm, 2 µm and 1 µm bar scales) b) Top-view SEM images of f-RGO layer deposited on top of the FTO substrate from a 1 mg mL^{-1} ethanol solution. Three panels show images with different magnification (20 µm, 2 µm and 1 µm bar scales). The areas delimitated by red dashed lines indicate regions shown by images with higher magnification.c) Top-view SEM image (SEI) of FTO/f-GO, where elemental EDX analysis is performed. d) Mass spectrum of the EDX analysis. e) C, f) Si and g) Sn mapping obtained

from the EDX analysis of FTO/f-GO. h) Top-view SEM image (SEI) of FTO/f-RGO, where elemental EDX analysis is performed. i) Mass spectrum of the EDX analysis. m) C, n) Si and l) Sn mapping resulted from the EDX analysis of FTO/f-RGO.

Top-view SEM images of a representative photocathode are shown in Figure 5.12. The images evidence the presence of spherically shaped aggregates with a diameter <50 nm. Elemental EDX analysis (Figures 5.12c-g) is carried out in order to clarify the aggregates composition and the uniformity of the Pt/C-Nafion overlay. The C mapping reported in Figure 5.12e indicates that the observed aggregates are attributed to C nanoparticles, while Pt and Nafion, which are identified by the elemental mapping of Pt (Figure 5.12f) and F (Figure 5.12g) atoms, are homogeneously distributed over the TiO_2 layer.

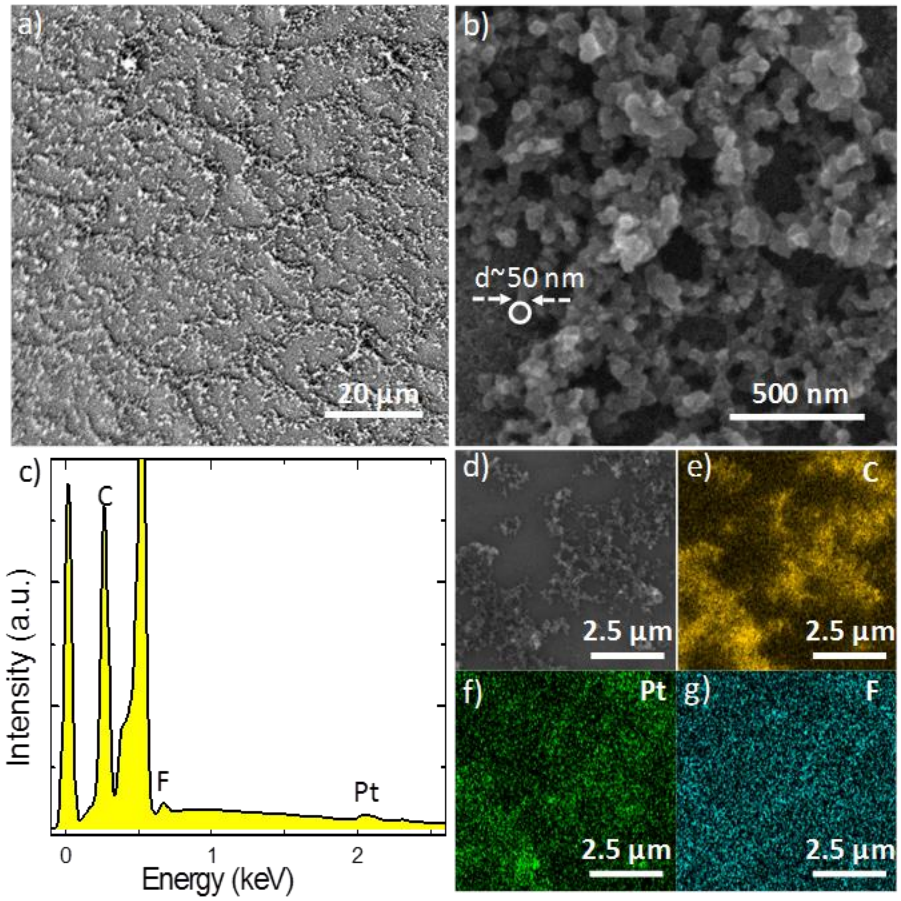

Figure 5.12. a) Top-view SEM image (SEI) of a Pt/C-Nafion layer covering a representative photocathode. b) Magnified SEM image (SEI) of panel a). c) Mass spectrum obtained by the EDX analysis of the images area shown in panel d). e) C, f) Pt and g) F mapping corresponding to the mass spectrum of panel c).

Figure 5.13 shows top-view SEM images of GO-Pt/C-Nafion photocathode before (Figure 5.13a) and after its immersion in the electrolyte at pH 10 (see Figure 5.13b), and after 20 h of operation at 0 V *vs*. RHE and continuous AM1.5 illumination condition (Figure 5.13c) (see electrochemical

measurements in the next section). After contact with the electrolyte, a clear redistribution of the Pt/C network onto the TiO_2 surface is evidenced by the formation of Pt/C aggregates with larger dimensions (Figure 5.13b), if compared with the pristine ones (Figure 5.13a). After 20-h operation the surface is clearly damaged and Pt/C network is not present anymore (Figure 5.13c). These effects could proceed via a Pt dissolution/re-deposition mechanism or 3D Ostwald ripening[426] of the Pt/C-Nafion, because of both C[427] and Pt [428]corrosion. The latter changes the adhesion of the Pt/C-Nafion overlay. After the detachment/dissolution of the Pt/C-Nafion overlay,[427] the underlying structure remains unprotected, and the hydrogen bubbling during HER causes a progressive "craterisation" of the surface. All these effects are evidenced in Figure 5.14, especially the "craterisation" and the consequent exposure of the FTO substrate to the electrolyte.

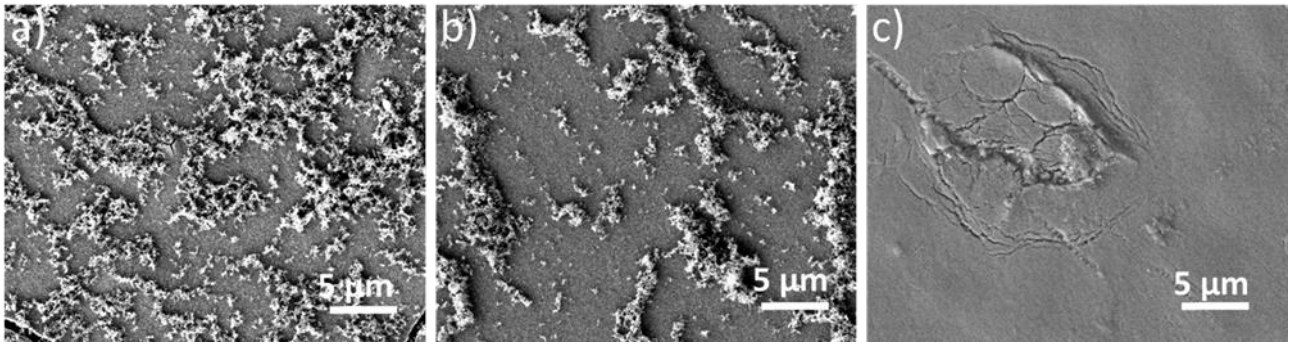

Figure 5.13. Top-view SEM images of the GO+Pt/C-Nafion a) immediately after its fabrication, b) after its immersion in the aqueous solution at pH 10 and c) after 20 hours of operation at 0 V vs. RHE and continuous AM1.5 illumination in the same aqueous solution at pH 10.

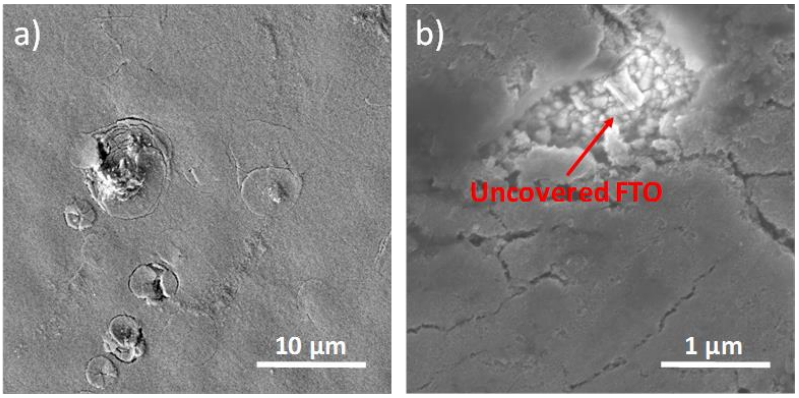

Figure 5.14. a) Top-view SEM images of the GO+Pt/C-Nafion after 20 hours of operation at 0 V vs. RHE and continuous AM1.5 illumination at pH 10. b) Top-view SEM images of the same photocathode focusing on a damaged area, where delamination/disruption of the device's structure is evidenced by the presence of uncovered regions of FTO.

5.5.2.4 Photoelectrochemical Characterization

The rr-P3HT:PCBM-based photocathodes based on GO and RGO as HSLs, TiO_2 as ESL, and Pt nanoparticles as EC are characterized by LSV in H_2SO_4 solution at pH 1. Acidic conditions are initially chosen because HER kinetics on Pt are faster in acids than in neutral and alkaline electrolytes.[429,430] LSVs of representative photocathodes based on GO and RGO deposited from dispersions at different concentration (0.5, 1 and 1.5 mg mL^{-1}) are reported in Figure 5.15. These results show that the best photoelectrochemical performances are obtained for the dispersion at 1 mg mL^{-1} for GO and 0.5 mg mL^{-1} for RGO.

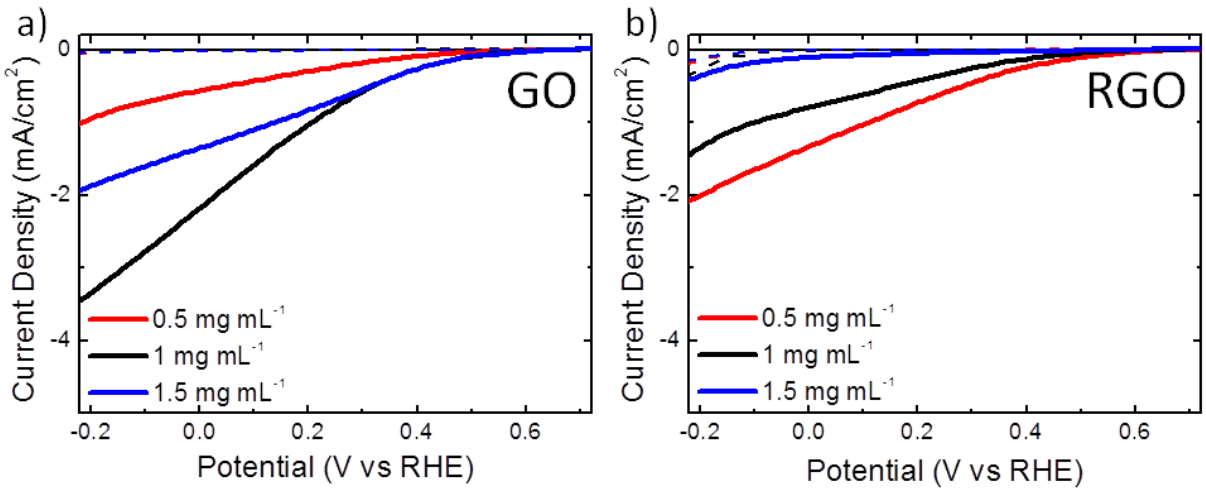

Figure 5.15. LSVs measured for the photocathodes using a) GO and b) RGO as HSLs deposited from dispersions in ethanol at different concentration: 0.5, 1 and 1.5 mg mL^{-1} (red, black and blue lines, respectively), measured in 0.5 M H_2SO_4 solution (pH 1), under dark (dashed lines) and AM1.5 illumination (100 mW cm^{-2}) (solid lines).

The results obtained for representative photocathodes based on GO and RGO, as deposited from 1 and 0.5 mg mL^{-1} dispersion in ethanol, respectively, are reported in Figure 5.16a. Their corresponding LSVs are compared with those of a HSL-free photocathode and the current-potential curve of Pt nanoparticles (*i.e.*, the EC) deposited directly onto FTO. The LSVs of the photocathodes show a photocurrent that increases as the potential decreases. The photocurrents are positively affected by the presence of GO and RGO films, which are thus confirming their role of HSLs. The FoM of the photocathodes are J_{0V} vs RHE = -2.16 mA cm^{-2}, V_o = 0.56 V vs. RHE, $\Phi_{saved,NPA,C}$ = 0.29%, $\Phi_{saved,ideal}$ = 0.21% for GO and J_{0V} vs RHE = -1.33 mA cm^{-2}, V_o = 0.50 V vs. RHE, $\Phi_{saved,NPA,C}$ = 0.18%, $\Phi_{saved,ideal}$ = 0.15% for RGO. The better performances obtained by using GO with respect those recorded by using RGO are linked with the excellent GO WF match (~4.9 eV) with the HOMO level of rr-P3HTm (~5 eV),[431] while the lower WF of RGO (~4.4 eV) could lead to a rectifying (i.e., Schottky barrier)[432] FTO/rr-P3HT contact for the hole extraction .[433]

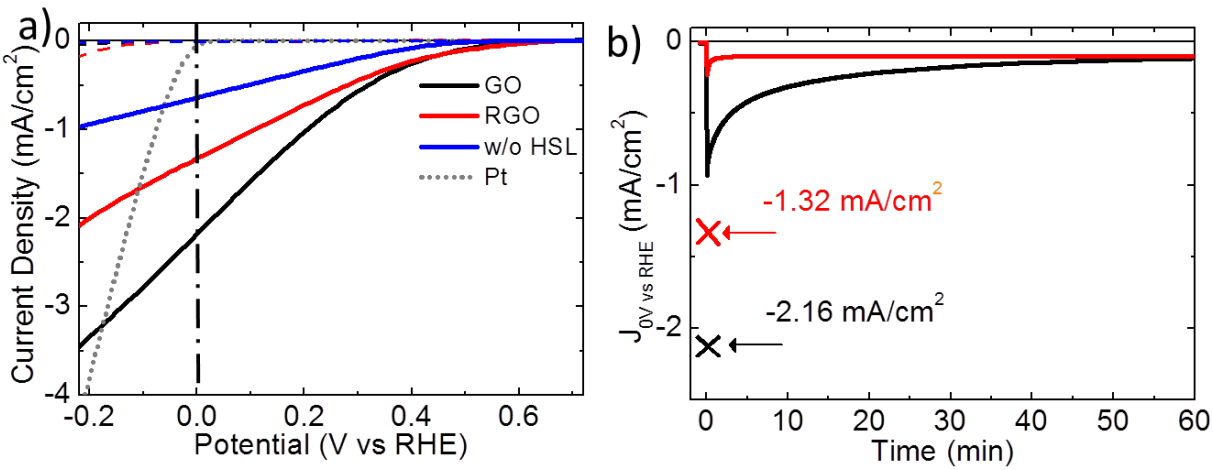

Figure 5.16. a) The LSVs measured for the photocathodes using GO (black lines) and RGO (red lines) as HSLs measured in 0.5 M H_2SO_4 solution (pH 1), under dark (dashed lines) and AM1.5 illumination (100 mW cm^{-2}) (solid lines). GO and RGO films are deposited from 1 mg mL^{-1} and 0.5 mg mL^{-1} dispersions in ethanol. The PEC responses of the photocathode without any HSL (blue lines) and the current-potential curve of Pt nanoparticles (EC) deposited directly onto FTO (short dashed grey line) are also shown. b) Potentiostatic stability tests of photocathodes using GO (black line) and RGO (red line), obtained by recording J0V vs RHE over 1 h of continuous AM1.5 illumination. The stability tests started after the measurement of the LSVs shown in panel a). The values recorded in the LSVs of panel a) are also indicated in panel b).

Furthermore, the inhomogeneity of the RGO layer, evidenced by SEM analysis, Figures 5.10d, also affects the quality of the RGO/rr-P3HT junctions, determining charge recombination pathways (*i.e.*, leakage currents) in presence of blend-uncovered flake aggregates.[433] In order to assess the stability of our photocathodes in HER-working conditions, we carried out potentiostatic stability tests. These are performed by recording J_{0V} vs RHE over 1 h continuous 1.5AM illumination and after recording the LSV shown in Figure 5.16a. The results, reported in Figure 5.16b, show a performance degradation of the photocathodes. In fact, after the first LSV (where J_{0V} vs RHE of -2.16 mA cm^{-2} and -1.32 mA cm^{-2} have been recorded for photocathodes using GO and RGO, respectively), J_{0V} vs RHE at t = 0 is -0.93 for GO-based device and -0.23 mA cm^{-2} for RGO-based one. No stabilization of the photocurrents towards constant values is observed, and after 1 h, J_{0V} vs RHE decreases of ~95% and ~93% for GO- and RGO-based devices, respectively, with respect to the corresponding J_{0V} vs RHE values in the LSV. The performances degradation can be caused by the detachment/dissolution of Pt from the TiO_2 surface, as previously reported for photocathodes in acid conditions.[434] The decrease of the photocurrents observed during the potentiostatic stability test pointed out the need to implement stabilizing strategies to improve the endurance of the as-prepared photoelectrodes. Moreover, delamination/disruption of the layered structure of the photocathodes is macroscopically observed by eye (Figure 5.17). These degradation effects are

attributed to the poor adhesion between the different layers of the FTO/GO (RGO)/rr-P3HT:PCBM structure after the immersion in the electrolyte.[435]

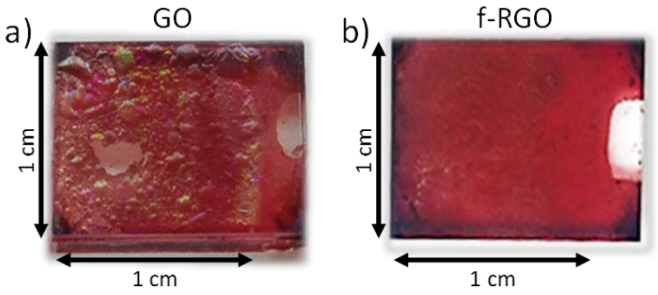

Figure 5.17. Photographs of a photocathode using a) GO and b) f-RGO as HSL after the potentiostatic stability test, obtained by recording J_{0V} vs RHE over 1 hour of continuous 1.5AM illumination

In order to overcome these problems, two different stabilizing strategies are designed, The first one relies on the fabrication of hydrogen-bonded FTO/graphene-based HSL/rr-P3HT:PCBM structures through the covalent linking between GO/RGO and a bi-functional silane compound, MPTMS.[436] The as-produced compounds (named f-GO and f-RGO, respectively) have silane groups anchored onto the f-GO and f-RGO flakes, while thiol groups (SH) are exposed to enhance the adhesion between adjacent layers of FTO/graphene-based HSL/rr-P3HT:PCBM structure. The second approach inhibits the electrochemical degradation of the electrode materials as well as the multi-layered structures delamination/disruption through the implementation of a solution-processed Pt/C-Nafion overlay. The procedure of the silane functionalization of GO and RGO as well as the formulation and the deposition of the Pt/C-Nafion overlay are reported in section 5.4.2.1 .

The LSVs in H_2SO_4 solution at pH 1 of representative photocathodes based on f-GO and f-RGO deposited from dispersions at different concentration (0.5, 1 and 1.5 mg mL^{-1}) are reported in (Figure 5.18), showing that the best photoelectrochemical performance for the dispersion at 0.5 mg mL^{-1} for f-GO and 1 mg mL^{-1} for f-RGO. The obtained values for the main FoM drastically decrease for the photocathodes based on f-GO (Figure 5-18a) ($J_{0V\ vs\ RHE}$ = -0.30 mA cm^{-2}, V_o = 0.23 V *vs*. RHE and $\Phi_{saved,ideal}$ = 0.03%) with respect to the ones based on GO ($J_{0V\ vs\ RHE}$ = -2.16 mA cm^{-2}, V_o = 0.50 V *vs*. RHE and $\Phi_{saved,ideal}$ = 0.21%). Different results are instead achieved with f-RGO (Figure 5-18b). In fact, a clear enhancement of the performance is observed for photocathodes based on f-RGO ($J_{0V\ vs\ RHE}$ = -1.82 mA cm^{-2}, V_o = 0.5 V *vs*. RHE and $\Phi_{saved,ideal}$ = 0.19%) if compared with RGO-based ones ($J_{0V\ vs\ RHE}$ = -1.33 mA cm^{-2}, V_o = 0.50 V *vs*. RHE and $\Phi_{saved,ideal}$ = 0.15%). The different

FoM values achieved by photocathodes based on the functionalized materials could be due to the different mechanism for the hole extraction of GO and f-GO with respect to that of RGO and f-RGO. [420,423,437] From the WF value and the level of the VB estimated by UPS measurements (Figures 3-15), GO and f-GO are insulators, being able to extract the charge carriers through a quantum mechanical tunneling process.[420,423,437] However, the presence of silane groups can alter the dipole formation between f-GO and rr-P3HT:PCBM,[438] thus varying the hole extraction processes.[439] Differently, RGO and f-RGO are metallic as deduced by UPS measurements (Figures 3.15) and can extract the charge carriers directly through the VB.[419,420,421] Here, the functionalization of the RGO flakes avoids the formation of aggregates, thus improving the quality of the contact between FTO/HTL and rr-P3HT.[419.420,439]

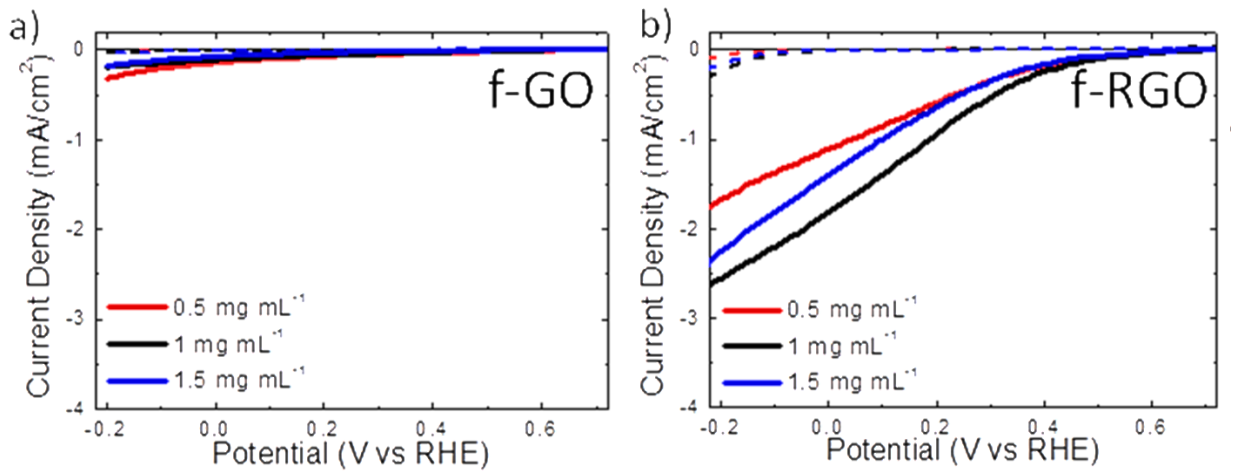

Figure 5.18. LSVs measured for the photocathodes using a) f-GO and b) f-RGO as HSLs deposited from dispersions in ethanol at different concentration: 0.5, 1 and 1.5 mg mL-1 (red, black and blue lines), measured in 0.5 M H_2SO_4 solution (pH 1), under dark (dashed lines) and AM1.5 illumination (100 mW cm^{-2}) (solid lines).

In addition, the potentiostatic stability measurements of the photocathode using f-RGO over 1 h of continuous AM1.5 illumination (Figure 5.19) have shown a clear improvement in stability with respect to ones based on GO and RGO (Figure 5.16b). After the first LSV scan (where J_{0V} vs RHE is -1.82 mA $^{cm-2}$), $J_{0V\ vs\ RHE}$ at t = 0 is -1.63 mA cm^{-2}, with a decrease of ~45% after 1 h operation, which however still provides a J_{0V} vs RHE of ~-1 mA cm^{-2}. The improved J_{0V} vs RHE (i.e., $\Phi_{saved,NPA,C}$ and $\Phi_{saved,ideal}$) over time obtained by the f-RGO-based photocathodes with respect to the ones achieved by RGO and GO is linked with an enhancement of the mechanical stability of the electrode. In fact, delamination/disruption of the photocathodes, shown by the GO- and RGO-based photocathodes (Figure 5.17b), is not observed here. This result proves the beneficial role of

the RGO flakes functionalization to strengthen the adhesion between the layers of the FTO/HSL/rr-P3HT:PCBM structure.

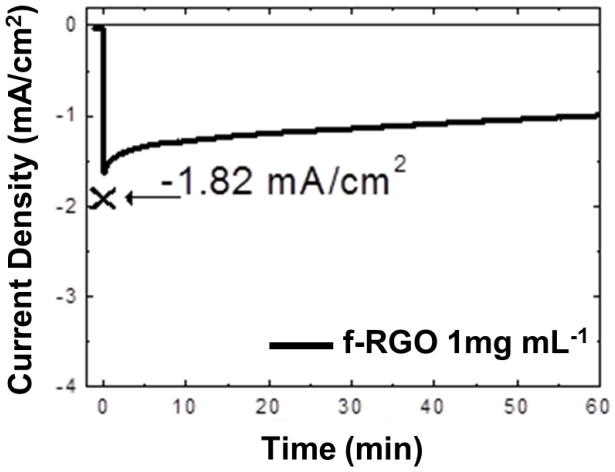

Figure 5.19. Potentiostatic stability test of photocathode using f-RGO obtained by recording $J_{0V\ vs\ RHE}$ over 1 h of continuous AM1.5 illumination.

However, degradation of the photocathodes using f-RGO are still significant ($J_{0V\ vs\ RHE}$ loss of ~45% after 1 h of operation), indicating other causes of instability, such as TiO_2 reduction in acidic condition[440] and Pt detachment.[441] In order to further increase the photocathodes stability, we also designed solution-processed Pt/C-Nafion overlay. Actually, in order to achieve durable and highly efficient photocathodes, the materials adopted for the protective overlay must be electrochemically stable in aqueous solution and, at the same time, sufficiently permeable to maintain the contact between the electrocatalytic Pt nanoparticles and the electrolyte,[442] allowing the photogenerated electrons to reach the Pt nanoparticles. Furthermore, the processing conditions of the coating must be compatible (*i.e.*, not damaging) with the underlying layers, easy scalable and cheap.[443] Here, we focused on a different coating of the FTO/graphene-based HSL/rr-P3HT:PCBM/TiO_2 structures, based on solution-processed conductive and catalytic Pt/C-Nafion blend. Based on the obtained photoelectrochemical results discussed above, this protective methodology is applied only for the photocathodes using GO and f-RGO as HSL. The PEC characterization of the photocathodes based on GO and f-RGO as HSL, and using Pt/C-Nafion overlay (named GO+Pt/C-Nafion and f-RGO+Pt/c Nafion, respectively) is reported in Figure 5.20a.

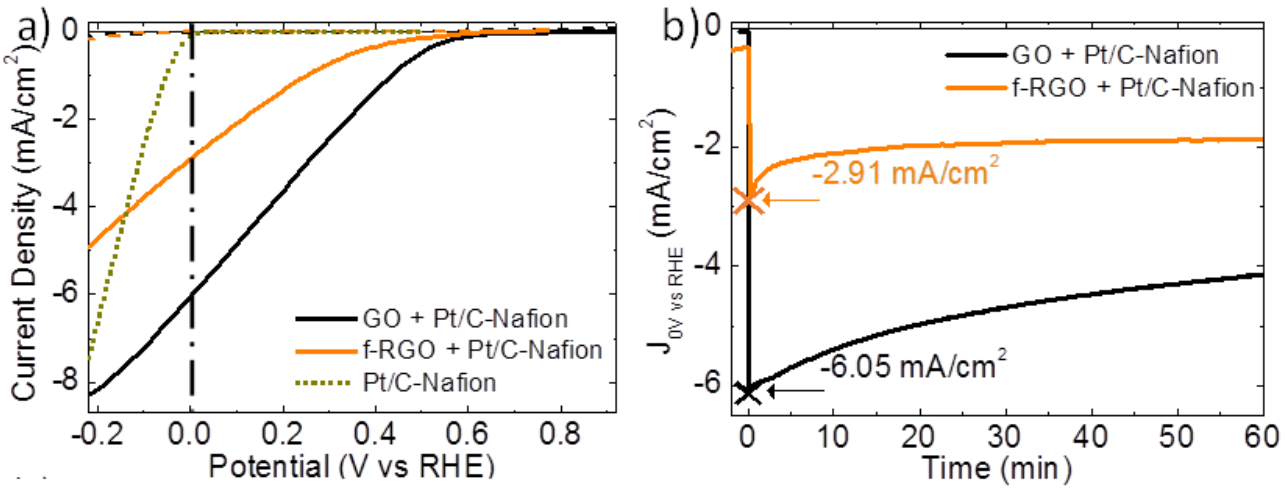

Figure 5.20. a) LSVs measured for the GO+Pt/C-Nafion (black lines) and f-RGO+Pt/C-Nafion (orange lines) as HSLs measured in 0.5 M H_2SO_4 solution (pH 1), under dark (dashed lines) and AM1.5 illumination (solid lines). GO and f-RGO films are deposited from 1 mg mL^{-1} dispersions in ethanol. The current-potential curve of Pt/C-Nafion overlay deposited directly on FTO (short dashed dark yellow line) is also shown. b) Potentiostatic stability tests of GO+Pt/C-Nafion (black line) f-RGO+Pt/C-Nafion (orange line), obtained by recording $J_{0V\ vs\ RHE}$ over 1 h of continuous AM1.5 illumination. The stability tests started after the measurement of the LSVs shown in panel a). The values recorded in the LSVs of panel a) are also indicated in panel b.

Linear sweep voltammetry (LSV) measurements show an improvement of the photoelectrochemical performance of the photocathodes with respect to those without Pt/C-Nafion overlay (Figure 5-18). The main obtained results are $J_{0V\ vs\ RHE}$ = -6.01 mA cm^{-2} (-2.93 mA cm^{-2}), V_o = 0.60 V (0.55 V) *vs*. RHE, $\Phi_{saved,NPA,C}$ = 1.11% (0.36%), $\Phi_{saved,ideal}$ = 0.77% (0.27%), for the GO+Pt/C-Nafion (f-RGO+Pt/C-Nafion). The photoelectrochemical performance achieved by the GO+Pt/C-Nafion-based photocathodes is remarkable. Beside the aforementioned improvements in photoelectrochemical performances, a clear increase of stability is also observed for the two photocathodes, as reported in Figure 5.20b. In fact, a remarkable $J_{0V\ vs\ RHE}$ = -4.14 mA cm^{-2} for the case of GO, and -1.88 mA cm^{-2} for the case of f-RGO is achieved, which correspond to a retention of 69% and 64%, respectively, after 1 h of continuous AM1.5 illumination.

Photoelectrochemical Responses at Different PH:

The development of photocathodes operating in neutral and alkaline conditions is crucial for their exploitation in tandem configuration systems.[444],[445] In order to address this target, we tested our optimized photocathodes (*i.e*., GO+Pt/c-Nafion and f-RGO+Pt/C-Nafion) at different pH, *i.e*., acid, neutral as well alkaline conditions (Figure 5.21). The LSV scans obtained at pH 1, 4, 7 and 10 for photocathodes using GO and f-RGO with Pt/C-Nafion overlay are reported in Figures 5.21a,b,

respectively. Remarkable PEC activity is observed at all the pH conditions. For example, $J_{0V\ vs\ RHE}$ are -1.64 (-0.89), -1.51 (-0.91), -1.41 (-0.45) mA cm^{-2} for GO+Pt/C-Nafion (f-RGO+Pt/C-Nafion) at pH 4, 7 and 10, respectively, are obtained.

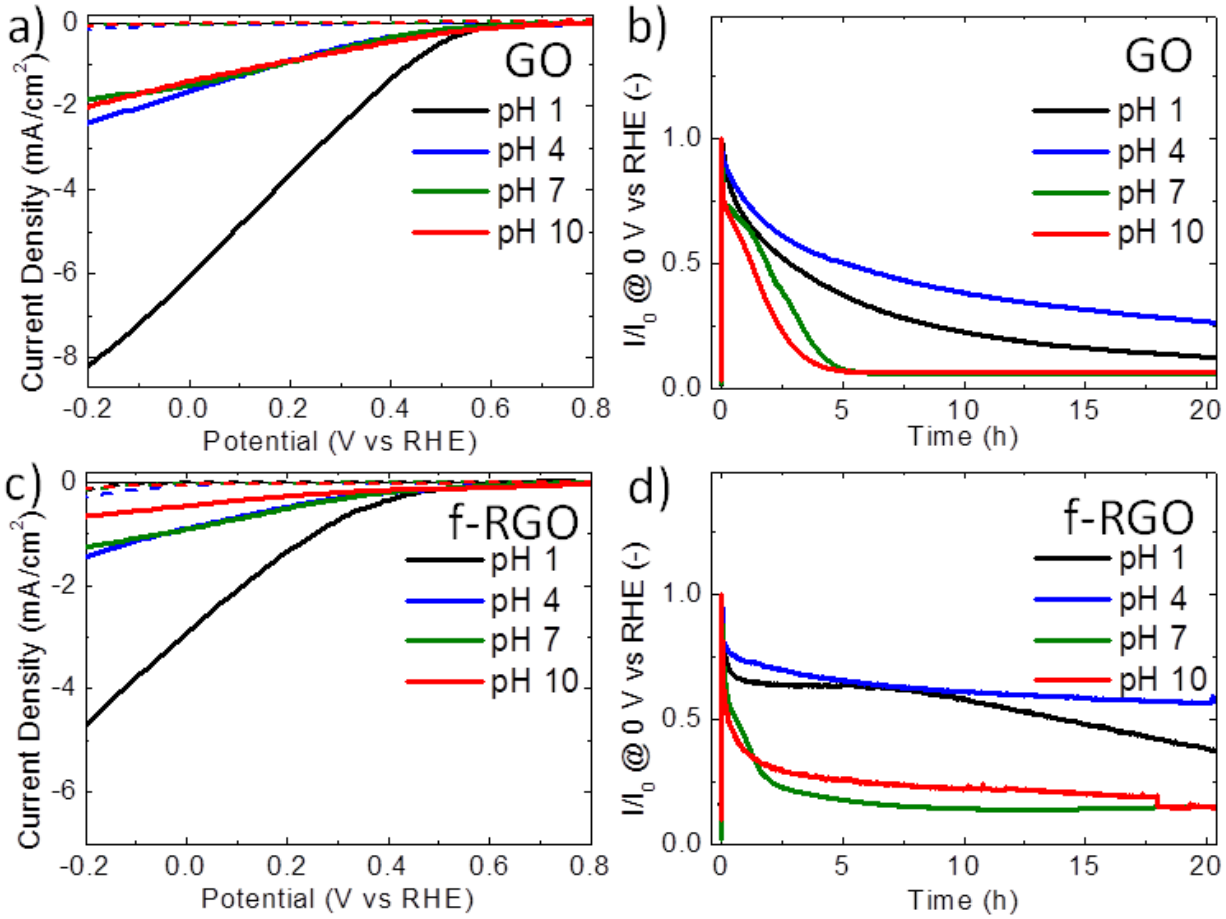

Figure 5.21. LSVs measured for the a) GO+Pt/C-Nafion and c) f-RGO+Pt/C-Nafion at pH 1 (black lines), 4 (blue lines), 7 (olive lines) and 10 (red lines) under dark (dashed lines) and AM1.5 illumination (solid lines). Potentiostatic stability tests b) GO+Pt/C-Nafion and d) f-RGO+Pt/C-Nafion, obtained by recording $J_{0V\ vs\ RHE}$ over 1 h of continuous AM1.5 illumination at pH 1 (black lines), 4 (blue lines), 7 (olive lines) and 10 (red lines). The photocurrents are normalized to the values of photocurrent at t = 0. The stability tests started after the measurement of the LSVs shown in panels a) and c).

Potentiostatic stability tests at different pH values for the GO+Pt/C-Nafion and f-RGO+Pt/C-Nafion are reported in Figures 5.21c,d, respectively. The data show better stability of the photocathodes operating at pH 1 and 4 with respect to pH 7 and 10. A retention of the J_{0V} vs RHE, with respect to its starting values, *i.e.*, 30% (64%) and 50% (66%) for pH 1 and 4, respectively, is measured for GO+Pt/C-Nafion (f-RGO+Pt/C-Nafion) after 5 h of continuous operation. After 20 h of endurance test for GO+Pt/C-Nafion (f-RGO+Pt/C-Nafion) shows a retention of the $J_{0V\ vs\ RHE}$, with respect to its starting values of 12% (38%) and 27% (57%) at pH 1 and 4, respectively. At pH 7 and 10 photocurrents decrease rapidly during the first 5 h of operation. The J_{0V} vs RHE decreases with

respect to its starting values of 93% at both pH 7 and 10 for the GO+Pt/C-Nafion, and of 74% and 82% at pH 7 and 10, respectively, for the f-RGO+Pt/C-Nafion. The degradation here observed is attributed to the electrochemical instability of the Pt/C-Nafion overlay at neutral and basic conditions. This is evidenced by top-view SEM images of GO-Pt/C-Nafion photocathode before (Figure 5.13a) and after its immersion in the electrolyte at pH 10 (Figure 5.13b) and after 20 h of operation at 0 V vs. RHE and continuous AM1.5 illumination (Figure 5.13c).

5.5.2.5 Flexible and large area photocathodes

Photoelectrodes based on organic materials, such as graphene derivatives and photo-active conjugated polymers (*e.g.,* rr-P3HT), could in principles offer low manufacturing cost at high volume, thanks to their fast, low temperature, solution processing deposition on flexible plastic substrates.[385] Thus, we used graphene-based HSLs for fabricating large-area (9 cm^2) solution-processed rr-P3HT:PCBM-based photocathodes on flexible ITO-PET substrates. Figure 5.22a and Figure 5.22b report the images of a representative solution-processed flexible 9 cm^2-area photocathode using GO as HSL and Pt/C-Nafion overlay (*i.e.*, GO+Pt/C-Nafion). Figure 5.22c shows the LSV measurements obtained for the large-area GO-based photocathodes as compared to those obtained for the corresponding 1 cm^2-area photocathode. The key results obtained for the main FoM of the 9 cm^2-area photocathode are $J_{0V\ vs\ RHE}$ = -2.80 mA cm^{-2}, V_o = 0.45 V *vs.* RHE, $\Phi_{saved,NPA,C}$ = 0.31%, $\Phi_{saved,ideal}$ = 0.23%. For the 9 cm^2-area device, the lower performances achieved with respect to the 1 cm^2-area one are attributed to the series resistance (R_s) of the photocathodes.[446] The series resistance is given by the sum of the resistance of the substrate (R_{FTO} or R_{ITO}), the resistance of the electrolyte (R_{el}) and the contact resistance (R_c). The values of R_{FTO} and R_{ITO} are equal to the sheet resistance (R_{sh}) of the substrates, which are ~15 Ω/□ for FTO/glass and ~30 Ω/□ for ITO/PET (here used as substrate for 1 cm^2-area and 9 cm^2-area photocathodes, respectively). The higher R_s values observed for ITO/PET with respect to that of FTO/Glass causes the decrease of V_{mpp} (defined as d(JV)/dV=0) for the 9 cm^2-area photocathode V_{mpp} = 0.26 V *vs.* RHE) with respect to that of 1 cm^2-area one V_{mpp} = 0.17 V *vs.* RHE and it leads to decrease of performance of cell respect to 1cm^2.

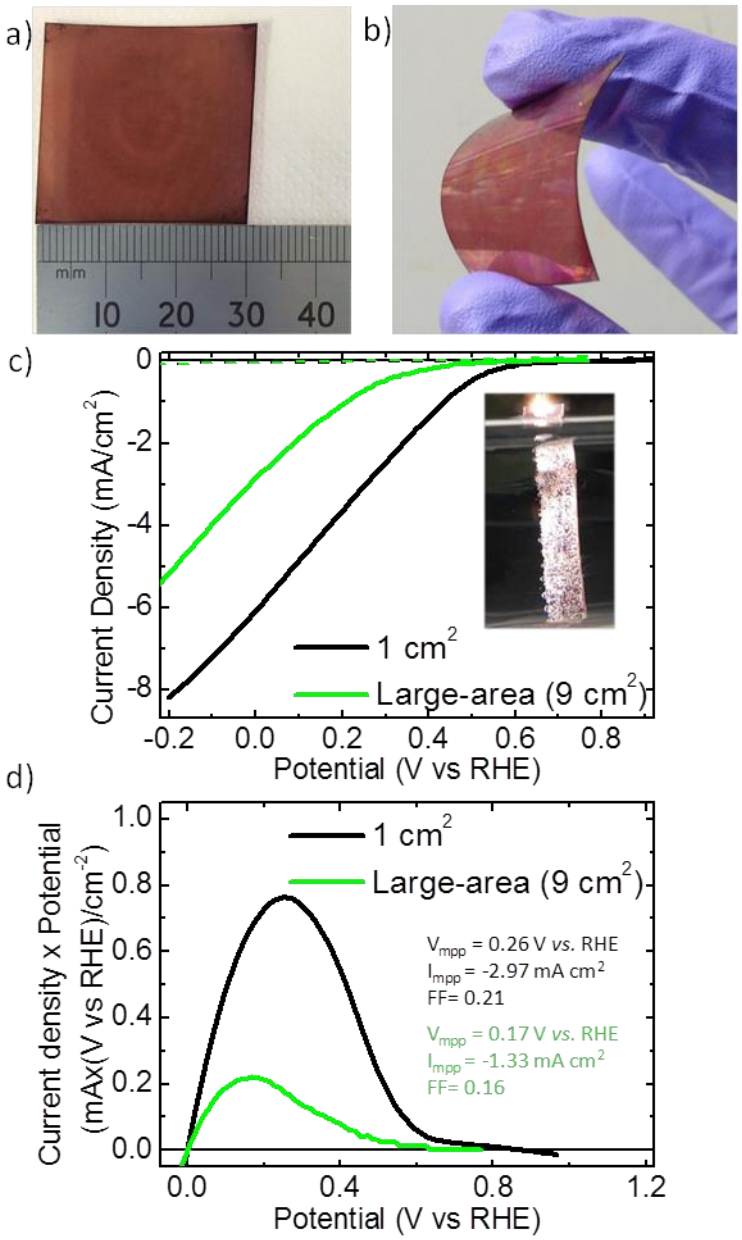

Figure 5.22. Photograph of a representative solution-processed large-area (9 cm^2) ITO-PET/GO/rr-P3HT:PCBM /TiO_2/Pt/C-Nafion photocathode a) before and b) after bending. c) LSVs and d) Current density x potential vs. potential curves measured for the GO+Pt/C-Nafion for 1 cm^2-area and 9 cm^2-area configurations (black and green lines, respectively) measured at pH 1 under dark (dashed lines) and AM1.5 illumination (solid lines). The inset in panel c) shows the hydrogen evolution on the surface of the photocathode operating at 0 V vs. RHE under 1.5AM illumination condition at pH 1. d) Vmpp, Jmpp, and FF, reported with the corresponding colours used for the LSVs, showing the decrease of FF by increasing the photocathode's area.

5.6 Summary

In conclusion, this chapter shows that fast fabrication techniques, entirely based on solution processing, can be employed for the realization of low-cost organic photocathodes with material interface engineered with 2D materials. Firstly, few-layer MoS_2 flakes, produced water-based

exfoliation of Li-intercalated bulk MoS_2, are demonstrated as a novel HSL. The electrical properties of the MoS_2 films are tuned by using solution processed $HAuCl_4$ doping. This increase the WF value from 4.6 up to 5.1 eV, which turn out to be matched with the HOMO level of the rr-P3HT. The morphology of the MoS_2 films and the optimization of the $HAuCl_4$ doping level led to solution-processed organic H_2-evolving photocathode with $J_{0\ V\ vs.\ RHE}$ of 1.21 mA cm^{-2}, V_o of 0.56 V *vs*. RHE and $\Phi_{saved,NPAC}$ approaching 0.5%. Secondly, solution-processed GO and RGO atomic-thick films have been used as HSL to further boost the efficiency and durability of rr-P3HT:PCBM-based photocathodes. More in detail, record-high performance and stability for solution-processed rr-P3HT:PCBM-based photocathodes are achieved at pH 1 by adopting silane-based functionalization of graphene derivatives-based HSLs, and a Pt/C-Nafion overlay,. Specifically, GO+Pt/C-Nafion photocathodes have shown $J_{0V\ vs\ RHE}$ = -6.01 mA cm^{-2}, V_o = 0.6 V *vs.* RHE, $\Phi_{saved,ideal}$ = 1.11%, while f-RGO+Pt/C-Nafion ones reported $J_{0V\ vs\ RHE}$ = -2.93 mA cm^{-2}, V_o = 0.55 V *vs.* RHE, $\Phi_{saved,ideal}$ = 0.27%. An operational activity of 20 h is reached at 0 V vs. RHE and under 1.5AM illumination condition. Moreover, the photocathodes are also effective at different pH values. The $\Phi_{saved,ideal}$ are 0.19%, 0.19% and 0.20% for GO+Pt/C-Nafion and 0.1%, 0.1% and 0.06% for f-RGO+Pt/C-Nafion, at pH 4, 7 and 10, respectively. We have furthermore demonstrated the up-scaling feasibility of our solution processed devices, fabricating a flexible 9 cm^2- area photocathode achieving $J_{0V\ vs\ RHE}$ = -2.80 mA cm^{-2}, V^o = 0.45 V *vs.* RHE, $\Phi_{saved,NPA,C}$ = 0.31%, $\Phi_{saved,ideal}$ = 0.23%. To summarize, all these results demonstrate that organic photocathodes based 2D materials represent an attracting technology to boost the commercialization of PEC devices for solar water splitting.

CHAPTER 6

CHAPTER 6: 2D Material Interfaces Engineering Perovskite Solar Cell (PSCs)

6.1 Perovskite Solar Cells (PSCs)

Hybrid organic-inorganic PSCs have been the most recent advance in third generation solar cells. In 2009, Miyasaka and coworkers published the first approach using methyl-ammonium lead iodide ($MAPbI_3$) and methyl-ammonium lead bromide ($MAPbBr_3$)perovskites as absorbers in DSSC with a limited PCE of 3.8% .[447] After that, Park's group showed a quantum dot solar cells (QDSC) using perovskite with a very promising 6.5% energy conversion efficiency (PCE),[448] however the structure still uses corrosive liquid electrolytes. In 2012 Park, Grätzel and colleagues[449] introduced a spiro-OMeTAD, which was developed for organic LEDs [450] as HTL in a solid state DSSC.[451] Subsequently, they introduced $MAPbI_3$ in a similar solid state devices forming a continuous film of perovskite, sandwiched between the electron transporting layer (ETL), *i.e*., TiO_2, and the spiro-OMeTAD. The latter not only improved the stability, as expected, but also boosted the efficiency up to 9%.[449] Since then, PSCs have gained a tremendous interest in the research community, and their development has been extremely fast. The efficiencies have improved rapidly as different structures and fabrication methods have been studied. To date, the efficiency of PSCs has exceeded 22.7%, as recently reported by researchers from KRICT and UNIST, holding the highest certified record for a single-junction PSC.[452]

Perovskite solar cells (PSCs) can be divided into three groups according to their device architecture: 1) perovskite-sensitized mesoporous architectures; 2) planar heterojunction configurations and 3) inverted structures.[453] The mesoscopic PSCs have a similar structure to the solid-state dye-sensitized solar cells. Typically, perovskite is used as light absorber material infiltrated into TiO_2. Nanoparticle network . The HTL, traditionally spiro-OMeTAD, is then coated on top of the perovskite film. Finally, the cell is completed by deposition of metal contact.[454] The invert and planar heterojunction PSCs, are instead made of a compact perovskite layer, which is grown without any supporting structure. electron transporting layer (ETL) and HTL are added in PSCs between the photoactive layer and the electrodes in order to separate the generated charges and collect them (holes at the photoanode and electrons at the back electrode) efficiently.[455] For what regards the ETL, compact layers of TiO_2 (50–80 nm)[456] or ZnO (25 nm)[457] are usually chosen to prevent holes recombination at the photoanode. Concerning the HTL, Spiro-OMeTAD is still the

standard material.[454] Actually, Spiro-OMeTAD can be easily integrated in PSCs since it can be solution-processed in water-based solvents. Thanks to the highest-occupied molecular orbital (HOMO) energy level of 5.03 eV, [458] which is a value approaching the valence band maximum (V_{BM}) of $CH_3 NH_3 PbI_3$ (5.4 eV),[459] Spiro-OMeTAD effectively transfers holes from the $CH_3NH_3PbI_3$ to the photoanode.[460] However, Spiro-OMeTAD is expensive, and for this reason many other materials have been proposed and tested as alternatives.[461] The long list of materials used as HTL instead of Spiro-OMeTAD includes: inorganic compounds such as copper(I) iodide (CuI),[461] organic polymers such as poly(3,4-ethylenedioxythiophene) polystyrene sulfonate (PEDOT:PSS),[462] as well as carbon-based nanomaterials such as GO and RGO.[463] Nevertheless, despite these recent results, Spiro-OMeTAD still represents the reference HTL material used for the fabrication of PSCs. A more significant limitation that poses severe concerns in view of the possible commercialization of PSCs is their lifetime stability,[464] which is adversely affected by the presence of the Spiro-OMeTAD. This is due to the fact that Spiro-OMeTAD, in its pristine form (amorphous), has low electrical conductivity (σ).[465] In order to increase the σ with the target to reach high device η, Spiro-OMeTAD is usually doped with a combination of tert-butylpyridine (TBP)[466] and lithium bis(trifluoromethanesulfonyl)imide (Li-TFSI).[467] Such doping process successfully increases its hole mobility (from 10^{-5} to 10^{-3} cm^2 V^{-1} s^{-1}) [468]and hence the σ (from 10^{-8} to 10^{-3} S cm^{-1}).[469] The doping process has also an effect on the HOMO level, which increases from 5.03 to 5.22 eV.[470] Unfortunately, the downside of such doping process is the reduced stability of the PSCs, which is currently the main drawback of such technology.[464] The Li-TFSI tends to desorb during cell operation, reducing the cell η (a 20% decrease in the first 120 h at room temperature with a humidity of ≈ 40%);[471] TBP instead causes the corrosion of the perovskite layer strongly affecting the η of the cells over time. [472] Another factor limiting the device stability regards the interface created by the Spiro-OMeTAD and the perovskite layer.[473] Recent studies reported evidence of iodine migration from the perovskite layer to the Spiro-OMeTAD, with consequent degradation of the cell η. [473] Furthermore, it is known that a direct contact between the perovskite and the metal electrode results in high recombination losses, which results in a decrease of V_{OC} and FF. [474] Such losses can occur in solution-processed PSCs due to the incomplete coverage of the perovskite by the HTL.[475] Another source of loss is the metal electrode that can also get in contact with the perovskite by migrating through the HTL.[476] One strategy to minimize such detrimental effect could be the increase of the HTL thickness, which is however associated with an increase of the PSCs series resistance, determining a reduction of the solar cell η.[477] Second strategy could be

the addition of an layer between the perovskite and the Spiro-OMeTAD layer to prevent shunting pathways. Such layer has a passive protective function, because it physically prevents the contact between the Au electrode and the perovskite layer.[478]

6.2 Device Fabricating Process

According to the difference of method fabricating active layer, there are usually two fabricating processes of active layer in perovskite hybrid solar cells: one step process and two-step process.

6.2.1 One Step Process Fabricating Perovskite Layer

One step process of fabricating the active layer is extensively used in perovskite hybrid solar cells. For one step process, the perovskite film is fabricated by themix solution of Methylammonium iodide (MAI) and Lead(II) halide PbX_2 (X=I, Br, I). The mole ration of each component is 1:1. The mix solution is usually dissolved in dimethylformamide (DMF) or dimethyl sulfide (DMSO) solvent, and then the solution is put under stirring for several hours. After these preparation procedures, the solution is drop casted or spin-coated on the substrate. After the spin-coating, a thermal annealing is usually performed of the perovskite film to guarantee the sufficient reaction of the two components. Lead(II) iodide (PbI_2) is firstly spin-coated as the precursor and then MAI is spin-coated on the top of PbI_2 layer.[479] Recently, this method has been modified by dripping a poorly polar or non-polar solvent either toluene[480] or chlorobenzene[481] during the drying step of spin coating forming bigger and defect less crystals pushing up the photocurrent.

6.2.2 Two Step Process Fabricating Perovskite Layer

Sequential deposition is widely used in the two-step process,[482] which divide the active perovskite layer into two parts-MAI and PbI_2. The Lead(II) chloride ($PbCl_2$) and Lead(II) bromide ($PbBr_2$) cannot be used because of solubility issues.[483] PbI_2 is dissolved in DMF or DMSO while and MAI is dissolved in ethanol or isopropanol. The PbI_2 solution is first spin-coated on the electrode buffer layer and then the MAI is spin-coated on the surface of PbI_2 solution. After the spin-coating, the perovskite film is annealed at 100°C for two hours.[484]

6-3 Solar Cell Characterization:

The most representative test for any type of PV solar cell is the study of current-voltage characteristics, (J-V curve). It is based on the definition of a solar cell as a device that generates both current and voltage without any external source while it is illuminated. The short circuit current (J_{sc}) and the open circuit voltage (V_{oc}) can be directly determined from the recorded J-V curve. J_{sc} is the current when the voltage is zero and V_{oc} is the voltage when the current is zero. The short circuit current density gives the maximum current density, which can be obtained from the solar cell at short circuit conditions. The maximum power, P_{max}, is the product of photocurrent and photovoltage at that voltage where the power output, *i.e*. V × J, is at its maximum.[485,486]

$$P_{max} = V_{max} \times J_{max}$$

A J-V curve is depicted in Figure 6.1, where the V_{oc} , J_{sc} and the P_{max} are also indicated.

Other important parameters, such as the FF and the energy conversion efficiency PCE can be determined using the J-V measurement data. The FF indicates the squareness of the J-V curve. Mathematically, FF is the ratio between maximum PCE divided by the theoretical maximum efficiency without any type of shunt, series or recombination losses or, *i.e.* the product of V_{oc} by J_{sc}. Its value can be determined from the equation[485,486]

$$FF = \frac{P_{max}}{V_{OC} \times J_{SC}}$$

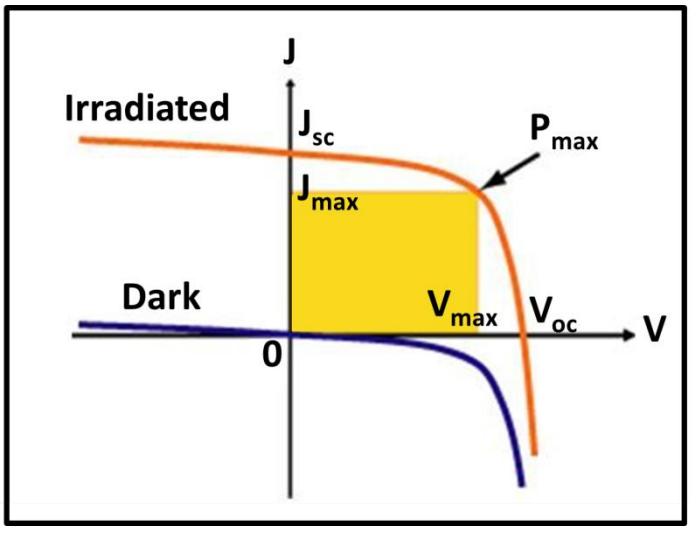

Figure 6.1. J-V curve.[487]

The value of the FF lies between 0 and 1.[488] The ideal value is 1, but in practice this cannot be achieved due to physical constraints on diode quality in the solar cell. The main reason for the deviation from the ideal behavior is the recombination occurring at the junction, which can be described in terms of series and shunt resistances. The increase in the series resistance indicates poor conductivity through the active layers and reduced charge carrier injection to the electrodes. The reduced shunt resistance is due to either imperfections within the photoactive layers or current leaks at the interface between layers in the solar cell.[485]

The energy conversion efficiency is

$$PCE(\%) = \frac{P_{out}}{P_{in}} \times 100 \ = \frac{J_{SC} \times V_{OC} \times FF}{P_{in}} \times 100$$

Where P_{in} is the irradiance of the incident light to the surface of a cell, which is irradiated by incident light. P_{in} is fixed to 100 mW cm^{-2} =1000 W m^{-2} according AM1.5G.[486]

Solar cells can be also characterized with the incident photonto current efficiency (IPCE) (also known as external quantum efficiency or EQE). IPCE describes as Incident photon-to converted electron efficiency, is a measurement of the ratio of incident photons they are converted into collected electrons at each wavelengths inside a PV device.

$$IPCE\ (\lambda) \ = 1240 \times \frac{J_{SC}}{\lambda\ P_{in}}$$

where λ is the wavelength.[488]

There are various factors to be taken into consideration in order to measure the performance of perovskite solar cells accurately. The main issue is the hysteresis in J-V curves, which is affected by the measurement setup and by the solar cell construction. The hysteresis is different for every cell. The origin of the hysteresis is not yet understood. In general, the J-V curves are obtained by sweeping the potential difference between the working and counter electrode and monitoring the current response simultaneously. The sweep rate should be carefully selected for each device. If the sweep rate is faster than the response time of the device, the recorded curve does not show steady-state performance. The direction of the sweep causes hysteresis in the J-V curves. The steady-state output gives the actual values. The real output of the device lies between the forward and reverse scan curves.[489,490] The measured current density values can be verified by measuring

and integrating the IPCE spectra over the AM1.5G solar spectrum. The integrated current density is

$$J_{SC,integrated} = \frac{F \times \int (E_{e\lambda} \times IPCE) d\lambda}{N_A}$$

where N_A is the Avogadro constant, F the Faraday constant, and $E_{e\lambda}$ the solar spectral irradiance. The integrated and measured current density values should be approximately equivalent if the measurements have been executed carefully.[490]

6.4 Solar Cell Measurements

The performances of the devices are measured under inert atmosphere with A.M. 1.5 G solar simulator at an intensity of 100 mW cm^{-2} using an Agilent B1500A Semiconductor Device Analyzer. A reference monocrystalline silicon solar cell from Newport Corp. is used to calibrate the light intensity. For the degradation study of the encapsulated devices, the as-fabricated cells are exposed in continuous solar irradiation, using an A.M. 1.5 G solar simulator, under ambient conditions with relative humidity (RH) constantly above 50% and data plots are obtained by periodically scanning the devices from scanned from short circuit (SC) to open circuit (OC). For the long-term stability tests of the sealed cells, the devices are prepared and encapsulated, using an UV-curable epoxy and a glass coverslip, inside a nitrogen filled glove box. Afterwards, the cells' maximum power point is tracked by a modular testing platform (Arkeo - Cicci research s.r.l.) composed by a white LED array (4200Kelvin) under ambient conditions. The LED intensity is calibrated at the equivalent of 1 Sun intensity by adjusting the J_{sc} value to be equal with the measured in the J-V curve using the solar simulator. The external quantum efficiency measurements are conducted immediately after device fabrication using an integrated system (Enlitech, Taiwan) and a lock-in amplifier with a current preamplifier under short-circuit conditions. The light spectrum is calibrated using a monocrystalline photodetector of known spectral response. The PSCs are measured using a Xe lamp passing through a mono chromator and an optical chopper at low frequencies (~200 Hz) in order to maximize the signal/noise (S/N) ratio. Micro-photoluminescence (µPL) studies at 295K are performed using a setup in backscattering geometry, with a He-Ne 543 nm continuous wave laser as an excitation source. With a microscope objective lens (Mitutoyo 50X) the laser beam is focused down to 1 µm on the sample, placed on an XYZ translation stage, at normal incidence. A spatial filter system is used to obtain the central part

of the beam and acquire a uniform energy distribution. In a typical µPL experiment, different excitation positions of the samples are checked with low laser power (controlled by a neutral density filter).

6.5 High Performance and Stable Perovskite Hybrid Solar Cells based on Few-Layer MoS_2 flakes

The following sections describe the use of MoS_2 flakes, whose production is described in Chapter 2, as interface between HTL and perovskite layer in order to enhance the lifetime of perovskite solar cells. The MoS_2 buffer layer acts in two ways to keep the high solar conversion efficiency stable over time. Firstly, the MoS_2 flakes provide an effective interface between the perovskite and the hole transporting layer, due to its high mobility(up to 200 $cm^2/(V\ s)$ at room temperature)[491] and good energy matching with the perovskite(Energy level of ~5.2eV for MoS_2 flakes and perovskite's valence band 5.0-5.5 eV).[492] This leads to the high initial efficiency of the cell, by reducing recombination of the electrons and holes that are generated by light conversion in the perovskite. Secondly, the MoS_2 buffer prolongs the life of the perovskite layer by preventing degradation and ion migration from the electrode. This also protects against direct electrical contact with the Au electrode which collects the photocurrent, ensuring that the high efficiency is maintained over time. All the results herein show have been acquired in collaboration with the groups of Prof. Aldo Di Carlo at the Department of Electronic Engineering University of Roma "Tor Vergata" Rome, Italy and Prof. Emmanuel Kymakis at the Department of Materials Technology and Photonics & Electrical Engineering at the "University of Crete", Heraklion, Greece.

6.5.1 Few-Layer MoS_2 Flakes as Active Buffer Layer for Stable PSC

In this section, liquid-phase exfoliated few layer MoS_2 flakes, produced following the protocols described in Chapter 2, are implemented in solution-processed PSCs with glass/FTO/compact-TiO_2/mesoporous-TiO_2/$CH_3NH_3PbI_3$/MoS_2/Spiro-OMeTAD/Au structure to create an "active" buffer layer (ABL) between the Spiro-OMeTAD and the perovskite layer with a dual function: (i) barrier toward the metal electrode migration, and (ii) additional energy-matching layer to further ease the hole collection of the Spiro-OMeTAD. The presented approach allows to build a novel PSCs with η matching that of the reference PSCs based on Spiro-OMeTAD, but with superior lifetime stability over a period of 550 h.[492]

6.5.1.1 Architecture of the PSCs

A raster scanning laser (Nd:YVO_4 pulsed at 30 kHz average output power P = 10 W) is used to etch the FTO/glass substrates (Pilkington, 8 Ω cm^{-1}, 25 mm × 25 mm), used as transparent conductive window. Small area cell (0.1 cm^2) and large area cell (1.05 cm^2) are realized using a specific pattern of the FTO substrates (the cell active area is calculated from the overlap area between FTO and gold electrodes). The patterned substrates are cleaned in an ultrasonic bath, using detergent with de-ionized water, acetone and IPA (10 min for each cleaning step). A 50 nm thick blocking TiO_2 (BL-TiO_2) layer is deposited onto the patterned FTO by spray pyrolysis deposition. A 150 nm layer nano crystalline mesoporous TiO_2 (18NR-Tpaste Dyesol diluted with terpineol and ethylcellulose) is screen-printed onto the BL-TiO_2 surface and sintered at 480 °C for 30 min. The mesoporous-TiO_2 thickness is measured using the profilometer Dektak Veeco 150. The perovskite layer is deposited by solvent-engineering method using spin-coating technique, which permits a complete perovskite coverage of the mesoporous TiO_2, avoiding recombination of the charge carriers at the HTL/TiO_2 interface. To obtain the perovskite dispersion, 1.1 m PbI_2 powder (Sigma Aldrich) and 1.1 m of CH_3NH_3I (Dyesol) are dispersed in dimethyl sulfoxide and stirred at 70 °C overnight. 110 µL of this dispersion is spin coated on the TiO_2 substrate at 1000 rpm for 10 s and 5000 rpm 30 s. 200 µL of toluene is poured on the substrate 10 s prior the end of the second ramp. Then, the perovskite layer growth is obtained after annealing step at 100 °C for 1 h. After the perovskite growth, a layer of (1) doped Spiro-OMeTAD or (2) MoS_2 flakes + Spiro-OMeTAD is deposited, as follows: (1) Spiro-OMeTAD was spin coated at 2000 rpm for 20 s on the perovskite layer from a dispersion in chlorobenzene (74 mg mL^{-1}) doped by the addition of 27 µL of TBP, 16 µL of Li-TFSI dispersion (520 mg in 1 mL of acetonitrile solvent) and 7 µL of cobalt additive (FK209, 0.25 m in acetronitrile). (2) MoS_2 in IPA are spin-coated onto the perovskite layer at 1700 rpm for 45 s. Then, the samples are annealed for one minute at 70 °C. After the MoS_2 flakes deposition, the perovskite surface of test samples is analyzed by scanning electron microscopy (SEM) to evaluate the uniformity of the deposition. Spiro-OMeTAD is then deposited on the MoS_2 flakes as reported in (1). The Spiro-OMeTAD and MoS_2 + Spiro-OMeTAD PSCs are at last introduced into a high vacuum chamber (10^{-6} mbar) to thermally evaporate Au back contacts (thickness 100 nm). No sealing is applied to the fabricated cells.

6.5.1.2 Morphological Characterization of the PSCs:

As described in the previous section, the MoS_2 flakes in IPA are spin-coated onto the perovskite layer to create the ABL. SEM images are taken after the deposition to evaluate the surface coverage (Figure 6.2). MoS_2 flakes coating the perovskite layer are observed. By systematically exploring all the parameters involved in the MoS_2 deposition process (*i.e.*, spin coating time, speed, and number of coatings, post-annealing steps), a planar layer of flakes that covers the perovskite crystals is obtained. Although some of the perovskite crystals remain uncovered, these deposition parameters are chose as a tradeoff between uniform and planar deposition and minimal buffer layer thickness.

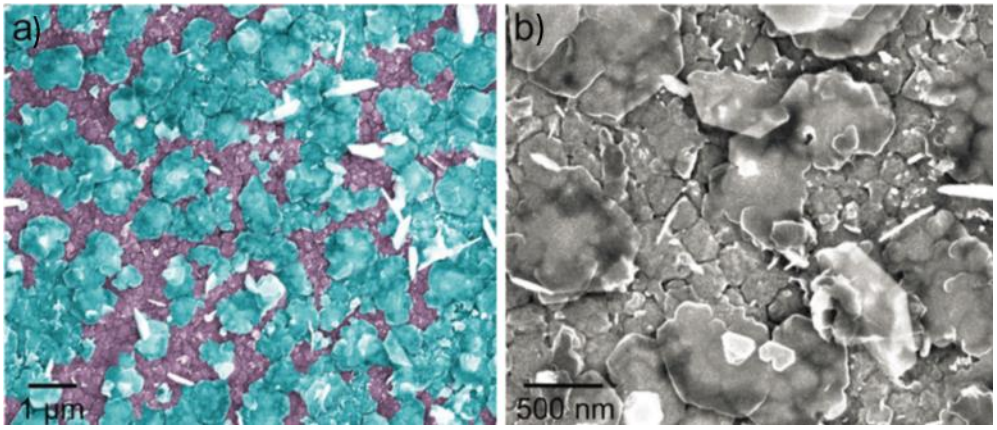

Figure 6.2. SEM images of the MoS_2 flakes spin-coated onto the perovskite layer of the cell. a) Image in false colors (dark cyan for MoS_2 flakes and purple for the underlying perovskite layer) highlighting the coverage provided by the spin-coating process of the MoS_2 flakes. b) MoS_2 flakes on top of the perovskite crystals.

In addition, SEM is carried out to ascertain the homogeneity of the MoS_2 deposition of the fabricated large-area cells.. Figure 6.3 reports r60 µm × 60 µm images (spaced by 100 µm) within the cell area of 1 cm^2. Cealry, the MoS_2 flakes coverage on top of the perovskite layer is homogenous.

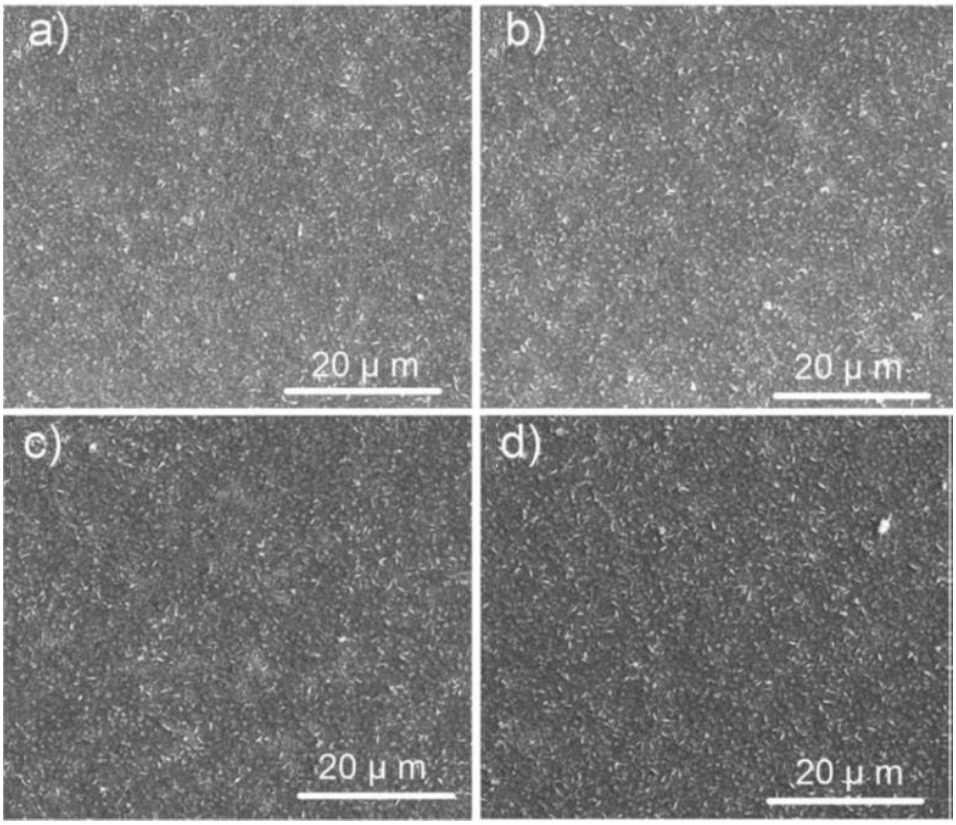

Figure 6.3. SEM images of the MoS_2 flakes spin-coated onto the perovskite layer of the cell. a-d) 60 µm × 60 µm images (spaced by 100 µm) within the cell area of 1 cm^2.

6.5.1.3 Photovoltaic Performance

The efficiency of the MoS_2 layer for the holes collection is expected to reside in the alignment between the V_{BM} of MoS_2 and $MAPbI_3$ (*i.e.*, a small energy offset between the two bands results in an efficient hole collection at the Au electrode).[493] The V_{BM} of the MoS_2 layer deposited on a Si substrate is −5.1 eV, as measured by UPS measurements (see Chapter 3), confirming the small energy offset between V_{BM} of MoS_2 and $MAPbI_3$ (−5.4 eV)[494].. Figure 6.4 shows schematically the energy band edge positions of the solar cells fabricated with the MoS_2 active buffer layer.

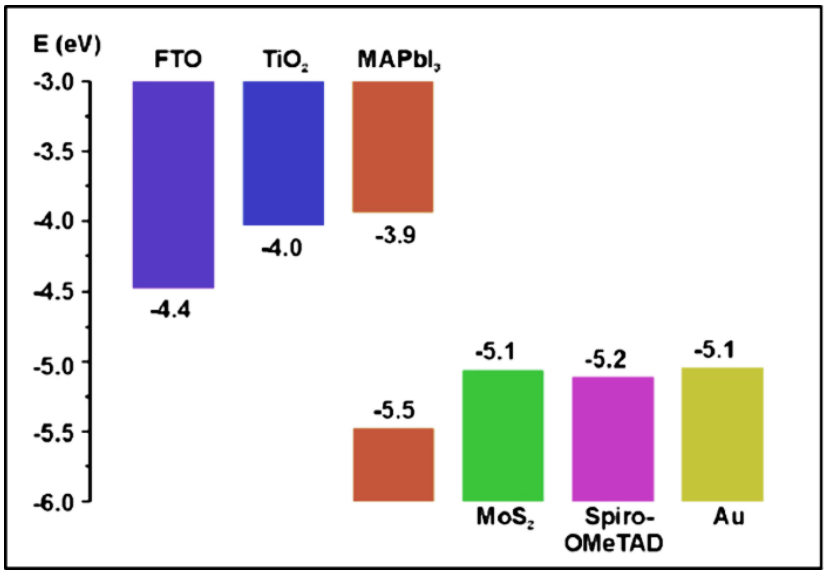

Figure 6.4. Energy levels of the fabricated PSCs with the MoS_2 active buffer layer.

Firstly, the photovoltaic performance of the PSC cell using the MoS_2 flakes as HTL, i.*e.,* glass/FTO/compact-TiO_2/mesoporous-TiO_2/$CH_3NH_3PbI_3$/MoS_2/Au structure, are evaluated in comparison with HTL-free PSC.. As shown in Figure 6.5, the use of MoS_2 flakes as HTL increase η with respect to that of the HTL-free cells (4.5% *vs*. 1.5%), confirming that the MoS_2 flakes ease the hole transport, and collection, towards the Au electrode.[495]

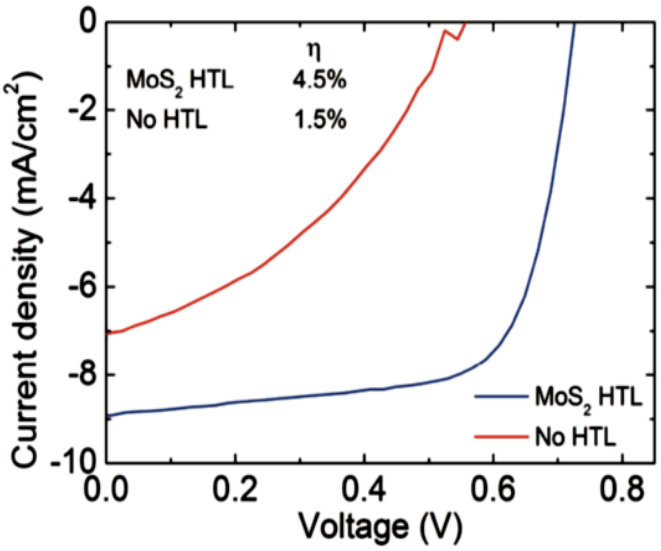

Figure 6.5. J-V curves of the cells fabricated with MoS_2 HTL and without HTL (0.1 cm^2 active area).

After this preliminary test, PSCs with glass/FTO/compact-TiO_2/mesoporous-TiO_2/$CH_3NH_3PbI_3$/MoS_2/Spiro-OMeTAD/Au structure are fabricated to fully assess the performance of MoS_2 as ABL. The results of the J-V measurements under illumination are reported

in Figure 6.6. In comparison with the reference PSCs, the cells with MoS_2 buffer layer show a decrease in V_{OC} (0.93V *vs*. 1.01 V) and fill factor (66.7% *vs*. 74.6%). However, the J_{SC} is found to significantly increase (−21.5 *vs*. −18.8 mA cm^{-2}) bringing the η to 13.3% (η = 14.2% for the reference PSCs).

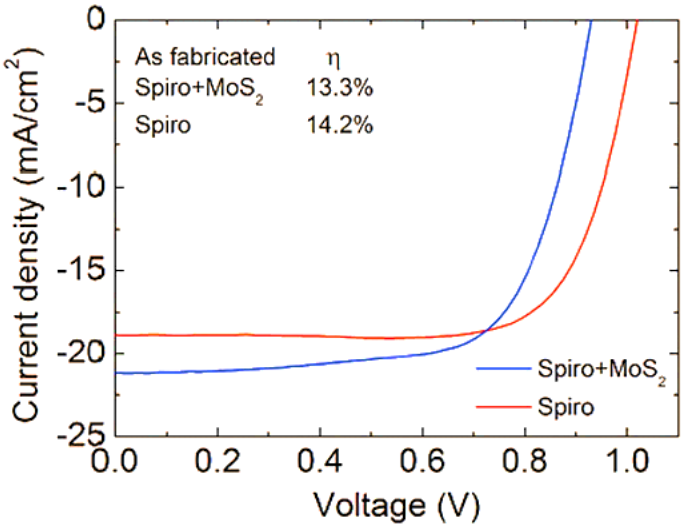

Figure 6-6. J-V curves of the cells measured after fabrication (0.1 cm^2 active area).

After an ageing test of 170 h, the PSCs are measured again under illumination (Figure 6.7). Remarkably, the PSCs with MoS_2 buffer layer have a η of 13.5% vs. 10.9% of the reference cell. The J-V characteristics of the PSCs are further measured after 550 h from fabrication. These results show better stability of the MoS_2-based sample with respect to the reference, *i.e*., a η of 12.4% *vs*. 9.3%. The MoS_2-based PSC shows a decrease in η of only 7%, *i.e*., a much lower value than the reference PSC (-34%). The improved stability of the MoS_2-based PSC with respect to the reference cell is ascribed to the surface passivation of the perovskite layer provided by the MoS_2 ABL, which prevents the iodine migration from the perovskite into the Spiro-OMeTAD and the formation of Au pathways from the metal electrode to the perovskite layer.[496,497]

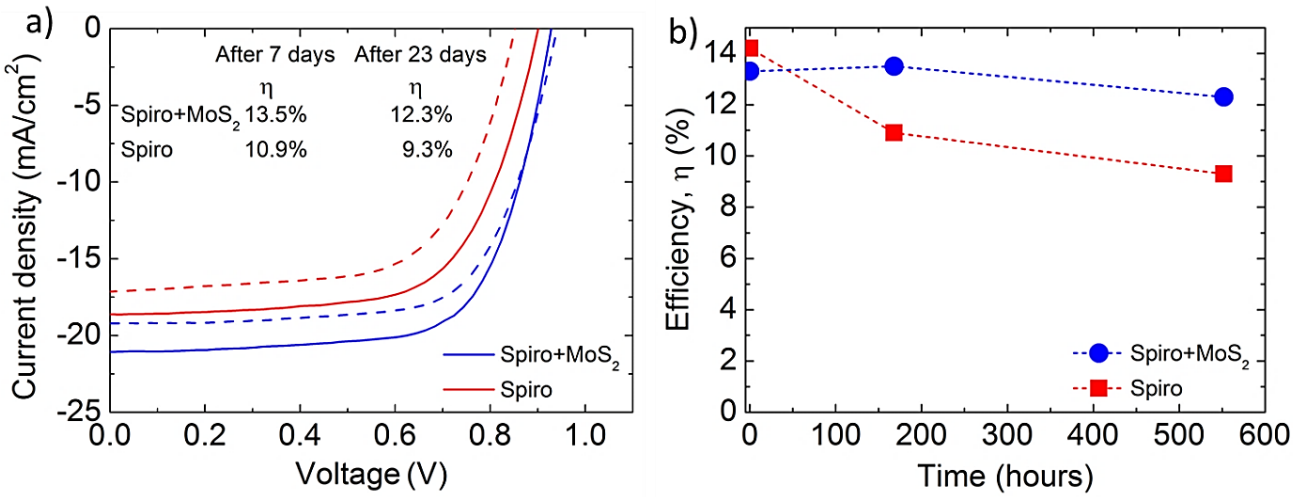

Figure 6-7. a) J-V curves of the cells measured after ageing tests (7 and 23 days). The devices were stored in a desiccator filled with silica (relative humidity ~ 30%) in dark conditions. b) η trend of cells with (blue) and without (red) MoS_2 over 550 h.

To verify whether the deposition of the MoS_2 ABL can be a viable approach in view of up scaling of the cells size,[498] PSCs with an active area of 1.05 cm^2 are fabricated (Figure 6.8). The J-V characteristics large-area cells are reported in Figure 6.8a, while Figure 6.8b displays a photograph of the as-prepared large-area cell. Remarkably, the η of the cell with the MoS_2 ABL achieved now the same value as the reference cell (11.5% vs. 11.4%), having a higher J_{SC} with respect to the reference PSC (−18.5 vs. −17.5 mA cm^{-2}), confirming the results obtained for small-area cells, reported in Figure 6.6.

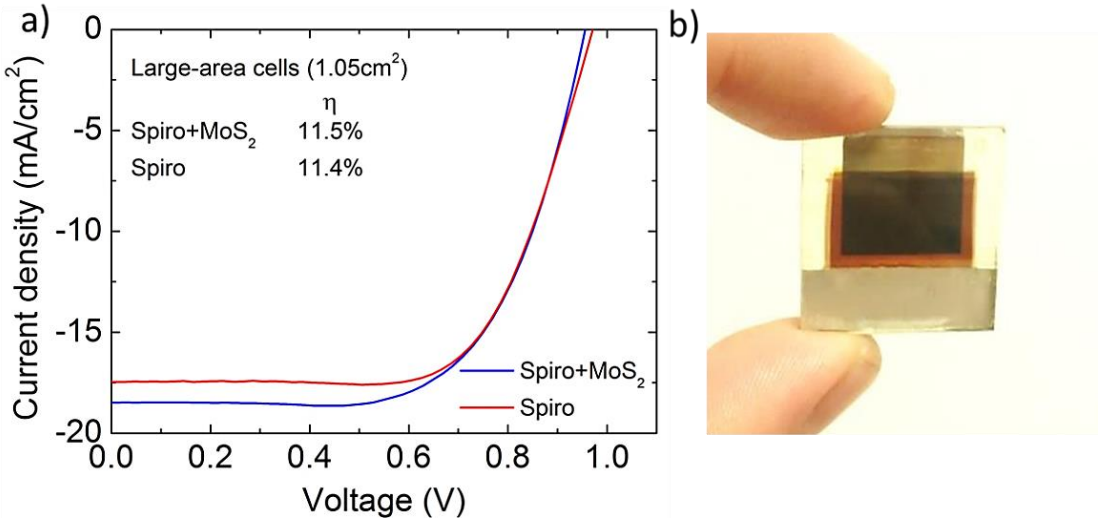

Figure 6.8. a) J/V curves of the large-area cells (1.05 cm^2 active area) with (blue curve) and without MoS_2 (red curve) measured under illumination (AM1.5G 100 mW cm^{-2}) using class A sun simulator. Mean photovoltaic parameters for a batch of six large-area PSCs made with the MoS_2 ABL: V_{OC} = 0.943 ± 0.026 V, J_{SC} = −18.11 ± 0.65 mA cm^{-2}, FF = 62.8 ± 3.4%, η = 10.7 ± 0.4%. b) Photograph of a large area cell with the MoS_2 ABL.

A statistical analysis of the J-V results is reported in Table 6.1 for both small and large area devices.

Table 6-1. Statistical analysis of the J/V parameters for the reference and MoS_2 ABL devices. The average values are calculated for both small ($0.1cm^2$, ten samples) and large ($1.05cm^2$, six samples) area devices. The J/V characteristics were measured at AM1.5G 1 Sun illumination condition under reverse scan direction (Scan Rate = 32mV/s).

Device	V_{OC} (V)	J_{SC} (mA/cm^2)	FF(%)	η(%)
0.1 cm^2-REF	0.998 ± 0.021	-19.20 ± 0.49	73.36 ± 1.71	14.05 ± 0.17
0.1 cm^2-MoS_2 ABL	0.938 ± 0.013	-21.09 ± 0.65	66.21 ± 2.45	13.09 ± 0.28
1.05 cm^2-REF	0.944 ± 0.022	-16.88 ± 0.60	70.03 ± 4.51	11.14 ± 0.56
1.05 cm^2-MoS_2 ABL	0.943 ± 0.026	-18.11 ± 0.65	62.83 ± 3.43	10.70± 0.40

The increase in J_{SC} is further testified by the IPCE measurements of the two cells (Figure 6.9). The IPCE graphs of the two cells in Figure 6.9 have analogous spectral trends. However, the curve associated with the MoS_2-based cell shows a higher IPCE value of around 10% in the 350-750 nm range, with respect to the reference. These IPCE trends are in agreement with the integrated current density values calculated from 300 to 850 nm at AM1.5G condition, which are 18.03 and 16.37 mA cm^{-2} for the PCSs with MoS_2 and the reference, respectively.

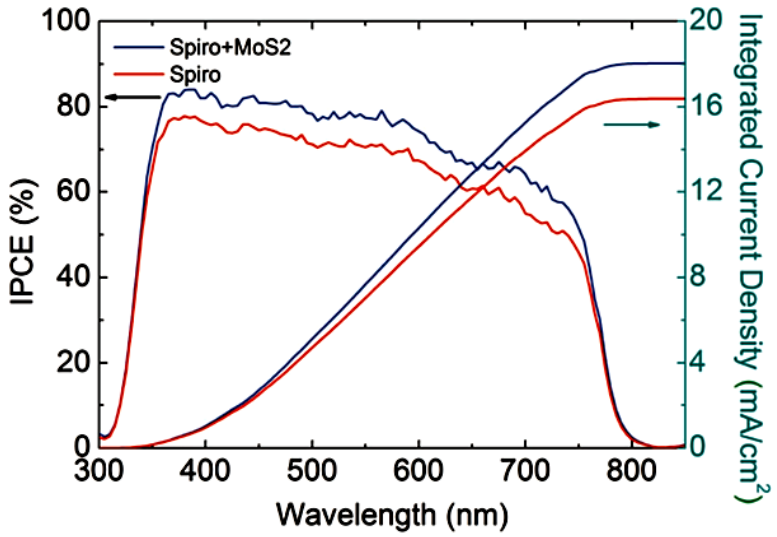

Figure 6.9. Left axis: IPCE spectra of the cells with (blue curve) and without (red curve) MoS_2 ABL. Right axis: integrated current densities in the two cases (AM1.5G).

In order to investigate the influence of the MoS_2 ABL on the regeneration efficiency of the perovskite and on the recombination pathways of the TiO_2-free carriers, the dynamic performance under pulsed light condition by means of transient photovoltage measurements (TPV) are tested,

as reported in Figure 6.10. The photo-voltage rise test (Figure 6.10a) is carried out on the PSCs in steady state operating conditions, *i.e.*, under dark at open circuit, and switching on the light source to monitor the subsequent rise in photovoltage. The transient rise time of the V_{OC} is generally correlated to two main processes: the electron transfer from the perovskite to TiO_2, and the hole transfer from the perovskite to the HTL.[499] The PSCs with MoS_2 ABL show faster V_{OC} rise time with respect to the reference cell (Figure 6.10a), indicating a more efficient hole transfer at the perovskite/ MoS_2 interface than at the perovskite/SpiroOMeTAD one.[500] Finally, to account for the difference in V_{OC} observed in Figure 6.6 between cells with and without MoS_2 ABL (0.93 V *vs.* 1.01 V), the transient decay curves of the two PSCs were measured (see Figure 6-10b, where a tri-exponential fitting of the curves is also reported). The reference PSC is characterized by a slow V_{oc} decay trend with a τ_3 time constant of around 22 s, one order of magnitude higher than that of the cell with the MoS_2 ABL (τ_3 = 2 s). Considering that the V_{oc} decay trend is given by the recombination of the free charges at the perovskite/HTL interface,[501] this indicates that the presence of the MoS_2 ABL can activate additional recombination mechanisms with respect to the configuration where only the bare Spiro-OMeTAD is present. In fact, the MoS_2 ABL device shows a sudden voltage drop from +0.6 to 0 of normalized V_{oc} in comparison with the reference PSC with Spiro-OMeTAD (Figure 6.10b).

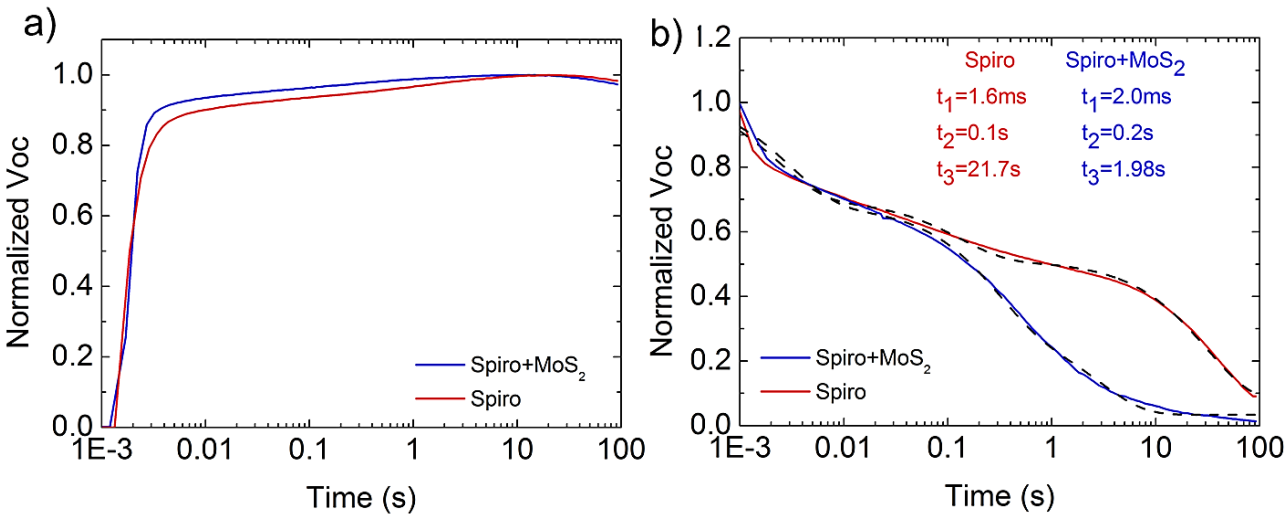

Figure 6.10. Transient photovoltage measurements of the cells with (blue curve) and without (red curve) MoS_2 ABL made with a switchable LED lamp. a) Transient V_{OC} rise, (from dark to light condition). b) Transient V_{OC} decay (from light to dark condition). The curves were fitted indicating the constant times (τ).

These results are in agreement with the J-V characteristic under dark conditions (Figure 6.11), where the PSC with the MoS_2 ABL has higher dark current values than the reference PSC in the

same voltage range from 0 to +0.6V. As already shown however, this V_{OC} decrease is compensated by the increase in J_{SC} (Figure 6.6) provided by the MoS_2 ABL, which overall also stabilize the PSCs.

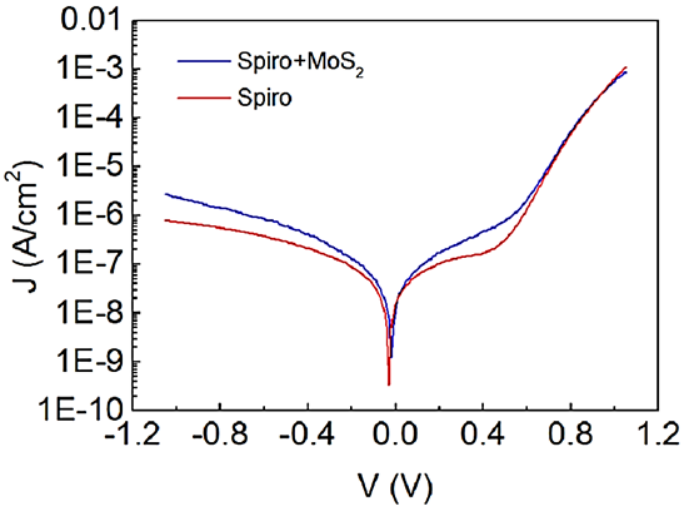

Figure 6.11. J-V characteristics in dark condition of the PSCs with (blue curve) and without (red curve) the MoS_2 ABL.

6.5.2 Ambient stable and Scalable PSCs using MoS_2 as hole transport interlayer

This section reports the use of MoS_2 flakes, produced by LPE of their bulk counterpart (as in the previous Section 6.4.1, see detail in Chapter 2), as HTL and ABL between the perovskite layer and the HTL (poly(triaryl amine) (PTAA)) in inverted PSCs. The replacement of poly(3,4-ethylenedioxythiophene) polystyrene sulfonate (PEDOT:PSS) HTL with exfoliated MoS_2 flakes in a thin –film form, resulted in comparable but less reproducible PCEs (12.46 vs 12.30 % at maximum). In contrast, when the MoS_2 flakes are introduced in between the state of the art HTL, *i.e.,* PTAA, and the $MAPbI_3$ absorber the devices PCE is increased (16.89 Vs 16.25 %). This effect, highly reproducible, is mainly due to improved hole extraction when MoS_2 is exploited. Additionally, but most importantly, the MoS_2 based PSCs' lifetime is significantly increased compared to the reference devices, due to the stabilization of the HTL/Perovskite interface In particular, encapsulated PSCs with MoS_2 interlayer retained 80% of their initial PCE (T_{80}) after ~568 hours of continuous illumination at maximum power output in ambient conditions. This is by far the highest ever reported lifetime for PSCs exposed in the above mentioned conditions to date. Moreover, this approach is scalable, i.e. the PSCs from small area (0.04 cm^2) to large area cells (0.5 cm^2), where MoS_2 and reference based devices resulted in averaged PCEs of ~13.17 and ~10.64 % respectively.

6.5.2.1 Architecture of the PSCs:

The PSCs are fabricated on pre-patterned ITO coated glass substrates (Naranjo Substrates) with dimensions of 20 x 15 mm and sheet resistance of ~20 Ω sq^{-1}. The impurities are removed from the ITO/glass through a three-step cleaning process (detergent deionized water, acetone, isopropanol). Before the deposition of the HTL, the substrates are placed inside an ultraviolet ozone cleaner in order to remove the organic contamination and increase the surface hydrophilicity of ITO coated substrates. In the case of $CH_3NH_3PbI_{3-x}Cl_x$ based PSCs, as the HTLs are used either the aqueous processed PEDOT:PSS (Heraeus) or the prepared MoS_2 dispersion. PEDOT:PSS is spin cast at 4000 rpm for 60 second and then annealed at 120 ^oC for 15 minutes, while MoS_2 thin film is prepared by spin casting the dispersion at 2000 rpm for 45 second for several times to achieve the desired thickness. Between each spin coating step the as prepared film is annealed at 100 ^oC for 1 minute. Contrary, in the case of the $CH_3NH_3PbI_3$ based PSCs, as the HTL is used the polymer PTAA (10 mg mL^{-1} in toluene) doped with 1.5% 2,3,5,6-Tetrafluoro-7,7,8,8-tetracyanoquinodimethane (F4TCNQ) small molecule. The PTAA thin film is prepared by spin casting the solution at 4000 rpm for 35 second, following by an annealing of the as prepared thin film at 110 ^oC for 10 minutes. Following the deposition of PTAA, the MoS_2 dispersion was spin cast at 2000 rpm for 45 second for two consecutive times. Afterwards, the $CH_3NH_3PbI_{3-x}Cl_x$ precursor solution is deposited onto PEDOT:PSS or MoS_2 thin films and the $CH_3NH_3PbI_3$ is deposited onto PTAA or PTAA/MoS_2 thin films. Then, a 2% PCBM in chlorobenzene solution is coated onto the perovskite layers at 1000 rpm. After that, 0.04% polyelectrolyte poly[(9,9-bis(30-(N,N-dimethylamino) propyl)-2,7-fluorene)-alt-2,7-(9,9-dioctylfluorene)] (PFN) in methanol is spin-coated on PCBM layer at 2000 rpm. Finally, the devices are transferred to vacuum chamber for Al electrode evaporation.

6.5.2.2 Photovoltaic Performance

As a preliminary test, to verify the merits of MoS_2 in devices, inverted PSCs using the architecture ITO/HTL/$MAPbI_{3-x}Cl_x$/PCBM/PFN/Al (Figure 6.12a) are fabricated, and PEDOT:PSS or MoS_2 are used as the HTLs. The energy levels of the different materials used in the device stack including the MoS_2 are presented in Figure 6.12b,[502] showing the almost perfect match between the V_{BM} of MoS_2 and the hybrid perovskite, indicating energy barrier-free hole extraction.

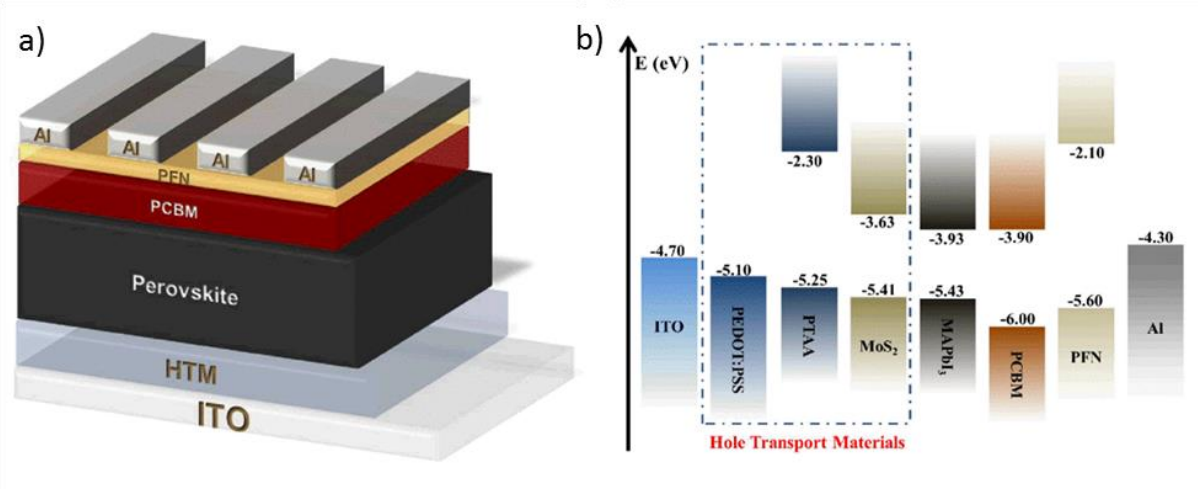

Figure 6.12. Structure, performance and photoluminescence response of the perovskite solar cells. Schematic a) device architecture and b) energy-band diagram under flat-band conditions of the fabricated planar inverted PSCs.

Figure 6.13a displays the J-V curves of the PEDOT:PSS and MoS_2 HTL based PSCs using the mixed halide perovskite ($MAPbI_{3-x}Cl_x$) as the solar absorber.

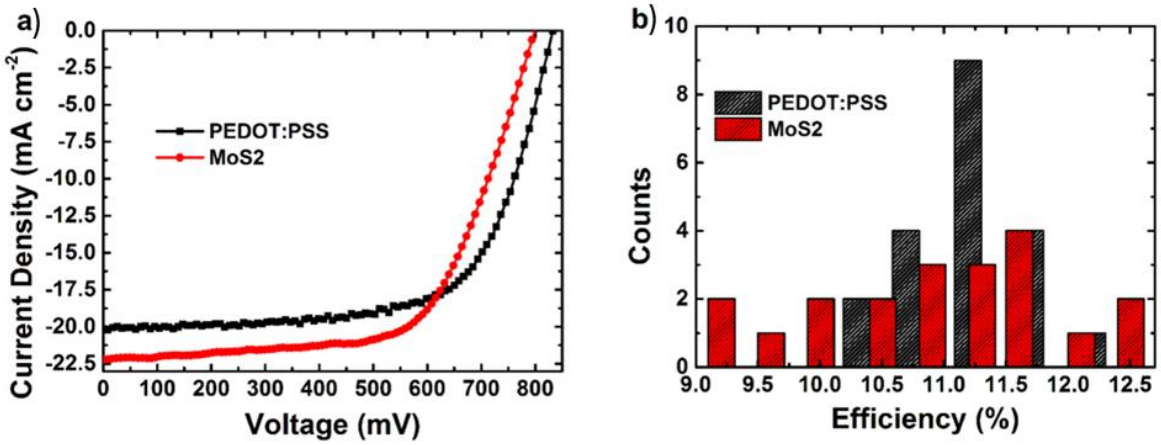

Figure 6.13. a) The J-V curves of PSCs based on PEDOT:PSS (black) and MoS_2 (red) HTLs measured under AM 1.5G (100 mW cm^{-2}) illumination. b) PCE distribution of the devices PEDOT:PSS (black) and MoS_2 (red) as HTLs, extracted from 20 identical devices.

As it can be seen in Table 6.2, a single spin coating step of the MoS_2 dispersion onto ITO leads to improvement of the PCE compared to the HTL-free device. However the PCE measured (7.80%) is by far lower with respect to that based on the PEDOT:PSS HTL ones (*i.e.*, 12.30%). This can be explained by the fact that a single spin-coating step cannot provide a uniform and compact MoS_2 layer covering the ITO substrate. This indicates that the PCE of the MoS_2 based devices should depends strongly on the MoS_2 flakes in a thin–film thickness and compactness. Therefore, investigations are conducted towards increasing MoS_2 layer thickness via successive spin-coating

steps. The optimum conditions are obtained when the ITO substrate was covered after 6 consecutive spin coatings of the MoS_2 dispersion.

Table 6.2. Photovoltaic Parameter of the devices with PEDOT:PSS and MoS_2 with different thicknesses HTLs

HTL	J_{sc} (mA/cm^2)	V_{oc} (mV)	FF (%)	Average PCE (Max.) (%)
No	10.11±3.24	701±38	45.6±5.6	3.23 (5.05)
PEDOT:PSS	20.08±1.32	832±8	67.3±1.1	11.24 (12.30)
MoS_2 (1 spin)	14.21±2.95	767±35	52.6±4.1	5.73 (7.80)
MoS_2 (5 spins)	21.33±1.46	796±33	59.0±3.2	10.02 (11.75)
MoS_2 (6 spins)	22.13±1.43	798±31	60.9±2.9	10.75 (12.46)
MoS_2 (7 spins)	21.84±1.49	797±31	60.0±2.6	10.44 (12.09)

An important enhancement in the J_{sc} from 20.08 to 22.13 mA cm^{-2} is observed, while, on the contrary, an important decrease was observed in both V_{oc} from 832 mV to 798 mV and in fill factor (FF) from 67.3% to 60.9% when MoS_2 in thin-film form is used as the HTL instead of PEDOT:PSS. As a result, using MoS_2 as the HTL, a PCE comparable with the PEDOT:PSS based PSCs is obtained (12.46 *vs*. 12.30 % at maximum). However, systematic investigation regarding the reproducibility of the devices (Figure. 6-13b), reveal that the MoS_2 based PSCs have low reproducibility if compared with the PEDOT:PSS cells.

In order to address the low observed device reproducibility and PCEs (~12.5%), the influence of MoS_2 thin film as an interfacial layer between the HTL and the perovskite of inverted PSCs is investigated using the structure ITO/HTL/MoS_2/Perovskite/PCBM/PFN/Al. Due to the absence of solvent orthogonality between the PEDOT:PSS solution and the MoS_2 dispersion (the spin-coating of MoS_2 dispersion washes out the as prepared PEDOT:PSS film) the state-of-the-art non-aqueous processed PTAA doped with 2,3,5,6-Tetrafluoro-7,7,8,8-tetracyanoquinodimethane (F4TCNQ) small molecule is used as HTL.[503,504] The HOMO and the LUMO energy levels of PTAA are -5.25 and -2.30 eV, respectively (Figure 6.12b).[505] Thus, by using the MoS_2 thin film with V_{BM} -5.41 eV as interfacial layer between the PTAA HTL (-5.25 eV) and the perovskite absorber (-5.43 eV), the hole extraction and in turn the performance of the device could potentially be improved.

Figure 6.14a displays the J-V curves of the PTAA and PTAA/MoS_2 HTL based PSCs using now the sequentially deposited $MAPbI_3$ as the solar absorber.[506] The thickness of MoS_2 thin film appeared to have less dependence in the performance of the device. Indeed, two consecutive spin-coatings of the MoS_2 dispersion onto the as prepared PTAA thin-films are adequate to achieve the highest possible PCE value (instead of 6 consecutive spin-coatings that required when MoS_2 is used as the HTL). In particular, the introduction of MoS_2 flakes in thin-films form as the interlayer between the PTAA and $MAPbI_3$ has a dual function. On one hand, it improves the PCE of inverted PSCs from 15.51 to 16.42 % (*i.e.* 6% enhancement, see Table 6-3). An appreciable enhancement in J_{sc} (from 20.05 to 20.71 mA cm^{-2}) and FF (from 76.63 to 78.41 %) is also observed, while V_{oc} value remained unchanged (from 1010 to 1011 mV). On the other hand, an improvement in the device reproducibility (Figure 6.14 b) is observed, overcoming the most important issue in the MoS_2 based HTL PSCs (where large deviation is observed). The standard deviations of the electrical parameters for both PSCs are extracted by fabricating 5 identical photovoltaic devices for each type consisting of 4 solar cells.

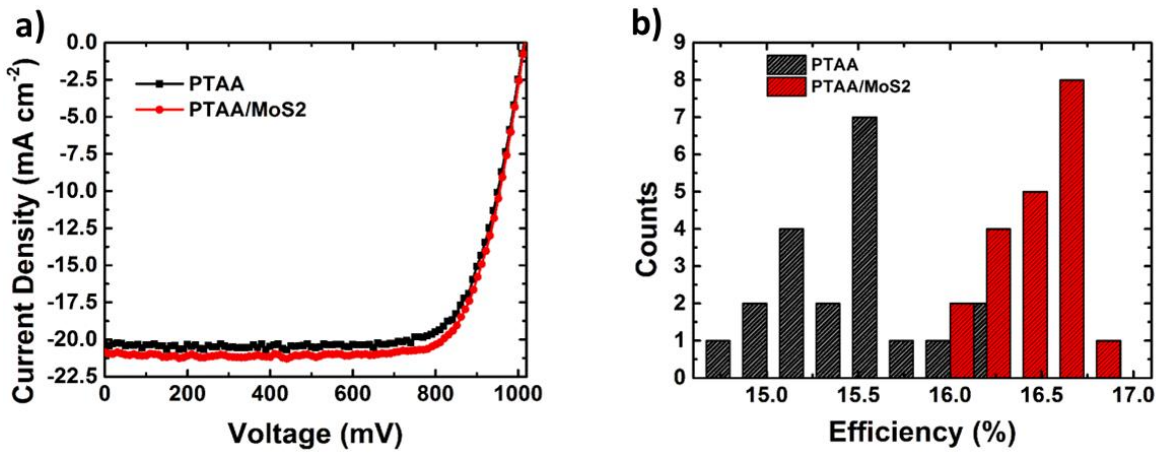

Figure 6.14. a) The J-V curves of PSCs based on PTAA (black) and PTAA/MoS_2 bilayer (red) HTLs measured under AM 1.5G (100 mW cm^{-2}) illumination. b) PCE distribution of the devices with (red) and without MoS_2 (black) interlayer extracted from 20 identical devices.

Table 6.3. Photovoltaic Parameter of the devices with the different HTLs

HTL	J_{sc} (Ma $^{cm-2}$)	V_{oc} (mV)	FF (%)	Average PCE (Max.) (%)
PTAA	20.05±0.48	1010±13	76.63±0.77	15.51 (16.25)
PTAA/MoS_2 (1 spin)	20.35±0.49	1010±10	77.88±0.61	16.01 (16.68)
PTAA/MoS_2 (2 spins)	20.71±0.35	1011±7	78.41±0.39	16.42 (16.89)
PTAA/MoS_2 (3 spins)	20.61±0.39	1009±8	78.11±0.35	16.24 (16.75)

To confirm the enhancement of the J_{sc} in the PTAA/MoS_2 compared to the neat PTAA HTL based devices, the EQE spectra for both PSCs are measured and compared (Figure 6.15a). It is clear, that the bilayer PTAA/MoS_2 HTL exhibits a broad and almost uniform increase in EQE, in the entire spectrum measured. Considering that the introduction of MoS_2 flakes in thin-film form reduces the offset between PTAA and $MAPbI_3$ due to the perfect alignment in the V_{BM} of MoS_2 and $MAPbI_3$, this enhancement in J_{sc} can only be explained in terms of improvement of charge inject and collection.[507] The integrated J_{sc} from EQE is not higher than 4% different from the actual measured J_{sc} values (see Table 6-3), indicating good accuracy of our electrical measurements.

In order to get an insight into the charge extraction properties of the photo generated carriers from the $MAPbI_3$ to the two different HTL systems, *i.e*., the PTAA and PTAA/ MoS_2, the samples' steady state PL spectra are measured and analyzed (Figure 6.15 b). The PL spectra are collected from perovskite films fabricated on glass/HTL substrates. It is evident that, the $MAPbI_3$ perovskite film deposited on PTAA/MoS_2 thin film shows a PL quenching, compared to the PTAA films, proving that MoS_2 interfacial layer has successfully enhanced the rate of carrier extraction at the HTL/perovskite interface.[507] Moreover, the introduction of MoS_2 as interfacial layer improves the reproducibility of the PL measurements (see error bar in Figure 6.15b). The PL result further supports our findings from the J-V and EQE spectra, suggesting that using MoS_2 as interlayer between the HTL and the perovskite absorber in PSC, the J_{sc} can be enhanced and the reproducibility of the device thus improved.

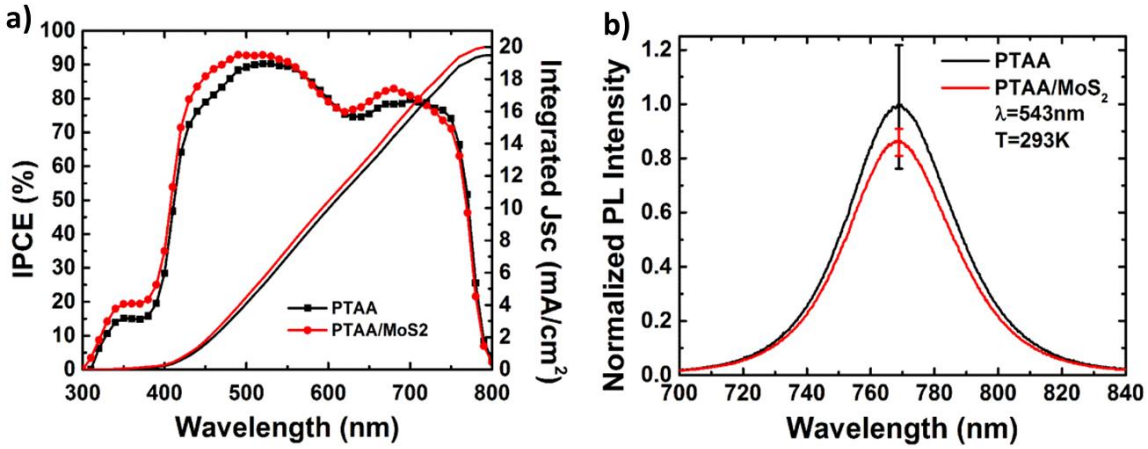

Figure 6.15. a) External quantum efficiency spectra of the PTAA (red) and PTAA/MoS_2 (black) based devices. b) Photoluminescence spectra (excitation at 543 nm) of $CH_3NH_3PbI_3$/PTAA (black) and MoS_2/PTAA/glass (red) substrates.

Figure 6-16 shows the stability measurements of the devices with and without the addition of MoS_2 thin film as the interfacial layer, under continuous solar illumination in ambient atmosphere. To obtain the data plot, the devices are scanned from SC to OC every 10 minutes. Surprisingly, as it can be seen in Figure 6.16a, the addition of MoS_2 as interfacial layer between PTAA and $MAPbI_3$ remarkably increases the device stability. In particular, on one hand the reference PSCs shows a significant decay of its PCE for the first few hours of the stress, where it finally almost completely fails after ~12 hours of stress. On the other hand the MoS_2 incorporated PSCs hugely improves the stability of the device performance, *i.e.*, after ~12 hours of the stress test the device preserved more than 97% of its initial PCE. By analyzing the characteristic values that determine the PCE, *i.e.*, J_{sc}, V_{oc} and FF, over time, (Figure 6.16b,c,d respectively) the most important difference is observed for J_{sc} and FF and less important for V_{oc} values. This implies that the incorporation of MoS_2 between the HTL and the perovskite absorber mostly affects and stabilizes this interface,[507] inhibits the light activated photocurrent degradation, but also seem to slightly stabilize the perovskite bulk.[506] In PSCs, HTLs plays key role because they act both as charge dissociation and transporting layer, as well as suppressing charge recombination.[508] As recently reported, PTAA HTL has very low conductivity and in order to effectively conduct holes its doping with F4TCNQ small molecule is mandatory. However as discussed above, this doping process induces a tradeoff between the PCE and the stability of the device, *i.e.*, the more efficient the device are the faster it degrades.[509]

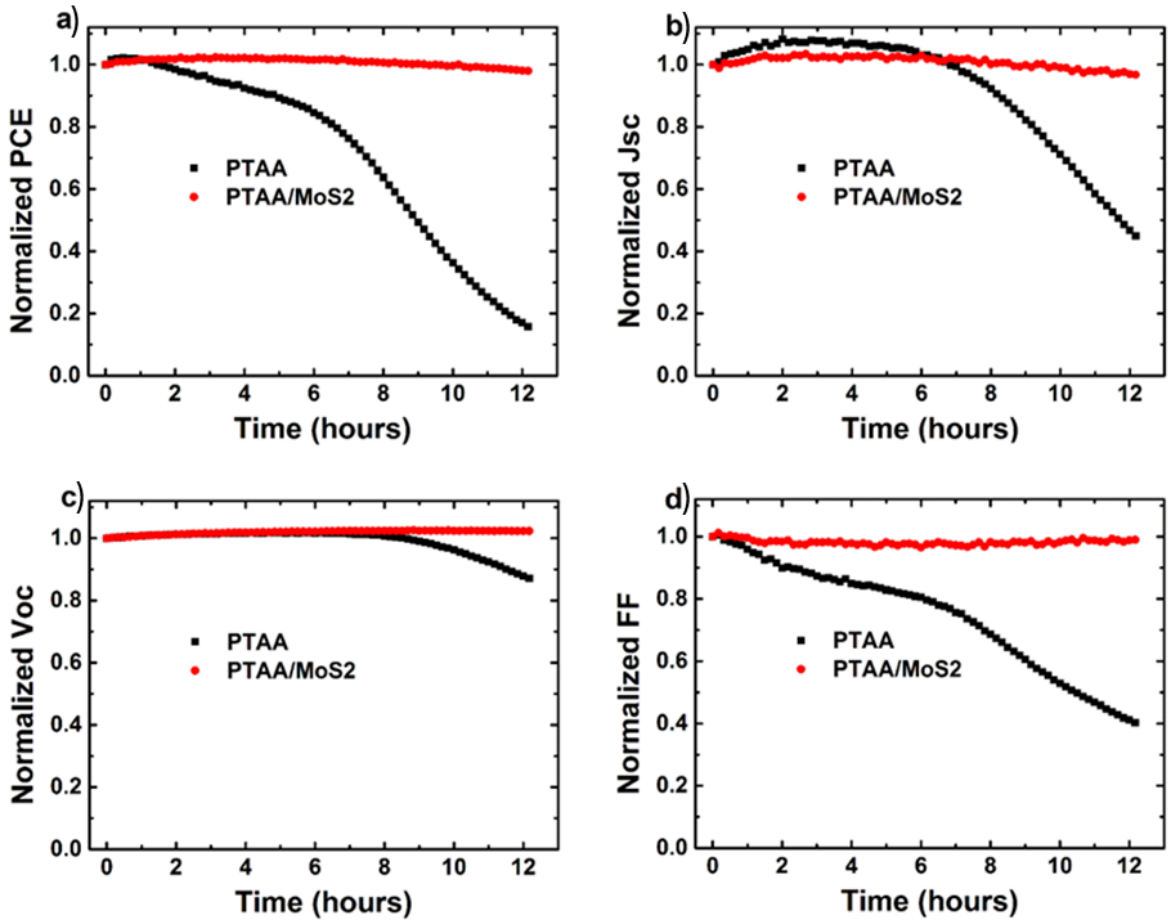

Figure 6.16. Unsealed perovskite solar cells stability. Evolution of normalized a) PCE, b) Jsc, c) Voc and d) FF of PTAA (black) and PTAA/MoS2 (red) HTMs based PSCs under continuous AM 1.5 G illumination (100 mW cm^{-2}) in ambient conditions (~50% RH).

In order to prove this aspect in our devices, inverted PSCs with and without MoS_2 thin film as interfacial layer are prepared and characterized, with the only difference compared to the previous presented J-V measurements being that the PTAA HTL is not doped with F4TCNQ small molecule. In Figure 6.17 are presented the J-V curves of the devices with and without the MoS_2 interfacial layer.

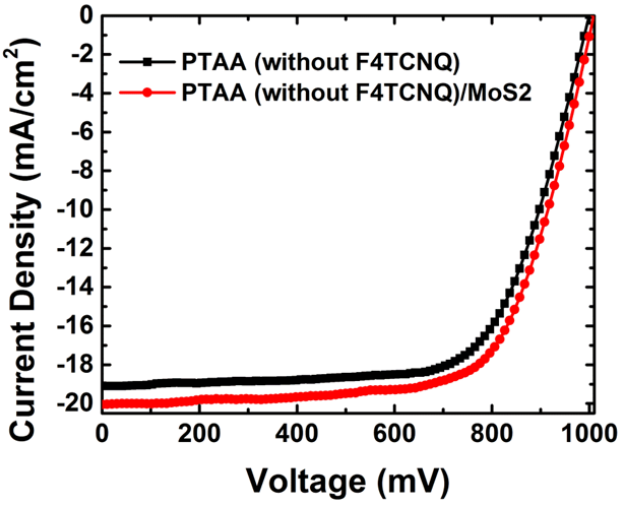

Figure 6.17. The J-V curves of PSCs based on undoped (F4TCNQ-free) PTAA (black) and PTAA/MoS_2 bilayer (red) HTLs measured under AM 1.5G (100 mW cm^{-2}) illumination.

In Table 6.4 the averaged photovoltaic characteristics for each device are summarized. Indeed without the addition of F4TCNQ in the PTAA and PTAA/MoS_2 HTLs the devices PCE are decreased by ~15% for both cells with an averaged PCE of 13.06% and 13.95% respectively.

Table 6-4. Photovoltaic parameters of undoped PTAA and undoped PTAA/MoS_2 based perovskite solar cells

Devices	J_{sc} (mA/cm^2)	V_{oc} (mV)	FF (%)	PCE (%)
Undoped PTAA	19.09	990	69.10	13.06
Undoped PTAA/MoS_2	20.05	995	69.94	13.95

Now regarding the lifetime of the undoped PTAA and PTAA/MoS_2 based PSCs, the degradation experiment is repeated using the same experimental conditions. As it can be seen in the Figure 6.18, the undoped PTAA based device retarded ~ 70% of its initial PCE after 12 hours of the stress, where in the same time scale the doped device retarded ~20% of its initial PCE. This indicates that the doping of PTAA with F4TCNQ on one hand improves the device performance but also and more importantly activates a process that speeds up the device failure. On the other hand, the addition of F4TCNQ in MoS_2 covered PTAA PSCs, does not have any important affect in the device degradation. This implies that the MoS_2 thin film acts as a barrier for F4TCNQ doped PTAA layer to come in contact with the perovskite layer, preventing in this way the PTAA film or the perovskite film (or both) to be degraded. The decay of J_{sc} and FF parameters for both cells are found to follow

an almost similar trend, with the degradation rate of PTAA/MoS_2 PSCs to be slightly slower. Most importantly, the V_{oc} trend for both cells is exactly the same with a very stable value during the entire stress test, indicating the absence of perovskite bulk degradation in the absence of the F4TCNQ dopant.

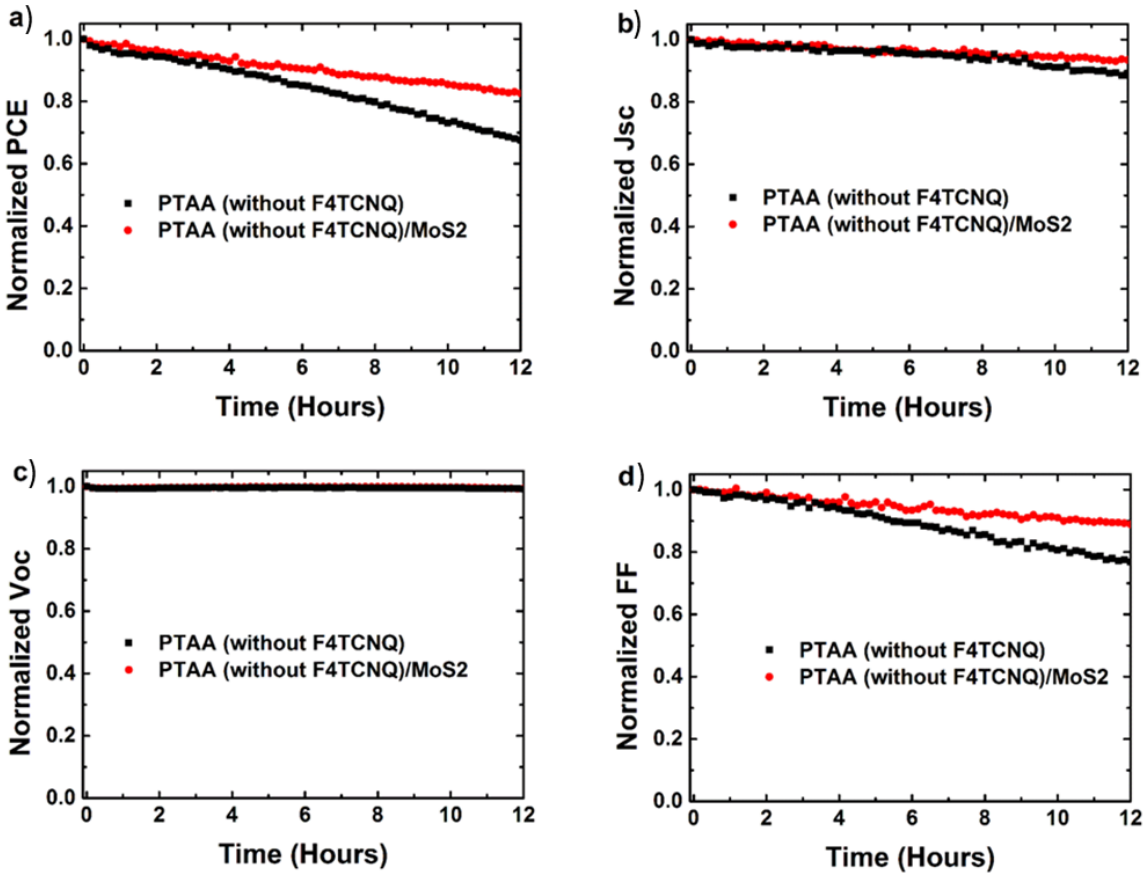

Figure 6.18. Evolution of normalized a) PCE, b) J_{sc}, c) V_{oc} and d) FF of undoped (F4TCNQ-free) PTAA (black) and PTAA/MoS_2 (red) HTLs based PSCs under continuous AM 1.5 G illumination (100 mW cm^{-2}) in ambient conditions.

Besides the preliminary stability tests of unsealed devices, to further explore the potential of MoS_2 based devices, PSCs with and without the MoS_2 interlayer are fabricated and encapsulated inside a nitrogen filled glove box and their long term lifetime is recorded in ambient conditions under continuous light exposure by constantly tracking the maximum power output. This stability test is included to a number of protocols that should be passed from a solar technology before the devices or modules are put into applications.[510] This protocol is not trivial to be passed by PSCs taking into account the hygroscopic nature of perovskite films, phase instabilities and light sensitivity.[511] Thus, this stress protocol is applied in devices with and without MoS_2 interlayer until

they both reach T_{80}, and an J-V scan is taken periodically to extract the device parameters (Figure 6.19).

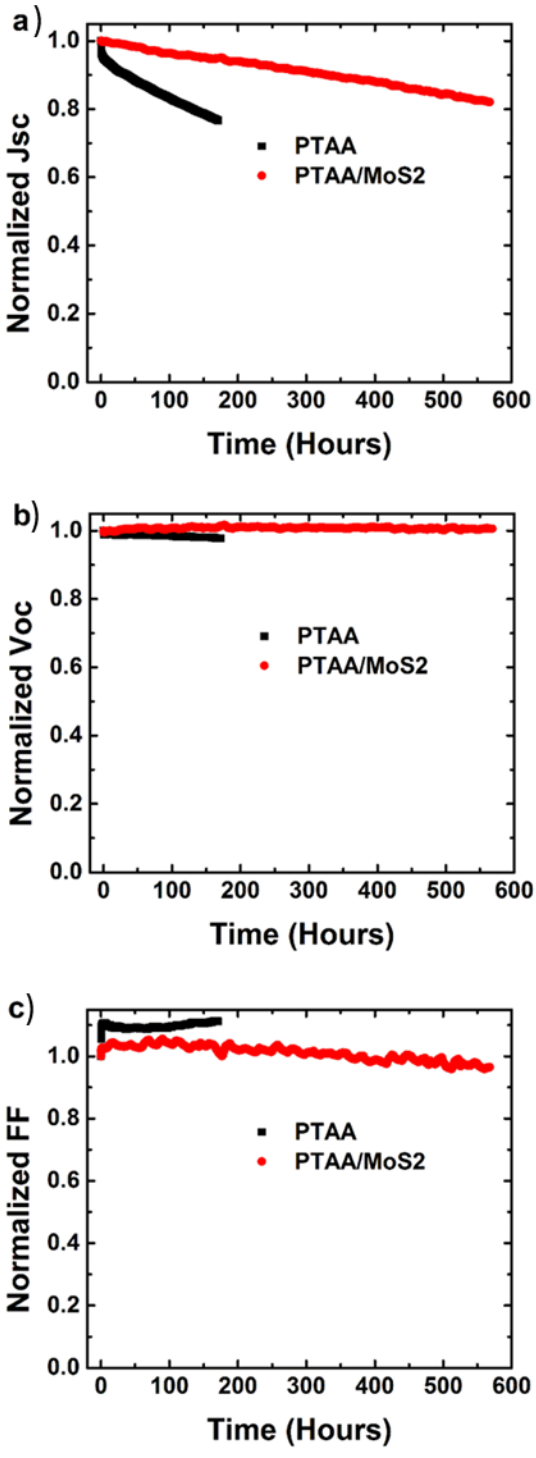

Figure 6.19. Normalized a) J_{sc}, b) V_{oc}, and c) FF trends of PTAA (black) and PTAA/MoS_2 based PSCs aged under continuous illumination and maximum power point tracking in a ambient atmosphere.

As shown in Figure 6.20, the reference device reach T_{80} after ~ 171 hours of the applied stress test showing a monotonic decay in PCE with a rate of ~ 0.115 %/hour (at the linear part), while the MoS_2 based at 171 hours retarded ~98% of its initial PCE. Surprisingly, MoS_2 based PSCs reach T_{80} after ~ 568 hours of continuous stress test showing a significantly slower decay rate of ~ 0.045 %/hour (at the linear part).

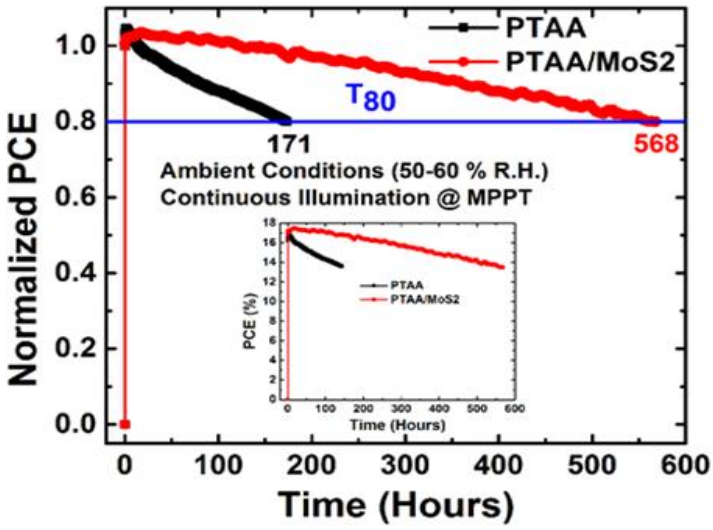

Figure 6.2. Lifetime test under continuous illumination at maximum power point tracking of devices with (red scatter) and without MoS_2 (black scatter) in ambient conditions. In the inset Figure are demonstrated the actual MPP values obtained for both devices

It is obvious that the proposed method of MoS_2 introduction as interfacial layer produces by far the most stable PSCs reported in the entire literature stressed in ambient conditions. Only two reports can be compared with our work in terms of long term stability, the one presenting T_{85} lifetime after ~500 hours (with very high performance of 21.4%), while the other presenting T_{95} lifetime after ~500 hours (with quite low performance of ~14%), but both stressing their devices in inert atmosphere and using the Cs-containing mixed cation [512] and the Rb-containing mixed cation [513] perovskites, respectively. In general, $MAPbI_3$ perovskite absorber (that we used also in our work) reported significantly lower lifetimes[514,515] compared with the multi-cation perovskites mainly using FA, Cs and Rb [512,513,516] a fact that further highlight the importance of our findings. The use of interface engineering for the formation of 2D/3D organic cation based-perovskite crystal structure, significantly improves the PSCs lifetime,[513] but again is by far inferior if compared with the multi-cation PSCs' lifetime. However, even the very stable triple cation perovskite, according to the device structure that is introduced, have presented lifetimes between 60 and 500 hours, demonstrating the crucial role of interfacial layers in PSCs lifetime.[512,516]

Finally, except from the effect of the MoS_2 interfacial layer in the PSCs performance and stability, the effect of MoS_2 interfacial layer in the device scaling up from small area (0.04 cm^2) to large area cell (0.5 cm^2) is studied. A trigger to perform the scaling up experiment is due to the significantly improved reproducibility in J-V characteristics and PL measurements of the MoS_2 incorporated samples. In Figure 6-21a are presented the J-V characteristics of PTAA and PTAA/MoS_2 based PSCs of both the small (solid lines) and large (dashed lines) area cells, while in Figure 6-21b displays a photograph of the as-prepared large-area cell. The obtained results are summarized in Table 6-5.

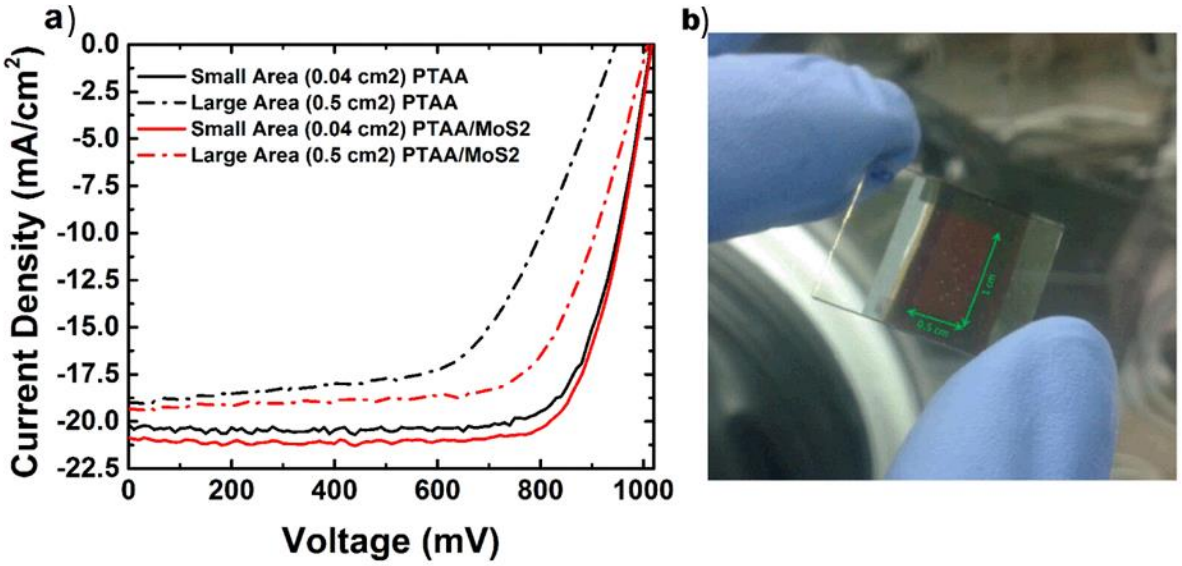

Figure 6.21. Performance of large area perovskite solar cells. a) J-V curves of the large-area cells (0.5 cm^2 active area) with (red dash-dot curve) and without MoS_2 (black dash-dot curve) measured under AM1.5G illumination with an intensity of 100 mW cm^{-2}. b) Photograph of a large-area cell with the MoS_2 interfacial layer.

Remarkably, the PCE of the large area cell with the MoS_2 interlayer is significantly higher compared to the reference large area cell (13.17% *vs*. 10.64%), having a higher V_{oc} with respect to the reference PSC (1009 *vs*. 949 mV). This indicates the better formation of $MAPbI_3$ in large area devices when MoS_2 is introduced as interfacial layer.

Table 6-5. Photovoltaic parameters of small (0.04 cm^2) and large area (0.5 cm^2) cells

Devices	J_{sc} (mA/cm^2)	V_{oc} (mV)	FF (%)	PCE (%)	PCE Drop (%)
Small Area PTAA	20.05	1010	76.63	15.51	-
Large Area PTAA	18.97	949	59.11	10.64	31.40
Small Area PTAA/MoS_2	20.71	1011	78.41	16.42	-
Large Area PTAA/MoS_2	19.35	1009	67.45	13.17	19.79

6.6 Summary

The introduction of MoS_2 flakes between the HTL and the $MAPbI_3$ absorber demonstrated to be effective in enhancing the efficiency of PSCs. Besides the higher PCE, MoS_2 significantly improve the stability of encapsulated devices stressed in ambient conditions under continuous light exposure by constantly tracking the maximum power output and the achieved T_{80} lifetimes are by far the highest reported in the entire literature of PSCs. Such superior device stability is ascribed to the twofold beneficial role of MoS_2, inhibiting both interface and structural aging pathways. Moreover, the beneficial role of MoS_2 in scalability of our devices is demonstrated by realizing large-area cells. These investigations pave the way towards high efficiency, large area and ultra-stable PSCs with lifetimes approaching to the industrial standards.

CHAPTER 7

CHAPTER 7: Conclusions and Future Directions

Energy efficiency improvement and fossil fuel-related energy demand reduction are considered as the most promising and safest way to mitigate climate change. The success of this technology does not entirely depend on a specific index. Instead, a set of technical and non-technical issues (*e.g.,* resource assessment, economics, environmental adversity and system design) can be effective. Among all of those factors, the success of energy technologies depends on their corresponding cost of energy. A subset of this index may include elements such as operative and maintaining cost and design feasibility (modularity, scalability and material cost). In this context, 2D materials have triggered a gold rush over the scientific research area for addressing the key-properties needed for advanced energy conversion and storage devices. A number of challenges still must be overcome in order to produce large, atomically uniform 2D layers, but the development of large scale and cost-effective production strategies of graphene and related materials for a commercial mass market is mandatory.

In the first stage of my Ph.D. thesis, production and characterization of 2D materials, such as graphene and Transition metal dichalcogenides -TMDs- (such as MoS_2 and $MoSe_2$) have been studied. Different procedures have been optimized to control the morphological properties of the materials (*i.e.,* dimensions and thickness and the edge-to-surface ratio), which are crucial for optimizing electrode performance in the final applications:

i) 2D materials such as graphene and 1T and 2H- MoX_2 (X=S, Se) have been produced by Li-aided intercalation and liquid phase exfoliation (LPE) in form of inks, providing scalable production and compatibility with large-area solution-processed deposition methods.

ii) Environmentally friendly solvothermal process in IPA has been demonstrated for the production of 2H-MoS_2 quantum dots (QDs) with average diameter of 6 nm.

iii) Once produced, the exfoliated materials have been characterized by different microscopic and spectroscopic techniques highlighting:

- Low oxidized byproducts percentage content (<5%).

- Defect-free flakes with mean lateral size on the order of few hundred nanometers and mean flake thickness in the 0.7-3 nm range.

In the second stage of my research work, I investigated the role of these 2D materials for energy conversion devices.

Transition metal dichalcogenides have been engineered for the design and fabrication of advanced pH-universal HER-electrocatalyst competing with state-of-the-art electrocatalysts technologies (the overpotential at 10 mA cm^{-2}-cathodic current density (η_{10}) 200 mA cm^{-2}). More in detail, I tackled the key-challenge to increase the number of electrocatalytic sites by designing and engineering HER-electrocatalytic active, solution-processed heterostructures between single-/few-layer TMD flakes/QDs and low-dimensional carbon-based materials (*i.e.,* graphene flakes or single wall carbon nanotubes –SWCNTs-). Such heterostructures have shown superior HER-electrocatalytic activity with respect to the one of the individual components. The most remarkable results achieved are summarized below:

i) Hybrid graphene flakes/2H-MoS_2 QDs heterostructures enable to reach a lower η_{10} (~136 mV) compared to both graphene flakes/2H-MoS_2 flakes (175 mV) and graphene flakes/1T-MoS_2 flakes (~151 mV) heterostructures. The as-produced 2H-MoS_2 QDs and the corresponding flexible graphene flakes/2H-MoS_2 QDs heterostructures are promising as viable and cost-effective HER-electrocatalysts.

ii) Electrochemical coupling between $MoSe_2$ flakes and graphene flakes or SWCNTs increases the $MoSe_2$ flakes HER-electrocatalytic activity. In detail, the optimization of the $MoSe_2$ flakes mass loading on SWCNTs and the electrode assembly via monolithic stacking of multiple heterostructures permit to achieve remarkable η_{10} of 100 mV and cathodic current density > 100 mA cm^{-2} at overpotential lower than 200 mV. Moreover, electrode thermal annealing in H_2 environment is effective for texturizing the $MoSe_2$ flakes basal plane, while electrode chemical bathing in n-butyllithium triggers the in situ semiconducting-to-metallic (2H-to-1T) phase conversion of the $MoSe_2$ flakes. In fact, unlike the 2H phase, the basal plane of the 1T phase is also HER-electrocatalytically active. However, the 1T phase is thermodynamically metastable, with relaxation energy of ~1.0 eV for the conversion to the stable 2H phase. Consequently, both thermal and chemical treatments generate new edge-/metallic-like HER-electrocatalytic sites in the $MoSe_2$ flakes. For example, The SWCNTs/$MoSe_2$ have shown a ~4.8-fold enhancement of the j_0

(from 29 to 167 μA cm^{-2}) after chemical treatment, and a ~20% decrease of the Tafel slope (from 67 to 54 mV dec^{-1}) after thermal annealing at 700 °C in Ar/H_2 (90/10%). The optimized heterostructures fully retain steady HER-electrocatalytic activities over more than 11 h, thus addressing proof-of-concept durability requirements.

iii) Transition Metal Choride (MCl_2)-chemical doping of single-/few-layer $MoSe_2$ flakes and the fabrication of stacked solution-processed heterostructures between MCl_2-doped $MoSe_2$ flakes and SWCNTs permit to achieve the key-requirements targeted in pH-universal large-scale H_2 production, *i.e.*, η_{10} of 80 mV for SWNTs/$MoSe_2$:$CdCl_2$ in acid condition, and 50 mV for SWCTNs/$MoSe_2$:$NiCl_2$ in alkaline condition.

Moreover, high-efficiency organic photocathodes, based on a rr-P3HT:PCBM bulk heterojunction sandwiched between charge-selective layers, have been developed. Specifically, the following results have been obtained:

i) MoS_2 flakes, produced by Li-aided exfoliation of the bulk MoS_2 powder, can be exploited as efficient HSLs for rr-P3HT:PCBM-based photocathodes. Solution-processed p-doping based on $HAuCl_4$ methanol solution allows us to tailor the Fermi levels, *i.e*. the work function (WF) values, of the MoS_2 films to higher values (from 4.6 eV of the pristine MoS_2 to 5.1eV). This determines a matching with the highest occupied molecular orbital (HOMO) level of rr-P3HT (5.1 eV), and an easing of the hole collection at the back-electrode (ITO). Interface engineering allows us to obtain a uniform and fully covered film morphology of MoS_2 flakes onto FTO, leading to solution-processed architectures with ϕ_{saved} of 0.423%, thus approaching the state-of-the-art values of 0.47% for solution-processed rr-P3HT:PCBM-based photocathodes.

ii) solution-processed graphene derivatives also behave as HSLs, boosting both the efficiency and the durability of rr-P3HT:PCBM-based photocathodes. In particular, the integration of graphene derivative-based HSL in organic photocathodes permits to achieve record-high performance. Graphene oxide-based photocathodes show ϕ_{saved} of 1.11% in 0.5 M H_2SO_4 solution. Moreover, the designed graphene derivative-based photocathodes can work in different pH environments, ranging from acid to basic. This is pivotal for their exploitation in tandem configurations, in which photoanodes operate only in restricted electrochemical conditions. Furthermore, all-solution processed fabrication of the graphene-based photocathodes is effective for the realization of

large-area (~9 cm^2) photocathodes on flexible substrate, achieving ϕ_{saved} of 0.31%. This is the first demonstration of scalable, flexible and high-efficient rr-P3HT:PCBM-based photocathodes.

Lastly, I have demonstrated how the incorporation and the interface engineering of MoS_2 flakes is pivotal in improving the photovoltaic performances of traditional HTL in perovskite solar cells (PSCs). I also demonstrated how the interface engineering is strongly improving the stability of the PSCs. The most important results are summarized below:

i) Solution-processed few-layer MoS_2 flakes are effective as active buffer layer between perovskite and Spiro-OMeTAD for increasing the efficiency and the stability of large-area (> 1 cm^2) devices. In detail, MoS_2 flakes have a twofold function: 1) they act as a protective layer, by preventing the formation of shunt contacts between the perovskite and the Au electrode; 2) they provide a hole transport layer from the perovskite to the Spiro-OMeTAD. As prepared PSC demonstrates a η of 13.3%, along with a higher lifetime stability over 550 h with respect to reference PSC without MoS_2 ($\Delta\eta/\eta=-7\%$ vs. $\Delta\eta/\eta=-34\%$). Large-area PSCs (1.05 cm^2 active area) demonstrate the scalability of this approach (η of 11.5%).

ii) MoS_2 flakes thin film as an interfacial layer between the HTL and the perovskite is beneficial for increasing the performance in inverted PSC given by the ITO/PTAA/MoS_2/Perovskite/PCBM/PFN/Al structure. In particular, the introduction of MoS_2 flakes between the PTAA and the perovskite absorber enhance the efficiency of the inverted PSCs, achieving record high PCE of ~17%. In addition, MoS_2 flakes interfacial layer significantly improves the stability of encapsulated devices stressed in ambient conditions. After ~568 hours of continuous solar light exposure at the maximum power output, the MoS_2 flakes-based devices retained ~80% of their initial PCE, with decay rate of ~ 0.045 %/hour. This is by far the highest ever reported lifetime for PSCs exposed in the above mentioned conditions to date. Moreover, the use MoS_2 flakes as active buffer layer in inverted PSC is scalable, as proved by the fabrication of large-area cells of 0.5 cm^2 with PCE higher than 13%.

In conclusion, this Ph.D. research has brought new knowledge, opening new prospective, to the current field of 2D material-based energy conversion devices. These methods contribute to advance the conversion of laboratory prototypes into large-area, light and flexible efficient energy conversion systems.

Future Directions:

Currently, the family of the 2D materials is continuously growing by exploiting the unusual and complementary physical properties of new 2D materials. Therefore a limitless combination of (opto)electronic, mechanical and thermal properties can be explored. This is only a primitive stage and it is foreseen that this thematic will have a boost in the near future. Following this consideration, my forthcoming activities will be focused on the optimization of production methods of 2D materials, as well the exfoliation of novel layered materials by adopting scalable solution-processed techniques. Hopefully, this will be advantageous for optimizing further the (photo)electrochemical (PEC) cells and PSCs presented in my Ph.D thesis. Moreover, by synergistically exploiting the properties of the available 2D materials, I will attempt to produce new hybrid devices with unprecedented functionalities, widening my research activity also on energy storage systems, like batteries and supercapacitors, which could be integrated in PEC cells and PSCs to give self-energy storing devices. By doing so, the 2D material-based design I have developed will be exploited to enhance the state-of-art performance of the technologies currently available.

References

[1] A.R. Oganov, R.J. Hemley, R.M. Hazen, *Rev. Mineral. Geochem*, **2013**,75,47.
[2] M.S. Dresselhaus, G. Dresselhaus, P.C. Eklund , Science of fullerenes and carbon nanotubes: their properties and applications ,**1996.**
[3] https://www.cheaptubes.com/carbon-nanotubes-applications/
[4] K. S. Novoselov, A. K. Geim, S. V. Morozov, D. Jiang, Y. Zhang, S. V. Dubonos, I. V. Grigorieva, and A. A. Firsov. *Science*, **2004**, 306, 666.
[5] A.K. Geim, K.S. Novoselov, *Nat Mater*, **2007,** 6, 183.
[6] P. R. Wallace, *Phys. Rev.* **1947**, 71, 622.
[7] A.Krishnan, E. Dujardin, M.M.Treacy, J. Hugdahl, T.W. Ebbesen, *Nature* **1997**,388, 451..
[8] K. S. Novoselov, D. Jiang, F. Schedin, T. J. Booth, V. V. Khotkevich, S. V. Morozov, A. K. Geim, *PNAS*,**2005**, 102, 10451.
[9] RSAS, Graphene. Scientific Background on the Nobel Prize in Physics **2010**.
[10] http://www.craigbanksresearch.com/page3.php
[11] A. H. C. Neto, F. Guinea, N. M. R. Peres, K. S. Novoselov, A. K. Geim, *Rev. Mod. Phys.*, **2009**, 81, 109.
[12] F. Bonaccorso, Z. Sun, T. Hasan, A.C. Ferrari , *Nat. Photonics*, **2010**, 4.9: 611.
[13] M. El Saba, Transport of Information-Carriers in Semiconductors and Nanodevices, **2017**.
[14] K. S. Novoselov, A. K. Geim, S. V. Morozov, D. Jiang, M. I. Katsnelson, I. V. Grigorieva, S. V. Dubonos , A. A. Firsov, *nature*, **2005**, 438, 197.
[15] S.Y. Zhou, G.-H. Gweon, A.V. Fedorov, P.N. First, W.A. de Heer, D.-H. Lee, F. Guinea, A.H. Castro Neto, A. Lanzara, *Nat. Mater*.,**2007**, 6, 770.
[16] M. Mecklenburg, B.C. Regan, *Phys. Rev. Lett*., **2011**, 106,116803.
[17] T. Ando , *nature*, **2009** , 1,17.
[18] N. W. Ashcroft , N. D. Mermin. *Solid State Physics. Harcourt College Publishers*, **1976**.
[19] A. K. Geim , *Science*, **2009**, 324,1530.
[20] S.V.Morozov, K.S. Novoselov, A.K. Geim, *Physics-Uspekhi*, **2008**,51,744.
[21] A.C. Ferrari, F. Bonaccorso, V. Fal'Ko, K.S. Novoselov,et al, *Nanoscale*, **2015**, 7, 4598.

[22] A.r A. Balandin, S. Ghosh, W. Bao, I. Calizo, D. Teweldebrhan, F. Miao, C. N. Lau,*Nano Lett*., **2008**, 8, 902.
[23] D. W. Kim, Y.H. Kim, H. S. Jeong , H.T. Jung, *Nat. Nanotechnol*., **2012**, 7, 29.
[24] R. R. Nair, P. Blake, A. N. Grigorenko, K. S. Novoselov, T. J. Booth, T. Stauber, N. M. R. Peres, A. K. Geim, *Scienc*e, **2008**, 320, 1308.
[25] K.F. Mak, L. Ju, F. Wang, T.F. Heinz, *Solid State Commun*., **2012**, 152, 1341.
[26] F. Bonaccorso, Z. Sun, T. Hasan, A.C. Ferrari, *Nat. Photonics,* **2010***, 4, 611.*
[27] E. Voloshina, Y. Dedkov, Electronic and magnetic properties of the graphene-ferromagnet interfaces: Theory vs. experiment. InTech, **2011**.
[28] F. Bonaccorso, Z. Sun, T .Hasan, A.C. Ferrari, *Nature photonics*, **2010**, 4,611.
[29] D.G. Papageorgiou, *Prog. Mater.Sci*., **2017**, 90, 75.
[30] C. Lee, X.D. Wei, J.W. Kysar, J. Hone,, *Science* , **2008**, 321,385.
[31] C.S. Ruiz-Vargas ,H.L. Zhuang ,P. Huang ,A. van der Zande ,S. Garg ,P. McEuen,.*Nano Lett*, **2011**,11,2259.
[32] R. Nicholl, H. Conley , N. Lavrik ,I. Vlassiouk, V. Sreenivas , *Nat Commun* ,**2015**,6.
[33] S. Deng, V. Berry. *Mater Today*, **2016**, 19,197.
[34] P. Zhang, L. Ma, F. Fan, Z. Zeng, C. Peng, P.E. Loya, ,*Nat Commun*, **2014**, 5 3782.
[35] E. Pop, V. Varshney, A. Roy. *MRS Bullettin*, **2012**, 37,1273.
[36] S.Berber, Y.K. Kwon, D. Tomanek, *Phys Rev Lett*. **2000**, 84, 4613.
[37] P. Kim, L. Shi, A. Majumdar,P.L. McEuen, *Phys. Rev. Lett*. **2001**, 87, 215502.
[38] A.A. Balandin,S. Ghosh ,W. Bao, I. Calizo, D. Teweldebrhan , F. Miao, *Nano Lett*, **2008**, 8, 902.
[39] V. Singh, D. Joung, L. Zhai , S. Das , S. I. Khondaker , S. Seal, *prog. mater. sci*., **2011**, 56, 1178.
[40] R. Balog, B. Jørgensen, L. Nilsson, M. Andersen, E. Rienks, M. Bianchi, M. Fanetti, E. Lægsgaard, A.Baraldi, S.Lizzit, Z. Sljivancanin, F. Besenbacher, B. Hammer, T. G. Pedersen, P. Hofmann, L. Hornekær, *Nat Mater*, **2010**, 9, 315.
[41] M.W.Lin, C. Ling, Y.Zhang, H. J. Yoon, M. Cheng, L.A. Agapito, N. Kioussis, N. Widjaja, Z. Zhou, *Nanotechnology,* **2011***,* 22, 265201.
[42] X.L. Li, X.R. Wang, L. Zhang, S.W. Lee, H.J. Dai, *Science,* **2008***,* 319, 1229.
[43] D. Jariwal, A. Srivastav, M. Ajayan, J. Nanosci. Nanotechnol, **2011**, 11, 6621.
[44] A. K. Geim , I. V. Grigorieva, Nature, 2013, 499, 419.
[45] H. R. Gutiérrez, N.P.López, A. L. Elías, A. Berkdemir, B. Wang, F. L. Urías, V. H. Crespi, H. Terrones, M. Terrones, Nano lett, 2012, 13, 3447.
[46] A. Splendiani, L. Sun, Y. Zhang, T. Li, J. Kim, C. Y. Chim,G. Galli and F. Wang, *Nano Lett*., **2010**, 10, 1271.
[47] S. F. Wu, J. S. Ross, G. B. Liu, G. Aivazian, A. Jones, Z. Y. Fei, W. G. Zhu, D. Xiao, W. Yao, D. Cobden and X. D. Xu, *Nat. Phys*., **2013**, 9, 149.
[48] B. Radisavljevic, A. Radenovic, J. Brivio, V. Giacometti ,A. Kis, *Nat. Nanotechnol*., **2011**, 6, 147.
[49] L. Britnell, R. V. Gorbachev, R. Jalil, B. D. Belle, F. Schedin, A. Mishchenko, T. Georgiou, M. I. Katsnelson, L. Eaves,S. V. Morozov, N. M. Peres, J. Leist, A. K. Geim, K. S. Novoselov , L. A. Ponomarenko, *Science*, **2012**, 335, 947.
[50] W. J. Yu, Z. Li, H. Zhou, Y. Chen, Y. Wang, Y. Huang, X. Duan, *Nat. Mater*., **2013**, 12, 246.
[51] O. Lopez-Sanchez, E. Alarcon Llado, V. Koman, A. Fontcuberta i Morral, A. Radenovic, A. Kis, *ACS Nano*, **2014**, 8, 3042.
[52] C. H. Lee, G. H. Lee, A. M. van der Zande, W. Chen, Y. Li, M. Han, X. Cui, G. Arefe, C. Nuckolls, T. F. Heinz, J. Guo, J. Hone , P. Kim, *Nat. Nanotechnol*., **2014**, 9, 676.
[53] E.P. Randviir, D.A.C. Brownson, C. E.Banks, *Mater. Today*, **2014**, 17, 426.
[54] F. Bonaccorso, A. Lombardo, T. Hasan, Z. Sun, L. Colombo, A. C. Ferrari, *Mater. Today*, **2012**, 15, 564.
[55] K. V. Emtsev, A. Bostwick, K. Horn, J. Jobst, G. L. Kellogg, L. Ley, J. L. McChesney, T. Ohta, S. A. Reshanov, J. Röhrl, E. Rotenberg, A. K. Schmid, D. Waldmann, H. B.Weber, T. Seyller: Nature materials, **2009**, 8, 203.
[56] C. Soldano, A. Mahmood, E. Dujardin: *Carbon*,**2010**, 48, 2127 .
[57] W. Kern, G.L. Schnable, *IEEE Trans Electron Devices*, **1979**, 26 , 647.
[58] A.E. Karu, M. Beer, *J Appl Phys*,**1966**, 37 ,2179.
[59] N.A. Kholin, *Surf. Sci*,**1984**, 139 ,155.
[60] N.R. Gall, E.V. Rut'Kov, A.Y. Tontegod, *Carbon*,**2000**, 38 , 663
[61] C. Charrier Diamond , *Relat .Mater*, **1994**, 3 , 41.
[62] J. Coraux, A.T. N. 'Diaye, C. Busse, T. Michely, *Nano. Lett*, **2008**, 8 , 565.
[63] A. Reina, X. Jia, J .Ho, D. Nezich, H. Son, V .Bulovic, *Nano Lett,* **2009**, 9 , 30.
[64] M.E. Ramon, A. Gupta, C. Corbet, D.A. Ferrer, *Acs Nano*, **2011** 5 ,7198
[65] C. Orofeo, H. Ago, B. Hu, M. Tsuji, *Nano Research*, **2011**, 4 , 531

[66] X. Li, W. Cai, J. An, S. Kim, J. Nah, D. Yang, R. Piner. *Science*,**2009**, 324 ,1312

[67] X. Li, W. Cai, L. Colombo, R.S. Ruoff, *Nano Lett*,**2009**, 9 ,4268

[68] G.A. Lopez, E. Mittemeijer , *Scr Mat*, **2004**, 51 ,1

[69] X. Li, Y. Zhu, W .Cai, M. Borysiak, B. Han, D. Chen. *Nano. Lett*, **2009**, 9 , 4359

[70] Maria Losurdo, Maria Michela Giangregorio, Pio Capezzuto and Giovanni Bruno, *Phys. Chem. Chem. Phys*., **2011**, 13, 20836.

[71] X. Li, C.W. Magnuson, A. Venugopal, J. An, J.W. Suk., *Nano Lett*, **2010**, 10 ,4328.

[72] X. Li, C.W. Magnuson, A. Venugopal. *J Am Chem Soc,* **2011**, 133 , 2816.

[73] K.L. Frese, *Surf. Sci*, **1987**, 182, 85

[74] T. Aoyama, M. Kiyotoshi, S .Yamazaki., *Jpn J Appl Phys Part 1,* **1999**, 38 , 2194

[75] Z. Luo, Y. Lu, D.W. Singer, M.E. Berck, L.A. Somers, B.R. Goldsmith, A.T.C. Johnson, *Chem. Mater*., **2011**, 23, 1441.

[76] H. Kim, C. Mattevi, M.R. Calvo, J.C. Oberg, L. Artiglia, S. Agnoli, C.F. Hirjibehedin, M. Chhowalla, E. Saiz, *ACS nano* **2012,** 6, 3614.

[77] T. Yoon, W.C. Shin, T.Y. Kim, J.H. Mun, T.S. Kim, B.J. Cho, *Nano lett*., **2012**, 12, 1448.

[78] K. S. Novoselov A. K. Geim, S. V. Morozov,2 D. Jiang, Y. Zhang, S. V. Dubonos, I. V. Grigorieva, A. A. Firsov: *Science* **2004**, 306, 666.

[79] A.C. Ferrari. *Solid State Communications*, **2007**, 143,47.

[80] J.H. Chen, C. Jang, S. Xiao, M. Ishigami, M.S. Fuhrer, *Nat. Nanotech*., **2008**, 3, 206.

[81] Y. Hernandez, V. Nicolosi, M. Lotya, F. M. Blighe, Z. Sun,S. De, I. T. Mcgovern, B. Holland, M. Byrne, Y. K. Gun'ko, J. J. Boland, P. Niraj, G. Duesberg, S. Krishnamurthy, R. Goodhue, J. Hutchison, V. Scardaci, A. C. Ferrari, J. N. Coleman: *Nature nanotechnology* , **2008**, 3, 563.

[82] UNIFAC TUC. DDBST GmbH. **2015**.

[83] T. Kuilla, S. Bhadra, D. Yao, N.H. Kim, S. Bose, *Prog. Polym. Sci*., **2010**, 11, 1350.

[84] C.I.L. Justino, A.R. Gomes, A.C. Freitas, A.C. Duarte, *TrAC Trends,* **2017***,* 91,53.

[85] H. Lee, M. Kim, I. Kim, H .Lee, *Adv. Mater.,***2016**,22, 4541.

[86] R. Raccichini, A. Varzi, S. Passerini, B .Scrosati, *Nat. Mater*., **2015**, 14,271.

[87] X.Wang, L. Zhi, K. Mullen, *Nano Lett.*, **2008**, 8, 323.

[88] J. R. Potts, D. R. Dreyer, C. W. Bielawski, R.S. Ruoff, *Polymer,* **2011***,* 52, 5.

[89] J. Sandler, M.S. Shaffer, T. Prasse, W. Bauhofer, K. Schulte, A.H. Windle, *Polymer*, **1999**, 40, 5967.

[90] Z. Yan, G. Liu, J.M. Khan, A.A. Balandin,*Nat.comm***. 2012**, 3, 827 .

[91] X. Wang, A. Pakdel, J. Zhang, Q. Weng, T. Zhai, C. Zhi, D. Golberg, Y. Bando, *Nanoscale Res. Lett.*, **2012**, 7, 1.

[92] B. Radisavljevic, A. Radenovic, J. Brivio, V. Giacometti , A. Kis, *Nat. Nanotechnol*.,**2011**, 6, 147.

[93] K. Guo, C. Si, C. Han, S. Pan, G. Chen, Y. Zheng, W. Zhu, J. Zhang, C. Sun, B. Wei, *Nanoscale*, **2017**,9, 14602.

[94] W.Zhang, P. Zhang, Z. Su, G. Wei, *Nanoscale*, **2015**,7, 18364.

[95] S.Wi, H. Kim, M. Chen, H. Nam, L. J. Guo, E. Meyhofer, X. Liang, *ACS Nano*, **2014**, 8, 5270.

[96] T. Stephenson, Z.Li, B. Olsen , D. Mitlin*, Energy Environ. Sci*., **2014**, 7, 209.

[97] D. Merki , X. Hu, *Energy Environ. Sci.,* **2011**, 4, 3878.

[98] J. Chen, N. Kuriyama, H. Yuan, H.T. Takeshita, T. Sakai, *JACS*, **2001**, 123, 11813.

[99] F. Bonaccorso, L.Colombo, G. Yu, M. Stoller, V. Tozzini, A. C. Ferrari, V. Pellegrini, *Science*,**2015**, 347, 1246501.

[100] X.Lee, H.Zhu, *J.Materiomics* , **2015**, 1 , 33.

[101] V. Nicolosi, M. Chhowalla, M. G. Kanatzidis, M. S. Strano and J. N. Coleman, *Science*, **2013**, 340, 1226419.

[102] F. Bonaccorso, A. Bartolotta, J. N. Coleman, C. Backes, *Adv. Mater*., **2016**, 28, 6136.

[103] S. H. El-Mahblawy, B. L. Evan, Phys. *Status Solidi B*, **1977**, 79, 713.

[104] C. Tsai, K. Chan, F. Abild-Pedersen, J. K. Norskov, *Phys. Chem. Chem. Phys.,* **2014**, 16, 13156.

[105] A. Capasso, A. E. Del Rio Castillo, H. Sun, A. Ansaldo, V. Pellegrini and F. Bonaccorso, *Solid State Commun.,* **2015**, 224, 53.

[106] A. Capasso, F. Matteocci, L. Najafi, M. Prato, J. Buha, L. Cinà, V. Pellegrini, A. Di Carlo and F. Bonaccorso, *Adv. Energy Mater.*, **2016**, 6, 1600920.

[107] F. Bonaccorso, A. Lombardo, T. Hasan, Z. Sun, L. Colombo, A. C. Ferrari, *Mater. Today*, **2012**, 15, 564.

[108] S. Bellani, L. Najafi, A. Capasso, A. E. Del Rio Castillo, M. R. Antognazza and F. Bonaccorso, *J. Mater. Chem. A*, **2017**, 5, 4384.

[109] G. Gao, Y. Jiao, F. Ma, Y. Jiao, E. Waclawik, A. Du, *J. Phys. Chem. C.,* **2015**, 119, 13124.

[110] H. Tsai, J. Heising, J.L. Schindler, C.R. Kannewurf, M.G. Kanatzidis, *Chem. Mater.,* **1997**, 9, 879.

[111] W.S. Hummers, R.E. Offeman, J. Am. Chem. Soc., 1958, 80, 1339.

[112] O. M. Maragò, F. Bonaccorso, R. Saija, G. Privitera, P. G. Gucciardi, M. A. Iatì, G. Calogero, P. H. Jones, F. Borghese, P. Denti, V. Nicolosi and A. C. Ferrari, *ACS Nano*, **2010**, 4, 7515.
[113] T. Hasan, F. Torrisi, Z. Sun, D. Popa, V. Nicolosi, G. Privitera, F. Bonaccorso and A. C. Ferrari, *Phys. Status Solidi B*, **2010**, 247, 2953.
[114] W. F. Linke, Solubilities: Inorganic and Metal-Organic Compounds, a Compilation of Solubility Data from the Periodical Literature, *3rd ed., New York: D. Van Nostrand Company,* **1965**.
[115] K. Li, M. Li, D. Xue, *J. Phys. Chem. A*, **2012**, 116, 4192.
[116] D.T. Richens, *Chem. Rev.* **2005**, 105, 1961.
[117] L.R. Snyder, *J. Chromatogr. Sci.*, **1978**, 16, 223.
[118] K.C. Kwon, K.S. Choi, C. Kim, S.Y. Kim, *Phys. Status Solidi A,* **2014**, 211, 1794.
[119] S.M. Kim, K.K. Kim, Y.W. Jo, M.H. Park, S.J. Chae, D.L. Duong, C.W. Yang, J. Kong, Y.H. Lee, *ACS Nano*, **2011**, 5, 1236.
[120] B. Martín-García, A. Polovitsyn, M. Prato and I. Moreels, *J. Mater. Chem. C.*, **2015**, 3, 7088.
[121] P. Schulz, E. Edri, S. Kirmayer, G. Hodes, D. Cahen, A. Kahn, *Energy Environ. Sci,.* **2014**, 7, 1377.
[122] A. Calloni, A. Abate, G. Bussetti, G. Berti, R. Yivlialin, F. Ciccacci, L. Duò, *J. Phys. Chem. C.,* **2015**, 119, 21329.
[123] V.G. Kravets, A.N. Grigorenko , R.R. Nair , P. Blake P, S. Anissimova ,K.S. Novoselov ,A.K. Geim , *Phys. Rev. B,* **2010**, 81 155413.
[124] M. Lotya, Y. Hernandez ,P.J. King, R.J. Smith , V. Nicolosi , L.S. Karlsson , F.M. Blighe , G.S. Duesberg , J.N. Coleman , *J. Am. Chem. Soc.,* **2009**, 131, 3611.
[125] A.C. Ferrari ,J.C. Meyer , V. Scardaci , C. Casiraghi , M. Lazzeri , F. Mauri , S. Piscanec ,D. Jiang, K.S. Novoselov, S. Roth, A.K. Geim, *Phys. Rev. Lett.*, **2006**, 97, 187401
[126] A.C. Ferrari ,D.M. Basko , *Nat. Nanotechnol.,* **2013**, 8, 235.
[127] A.C. Ferrari , J. Robertson, *Phys. Rev. B*, **2000**, 61, 14095.
[128] A.C. Ferrari , J. Robertson , *Phys. Rev. B*, **2001**, 64, 075414
[129] C.Y. Su , Y. Xu , W. Zhang , J. Zhao, X. Tang, C. Tsai, L. Li, *J. Chem. Mater.,* **2009**, 21, 5674.
[130]M.V. Bracamonte, G.I. Lacconi, S.E. Urreta, L.E. Foa Torres , *J. Phys. Chem. C,* **2014**, 118, 15455.
[131] M. Lotya,Y. Hernandez,P.J. King, R.J. Smith, V. Nicolosi, L.S. Karlsson, F.M. Blighe , G.S. Duesberg, J.N. Coleman, *J. Am. Chem. Soc.,* **2009**, 131, 3611.
[132] J.N. Coleman, *Acc. Chem. Res.,* **2013**, 46, 14.
[133] O.M. Maragó, F. Bonaccorso, R. Saija, G. Privitera, P.G. Gucciardi, M.A. Iati, G. Calogero, P.H. Jones, F. Borghese, P. Denti, V. Nicolosi, *ACS Nano*, **2010**, 4, 7515.
[134] J. Hassoun, F. Bonaccorso, M. Agostini, M . Angelucci, M.G. Betti, R. Cingolani, M. Gemmi, C. Mariani, S. Panero , V. Pellegrini, B. Scrosati , *Nano Lett.,* **2014**, 14, 4901.
[135] D. Graf, F. Molitor, K. Ensslin, C. Stampfer ,A. Jungen,C. Hierold , L. Wirtz , *Nano Lett*., **2007**, 7, 238.
[136] D. Yang, A. Velamakanni , G. Bozoklu , S. Park, M. Stoller , R.D. Piner, S. Stankovich , I. Jung. R.S. Ruoff, *Carbon,* **2009**, 47, 145.
[137] R. Buzio, A. Gerbi, C. Bernini, A.E. Del Rio Castillo, F. Palazon, A.S. Siri, V. Pellegrini, L. Pellegrino, F. Bonaccorso, *Nanoscale*, **2017**, in press.
[138] J.I Paredes, S. Villar-Rodil, A. Martínez-Alonso, J.M. Tascón, *Langmuir*, **2008**, 24, 10560.
[139]Q. Lai, S. Zhu, X. Luo, M. Zou, S. Huang, *AIP Adv.* **2012**, 2, 32146.
[140] D. Li, M.B. Muller, S. Gilje, R.B. Kaner, G.G. Wallace, *Nat Nano.* **2008**, 3, 101.
[141] D. A. Skoog, F. J. Haller, T. A. Niemann. Principles of Instrumental Analysis; Hartcourt Brace & Company: Philadelphia; **1998**.
[142] X.L. Hou, J.L. Li, S.C. Drew, B. Tang, L. Sun, X.G. Wang, *J. Phys. Chem. C* . **2013**, 117, 6788.
[143] X. Zhao, Q. Zhang, D. Chen, P. Lu, *Macromolecules* . **2010**, 43, 2357.
[144] I.K. Moon, J. Lee, R.S. Ruoff, H. Lee, *Nat. Commun.* **2010,** 1, 73.
[145] P. Venezuela, M. Lazzeri, F. Mauri, *Phys. Rev. B*. **2011**, 84, 35433.
[146] O. Marago, F. Bonaccorso, R. Saija, G. Privitera, P.G. Gucciardi, M.A. Iatì, G. Calogero, P.H. Jones, F. Borghese, P. Denti, *ACS Nano*. **2010**, 4, 7515.
[147] A. Dualeh, N. Tétreault, T. Moehl, P. Gao, M.K. Nazeeruddin, M. Grätzel, *Adv. Funct. Mater.* **2014**, 24, 3250.
[148] P. Wang, Z.G. Liu, X. Chen, F.L. Meng, J.H. Liu, X.J. Huang,. *J. Mater. Chem. A*. **2013**, 1, 9189.
[149]A. Lazauskas, J. Baltrusaitis, V. Grigaliūnas, A. Guobienė, I. Prosyčevas, P. Narmontas, B. Abakevičienė, S. Tamulevičius, *Superlattices Microstruct.* **2014**, 75, 461.
[150] Y. Huang, J. Wu, K.C. Hwang, *Phys. Rev. B.* **2006,** 74, 245413.
[151] K.S. Novoselov, A.K. Geim, S.V. Morozov, D. Jiang, Y. Zhang, S.V. Dubonos, I.V. Grigorieva, A.A. Firsov, *Science.* **2004**, 306, 666.

[152] D. Yang, A. Velamakanni, G. Bozoklu, S. Park, M. Stoller, R.D. Piner, S. Stankovich, I. Jung, D.A. Field, C.A. Ventrice *Carbon*, **2009**, 47, 145.
[153]M. Dhayal, R. Kapoor, P.G. Sistla, R.R. Pandey, S. Kar, K.K. Saini, G. Pande, *Mater. Sci. Eng. C.* **2014**, 37, 99.
[154] M. Dhayal, M.R. Alexander, J.W. Bradley, *Appl. Surf. Sci.* **2006**, 252, 7957.
[155] Z. Bo, X. Shuai, S. Mao, H. Yang, J. Qian, J. Chen, J. Yan, K. Cen, *Sci. Rep.* **2014**, 4, 4684.
[156] K. Dave, K.H. Park, M. Dhayal, *RSC Adv.* **2015**, 5, 95657.
[157] C. Mattevi, G. Eda, S. Agnoli, S. Miller, K.A. Mkhoyan, O. Celik, D. Mastrogiovanni, G. Granozzi, E. Garfunkel, M. Chhowalla, *Adv. Funct. Mater.* **2009**, 19, 2577.
[158] X. Dong, C.Y. Su, W. Zhang, J. Zhao, Q. Ling, W. Huang, P. Chen, L.J. Li, *Phys. Chem. Chem. Phys.* **2010**, 12, 2164.
[159] H.A. Becerril, J. Mao, Z. Liu, R.M. Stoltenberg, Z. Bao, Y. Chen, *ACS Nano*, **2008**, 2, 463.
[160] P.V. Kumar, M. Bernardi, J.C. Grossman, *ACS Nano*. **2013**, 7, 1638.
[161] B. Kang, S. Lim, W. Lee, S.B. Jo, K. Cho, *Adv. Mater.* **2013**, 25, 5856.
[162] L. Sygellou, G. Paterakis, C. Galiotis, D. Tasis, *J. Phys. Chem. C.* **2016**, 120, 281.
[163] H. Yamaguchi, S. Ogawa, D. Watanabe, H. Hozumi, Y. Gao, G. Eda, C. Mattevi, T. Fujita, A. Yoshigoe, S. Ishizuka, *Phys. status solidi* . **2016**, 213, 2380.
[164] D.S. Sutar, G. Singh, V. Divakar Botcha, *Appl. Phys. Lett.* **2012**, 101, 103103
[165] B. Martin-Garcia, A. Polovitsyn, M. Prato, I. Moreels, *J. Mater. Chem. C* . **2015**, 3, 7088.
[166] P.A. Johnson, R. Levicky, *Langmuir* . **2004**, 20, 9621.
[167] J.A. Rodriguez, T. Jirsak, A. Freitag, J.C. Hanson, J.Z. Larese, S. Chaturvedi, *Catal. Letters*. **1999**, 62, 113.
[168] K. Hamrin, G. Johansson, U. Gelius, C. Nordling, K. Siegbahn, *Phys. Scr.* **1970**, 1, 277.
[169] S. Hou, S. Su, M.L. Kasner, P. Shah, K. Patel, C. Madarang, *J. Chem. Phys. Lett*. **2010**, 501, 68.
[170] C.Y. Lee, Q. Le, C. Kim, S.Y. Kim, *Phys. Chem. Chem. Phys.* **2015**, 17, 9369.
[171] W. Li, B. Zhou, M. Wang, Z. Li, R. Ren, *J. Mater. Sci.* **2015**, 50, 5402.
[172] X. Dong, C.Y. Su, W. Zhang, J. Zhao, Q. Ling, W. Huang, P. Chen, L. Li, J. *Phys. Chem. Chem. Phys*. **2010**, 12, 2164.
[173] L. Jiang, S. Zhang, S.A. Kulinich, X. Song, J. Zhu, X. Wang, H. Zeng, *Materials Research Letters*, **2015**,3, 177.
[174] W. Zhou, *Nature nanotechnology,* **2014**, 9.5: 333.
[175] F. Dybała, M. P. Polak, J. Kopaczek, P. Scharoch, K. Wu, S. Tongay and R. Kudrawiec, *Sci. Rep*., **2016**, 6, 26663.
[176] W. Zhao, R. M. Ribeiro, M. Toh, A. Carvalho, C. Kloc, A. H. C. Neto and G. Eda, *Nano Lett*., **2013**, 13, 5627.
[177] G. Eda, H. Yamaguchi, D. Voiry, T. Fujita, M. Chen and M. Chhowalla, *Nano Lett*., **2011**, 11, 5111.
[178] H. Zhang, S. B. Lu, J. Zheng, J. Du, S. C. Wen, D. Y. Tang and K. P. Loh, *Opt. Express*, **2014**, 22, 7249.
[179] J. Benson, M. Li, S. Wang, P. Wang, and P. Papakonstantinou, *ACS Appl. Mater. Interfaces*, **2015**, 7, 14113.
[180] J. P. Wilcoxon and G. A. Samara, Phys. Rev. B: Condens. *Matter Mater. Phys*., **1995**, 51, 7299.
[181] L. Muscuso, S. Cravanzola, F. Cesano, D. Scarano, and A. Zecchina, *J. Phys. Chem. C*, **2015**, 119, 3791.
[182] L. Najafi, S. Bellani, B. Martin-Garcia, R. Oropesa-Nuñez, A.E. Del Rio Castillo, M. Prato, F. Bonaccorso, *Chem. Mater.,* **2017**, 29 , 5782.
[183] J. Verble, T. Wieting, *Phys. Rev. Lett.,* **1970**, 25, 362.
[184] G. Frey, R. Tenne, M. Matthews, M. Dresselhaus, and G. Dresselhaus, *Phys. Rev. B*, **1999**, 60, 2883.
[185] R. Saito, Y. Tatsumi, S. Huang, X. Ling, M.S. Dresselhaus, *J. Phys. Condens. Matter,* **2016**, 28, 353002.
[186] S. Bellani, L. Najafi, A. Capasso, A.E.D.R. Castillo, M.R. Antognazza, F. Bonaccorso, *J. Mater. Chem. A*, **2017**, 5, 4384.
[187] M. Dieterle , G. Mestl, *Phys. Chem. Chem.l Phys.,* **2002**, 4, 822.
[188] M. A. Py, K. Maschke, *Phys. B,* **1981**, 105, 370.
[189] P. A. Spevack, N.S. McIntyre, *J. Phys. Chem*., **1992**, 96, 9029.
[190] S. L. Zhang, X. Wang, K. Ho, J. Li, P. Diao, and S. Cai, *J. Appl. Phys.,* **1994**, 76, 3061.
[191] H. Richter, Z. P. Wang and L. Ley, *Solid State Commun.,* **1981**, 39, 625.
[192] U. Halim, C.R. Zheng, Y. Chen, Z. Lin, S. Jiang, R. Cheng, Y. Huang, X. Duan, *Nat. Commun.* **2013**, 4, 2213.
[193] E.D. Joensen, N. Crozier, R. F. Frindt, *J. Phys. C: Solid State Phys.,* **1987**, 20, 4043.
[194] N. Yue , J. Weicheng , W. Rongguo ,D. Guomin, H.J. Yifan , *Mater. Chem. A,* **2016**, 4, 8198.
[195] T. Wang , D. Gao , J. Zhu, P. Papakonstantinou , Y. Li , M.X. Li, *Chem.-Eur. J.,* **2013**, 19, 11939.
[196] A. Capasso, F. Matteocci, L. Najafi, M. Prato, J. Buha, L. Cinà, V. Pellegrini, A.D. Carlo, F. Bonaccorso, *Adv. Energy Mater*. **2016**, 6, 1600920.
[197] A. Jawaid, D. Nepal, K. Park, M. Jespersen, A. Qualley, P. Mirau, L.F. Drummy, R.A. Vaia, *Chem. Mater.* **2016**, 28, 337.
[198] V. Nicolosi, M. Chhowalla, M. G. Kanatzidis, M. S. Strano and J. N. Coleman*, Science*, **2013**, 340, 1226419.
[199] A. Ambrosi, Z. Sofer, M. Pumera, *Small*, **2015**, 11, 605.
[200] M. A. Py and R. R. Haering, Can. *J. Phys.,* **1983**, 61, 76

[201] M. Kertesz, R. Hoffmann*, J. Am. Chem. Soc*., **1984**, 106, 3453
[202] D. Voiry, M. Salehi, R. Silva, T.i Fujita, M.i Chen, T. Asefa, V. B. Shenoy, G. Eda, and M. Chhowalla, *Nano Lett*., **2013**, 13, 6222.
[203] a) G. Eda, S. A. Maier, *ACS Nano*, **2013**, 7, 5660. b) R. A. Bromley, R. B. Murray, A. D. Yoffe*, J. Phys. C: Solid State Phys.,* **1972**, 5, 759.
[204] a) M. M. Ugeda, A. J. Bradley, S.-F. Shi, F. H. da Jornada, Y. Zhang, D. Y. Qiu, W. Ruan, S.-K. Mo, Z. Hussain, Z.-X. Shen, F. Wang, S. G. Louie, M. F. Crommie, *Nat. Mater.,* **2014**, 13, 1091.
[205] G. Eda, H. Yamaguchi, D. Voiry, T. Fujita, M. Chen and M. Chhowalla, *Nano Lett*., **2011**, 11, 5111.
[206] A. Castellanos-Gomez, N. Agraït, and G. Rubio-Bollinger, *Appl. Phys. Lett*., **2010**, 96, 213116.
[207] P. Tonndorf, R. Schmidt, P. Böttger, X. Zhang, J. Börner, A. Liebig, M. Albrecht, C. Kloc, O. Gordan, D. R. Zahn S. Michaelis de Vasconcellos, R. Bratschitsch*, Opt. Express*, **2013**, 21, 4908.
[208] E. Xenogiannopoulou, P. Tsipas, K. E. Aretouli, D. Tsoutsou, S. A. Giamini, C. Bazioti, G. P. Dimitrakopulos, P. Komninou, S. Brems, C. Huyghebaert, I. P. Radu and A. Dimoulas*, Nanoscale*, **2015**, 7, 7896.
[209] N. Kumar, Q. Cui, F. Ceballos, D. He, Y. Wang and H. Zhao, *Nanoscale*, **2014**, 6, 4915.
[210] D. Nam, J. U. Lee, H. Cheong, *Sci Rep*., **2015**, 25, 17113.
[211] P. Soubelet, A. E. Bruchhausen, A. Fainstein, K. Nogajewski, C. Faugeras, *Phys. Rev. B*, **2016**, 93, 155407.
[212] J. C. Shaw, H. Zhou, Y. Chen, N. O. Weiss, Y. Liu, Y. Huang, X. Duan, *Nano Res*., **2014**, 7, 511.
[213] Z. Luo, Y. Li, M. Zhong, Y. Huang, X. Wan, J. Peng, J. Weng, *Photon. Res*., **2015**, 3, 79.
[214] Z. Zhang, X. Yang, Y. Fu, K. Du, *J. Power Sources*, **2015**, 296, 2.
[215] X. Wang, Y. Gong, G. Shi, W. L. Chow, K. Keyshar, G. Ye, R. Vajtai, J. Lou, Z. Liu, E. Ringe, B. K. Tay, P. M. Ajayan, *ACS Nano,* **2014**, 8, 5125
[216] H. Tang, K. P. Dou, C. C. Kaun, Q. Kuang and S. H. Yang*, J. Mater. Chem. A,***2014**, 2, 360.
[217] P. A. Spevack, N. S. Mcintyre, *J. Phys. Chem.,* **1993**, 97, 11020.
[218] A. Jawaid, D. Nepal, K. Park, M. Jespersen, A. Qualley, P. Mirau, L. F. Drummy and R. A. Vaia, *Chem. Mater*., **2016,** 28, 337.
[219] H. Wang, D. Kong, P. Johanes, J. J. Cha, G. Zheng, K. Yan, N. Liu and Y. Cui, *Nano Lett.,* **2013**, 13, 3426.
[220] R. Saito, G. Dresselhaus, M. S. Dresselhaus, *Phys. Rev. B*., **2000**, 61, 2981.
[221] H. Kataura, Y. Kumazawa, Y. Maniwa, I. Umezu, S. Suzuki, Y. Ohtsuka and Y. Achiba*, Synth. Met*., **1999**, 103, 2555.
[222] S. M. Bachilo, M. S. Strano, C. Kittrell, R. H. Hauge, R. E. Smalley,1 R. B. Weisman, *Science*, **2002**, 298, 2361.
[223] A. M. Rao, E. Richter, S. Bandow, B. Chase, P. C. Eklund, K. A. Williams, S. Fang, K.R. Subbaswamy, M. Menon, A. Thess, *Science*, **1997**, 275, 187
[224] H. Telg, J. Maultzsch, S. Reich, F. Hennrich, C. Thomsen, *Phys. Rev. Lett*., **2004**, 93, 177401.
[225] Z. Shi, Y. Lian, X. Zhou, Z. Gu,.Y. Zhang, S. Iijima, L. Zhou, K. T. Yue, S. Zhang, Carbon, 1999, 37, 1449.
[226] A. C. Ferrari, *Solid State Commun*., **2007**, 143, 47.
[227] A. C. Ferrari, J. C. Meyer, V. Scardaci, C. Casiraghi, M. Lazzeri, F. Mauri, S. Piscanec, D. Jiang, K. S. Novoselov, S. Roth A. K. Geim. *Phys. Rev. Lett.,* **2006**, 97, 187401.
[228]F. Tuinstra, J. L. Koenig*, J. Chem. Phys*., **1970**, 53, 1126.
[229] S. Piscanec, M. Lazzeri, J. Robertson, A. C. Ferrari, F. Mauri, *Phys Rev B,* **2007,** 75, 035427.
[230] M. Lazzeri, S. Piscanec, F. Mauri, A. C. Ferrari, J. Robertson, *Phys Rev B*, **2006**, 73, 155426.
[231]A. C. Ferrari, *Solid State Commun*., **2007**, 143, 47.
[232] J.A. Turner, *Science*, **2004**, 305, 972.
[233] S. Dunn, *Int. J. Hydrog. Energy* **2002**, 3, 235.
[234] K. Maeda, K. Teramura, D.Lu, T. Takata, N. Saito, Y. Inoue, *Nature*, **2006**, 440, 295.
[235] A. Vojvodic, J.K. Nørskov, *Science*, **2011** , 334, 1355.
[236] R. Subbaraman, D. Tripkovic, D. Strmcnik, *science,* **2011**, 334, 1256.
[237] J. Suntivich, K.J. May, H.A. Gasteiger*, science* , **2011** , 334, 1383.
[238] X. Zou, Y. Zhang, *Chem. Soc. Rev*., **2015**, 44, 5148.
[239] Q .Lu, Y. Yu, Q. Ma, B. Chen, H. Zhang, *Adv. Mater,***2016***,* 28, 1917.
[240] M. Pumera, Z. Sofer, A. Ambrosi, *J. Mater. Chem. A*., **2014**, 2, 8981.
[241] B. E., Conway, B. V. Tilak, , *Electrochim. Acta*,**2002**, 47, 3571.
[242] M. Boudart, *Chem. Rev., **1995**,* 95, 661.
[243] S.A. Vilekar, I. Fishtik, R. Datta, *J. Electrochem. Soc.*, **2010**, 157, B1040.
[244] Y. Li, H. Wang, L. Xie, Y. Liang, G. Hong, H. Dai, *JACS*, **2011**, 133, 7296.
[245] A. R. Kucernak, C. Zalitis*, J. Phys. Chem. C*, **2016**, 120, 10721.
[246] W. Sheng, H.A. Gasteiger, Y. Shao-Horn, *J. Electrochem. Soc*., **2010**, 157, B1529.
[247] D. Mukherjee, P.M. Austeria, S. Sampath, *ACS Energy Letters*, **2016**, 1, 367.

[248] J. L. Ambrose, Y. Zhou, K. Haase, H. R. Mayne,R. Talbot, B. C. Sive, *Atmos. Meas. Tech*., **2012**, 5, 1229.
[249] B. Seo, S.H. Joo - Nano convergence, **2017** ,4,9.
[250] L. Wang, C.Y. Lee, P. Schmuki, (2013). *J. Mater. Chem. A*, **2013**, 2, 212.
[251] C. Si, J. Zhang, Y. Wang, W. Ma, H. Gao, L. Lv, Z. Zhang, *ACS applied materials & interfaces*, **2017**, 9, 2485.
[252] T.F. aramillo, K.P. Jørgensen, J. Bonde, J.H. Nielsen, S. Horch, I. Chorkendorff, *Science*, **2007** ,317, 100.
[253] J. Kibsgaard, Z. Chen, B.N. Reinecke, T.F. Jaramillo, *Nat. Mater*. **2012**, 11, 963.
[254] M.V. ollinger, J.V. Lauritsen, K.W. Jacobsen, J.K. Nørskov, S. Helveg, F. Besenbacher, *Phys. Rev. Lett*., **2001** ,87, 196803.
[255] M. Chhowalla, H.S. Shin, G. Eda, L.J. Li, K.P. Loh, H. Zhang, *Nat. Chem*, **2013** ,5, 263.
[256] H.L. Tsai, J. Heising, J.L. Schindler, C.R. Kannewurf, M.G. Kanatzidis, *Chem. Mater*. **1997** ,9, 879.
[257] J. Kibsgaard, Z. Chen, B.N. Reinecke, T.F. Jaramillo, *Nat. Mater*. **2012**,11, 963.
[258] J. Yang, H.S. Shin*, J. Mater. Chem. A*, **2014** ,2, 5979.
[259] D. Hou, W. Zhou, K. Zhou, Y. Zhou, J. Zhong, L. Yang, J. Lu, G. Li, S. Chen, *J. Mater. Chem. A*, **2015** ,3, 15962
[260] J. Benson, M. Li, S. Wang, P. Wang, P. Papakonstantinou, *ACS Appl. Mater. Interfaces*, **2015**, 7, 14113
[261] D. Voiry, M. Salehi, R. Silva, T. Fujita, M. Chen, T. Asefa, V.B. Shenoy, G.T. Eda, M. Chhowalla, *Nano Lett*. **2013**, 13, 6222.
[262] M. Chhowalla, H.S. Shin, G. Eda, L. Li, K.P. Loh, H. Zhang, *Nat. Chem*. **2013**, 5, 263.
[263] W. Qiao, S. Yan, X. Song, X. Zhang, Y. Sun, X. Chen, W. Zhong, Y. Du, *RSC Adv*. **2015**, 5, 97696.
[264] J. Benson, M. Li, S. Wang, P. Wang, P. Papakonstantinou, *ACS Appl. Mater. Interfaces,* **2015**, 7, 14113.
[265] B.E. Conway, E. Gileadi, *Trans. Faraday Soc.* **1962**, 58, 2493.
[266] T. Liang, W.G. Sawyer, S.S. Perry, S.B. Sinnott, S.R. Phillpot , *J. Phys. Chem. C*, **2011**, 115, 10606.
[267] S. Mukherjee, R. Maiti, A.K. Katiyar, S. Das, S.K. Ray, *Sci. Rep*., **2016**, 6, 29016.
[268] C. G. Morales-Guio, L. Stern, X. Hu, *Chem. Soc. Rev*. 2014, **43**, 6555–6569;
[269] D. McAteer, Z. Gholamvand, N. McEvoy, A. Harvey, G. Duesberg, J. N. Coleman, *ACS Nano*, **2016**, 10, 672.
[270] Y. Xu, H. Bai, G. Lu, C. Li, G. Shi, *J. Am. Chem. Soc*., **2008**, 130, 5856.
[271] D. Cohen-Tanugi, J. C. Grossman, *Nano Lett*., **2012**, 12, 3602.
[272] M. Endo, H. Muramatsu, T. Hayashi, Y. A. Kim, M. Terrones, M. S. Dresselhaus, *Nature*, **2005**, 433, 476.
[273] R. L. Whitby, T. Fukuda, T. Maekawa, S. L. James, S. V. Mikhalovsky, *Carbon*, **2008**, 46, 949.
[274] Q. Ma, M. Isarraraz, C. S. Wang, L. Bartels, *ACS Nano*, **2014**, 8, 4672.
[275] S. Bellani, L. Najafi, A. Capasso, A. E. Del Rio Castillo, M. R. Antognazza and F. Bonaccorso, *J. Mater. Chem. A,* **2017**, 5, 4384.
[276] P. A. Spevack, N. S. Mcintyre, *J. Phys. Chem*., **1993**, 97, 11020.
[277] L. H. Yuwen, J. J. Zhou, Y. Q. Zhang, Q. Zhang, J. Y. Shan, Z. M. Luo, L. X. Weng, Z. G. Teng, L. H. Wang, *Nanoscale*, **2016**, 8, 2720.
[278] X. L. Zhou, J. Jiang, T. Ding, J. J. Zhang, B. C. Pan, J. Zuo, Q. Yang, *Nanoscale*, **2014**, 6, 11046.
[279] H. Tang, K. P. Dou, C. C. Kaun, Q. Kuang and S. H. Yang, *J. Mater. Chem. A*, **2014**, 2, 360.
[280] J. Kibsgaard, Z. B. Chen, B. N. Reinecke, T. F. Jaramillo*, Nat. Mater.,* **2012**, 11, 963.
[281] Y. Yan, B. Y. Xia, X. Ge, Z. Liu, J.-Y. Wang, X. Wang, *ACS Appl. Mater. Interfaces*, **2013**, 5, 12794.
[282] T. F. Jaramillo, K. P. Jørgensen, J. Bonde, J. H. Nielsen, S. Horch, I. Chorkendorff, *Science,* **2007**, 317, 100.
[283] Y. Q. Guo, K. Xu, C. Z. Wu, J. Y. Zhao, Y. Xie, *Chem. Soc. Rev.,* **2015**, 44, 637.
[284] D. Kiriya, P. Lobaccaro, H. Y. Y. Nyein, P. Taheri, M. Hettick, H. Shiraki, C. M. Sutter-Fella, P. Zhao, W. Gao, R. Maboudian, J. W. Ager, A. Javey, *Nano Lett.,* **2016**, 16, 4047.
[285] R. Kappera, D. Voiry, S. E. Yalcin, B. Branch, G. Gupta, A. D. Mohite, M. Chhowalla, *Nat. Mater*., **2014**, 13, 1128.
[286] E. S. Jones, J. F. Mosher, R. Speiser, J. W. Spretnak, *Corrosion*, **1958**, 14, 20.
[287] J. Staszak-Jirkovsky, C. D. Malliakas, P. P. Lopes, N. Danilovic, S. S. Kota, K. C. Chang, B. Genorio, D. Strmcnik, V. R. Stamenkovic, M. G. Kanatzidis, N. M. Markovic, *Nat. Mater*., **2016**, 15, 197.
[288] R. Subbaraman, D. Tripkovic, K. C. Chang, D. Strmcnik, A. P. Paulikas, P. Hirunsit, M. Chan, J. Greeley, V. Stamenkovic, N. M. Markovic, *Nat. Mater.,* **2012**, 11, 550.
[289] M. Pumera, Z. Sofer, A. Ambrosi, *J. Mater. Chem. A*, **2014**, 2, 8981.
[290] R. Lv, J. A. Robinson, R. E. Schaak, D. Sun, Y. Sun, T. E. Mallouk, M. Terrones, *Acc. Chem. Res*., **2014**, 48, 56.
[291] D. McAteer, Z. Gholamvand, N. McEvoy, A. Harvey, E. O'Malley, G. S Duesberg, J. N. Coleman, *ACS Nano*, **2016**, 10, 672.
[292] Z. Gholamvand, D. McAteer, C. Backes, N. McEvoy, A. Harvey, N. C. Berner, D. Hanlon, C. Bradley, I. Godwin, A. Rovetta, M. E. G. Lyons, G. S. Duesberg, J. N. Coleman, *Nanoscale*, **2016**, 8, 5737.
[293] H. Tang, K. P. Dou, C. C. Kaun, Q. Kuang, S. H. Yang, *J. Mater. Chem. A*, **2014**, 2, 360.
[294] S. K. Behera, P. Deb, A. Ghosh, *ChemistrySelect,* **2017**, 2, 3657.

[295] J. D. Holladay, J. Hu, D. L. King, Y. Wang, *Catal. Today*, **2009**, 139, 244.
[296] H. Wang, Z. Lu, D. Kong, J. Sun, T. M. Hymel, Y. Cui, *ACS Nano*, **2014**, 8, 4940.
[297] D. Damien, A. Anila, D. Chatterjeeb, M. M. Shaijumon, *J. Mater. Chem. A*, **2017**, DOI: 10.1039/C6TA09645J.
[298] G. Ye, Y.Gong, J. Lin, B. Li, Y. He, S. T. Pantelides, W. Zhou, R. Vajtai, P. M. Ajayan, *Nano Lett*., **2016**, 16, 1097.
[299] G. Gao, Y. Jiao, F. Ma, Y. Jiao, E. Waclawik, and A. Du, *J. Phys. Chem. C*, **2015**, 119, 13124.
[300] P. Wang, L. L. Wilson, D. J. Wesolowski, J. Rosenqvist, A. Anderko, *Corros. Sci.,* **2010**, 52, 1625.
[301] C. Xu, S. Peng, C. Tan, H. Ang, H. Tan, H. Zhanga, Q. Yan, *J. Mater. Chem. A,* **2014**, 2, 5597.
[302] J. F. Xie, J. J. Zhang, S. Li, F. Grote, X. D. Zhang, H. Zhang, R. X. Wang, Y. Lei, B. C. Pan, Y. Xie, *J. Am. Chem. Soc*., **2013**, 135, 17881.
[303] H. L. Tsai, J. Heising, J. L. Schindler, C. R. Kannewurf, M. G. Kanatzidis, *Chem. Mater*., **1997**, 9, 879.
[304] Holladay, J. D., Hu, J., King, D. L., & Wang, Y. An overview of hydrogen production technologies. *Catal. Today*. **139**, 244–260 (2009).
[305] Zeng, K., & Zhang, D. Recent progress in alkaline water electrolysis for hydrogen production and applications. *Prog. Energy Comb. Sci*., **36**, 307–326 (2010).
[306] Dworak, R., Lohrberg K., Müller R. Lurgi's experience with steel and Raney-nickel as cathode material, *Modern chlor-alkali technology*, 257–264 (1992).
[307] Brown, D. E., Mahmood, M. N., Man, M. C. M., & Turner, A. K. Preparation and characterization of low overvoltage transition metal alloy electrocatalysts for hydrogen evolution in alkaline solutions. *Electrochim. Acta*. **29**, 1551–1556 (1984).
[308] Cairns, J. F., Cook, M. R., Hayes, P. M., Hodgson, D. R., Izzard, P.A., Mockford, M. J., Paul, E. and Rourke, F. Advances in ICI's activated cathode technology for chlor-alkali production. *Proc. Electrochem. Soc.* **98**, 289–296 (1998).
[309] Pletcher, D., & Li, X. Prospects for alkaline zero gap water electrolysers for hydrogen production. *Int. J. Hydrogen Energy*, **36**, 15089–15104 (2011).
[310] Carmo, M., Fritz, D. L., Mergel, J., & Stolten, D. A comprehensive review on PEM water electrolysis. Int. J. Hydrogen Energy, **38**, 4901–4934 (2013).
[311] Barbir, F. PEM electrolysis for production of hydrogen from renewable energy sources. *Solar Energy*. **78**, 661–669 (2005).
[312] Grigoriev, S. A., Porembsky, V. I., & Fateev, V. N. Pure hydrogen production by PEM electrolysis for hydrogen energy. *Int. J. Hydrogen Energy*. **31**, 171–175 (2006).
[313] Nicolosi, V., Chhowalla, M., Kanatzidis, M. G., Strano, M. S., & Coleman, J. N. Liquid exfoliation of layered materials. *Science*. **340**, 1226419–1226437 (2013).
[314] Bonaccorso, F., Bartolotta, A., Coleman, J. N., & Backes, C. 2D-Crystal-Based Functional Inks. *Adv. Mater.* **28**, 6136–6166 (2016).
[315] Bonaccorso, F., Lombardo, A., Hasan, T., Sun, Z., Colombo, L., & Ferrari, A. C. Production and processing of graphene and 2d crystals. *Mater. Today*. **15**, 564–589 (2012).
[316] Yang, L., Majumdar, K., Liu, H., Du, Y., Wu, H., Hatzistergos, M., Hung, P.Y., Tieckelmann, R. Tsai, W., Hobbs, C. & Ye, P. D. Chloride molecular doping technique on 2D materials: WS_2 and MoS_2. *Nano Lett.* **14**, 6275–6280 (2014).
[317] Schmidt, H., Giustiniano, F., & Eda, G. Electronic transport properties of transition metal dichalcogenide field-effect devices: surface and interface effects. *Chem. Soc. Rev.* **44**, 7715–7736 (2015).
[318] Ryder, C. R., Wood, J. D., Wells, S. A., & Hersam, M. C. Chemically tailoring semiconducting two-dimensional transition metal dichalcogenides and black phosphorus. *ACS Nano*. **10**, 3900–3917 (2016).
[319] S. Bellani, L. Najafi, B. Martin-Garcia, A. Ansaldo, A.E.D.R. Castillo, M. Prato, I. Moreels, F. Bonaccorso, *J. Phys. Chem. C,* DOI: 10.1021/acs.jpcc.7b05904 , **2017**.
[320] N.B. McKeown, P.M. Budd, *Chem. Soc. Rev.* **2006**, 35, 675.
[321] M. Dincă, J.R. Long, *Angew. Chem. Int. Ed.* **2008** , 47, 6766.
[322] L.J. Murray, M. Dincă, J.R. Long,. *Chem. Soc. Rev.* **2009** , 38, 1294.
[323] D. Jariwala, V.K. Sangwan, C.C. Wu, P.L. Prabhumirashi, M. Geier, T. Marks, L.J. Lauhon, M.C. Hersam, *Proc, Natl. Acad. Sci. U.S.A.* **2013**, 110, 18076.
[324] H. Wang, D. Kong, P. Johanes, J.J. Cha, G. Zheng, K. Yan, N. Liu, Y. Cui, *Nano Lett.,* **2013***,* 13, 3426.
[325] S. Tongay, J. Zhou, C. Ataca, K. Lo, T.S. Matthews, J. Li, J.C. Grossman, J. Wu, *Nano Lett*., **2012**, 12, 5576.
[326] E. Xenogiannopoulou, P. Tsipas, K.E. Aretouli, D. Tsoutsou, S.A. Giamini, C. Bazioti, G.P. Dimitrakopulos, P. Komninou, S. Brems, C. Huyghebaert, I.P. Radu, A. Dimoulas, A, N*anoscale*, **2015**, 7, 7896.
[327] N. Kumar, Q. Cui, F. Ceballos, D. He, Y. Wang, H. Zhao, *Nanoscale*, **2014**, 6, 4915.
[328] D. Nam, J. Lee, H. Cheong, *Sci Rep*., **2015**, 25, 17113.
[329] P. Soubelet, A.E. Bruchhausen, A. Fainstein, K. Nogajewski, C. Faugeras, *Phys. Rev. B*, **2016**, 93, 155407.
[330] M.S. Choi, D. Qu, D. Lee, X. Liu, K. Watanabe, T. Taniguchi, W. Yoo, *ACS Nano*, **2014**, 8, 9332.

[331] Y. Shi, J. Huang, L. Jin, Y.T. Hsu, S.F. Yu, L.J. Li ,H.Y. Yang, *Sci. Rep.*, **2013**, 3, 1839 .
[332] A. Nipane, D. Karmakar, N. Kaushik, S. Karande, S. Lodha, *ACS Nano*., **2016**, 10, 2128.
[333] J.D. Lin, C. Han, F. Wang, R. Wang, D. Xiang, S. Qin, X.A. Zhang, L. Wang, H. Zhang, A.T. Wee, W. Chen, *ACS Nano*, **2014**, 8, 5323.
[334] X. Wang, Y. Gong, G. Shi, W.L. Chow, K. Keyshar, G. Ye, R. Vajtai, J. Lou, Z. Liu, E. Ringe, B.K. Tay, *ACS Nano*, **2014**, 8, 5125.
[335] Q. Ma, M. Isarraraz, C.S. Wang, E. Preciado, V. Klee, S. Bobek, K. Yamaguchi, E. Li, P.M. Odenthal, A. Nguyen, D. Barroso, *ACS Nano*, **2014**, 8, 4672.
[336] J. Meyer, P.R. Kidambi, B.C. Bayer, C. Weijtens, A. Kuhn, A. Centeno, A. Pesquera, A. Zurutuza, J. Robertson, S. Hofmann, *Sci. Rep.*, **2014**, 4, 5380.
[337] W. Davison, G. Seed, *Geochim. Cosmochim. Acta*, **1983**, 47, 67.
[338] H. Tamura, K. Goto, M. Nagayama, *Corros. Sci.,* **1976***,* 16, 197.
[339] L. Najafi, S. Bellani, B. Martin-Garcia, R. Oropesa-Nuñez, A.E.D.R. Castillo, M. Prato, I. Moreels, F. Bonaccorso, *Chem. Mate*r. **2017**, 29, 5782.
[340] H. Li, K. Yu, C. Li, Z. Tang, B. Guo, X. Lei, H. Fu, Z. Zhu, *Sci. Rep.*, **2015**, 5, 18730 .
[341] S.K. Behera, P. Deb, A. Ghosh, *ChemistrySelect*, **2017**, 2, 3657.
[342] B. Qu, C. Li, C. Zhu, S. Wang, X. Zhang, Y. Chen, Nanoscale, **2016**, 8, 16886.
[343] T. Shinagawa, A.T. Garcia-Esparza, K. Takanabe, *Sci. Rep*., **2015**, 5, 13801.
[344] X. Zou, Y. Zhang, *Chem. Soc. Rev*., **2015**, 44, 5148.
[345] P. Liu, J. Zhu , J. Zhang , P. Xi, K. Tao , D. Gao, D. Xue , *ACS Energy Lett*., **2017**, 2, 745.
[346] H. Wang , Z. Lu , S. Xu ,D. Kong , J. Cha, G. Zheng , P.C. Hsu, K. Yan, D. Bradshaw, F.B. Prinz , Y. Cui, *Proc. Natl. Acad. Sci. U. S. A.* **2013**, 110, 19701.
[347] J. Staszak-Jirkovsky, C.D. Malliakas, P.P. Lopes, N. Danilovic, S.S. Kota, K.C. Chang, B. Genorio, D. Strmcnik, V.R. Stamenkovic, M.G. Kanatzidis, N.M. Markovic, *Nat. Mater*., **2016**, 15, 197.
[348] R. Subbaraman, D. Tripkovic, K.C. Chang, D. Strmcnik, A.P. Paulikas, P. Hirunsit, M. Chan, J. Greeley, V. Stamenkovic, N.M. Markovic, *Nat. Mater.* **2012,** 11, 550 .
[349] J.D. Wiensch, J. John, J.M. Velazquez, D.A. Torelli, A.P. Pieterick, M.T. McDowell, K. Sun, X. Zhao, B. Brunschwig, N.S. Lewis, *ACS Energy Lett.*, **2017**, 2, 2234.
[350] Z. Chen, H. Dinh, E. Miller, Photoelectrochemical Water SplittingStandards - Experimental Methods, and Protocols, SpringerBriefs in Energy, **2013**.
[351] T. Hisatomi, J. Kubota and K. Domen, *Chem. Soc. Rev*., **2014***,* 43, 7520.
[352] W. A. Smith, I. D. Sharp, N. C. Strandwitzd and Juan Bisquert, *Energy Environ. Sci*., **2015**, 8, 2851.
[353] M. R. Nellist, F. A. L. Laskowski, F. D. Lin, T. J. Mills and S. W. Boettcher, *Acc. Chem. Res*., **2016**, 49, 733.
[354] B. Parkinson, J. Turner, *RSC*, **2014**.
[355] A. Fujishima, K.Honda, *Nature*, **1972**, 238, 37.
[356] H. Gerischer, Pure *Appl. Chem*., **1980**, 52, 2649.
[357] M. Gratzel, *Nature*, **2001**, 414, 338.
[358] M. G. Walter, E. L. Warren, J. R. McKone, S. W. Boettcher, Q. X. Mi, E. A. Santori and N. S. Lewis, *Chem. Rev.,* **2010**, 110, 6446.
[359] W.Shockley, H. J. Queisser, *J. Appl. Phys*., **1961**, 32, 510.
[360] A. J. Bard, *J. Photochem*. **1979**, 10, 59.
[361] M. C. Hanna A. J. Nozik, *J. Appl. Phys*., **2006**, 100, 074510.
[362] S. Haussener, C. Xiang, J. M. Spurgeon, S. Ardo, N. S. Lewis and A. Z. Weber, *Energy Environ. Sci.,* **2012**, 5, 9922.
[363] S. Hu, C. Xiang, S. Haussener, A. D. Bergerc and N. S. Lewis, *Energy Environ. Sci.,* **2013**, 6, 2984.
[364] M. S. Prévot and K. Sivula, *J. Phys. Chem. C*, **2013**, 117, 17879
[365] J. W. Ager, M. R. Shaner, K. A. Walczak, I. D. Sharp, S. Ardo, *Energy Environ. Sci*., **2015**, 8, 2811.
[366] O. Khaselev, J. A. Turner, *Science*, **1998**, 280, 425
[367] M. M. May, H.-J. Lewerenz, D. Lackner, F. Dimroth and T. Hannappel, *Nat. Comm*., **2015**, 6, 8286.
[368] L. Gao, Y. Cui, R. H. J. Vervuurt, D. van Dam, R. P. J. van Veldhoven, J. P. Hofmann, A. A. Bol, J. E. M. Haverkort, P. H. L. Notten, E. P. A. M. Bakkers and E. J. M. Hensen, *Adv. Funct. Mater*., **2016**, 26, 679;
[369] M. Woodhouse, A. Goodrich, Manufacturing cost analysis relevant to single-and dual-junction photovoltaic cells fabricated with III-Vs and III-Vs grown on Czochralski silicon, National Renewable Energy Laboratory, **2014**.
[370] A. Louwen, W. van Sark, R. Schropp, A. Faaij, Sol. *Energ. Mat. Sol. Cells*, **2016**, 147, 295.
[371] C. R. Cox, J. Z. Lee, D. G. Nocera and T. Buonassisi, *PNAS,* **2014**, 111, 14057.
[372] T. J. Jacobsson, V. Fjallstrom, M. Sahlberg, M. Edoff and T. Edvinsson, *Energy Environ. Sci.,* **2013**, 6, 3676.
[373] H. Zhou, Q. Chen, G. Li, S. Luo, T.-b. Song, H.-S. Duan, Z. Hong, J. You, Y. Liu and Y. Yang, *Science*, **2014**, 345, 542.

[374] A. Paracchino, N. Mathews, T. Hisatomi, M. Stefik, S. D. Tilley and M. Grätzel, *Energy Environ. Sci*., **2012**, 5, 8673.
[375] A. A. Dubale, A. G. Tamirat, H.-M. Chen, T. A. Berhe, C.-J. Pan, W.-N. Su and B.-J. Hwang, *J. Mater. Chem. A*, **2016**, 4, 2205;
[376] P. Zhai, S. Haussener, J. Ager, R. Sathre, K. Walczak, J. Greenblatt and Thomas McKone, *Energy Environ. Sci*., **2013**, 6, 2380;
[377] L. Ji, M. D. McDaniel, S. Wang, A. B. Posadas, X. Li, H. Huang, J. C. Lee, A. A. Demkov, A. J. Bard, J. G. Ekerdt, E. T. Yu, *Nat. Nano*., **2015**, 10, 84.
[378] J. L. Young, K. X. Steirer, M. J. Dzara, J. A. Turner and T. G. Deutsch, *J. Mater. Chem. A*, **2016**, 4, 2831.
[379] M. Crespo-Quesada, L. M. Pazos-Outón, J. Warnan, M. F. Kuehnel, R. H. Friend and E. Reisner, *Nature Communications,* **2016**, 7, 12555.
[380] A. Paracchino, V. Laporte, K. Sivula, M. Gr¨atzel and E. Thimsen, *Nat. Mater*., **2011**, 10, 456.
[381] A. Paracchino, N. Mathews, T. Hisatomi, M. Ste・k, S. D. Tilley and M. Gr¨atzel, *Energy Environ. Sci*., **2012**, 5, 8673.
[382] M. Crespo-Quesada, L. M. Pazos-Out´on, J. Warnan, M. F. Kuehnel, R. H. Friend and E. Reisner, *Nat. Commun*., **2016**, 7, 12555.
[383] S. Hu, N. S. Lewis, J. W. Ager, J. Yang, J. R. McKone and N. C. Strandwitz, *J. Phys. Chem. C*, **2015**, 119, 24201.
[384] G. Yu, J. Gao, J. C. Hummelen,, F. Wudl, *Science* **1995**, 270, 1789..
[385] R. Øndergaard, M. Hösel, D. Angmo, F.C. Krebs, *Mater. Today*, **2012**, 15, 36.
[386] S. Bellani, L. Najafi, A. Capasso, A.E.D.R. Castillo, M.R. Antognazza, F. Bonaccorso, *J. Mater. Chem. A*, **2017**, 5, 4384.
[387] Z. Chen, T. F. Jaramillo, T. G. Deutsch, A. Kleiman- Shwarsctein, A. J. Forman, N. Gaillard, R. Garland, K. Takanabe, C. Heske, M. Sunkara, *J. Mater. Res.,* **2010**, 25, 3.
[388] H. D¨oscher, J. L. Young, J. F. Geisz, J. A. Turner and T. G. Deutsch*, Energy Environ. Sci*., **2016**, 9, 74.
[389] Z. Li, W. Luo, M. Zhang, J. Feng and Z. Zoua, *Energy Environ. Sci*., **2013**, 6, 347.
[390] D. Wei and G. Amaratunga, Int. *J. Electrochem. Sci*., **2007**, 2, 897.
[391] R. van de Krol and M. Gr¨atzel, Photoelectrochemical Hydrogen Production, *Springer*, **2012**.
[392] R.H. Coridan, A.C. Nielander, S.A. Francis, *Energy Environ. Sci*., **2015**, 8, 2886.
[393] M. P. Gustafson, N. Clark, B. Winther-Jensen and D. R. MacFarlane, *Electrochim. Acta,* **2014**, 140, 309.
[394] M. Haro, C. Solis, V. M. Blas-Ferrando, O. Margeat, S. B. Dhkil, C. Videlot-Ackermann, J. Ackermann, F. Di Fonzo, A. Guerrero and S. Gimenez, *ChemSusChem*, **2016**, 9, 3062.
[395] T . Bourgeteau, D. Tondelier, B. Geffroy, R. Brisse, R. Cornut, V. Artero and B. Jousselme, *ACS Appl. Mater*. *Interfaces*, **2015**, 7, 16395.
[396] G. Yu, J. Gao, J. C. Hummelen, F. Wudl, A. J. Heeger, *Science*, **1995**, 270, 1789.
[397] R. Søndergaard, M.s Hösel, D. Angmo, T. T. Larsen-Olsen, F. C. Krebs, *Mater. Today*., **2012**, 15, 36.
[398] H. C. Rojas, S. Bellani, F. Fumagalli, G. Tullii, S. Leonardi, M. T. Mayer, M. R. Schreier, M. Grätzel, G. Lanzani, F. D. Fonzo and M. R. Antognazza, *Energy Environ. Sci*., **2016**, 9, 3710.
[399] A. Marrocchi, D. Lanari, A. Facchetti and L. Vaccaro*, Energy Environ. Sci*., **2012**, 5, 8457.
[400] E. Lanzarini, M. R. Antognazza, M. Biso, A. Ansaldo, L. Laudato, P. Bruno, P. Metrangolo, G. Resnati, D. Ricci and G. Lanzani, *J. Phys. Chem. C,* **2012**, 116, 10944.
[401] G. Suppes, E. Ballard and S. Holdcroft, *Polym. Chem*., **2013**, 4, 5345.
[402] S. Bellani, D. Fazzi, P. Bruno, E. Giussani, E. V. Canesi, G. Lanzani and M. R. Antognazza, *J. Phys. Chem. C*, **2014**, 118, 6291
[403] A. Mezzetti, F. Fumagalli, A. Alfano, D. Iadicicco, M. R. Antognazza and F. Di Fonzo, *Faraday Discuss*., **2016**.
[404] T. Bourgeteau, D. Tondelier, B. Geffroy, R. Brisse, S. Campidelli, R. Cornut and B. Jousselme, *J. Mater. Chem. A*, **2016**, 4, 4831.
[405] F. Fumagalli, S. Bellani, M. Schreier, S. Leonardi, H. C. Rojas, A. Ghadirzadeh, G. Tullii, A. Savoini, G. Marra, L. Meda, M. Grätzel, G. Lanzani, M. T. Mayer, M. R. Antognazza and F. Di Fonzo, *J. Mater. Chem. A,* **2016**, 4, 2178;
[406] M. Haro, C. Solis, G. Molina, L. Otero, J. Bisquert, S. Gimenez and A. Guerrero*, J. Phys. Chem. C***, 2015**, 119, 6488;
[407] C. G. Morales-Guio, L. Liardet, M. T. Mayer, S. D. Tilley, M Grätzel, X. Hu, *Angew. Chem.*, **2015**, 127, 674-677.
[408] E. Fabbri, A. Habereder, K. Waltar, R. Kotz, T. J. Schmidt, Catal. *Sci. Technol.* **2014**, 4, 3800.
[409] M. A. Modestino, K. A. Walczak, A. Berger, C. M. Evans, S. Haussener, C. Koval, J. S. Newman, J. W. Ager and R. A. Segalman, *Energy Environ. Sci*., **2014**, 7, 297.
[410] S. Y. Reece, J. A. Hamel, K. Sung, T. D. Jarvi, A. J. Esswein, J. J. H. Pijpers and D. G. Nocera, *Science*, **2011**, 334, 645.
[411] P. Samorì, V. Palermo, X. Feng, *Adv. Mater*., **2016**, 28, 6027
[412] F. Bonaccorso, L. Colombo, G. Yu, M. Stoller, V. Tozzini, A. C. Ferrari, R. S. Ruoff and V. Pellegrini, *Science,* **2015**, 347, 1246501.
[413] F. Bonaccorso, A. Bartolotta, J. N. Coleman, C. Backes, *Adv. Mater*., **2016**, 28, 6136.

[414] J.-M. Yun, Y.-J. Noh, J.-S. Yeo, Y.-J. Go, S.-I. Na, H.-G. Jeong, J. Kim, S. Lee, S.-S. Kim, H. Y. Koo, T.-W. Kim and D.-Y. Kim, *J. Mater. Chem. C*, **2013**, 1, 3777.
[415] A. P. Peixoto and J. C. da Costa, *AIP Conf. Proc.,* **2014**, 39, 1598.
[416] Y. Shi, K. K. Kim, A. Reina, M. Hofmann, L. J. Li and J. Kong, *ACS Nano*, **2010**, 4, 2689;
[417] H. Zhang, S. B. Lu, J. Zheng, J. Du, S. C. Wen, D. Y. Tang and K. P. Loh, *Opt. Express*, **2014**, 22, 7249.
[418] D. Merki, S. Fierro, H. Vrubel and X. Hu, *Chem. Sci*., **2011**, 2, 1262.
[419] N. Balis, E. Stratakis, E. Kymakis, *Mater. Today*, **2016**, 19, 580.
[420] B. Cao, X. He, C.R. Fetterly, B.C. Olsen, E.J. Luber, J.M. Buriak, *ACS Appl. Mater. Interfaces,* **2016**, 8, 18238.
[421] Z. Yin, J. Wei, Q. Zheng,. *Adv. Sci*. **2016**, 3, 1.
[422] J.M. Yun, J.S. Yeo, J. Kim, H.G. Jeong, D.Y. Kim, Y.J. Noh, S.S. Kim, B.C. Ku, S.I. Na, *Adv. Mater*. **2011**, 23, 4923.
[423] N. Balis, E. Stratakis, E. Kymakis, *Mater. Today,* **2016**, 19, 580.
[424] D. Konios, M. Stylianakis, E. Stratakis, E. Kymakis,. *J. Colloid Interface Sci*. **2014**, 430, 108.
[425]B. Konkena, S. Vasudevan, *J. Phys. Chem. Lett.* **2012**, 3, 867.
[426] A. Baldan, *J. Mater. Sci.* **2002**, 37, 2171.
[427] A. Zadick, L. Dubau, N. Sergent, G. Berthomé, M. Chatenet, *ACS Catal.* **2015**, 5, 4819.
[428] S. Cherevkoz, A.R. Zeradjanin, G.P. Keeley, K.J.J. Mayrhofer*, J. Electrochem. Soc.* **2014**, 161, 822.
[429] K. Elbert, J. Hu, Z. Ma, Y. Zhang, G. Chen, W. An, P. Liu, H.S. Isaacs, R.R. Adzic, J.X. Wang, *ACS Catal*. **2015**, 5, 6764.
[430] J. Durst, A. Siebel, C. Simon, F. Hasche, J. Herranz, H.A. Gasteiger, *Energy Environ. Sci.* **2014**, 7, 2255.
[431] E. Lanzarini, M.R. Antognazza, M. Biso, A. Ansaldo, L. Laudato, P. Bruno, P. Metrangolo, G. Resnati, D. Ricci, G. Lanzani,. *J. Phys. Chem. C* , **2012**, 116, 10944.
[432] Y. Shen, A.R. Hosseini, M.H. Wong, G.G. Malliaras, *ChemPhysChem*, **2004**, 5, 16.
[433] Z. Yin, J. Wei, Q. Zheng, *Adv. Sci.* **2016**, 3, 1.
[434] C.G. Morales-Guio, S.D. Tilley, H. Vrubel, M. Grätzel, X. Hu, *Nat. Commun.* **2014**, 5, 3059.
[435] R. Bkakri, O.E. Kusmartseva, F.V. Kusmartsev, M. Song, A. Bouazizi, *J. Lumi.n* **2015**, 161, 264.
[436] B. Martin-Garcia, A. Polovitsyn, M. Prato, I. Moreels,. *J. Mater. Chem. C.* **2015**, 3, 7088.
[437] J.M. Yun, J.S. Yeo, J. Kim, H.G. Jeong, D.Y. Kim, Y.J. Noh, S.S. Kim, B.C. Ku, S.I. Na, *Adv. Mater*. **2011**, 23, 4923.
[438] M.F. Calhoun, J. Sanchez, D. Olaya, M.E. Gershenson, V. Podzorov, *Nat Mater,* **2008**, 7, 84.
[439] A. Schlierf, P. Samori, V. Palermo, *J. Mater. Chem. C.* **2014**, 2, 3129.
[440] R.L. Smith, G.S. Rohrer, *J. Solid State Chem*. **1996**, 124, 104.
[441] B. Seger, T. Pedersen, A.B. Laursen, P.C.K. Vesborg, O. Hansen, I. Chorkendorff, *J. Am. Chem. Soc.* **2013**, 135, 1057.
[442] S. Hu, N.S. Lewis, J.W. Ager, J. Yang, J.R. McKone, N.C. Strandwitz, *J. Phys. Chem. C.* **2015**, 119, 24201.
[443] L. Ji, M.D. McDaniel, S. Wang, A.B. Posadas, X. Li, H. Huang, J.C. Lee, A.A. Demkov, A.J. Bard, J.G.A. Ekerdt, *Nat Nano,* **2015**, 10, 84.
[444] E. Fabbri, A. Habereder, K. Waltar, R. Kotz, T. J. Schmidt, *Catal. Sci. Technol*. **2014**, 4, 3800.
[445] S. Ida, K. Yamada, T. Matsunaga, H. Hagiwara, Y. Matsumoto, T. Ishihara, *J. Am. Chem. Soc.* **2010**, 132, 17343.
[446] A. Zadick, L. Dubau, N. Sergent, G. Berthomé, M. Chatenet, *ACS Catal.* **2015**, *5*, 4819.
[447] A. Kojima, K. Teshima, Y. Shirai, and T. Miyasaka, *J. Am. Chem. Soc.,* **2009**, 131, 6050.
[448] J.H. Im, C.R. Lee, J.W. Lee, S.W. Park, N.G. Park, *Nanoscale*, **2011**, 3, 4088.
[449] H.S. Kim, C.R. Lee, J.H. Im, K.B. Lee, T. Moehl, A. Marchioro, S.J. Moon, R. Humphry Baker, J.H. Yum, J. E. Moser, M. Grätzel, and N.G. Park, *Sci. Rep.* **2012***,* 2, 591.
[450]J. Salbeck, N. Yu, J. Bauer, F. Weissörtel, H. Bestgen, *Synthetic Metals*, **1997**, 91,209.
[451] U.Bach, *Nature* ,**1998**, 395, 583.
[452] NREL Efficiency Chart. https://www.nrel.gov/pv/assets/images/efficiency-chart.png (**2017**)
[453] B.Wang, X. Xiao, T. Chen. *Nanoscale,* **2014** *,* 6, 12287.
[454] J. Burschka, N. Pellet, S. J. Moon, R. Humphry-Baker, P. Gao, M. K.Nazeeruddin, M. Gratzel, *Nature*, **2013**, 499, 316.
[455] S. Chatterjee, A. Bera, A. J. Pal, *ACS Appl. Mater. Interfaces* , **2014**, 6, 20479.
[456] F. Matteocci, G. Mincuzzi, F. Giordano, A. Capasso, E. Artuso, C. Barolo, G. Viscardi, T. M. Brown, A. Reale, A. Di Carlo*, Org. Elec-tron,* **2013**, 14, 1882.
[457] D. Liu, T. L. Kelly, *Nat. Photonics* , **2014**, 8, 133.
[458] T. Leijtens, I.-K. Ding, T. Giovenzana, J. T. Bloking, M. D. McGehee, A. Sellinger, *ACS Nano* , **2012**, 6, 1455.
[459] J. H. Noh, S. H. Im, J. H. Heo, T. N. Mandal, S. I. Seok, *Nano Lett*., **2013**, 13, 1764.
[460] K. Wojciechowski, M. Saliba, T. Leijtens, A. Abate, H. J. Snaith, *Energy Environ. Sci*., **2014**, 7, 1142.
[461] J. A. Christians, R. C. M. Fung, P. V. Kamat, *J. Am. Chem. Soc*. **2014**,136, 758.

[462] O. Malinkiewicz, C. Roldán-Carmona, A. Soriano, E. Bandiello, L. Camacho, M. K. Nazeeruddin, H. J. Bolink, *Adv. Energy Mater.* **2014**, 4, 1400345.
[463] Z. Wu, S. Bai, J. Xiang, Z. Yuan, Y. Yang, W. Cui, X. Gao, Z. Liu, Y. Jin, B. Sun, *Nanoscale* , **2014**, 6, 10505.
[464] J. Seo, J. H. Noh, S. I. Seok, *Acc. Chem. Res*., **2016**, 49, 562.
[465] J. Burschka, A. Dualeh, F. Kessler, E. Baranoff, N.-L. Cevey-Ha,C. Yi, M. K. Nazeeruddin, M. Graetzel, *J. Am. Chem. Soc.* **2011**, 133,18042.
[466] K. Walzer, B. Maennig, M. Pfeiffer, K. Leo, *Chem. Rev*., **2007**, 107, 1233.
[467] a) A. Abate, T. Leijtens, S. Pathak, J. Teuscher, R. Avolio, M. E. Errico, J. Kirkpatrik, J. M. Ball, P. Docampo, I. McPherson, H. J. Snaith, *Phys. Chem. Chem. Phys*., **2013**, 15, 2572.
[468] T. Leijtens, J. Lim, J. Teuscher, T. Park, H. J. Snaith, *Adv. Mater*., **2013**, 25, 3227.
[469] W. H. Nguyen, C. D. Bailie, E. L. Unger, M. D. McGehee, *J. Am. Chem. Soc.*, **2014**, 136, 10996.
[470] T. Salim, S. Sun, Y. Abe, A. Krishna, A. C. Grimsdale, Y. M. Lam, *J. Mater. Chem. A*., **2015**, 3, 8943.
[471] J. Liu, Y. Wu, C. Qin, X. Yang, T. Yasuda, A. Islam, K. Zhang, W. Peng, W. Chen, L. Han, *Energy Environ. Sci*., **2014**, 7, 2963.
[472] J. Krüger, R. Plass, L. Cevey, M. Piccirelli, M. Grätzel, U. Bach, *Appl. Phys. Lett*., **2001**, 79, 2085.
[473] G. Divitini, S. Cacovich, F. Matteocci, L. Cinà, A. Di Carlo, C. Ducati, *Nat. Energy,* **2016**, 1, 15012.
[474] E. J. Juarez-Perez, M. Wußler, F. Fabregat-Santiago, K. Lakus-Wollny, E. Mankel, T. Mayer, W. Jaegermann, I. Mora-Sero, *J. Phys. Chem. Lett*., **2014**, 5, 680.
[475] G. E. Eperon, V. M. Burlakov, P. Docampo, A. Goriely, H. J. Snaith, *Adv. Funct. Mater*., **2014**, 24, 151.
[476] R. Roesch, K. R. Eberhardt, S. Engmann, G. Gobsch, H. Hoppe, *Sol. Energy Mater Sol. Cells*, **2013**, 117, 59.
[477] A. Dualeh, T. Moehl, N. Tétreault, J. Teuscher, P. Gao, M. K. Nazeeruddin, M. Grätzel, *ACS Nano* , **2014**, 8, 362
[478] S. Guarnera, A. Abate, W. Zhang, J. M. Foster, G. Richardson, A. Petrozza, H. J. Snaith, *J. Phys. Chem. Lett.,* **2015**, 6, 432.
[479] A. Kojima, K.Teshima, Y. Shirai, T. Miyasaka, *JACS*,**2009**, 131, 6050.
[480] N. J. Jeon, J. H. Noh, Y. C. Kim, W. S. Yang, S. Ryu, and S. Il Seok, *Nat. Mater*., **2014**, 13, 897.
[481] M. Xiao, F. Huang, W. Huang, Y. Dkhissi, Y. Zhu, J. Etheridge, A. Gray- Weale, U. Bach, Y.-B. Cheng, and L. Spiccia, *Angew. Chem. Int. Ed.,* **2014**, 126, 10056.
[482] J. Burschka, N. Pellet, S.Moon, R.Humphry-Baker, P. Gao, M.K. Nazeeruddin , M. Grätzel, *Nature*, **2013**, 499, 316.
[483] Z. Xiao, C. Bi, Y. Shao, Q. Dong, Q. Wang, Y. Yuan, C. Wang, Y. Gaob, J. Huang, *Energy Environ. Sci*, **2014**, 7, 2619.
[484] L.C. Chioaru, L. Craciun, O. Oprea, I. Jitaru, *Adv. Mater*, **2011**,5, 1097.
[485] M. Wright, A. Uddin, *Sol. Energy Mater Sol. Cells*, **2012**, 107, 87.
[486] X. Yang, M. Yanagida, L. Han*, Energy and Environ. Sci*., **2013**, 6, 54.
[487] http://solarcellcentral.com/solar_page.html
[488] A. Hagfeldt, G. Boschloo, L. Sun, L. Kloo, H. Pettersson, *Chem. Rev*. , **2010**, 110, 6595.
[489] S.D. Stranks, H.J. Snaith, *Nature*, **2015**, 10, 391.
[490] J.A. Christians, J.S. Manser, P.V. Kamat, *J. Phys. Chem. Lett.,* **2015**, 6, 852.
[491] X. Li, H. Zhu, *J. Materiomics.,* **2015**,1, 33.
[492] A. Capasso, F. Matteocci, L. Najafi, M. Prato, J. Buha, L. Cinà, A.D. Carlo, F. Bonaccorso, *Adv. Energy Mater.*,**2016**, 6,16.
[493] M. A. Green, A. Ho-Baillie, H. J. Snaith, *Nat. Photonics* , **2014**, 8, 506.
[494] J. H. Noh, S. H. Im, J. H. Heo, T. N. Mandal, S. I. Seok, *Nano Lett*. **2013**, 13, 1764.
[495] A. Capasso, A. E. D. R. Castillo, L. Najafi, V. Pellegrini, F. Bonaccorso, F. Matteocci, L. Cinà, A. D. Carlo, presented at 2015 IEEE 15th Int. Conf. on Nanotechnology (IEEE-NANO), 27–30 July **2015**.
[496] G. Divitini, S. Cacovich, F. Matteocci, L. Cinà, A. Di Carlo, C. Ducati, *Nat. Energy,* **2016**, 1, 15012.
[497] F. Matteocci, Y. Busby, J.-J. Pireaux, G. Divitini, S. Cacovich, C. Ducati, A. Di Carlo, *ACS Appl. Mater. Interfaces* , **2015**, 7, 26176.
[498] A. C. Ferrari, F. Bonaccorso, V. Fal'ko, K. S. Novoselov, S. R. T. Neil, Q. Tannock, T. Lofwander, J. Kinaret, *Nanoscale* **2015**, 7, 4598.
[499] J. Halme, P. Vahermaa, K. Miettunen, P. Lund, *Adv. Mater*., **2010**, 22, 210.
[500] F. Matteocci, S. Razza, F. Di Giacomo, S. Casaluci, G. Mincuzzi, T. M. Brown, A. D'Epifanio, S. Licoccia, A. Di Carlo, *Phys. Chem. Chem. Phys*., **2014**, 16, 3918
[501] A. L. Palma, L. Cinà, S. Pescetelli, A. Agresti, M. Raggio, R. Paolesse, F. Bonaccorso, A. Di Carlo, *Nano Energy,* **2016**, 22, 349.
[502] C.C. Chueh, C.Z. Li, A. K.Y. Jen, *Energy Environ. Sci.,* **2015**, 8, 1160.
[503] C. Bi, Q. Wang, Y. Shao, Y. Yuan, Z. Xiao, J. Huang, *Nat. Commun*., **2015**, 6, 7747.
[504] Y. Bai, Q. Dong, Y. Shao, Y. Deng, Q. Wang, L. Shen, D. Wang, W. Wei, J. Huang, *Nat. Commun*., **2016**, 7, 12806.

[505] A. Intaniwet, C. A. Mills, P. J. Sellin, M. Shkunov, J. L. Keddie, *ACS Appl. Mater. Interfaces*, **2010**, 2, 1692.
[506] A. Berkdemir, H. R. Gutiérrez, A. R. Botello-Méndez, N. Perea-López, A. Laura Elías, C. Chia, B. Wang, V. H. Crespi, F. López-Urías, *Sci. Rep*, **2013**, 3, 1755.
[507] G. Kakavelakis, T. Maksudov, D. Konios, I. Paradisanos, G. Kioseoglou, E. Stratakis, E. Kymakis, *Adv. Energy Mater*., **2017**, 7, 1602120.
[508] P. Docampo, J.M. Ball, M. Darwich, G.E. Eperon, H.J. Snaith, *Nat. Commun*., **2013**, 4, 2761.
[509] Z. Hawash, L. K. Ono, S. R. Raga, M. V. Lee and Y. Qi, *Chem. Mater*., **2015**, 27, 562.
[510] Y. Rong , L. Liu , A. Mei , X. Li , H. Han, *Adv. Energy Mater*., **2015**, 5, 1501066.
[511] N. H. Tiep, Z. L. Ku, H. J. Fan, *Adv. Energy Mater.,* **2016**, 6, 1501420.
[512] H. Tan, A. Jain, O. Voznyy, X. Lan, F. P. G. de Arquer, J. Z. Fan, R. Quintero-Bermudez, M. Yuan, B. Zhang, Y. Zhao, F. Fan, P. Li, L. N. Quan, Y. Zhao, Z.-H. Lu, Z. Yang, S. Hoogland, E. H. Sargent, *Science* , **2017**, 355, 722.
[513] M. Saliba, T. Matsui, K. Domanski, J.-Y. Seo, A. Ummadisingu, S. M. Zakeeruddin, J.-P. Correa-Baena, W. R. Tress, A. Abate, A. Hagfeldt, M. Grätzel, *Science*, **2016**, 35, 206.
[514] A. Agresti, S. Pescetelli, B. Taheri, A. E. Del Rio Castillo, L. Cina, F. Bonaccorso, A. Di Carlo, *ChemSusChem* , **2016**, 9, 2609.
[515] F. Fu, T. Feurer, T. P. Weiss, S. Pisoni, E. Avancini, C. Andres, S. Buecheler, A. N. Tiwari, *Nat. Energy*,**2016**, 2, 16190.
[516] E. H. Anaraki, A. Kermanpur, L. Steier, K. Domanski, T. Matsui, W. Tress, M. Saliba, A. Abate, M. Gratzel, A. Hagfeldt, J.-P. Correa-Baena, *Energy Environ. Sci.,* **2016**,9, 3128.